

**ULTRAFAST ALL-OPTICAL SWITCHING BASED ON  
IN<sub>Ga</sub>AsP GROWN BY He-PLASMA-ASSISTED  
MOLECULAR BEAM EPITAXY**

by

**Li Qian**

A thesis submitted in conformity with the requirements  
for the degree of Doctor of Philosophy  
Graduate Department of Electrical and Computer Engineering  
University of Toronto

© Copyright by Li Qian (2000)



National Library  
of Canada

Acquisitions and  
Bibliographic Services

395 Wellington Street  
Ottawa ON K1A 0N4  
Canada

Bibliothèque nationale  
du Canada

Acquisitions et  
services bibliographiques

395, rue Wellington  
Ottawa ON K1A 0N4  
Canada

*Your file* *Votre référence*

*Our file* *Notre référence*

The author has granted a non-exclusive licence allowing the National Library of Canada to reproduce, loan, distribute or sell copies of this thesis in microform, paper or electronic formats.

The author retains ownership of the copyright in this thesis. Neither the thesis nor substantial extracts from it may be printed or otherwise reproduced without the author's permission.

L'auteur a accordé une licence non exclusive permettant à la Bibliothèque nationale du Canada de reproduire, prêter, distribuer ou vendre des copies de cette thèse sous la forme de microfiche/film, de reproduction sur papier ou sur format électronique.

L'auteur conserve la propriété du droit d'auteur qui protège cette thèse. Ni la thèse ni des extraits substantiels de celle-ci ne doivent être imprimés ou autrement reproduits sans son autorisation.

0-612-53724-2

**Canada**

# **ULTRAFAST ALL-OPTICAL SWITCHING BASED ON IN<sub>Ga</sub>AsP GROWN BY He-PLASMA-ASSISTED MOLECULAR BEAM EPITAXY**

**Ph. D. Thesis, 2000**

**Li Qian**

**Graduate Department of Electrical and Computer Engineering**

**University of Toronto**

## **ABSTRACT**

We present the first experimental study of the optical properties of HELP InGaAsP (InGaAsP grown by He-plasma-assisted molecular beam epitaxy) relevant to all-optical switching, and the first demonstration of picosecond switching using this material.

We observed an optical response time of 15 ps, a nonlinear index change as large as 0.077, a sharp absorption band edge, and a small absorption tail in HELP InGaAsP. The unique coexistence of ultrafast response, large interband nonlinearity, and small band-tail absorption, never before reported, makes HELP InGaAsP particularly suitable for ultrafast all-optical switching. Additionally, faster response (subpicosecond) was achieved by doping the material with beryllium, and moderate doping (up to  $\sim 10^{18} \text{ cm}^{-3}$ ) did not significantly alter the absorption edge.

We systematically studied the response time variations with doping concentration, annealing temperature, carrier density, and wavelength. We conclude that, (a) Be doping reduces the response

---

time by compensating for donor-like mid-gap states, thus increasing the electron trap concentration; (b) annealing removes defects responsible for fast carrier trapping; (c) the response time increases with carrier density due to limited trap states; (d) the response time varies with wavelength due to difference in electron and hole trapping cross-sections, which were determined based on experimental results and a phenomenological two-trap-level rate equation model.

We investigated two types of HELP-InGaAsP-based all-optical switching devices, the nonlinear directional coupler (NLDC) and the asymmetric Fabry-Pérot (AFP) switch.

Based on numerical modelling and waveguide loss measurements, we conclude that, while HELP-InGaAsP-based passive NLDCs are in principle viable, practical devices will tend to require high switching energy, and will likely experience low contrast and high insertion loss.

We demonstrated that AFP devices will outperform NLDCs in contrast ratio, throughput, bandwidth, switching time, and polarization-sensitivity. We designed and fabricated three prototype AFP devices, and achieved polarization-independent switching with a 5 ps switching window, 20 dB contrast ratio,  $\geq 10\%$  throughput, 25–40 nm bandwidth (at  $\geq 10$  dB contrast ratio), and 0.5–1.4 pJ/ $\mu\text{m}^2$  switching energy density.

HELP InGaAsP is a promising material for ultrafast switching and other applications requiring ultrafast nonlinear operations. The HELP-InGaAsP-based AFP device we demonstrated is well suited for demultiplexing high-bit-rate data in practical optical communications systems.

## **ACKNOWLEDGMENTS**

First and foremost, I like to thank my supervisor, Professor Peter W. E. Smith, for his valuable advice, constant encouragement, and guidance throughout the course of my research. My deeply felt gratitude also extends to Dr. Seldon D. Benjamin, for his helpful advice and guidance during the early stage of this work, and to Dr. Brad J. Robinson, for his insightful suggestions and his expertise in growing the samples used in this work. I am grateful to Dr. Heidi Pinkney, who took a great deal of trouble to process the waveguide samples for this work, and with whom I had many constructive discussions.

My thanks extend to Professor David A. Thompson for his advice and suggestions, to my colleagues, Lawrence, David, Vani, and Thomas, for their input, suggestions, and helpful discussions, and to Fred, who patiently taught me how to use the scanning electron microscope. I also like to thank Professor Peter R. Herman, who first started me on a career in photonics. My achievements today owe a great deal to my parents and others who brought me up, to whom I will remain grateful throughout my life.

I like to acknowledge the financial support from Nortel Networks, Natural Science and Engineering Research Council (NSERC), Photonics Research Ontario, Materials and Manufacturing Ontario. I thank NSERC, University of Toronto, and the Government of Ontario for the scholarships they provided for my graduate research.

Finally, I like to express my heartfelt gratitude towards Florin, who has spent many sleepless nights proofreading and typesetting for this thesis, and without whose affection, friendship, criticism and support, this work would have been impossible to complete.

# TABLE OF CONTENTS

Abstract .....	ii
Acknowledgments .....	iv
List of Tables .....	viii
List of Figures .....	ix
List of Abbreviations .....	xvii
Chapter 1: Introduction .....	1
1.1 Why ultrafast all-optical switching? .....	1
1.1.1 Multiplexing optical signals .....	2
1.1.2 Ultrafast optical switching .....	2
1.1.3 Current telecommunications systems in the laboratories and in the real world .....	5
1.2 Motivation and aim of this work .....	6
1.3 Main contribution of this work .....	7
1.4 Organization of the thesis .....	8
Chapter 2: All-Optical Switching: Mechanisms and Device Configurations .....	9
2.1 Switching mechanisms .....	9
2.1.1 Switching mechanisms based on nonlinear absorption .....	9
2.1.2 Switching mechanisms based on nonlinear refraction .....	11
2.1.2.1 Polarization rotation type .....	11
2.1.2.2 Wave-vector matching type .....	12
2.1.2.3 Interferometric type .....	12
2.1.2.4 Wavelength shifting type .....	13
2.1.3 Switching mechanisms based on cascaded second-order nonlinearity .....	14
2.2 All-optical switching devices .....	14
2.2.1 Device requirements .....	14
2.2.2 Demonstrated all-optical switching devices .....	16
2.2.2.1 Nonlinear directional couplers (NLDC) .....	16
2.2.2.2 Mach-Zehnder (MZ) devices .....	17
2.2.2.3 Nonlinear optical loop mirrors (NOLM) .....	20
2.2.2.4 Nonlinear semiconductor element in a fibre loop mirror .....	22
2.2.2.5 Asymmetric Fabry-Pérot devices (AFP) .....	24
2.2.2.6 Summary of ultrafast all-optical devices .....	26
Chapter 3: Materials for Ultrafast All-Optical Switching .....	28
3.1 Optical nonlinearities .....	28
3.2 Material requirements .....	30
3.3 Fast nonlinear processes in semiconductors .....	32
3.3.1 Fast nonlinear phenomena in conventional semiconductors .....	32
3.3.2 Semiconductors with ultrafast carrier lifetimes .....	37
3.4 Summary .....	43

Chapter 4: Optical Characterization of HELP InGaAsP .....	44
4.1 Diagnostic tools and techniques .....	44
4.1.1 Optical Parametric Oscillator .....	44
4.1.2 Pump-probe technique for measuring material response times .....	46
4.1.3 Z-scan technique for measuring light-induced index change .....	50
4.1.4 Fourier transform infrared spectroscopy for measuring absorption spectra .....	51
4.2 Initial studies on carrier-induced index change, response time, and absorption .....	53
4.2.1 Optical response times .....	54
4.2.2 Light-induced index changes .....	55
4.2.3 Absorption spectra around band edge .....	56
4.3 Doping, annealing and other conditions affecting material properties .....	58
4.3.1 Effects of Be doping .....	58
4.3.1.1 Material response times of Be-doped HELP InGaAsP .....	60
4.3.1.2 Absorption spectra of Be-doped HELP InGaAsP .....	64
4.3.2 Effects of helium plasma condition during growth .....	66
4.3.3 Effects of annealing .....	70
4.3.2.1 Material response times of annealed HELP InGaAsP .....	71
4.3.2.2 Absorption spectra of annealed HELP InGaAsP .....	77
4.3.4 Response time variation with carrier density .....	81
4.4 Dual-wavelength study on material response times .....	85
4.4.1 Probe wavelength above the band edge .....	85
4.4.2 Probe wavelength in the band tail .....	88
4.4.3 Probe wavelength below the band edge .....	88
4.5 Rate equation modelling .....	90
4.5.1 Defect levels in HELP InGaAsP .....	90
4.5.2 Two-trap-level rate equation modelling .....	92
4.6 Dual-pulse experiments .....	95
4.7 Conclusions .....	97
Chapter 5: All-Optical Switching Devices Based on HELP InGaAsP .....	99
5.1 Nonlinear directional coupler .....	99
5.1.1 Theoretical considerations .....	99
5.1.1.1 Principle of operation .....	99
5.1.1.2 Modelling tools .....	102
5.1.1.3 Design parameters .....	106
5.1.2 Single waveguide experiments .....	114
5.1.2.1 Waveguide structures: growth and processing .....	115
5.1.2.2 Imaging the output facet and the output modes .....	117
5.1.2.3 Absorption measurements on single waveguide structures .....	122
5.1.3 Possible problems in the practical implementation of NLDC devices .....	127
5.2 Asymmetric Fabry-Pérot device .....	130
5.2.1 Theoretical considerations .....	130

5.2.1.1 Device configuration and principle of operation .....	130
5.2.1.2 Device Modelling .....	132
5.2.1.3 Design parameters .....	134
5.2.2 AFP device prototypes based on Be-doped HELP InGaAsP .....	138
5.2.2.1 Device structure and fabrication .....	138
5.2.2.2 Device characterization methods .....	140
5.2.2.3 Device demonstration .....	142
5.2.2.4 Summary and discussion of device performance .....	152
5.3 Conclusions .....	156
Chapter 6: Conclusions and Future Work .....	158
6.1 Summary and conclusions .....	158
6.1.1 Material studies .....	158
6.1.2 Device studies .....	159
6.2 Original Contributions .....	161
6.3 Directions of future research .....	163
6.3.1 Improvements on the current AFP device .....	163
6.3.2 Ultrafast all-optical switches in high speed WDM/TDM optical networks .....	164
6.3.3 Ultrafast HELP-InGaAsP-based devices .....	166
Appendix A: Z-Scan Technique for Measuring Light-Induced Index Change .....	167
Appendix B: Free-Electron Absorption and Free-Hole Absorption in HELP InGaAsP .....	173
Appendix C: Bányai-Koch Model Formulation and Parameters Used in This Work .....	178
References .....	184

# LIST OF TABLES

Table 1.1	Terahertz transmission experiments .....	6
Table 2.1	Comparison of demonstrated ultrafast all-optical devices (present study not included) .....	27
Table 4.1	Samples and measurements performed in the initial studies .....	53
Table 4.2	Description of samples used for study of Be-doping effects .....	59
Table 4.3	Samples used to determine optimal He-plasma conditions .....	67
Table 4.4	Samples used in annealing study .....	70
Table 5.1	Coupling lengths (LTE and LTM) calculated by Fwave IV for three coupler geometries with the layer structure illustrated in Figure 5.8 .....	109
Table 5.2	Comparison of device parameters and performances .....	152

# LIST OF FIGURES

Figure 1.1	Fibre absorption spectrum. After [1].	1
Figure 1.2	Schematics for (a) TDM, (b) WDM and (c) CDMA.	3
Figure 1.3	Physical limits of optical switching. After [9].	4
Figure 1.4	The transmission capacity of optical fibre systems. After [10]	5
Figure 2.1	Switching mechanisms and switching devices	10
Figure 2.2	Schematic diagram of switching based on nonlinear absorption	11
Figure 2.3	Polarization rotation switch (a) based on Kerr medium, control is linearly polarized; (b) based on spin-polarization, control is circularly polarized.	12
Figure 2.4	Nonlinear Mach-Zehnder interferometer with (a) nonlinear element (NLE) only in one arm and (b) unequal nonlinear path lengths	13
Figure 2.5	Periodic power exchange between the two waveguides of a coupler	16
Figure 2.6	Schemes of using slow nonlinear element to achieve fast switching: (a) A symmetric MZ interferometer with two control pulses, after [87]. (b) An asymmetric MZ interferometer, after [89]. (c) a UNI device, after [92].	19
Figure 2.7	Schematic of a NOLM	20
Figure 2.8	Polarization-independent implementation of a NOLM using two identical, cross-spliced birefringent fibres. After [101].	21
Figure 2.9	Generic configuration for a nonlinear element in a loop mirror	23
Figure 2.10	Generic configuration of an AFP. Data beams drawn at an angle for clarity. They are in fact normal to the device to ensure polarization-independent operation.	24
Figure 3.1	Material requirements for ultrafast all-optical switching deriving from device requirements.	31
Figure 3.2	Optical selection rules and transition probabilities for transitions occur at the centre of the Brillouin zone (G-point). The numbers near the arrows representing the transition probabilities. After [142]	34
Figure 3.3	Carrier tunnelling in quantum well structures. (a) Tunnelling in type I quantum wells. After [145] (b) Tunnelling in type II quantum wells, where the first excited state in the well is lower than the conduction band bottom of the barrier layer at G-point, but higher than that at the X-point. After [146].	36
Figure 3.4	Gas-source Molecular Beam Epitaxy (MBE) system at McMaster University, equipped with the Electron Cyclotron Resonance (ECR) chamber for plasma-assisted growth. MFM = mass flow meter. After [173].	42
Figure 4.1	Schematic of the optical parametric oscillator (OPO). The gain medium, KTP (KTiOPO <sub>4</sub> ), is pumped by a tunable mode-locked Ti-sapphire laser. The laser cavity is stabilized by an EMT (electromechanical transducer). The signal output is taken from the resonating cavity. The idler is not resonated and it is taken directly after the parametric generation. The signal and idler have orthogonal polarizations.	45

Figure 4.2	Tuning ranges of the OPO signal and idler outputs, obtained by tuning the Ti-sapphire wavelength. Signal tuning is limited to 1.46 $\mu\text{m}$ –1.64 $\mu\text{m}$ by the bandwidth of the cavity mirrors. Symbols represent measured data, lines are calculated. After [176].	46
Figure 4.3	Above-band absorption ( $h\nu_1$ ) versus band-tail absorption ( $h\nu_2$ ). The left diagram illustrates that absorption obeys the k-selection rule, the right diagram shows the Density Of States (DOS) involved in these transitions. For above-band transitions, valence band DOS is much higher than conduction band DOS, whereas for band-tail transitions, the DOS's are comparable.	47
Figure 4.4	Schematic diagram of the pump-probe experiment. This set up allows for easy conversion between single-wavelength and dual-wavelength operation, as well as between single-pulse and dual-pulse operation.	49
Figure 4.5	Schematic diagram of the Z-scan experiment which measures the average index change in the sample induced by pulses from the OPO over the pulse duration ( $\sim 1$ ps)	50
Figure 4.6	Principle of operation of an FTIR spectrometer based on a Michelson interferometer (After [3]). The spectrum of the "source" is obtained by performing a Fourier Transform on its auto-correlation signal, detected at the output of the Michelson interferometer.	52
Figure 4.7	Schematic diagram of the Bomem Michelson spectrometer. The test sample is placed at the "main focus." After [3]	52
Figure 4.8	Change in transmission measured by single-wavelength pump-probe technique in sample 1640 (HELP sample) using 1 ps pulses at 1.55 $\mu\text{m}$ , showing a 15 ps optical response time.	54
Figure 4.9	Comparison of index changes induced in sample 1640 (HELP InGaAsP) and sample 1639 (standard InGaAsP) by 1ps pulses of varying intensity and at a series of wavelengths detuned from the band edge. Points are actual data; curves are guides for the eye.	56
Figure 4.10	Absorption spectra of InGaAsP samples around band edge illustrating the major advantage of HELP growth over low-temperature growth. Comparison between the HELP sample and the standard sample (a) indicates that high crystalline quality is maintained in the HELP sample. The lack of an identifiable band edge in the low-temperature-grown sample (with Be doping) (b) indicates a poor crystalline quality. (Data for the standard and HELP samples have been modified to compensate for the Fabry-Pérot effects.)	57
Figure 4.11	Optical response times of HELP InGaAsP samples with various Be doping concentrations, measured by single-wavelength pump-probe technique at 1.50 $\mu\text{m}$ for pump pulse energies of (a) 0.1 nJ and (b) 0.6 nJ.	61
Figure 4.12	(a) Optical response of sample 2460 (standard InGaAsP doped with $6 \times 10^{18} \text{ cm}^{-3}$ Be), measured by single-wavelength pump-probe technique at 1.50 $\mu\text{m}$ . (b) Linear fit of the data in (a) on a natural log scale yields a response time of 325 ps.	62
Figure 4.13	Absorption spectra of the InGaAsP samples around the band edge, obtained by FTIR measurements. The steepness of the absorption edge is maintained in the HELP samples with doping concentration up to $1 \times 10^{18} \text{ cm}^{-3}$ , indicating good crystalline quality. Even with $1 \times 10^{18} \text{ cm}^{-3}$ doping, there is still an identifiable band edge. The samples are not antireflection coated, so small Fabry-Pérot fringes are seen in the low absorption region.	65

Figure 4.14 Comparison of band edge absorption spectra of a heavily-doped HELP sample and a heavily-doped standard sample indicates that HELP growth introduce little additional absorption at the band tail. ....	66
Figure 4.15 Comparison of optical response times of two undoped HELP InGaAsP samples, one grown under the standard plasma conditions (1969), the other under doubled helium flow rate and doubled microwave power (1971). Response times are measured at 1.50 $\mu\text{m}$ (above band) with pump pulse energies of (a) 0.14 nJ and (b) 0.55 nJ. ....	68
Figure 4.16 Comparison of optical response times of two Be-doped ( $3 \times 10^{17} \text{ cm}^{-3}$ ) HELP InGaAsP samples, one grown under the standard plasma conditions (1970), the other under half the helium flow rate and half the microwave power (1973). Response times are measured at 1.50 $\mu\text{m}$ (above band) with pump pulse energies of (a) 0.14 nJ and (b) 0.35 nJ. ....	69
Figure 4.17 Optical response times of the undoped HELP samples of various anneals measured at 1.50 $\mu\text{m}$ (above-band) for carrier densities of (a) $7 \times 10^{16} \text{ cm}^{-3}$ and (b) $2 \times 10^{17} \text{ cm}^{-3}$ . ....	72
Figure 4.18 Optical response times of the lightly Be-doped ( $3 \times 10^{17} \text{ cm}^{-3}$ ) HELP samples of various anneals, measured at 1.50 $\mu\text{m}$ (above-band) for carrier densities of (a) $8 \times 10^{16} \text{ cm}^{-3}$ and (b) $5 \times 10^{17} \text{ cm}^{-3}$ . ....	74
Figure 4.19 Optical response times of the medium Be-doped ( $1 \times 10^{18} \text{ cm}^{-3}$ ) HELP samples of various anneals measured at 1.50 $\mu\text{m}$ (above-band) for carrier densities of (a) $8 \times 10^{16} \text{ cm}^{-3}$ and (b) $7 \times 10^{17} \text{ cm}^{-3}$ . ....	75
Figure 4.20 Optical response times of the heavily Be-doped ( $6 \times 10^{18} \text{ cm}^{-3}$ ) HELP samples of various anneals measured at 1.50 $\mu\text{m}$ (above-band) for carrier densities of (a) $8 \times 10^{16} \text{ cm}^{-3}$ and (b) $5 \times 10^{17} \text{ cm}^{-3}$ . ....	76
Figure 4.21 Absorption spectra of undoped HELP InGaAsP of various anneals around the band edge. A blue shift of $\sim 30 \text{ nm}$ is observed between the as-grown material and the $600^\circ\text{C}$ annealed material. ....	78
Figure 4.22 Absorption spectra of two standard undoped InGaAsP (as grown and $600^\circ \text{C}$ annealed) around the band edge. No band edge blue shift is observed, indicating that the blue shift observed in Figure 4.21 is due to HELP growth. ....	78
Figure 4.23 Absorption spectra of lightly Be-doped ( $3 \times 10^{17} \text{ cm}^{-3}$ ) HELP InGaAsP of various anneals around the band edge. Slight band edge blue shifts with increasing annealing temperature are observed. ....	79
Figure 4.24 Absorption spectra of medium Be-doped ( $1 \times 10^{18} \text{ cm}^{-3}$ ) HELP InGaAsP of various anneals around the band edge. Annealing does not alter the band edge absorption. ....	79
Figure 4.25 Absorption spectra of heavily Be-doped ( $6 \times 10^{18} \text{ cm}^{-3}$ ) HELP InGaAsP of various anneals around the band edge. Annealing does not result in improved band edge, but only reduces the above-band absorption. ....	80
Figure 4.26 Optical response times of undoped as-grown HELP InGaAsP measured by above-band single-wavelength (1.50 $\mu\text{m}$ ) pump-probe technique under various carrier densities, clearly showing the "bottleneck" effect. ....	82
Figure 4.27 Optical response times of lightly Be-doped as-grown HELP InGaAsP measured by above-band single-wavelength (1.50 $\mu\text{m}$ ) pump-probe technique under various carrier densities. A slightly smaller "bottleneck" effect is observed here than in the undoped case, due to increase in empty trap concentration. ....	82
Figure 4.28 Optical response times of medium Be-doped as-grown HELP InGaAsP measured by above-band single-wavelength (1.50 $\mu\text{m}$ ) pump-probe technique under various carrier densities. The bottleneck	

effect observed here is smaller than in the undoped and lightly doped cases, due to increase in empty trap concentration. ....	83
Figure 4.29 Optical response times of heavily Be-doped as-grown HELP InGaAsP measured by above-band single-wavelength (1.50 $\mu\text{m}$ ) pump-probe technique under various carrier densities. No obvious "bottleneck" effect is observed in the as-grown sample (a), due to increase in empty trap concentration as well as increase in hole concentration. However, the "bottleneck" effect appears in the 600° C-annealed sample (b), due to drastic decrease in trap concentration by annealing. ....	84
Figure 4.30 Optical response times obtained by dual-wavelength pump-probe technique on (a) undoped and (b) Be-doped ( $1 \times 10^{18} \text{ cm}^{-3}$ ) HELP InGaAsP, under different pump pulse energies. Pump and probe wavelengths are 1510 and 1513 nm, respectively. The inset shows their position relative to the absorption edge. ....	86
Figure 4.31 Optical response times obtained by dual-wavelength pump-probe technique on (a) undoped and (b) Be-doped ( $1 \times 10^{18} \text{ cm}^{-3}$ ) HELP InGaAsP, under different pump pulse energies. Pump and probe wavelengths are 1516 and 1550 nm, respectively. The inset shows their position relative to the absorption edge. ....	87
Figure 4.32 Optical response times obtained by dual-wavelength pump-probe technique on (a) undoped and (b) Be-doped ( $1 \times 10^{18} \text{ cm}^{-3}$ ) HELP InGaAsP under different pump pulse energies. Pump and probe wavelengths are 1523 and 1600 nm, respectively. The inset shows their position relative to the absorption edge. ....	89
Figure 4.33 Schematic energy band diagram for the two-trap-level rate equation model, $E_F(\text{He})$ indicating the Fermi level of the undoped material, and $E_F(\text{He}+\text{Be})$ indicating that of the doped material. ....	92
Figure 4.34 Normalized conduction-band electron density ( $N_e$ ) decay curves for HELP InGaAsP samples of various doping concentrations. The symbols represent the decay curves of free-electron absorption ( $\alpha_{\text{fea}} \propto N_e$ ) obtained by dual-wavelength pump-probe measurements with the probe wavelength below the band edge. ....	94
Figure 4.35 Response times of the heavily Be-doped ( $6 \times 10^{18} \text{ cm}^{-3}$ ) HELP InGaAsP sample (2002) obtained by dual-wavelength dual-pulse pump-probe technique for (a) probe wavelength above the band, and (b) probe wavelength at band tail, indicating that fast, high-repetition-rate switching with this material is possible. ....	96
Figure 5.1 A coupler consisting of two closely-spaced identical waveguides. The coupling length $L$ is the distance over which one complete energy exchange takes place. (Same as Figure 2.5, redrawn here for convenience) ....	100
Figure 5.2 Cross-section of a coupler and the field amplitudes of the even and odd modes. ....	100
Figure 5.3 A typical Fwave IV output window: Coupler structure and field contour lines of a mode are shown in the lower panel. The upper panel gives the value of the effective index of this mode and indicates it is a quasi-TE mode (Horizontal). ....	102
Figure 5.4 Experimental and calculated absorption spectra of $\text{In}_{0.60}\text{Ga}_{0.40}\text{As}_{0.84}\text{P}_{0.16}$ . The experimental spectrum is measured by FTIR spectrometer on an undoped HELP InGaAsP; the calculated spectrum is obtained by program BK, with two input parameters (transition strength and broadening parameter) adjusted to yield a good fit with the experimental spectrum. ....	103

Figure 5.5	(a) Band edge absorption as a function of carrier density, calculated with the Bányai-Koch model. (b) Index change as a function of carrier density, calculated from (a) using Kramers-Krönig relation. ....	104
Figure 5.6	An example of numerical simulation of the index change as a function of time and position along a waveguide. This type of graph can be used to determine the distance over which uniform index is induced along the waveguide, and the accumulated phase change in the waveguide. ....	105
Figure 5.7	Cross-section of a NLDC consisting of buried ridge waveguides. W: ridge width. H: ridge height. S: guide separation. ....	107
Figure 5.8	Effective indices and field contours in an NLDC, as calculated by Fwave IV. The parameters used for calculation are: W = 3 $\mu\text{m}$ , H = 0.5 $\mu\text{m}$ , S = 2 $\mu\text{m}$ , cladding thickness = 0.75 $\mu\text{m}$ , cladding and substrate index = 3.17, guiding layer thickness = 0.5 $\mu\text{m}$ , guiding layer index = 3.42, wavelength = 1.55 $\mu\text{m}$ . (a) Even TE mode, (b) Odd TE mode, (c) Even TM mode, (d) Odd TM mode. ....	108
Figure 5.9	Coupling length as a function of guide separation for couplers with 2 $\mu\text{m}$ and 3 $\mu\text{m}$ ridge widths. Simulation for the same structure as in Figure 5.8. ....	109
Figure 5.10	Power exchange along a linear directional coupler with a coupling length of 100 $\mu\text{m}$ . After [195]. ....	110
Figure 5.11	Calculated induced index change at 1550 nm as a function of time and waveguide position. Control pulse: 2 ps Gaussian, peak intensity = 2 $\text{GW}/\text{cm}^2$ , wavelength = 1500 nm. Waveguide material: InGaAsP, band edge = 1500 nm, carrier lifetime = 15 ps. Applying this result to coupler 2 in Table 5.1, one obtains $\sim 80$ pJ switching energy. ....	112
Figure 5.12	Calculated induced index change at 1570 nm as a function of time and waveguide position. Control pulse: 2 ps Gaussian, peak intensity = 2.5 $\text{GW}/\text{cm}^2$ , wavelength = 1540 nm. Waveguide material parameters as in Figure 5.11. Applying this result to coupler 2 in Table 5.1, one obtains $\sim 100$ pJ switching energy. ....	112
Figure 5.13	Calculated induced index change at 1570 nm as a function of time and waveguide position. Control pulse: 2 ps Gaussian, peak intensity = 2.0 $\text{GW}/\text{cm}^2$ , wavelength = 1530 nm. Waveguide material parameters as in Figure 5.11. Applying this result to coupler 1 in Table 5.1, one obtains $\sim 40$ pJ switching energy. ....	113
Figure 5.14	(a) & (b) Schematic representations of structures A and B, respectively (c) & (d) Waveguides processed by etching. Structure A has a thicker guiding layer for better coupling; structure B is the same as that analysed by Fwave IV (see Figures 5.8 & 5.9) and the simulation program PP (see Figures 5.11–5.13). ....	115
Figure 5.15	SEM images of wet-etched waveguides, showing smooth surfaces and relatively vertical walls. (a) Structure A. (b) Structure B. ....	116
Figure 5.16	SEM images of RIE-processed waveguides. (a) Structure A (note rough top surface of the guiding layer). (b) Structure B (note large, rough pedestals). ....	117
Figure 5.17	SEM images showing large contaminants found in waveguides. (a) RIE-processed sample. (b) Wet-etched sample. ....	117
Figure 5.18	Various types of mechanical damage found in waveguides. (a), (b) RIE-processed waveguides. (c), (d) Wet-etched waveguides. ....	118

Figure 5.19 Schematic diagram of the experimental setup for coupling light from fibre to waveguide, and for imaging the output sample facet, and the output waveguide mode. ....	119
Figure 5.20 Output facet images. (a) With light output from a waveguide, when the tapered fibre tip is aligned with it. (b) Without light output, when the waveguide is moved laterally away from the fibre tip. The magnification of the image is not high enough to resolve the ridges of the waveguides. ....	120
Figure 5.21 Left: Output mode image of a 4 $\mu\text{m}$ -wide waveguide of structure A. Right: Image obtained when the tapered fibre tip is moved away from the waveguide. Input light is (a) TE polarized, and (b) TM polarized. ....	121
Figure 5.23 Field contours of higher-order modes in a 4 $\mu\text{m}$ -wide waveguide of structure A, calculated by Fwave IV. The largest contour is the 1% field contour, others are field contours from 10% to 90% at an increment of 10%. (a) TE mode. (b) TM mode. ....	121
Figure 5.22 Left: Output mode images of (a) a 5 $\mu\text{m}$ -wide waveguide and (b) a 4 $\mu\text{m}$ -wide waveguide of structure B. Right: Images obtained when the tapered fibre tip is moved away from the waveguide. ....	121
Figure 5.24 Schematic diagram of the experimental set up for measuring the absorption coefficient of the waveguide material. ....	123
Figure 5.25 Normalized transmission of TM polarized light through a 3 $\mu\text{m}$ -wide waveguide of structure A (wet-etched) as a function of wavelength. Parameters used for theoretical fitting are $L=430 \mu\text{m}$ , $\gamma=0.45$ . Absorption coefficient obtained from fitting is $37 \text{ cm}^{-1}$ . ....	125
Figure 5.26 Normalized transmission of TE polarized light through a 3 $\mu\text{m}$ -wide waveguide of structure A (wet etched) as a function of wavelength. Parameters used for theoretical fitting are $L=430 \mu\text{m}$ , $\gamma=0.45$ . Absorption coefficient obtained from fitting is $37 \text{ cm}^{-1}$ . ....	125
Figure 5.27 Normalized transmission of TM polarized light through a 6 $\mu\text{m}$ -wide waveguide of structure A (wet etched) as a function of wavelength. Parameters used for theoretical fitting are $L=430 \mu\text{m}$ and $\gamma=0.5$ . Absorption coefficient obtained from fitting is $32 \text{ cm}^{-1}$ . ....	126
Figure 5.28 Normalized transmission of TM polarized light through a 5 $\mu\text{m}$ -wide waveguide of structure B (RIE-etched) as a function of wavelength. Parameters used for theoretical fitting are $L=430 \mu\text{m}$ , $\gamma=0.365$ . Absorption coefficient obtained from fitting is $47 \text{ cm}^{-1}$ . ....	126
Figure 5.29 NLDCs with input and output waveguide branches to facilitate coupling light into and out of individual waveguides. ....	129
Figure 5.30 All-optical asymmetric Fabry-Pérot switching device configuration using HELP InGaAsP as active medium. For clarity, the data beams shown are not normal to the device, but normal incidence is used in actual implementation to ensure polarization-independent switching. ....	131
Figure 5.31 Absorption spectra of InGaAsP at low and high carrier densities, with relation to clock and data wavelengths. ....	131
Figure 5.32 Simulation results of an AFP device. Parameters used in simulation: Front layer = SiON, thickness = 241 nm, $n = 1.73$ ; Active layer = $\text{In}_{0.55}\text{Ga}_{0.45}\text{As}_{0.96}\text{P}_{0.04}$ , thickness = 3.13 $\mu\text{m}$ , carrier lifetime = 3 ps; Back mirror = 12 pairs of $\lambda/4 \text{ In}_{0.67}\text{Ga}_{0.33}\text{As}_{0.7}\text{P}_{0.3}/\text{InP}$ ; Control pulse = 1 ps Gaussian pulse at 1520 nm, peak intensity = 0.2 $\text{GW}/\text{cm}^2$ . (a) Off-time and	

on-time throughput. (b) Contrast ratio. (c) Switching window (relative reflectivity as a function of time). .....	133
Figure 5.33 Simulation results for off-time and on-time throughputs and contrast ratio spectra of three AFP devices with different parameters. (a) Front reflection = 4%, back reflection = 70%, thickness of active layer = 2.5 $\mu\text{m}$ , Finesse=0.72 (b) Front reflection = 0.3%, back reflection = 20%, thickness of active layer = 4.03 $\mu\text{m}$ , Finesse=0.18 (c) Front reflection = 0.3%, back reflection = 60%, thickness of active layer = 4.25 $\mu\text{m}$ , Finesse=0.22. Switching energy is the same for all three cases. ....	135
Figure 5.34 Simulations of switching windows produced by three different control pulse shapes, assuming a 5 ps carrier lifetime. Control pulses are at left, resulting windows at right. (a) Gaussian pulse. (b) Trapezoidal pulse. (c) Tailored-shape pulse. All three pulses yield a >20 dB contrast ratio for 5 ps, but the switching energy of (a) is 5 $\times$ that of (c). ....	137
Figure 5.35 Asymmetric Fabry-Pérot (AFP) device structure adopted in this work. ....	139
Figure 5.36 Experimental setup for measuring the low-intensity reflection spectra of our AFP devices. ....	140
Figure 5.37 Experimental set up for characterizing AFP device prototypes, using the tunable outputs of the Optical Parametric Oscillator (OPO) as control (pump) and data (probe). ....	141
Figure 5.38 Low-intensity reflection spectrum of the first AFP device. ....	143
Figure 5.39 Comparison of the absorption band edge calculated in our simulation with Pearsall's band-gap energy formula [208] with the absorption edge measured by FTIR. The large discrepancy explains the large shift from the wavelength designed for a reflectivity null. ....	143
Figure 5.40 Switching window of the first AFP device at 1495 nm after excitation by a 1.1 ps pump pulse at 1513 nm. Switching energy density is 0.5 $\text{pJ}/\mu\text{m}^2$ . ....	144
Figure 5.41 Relationship between contrast ratio, switching energy and switching time. The plot helps to identify an optimal operation region, marked grey. Control wavelength = 1515 nm, data wavelength = 1495 nm. ....	145
Figure 5.42 Reflection spectra of the high-reflection stack of the second AFP device. Measured spectrum is dotted, spectrum calculated from the simulation program is solid grey. ....	146
Figure 5.43 Reflection spectra of the second AFP device. (a) Before depositing the low-reflection dielectric layer. (b) With the low-reflection layer in place, showing a null at 1574 nm. ....	147
Figure 5.44 Switching window of the second AFP device at 1572 nm after excitation by a 1.1 ps control pulse at 1519 nm. Switching energy density is $\sim 0.5 \text{ pJ}/\mu\text{m}^2$ . ....	148
Figure 5.45 Contrast ratios and switching times of the second AFP device, measured under various switching energy densities. ....	148
Figure 5.46 Contrast ratio and throughput obtained from the second AFP device and plotted as functions of wavelength. Control wavelength is $\sim 1519 \text{ nm}$ . (a) Under conditions of low switching energy density (0.5 $\text{pJ}/\mu\text{m}^2$ ). (b) Under conditions of high switching energy density (1.4 $\text{pJ}/\mu\text{m}^2$ ). ....	149
Figure 5.47 Low-intensity reflection spectrum of the third AFP device. ....	150
Figure 5.48 Switching window of the third AFP device at 1542 nm after excitation by a 1.1 ps control pulse at 1515 nm. (a) Switching energy density = 0.5 $\text{pJ}/\mu\text{m}^2$ . (b) Switching energy density = 1.2 $\text{pJ}/\mu\text{m}^2$ . ....	150

---

Figure 5.49	Contrast ratio and throughput obtained from the third AFP device and plotted as functions of wavelength. (a) Under conditions of low switching energy density ( $0.5 \text{ pJ}/\mu\text{m}^2$ ). (b) Under conditions of high switching energy density ( $1.2 \text{ pJ}/\mu\text{m}^2$ ). .....	151
Figure 6.1	Examples of applications of ultrafast all-optical switches in WDM/TDM optical networks. All-optical switches can be used in optical nodes as, (a) high-speed demultiplexers in time-slotted systems, or, (b) high-speed optical header processors and optical routers in packet-switching systems. ....	165
Figure A.1	Effects of a thin sample location on the incident beam. (a) Sample placed before focus causes self-defocusing, leading to beam narrowing in the far-field. (b) Sample placed after focus causes self-focusing, leading to beam broadening in the far-field. After [213]. ....	165
Figure A.2	Calculated Z-scan transmittance for a negative (dashed) and a positive (solid) nonlinearity. After [177] .....	168
Figure A.3	Example of removing nonlinear absorption and sample inhomogeneity effects from Z-scan data. (a) High-intensity and low-intensity open aperture scan; (b) High-intensity and low-intensity standard Z-scan; and (c) result of division of standard z scan data by open-aperture scan data, which gives the Z-scan "signature," with contribution only from the nonlinear refractive index. ....	170
Figure B.1	Qualitative band structure of InGaAsP and possible transitions due to free electron and free-hole absorption. ....	171

# LIST OF ABBREVIATIONS

AFP	asymmetric Fabry-Pérot
AR	antireflection
AES	Auger electron spectroscopy
BAP	Bir-Aronov-Pikus
BER	bit error rate
CDMA	code-division multiple access
DFB	distributed feedback
DP	D'yakonov-Perel'
ECR	electron cyclotron resonance
EDFA	erbium-doped fibre amplifiers
EMT	electromechanical transducer
EY	Elliot-Yafet
FCA	free-carrier absorption
FEA	free-electron absorption
FHA	free-hole absorption
FP	Fabry-Pérot
FTIR	Fourier transform infrared
HELP InGaAsP	InGaAsP grown by helium-plasma-assisted molecular beam epitaxy
HELP	helium-plasma-assisted molecular beam epitaxy
HH	heavy hole
ID	identification number
IVBA	inter-valence-band absorption
KTP	potassium titanyl phosphate ( $\text{KTiOPO}_4$ )
LH	light hole
LT	low-temperature
LTG	low-temperature-grown/growth
MBE	molecular beam epitaxy
MFM	mass flow meter
MQW	multiple quantum well
MZ	Mach-Zehnder
NLDC	nonlinear directional coupler
NLE	nonlinear element
NOLM	nonlinear optical loop mirror
NTT	Nippon Telegraph and Telephone Corporation
OPO	optical parametric oscillator
OTDM	optical time-division-multiplexing
QW	quantum well
RHEED	reflection high-energy electron diffraction

RIE	reactive ion etching
SA	saturable absorber
SEM	scanning electron microscope
SLA	semiconductor laser amplifier
SLALOM	semiconductor laser amplifier in a loop mirror
TDM	time-division-multiplexing
TE	transverse electric
TM	transverse magnetic
TOAD	terahertz optical asymmetric demultiplexer
UNI	ultrafast nonlinear interferometer
WDM	wavelength-division-multiplexing

# Chapter 1

## INTRODUCTION

### 1.1 WHY ULTRAFAST ALL-OPTICAL SWITCHING?

The global village's hunger for information shows no sign of abating: every day more information has to be sent faster and further. This rapidly growing appetite for information creates, in its turn, the need for transmission media capable of sustaining it, and optical fibre, with its extremely low loss ( $<0.3$  dB/km) over an enormous bandwidth (25 THz) (Fig. 1.1) has been universally recognized as the best candidate for the job. Moreover, the advent of the erbium-doped fibre amplifiers (EDFAs) made possible the transmission of optical signals for thousands of kilometers without the need to convert optical signals into electronic signals for regeneration and amplification [2, 3], thereby eliminating the electronic bottleneck in transmission. The continuous expansion of the usable fibre bandwidth has focused current research onto its efficient utilization.

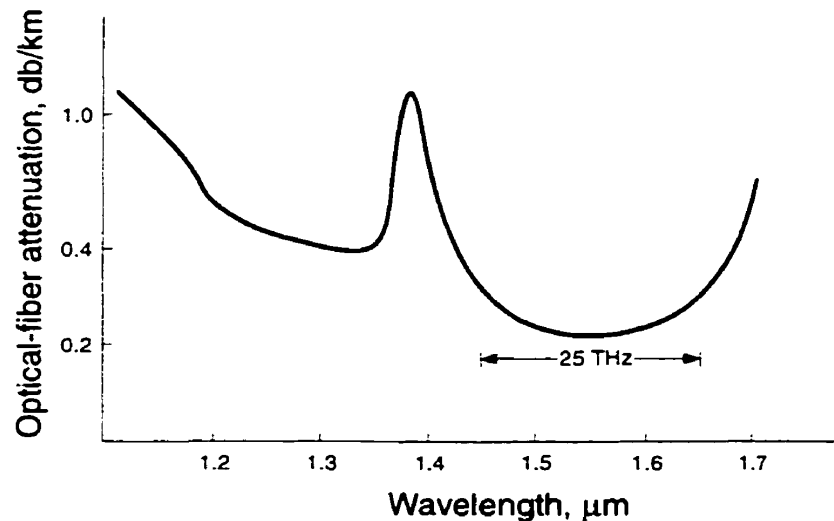


**Figure 1.1** Fibre absorption spectrum. After [1].

How can optical signals be transmitted using the entire fibre bandwidth of more than 25 THz? Theoretically, the most direct method would be to modulate the optical signal at 25 THz, which would require a modulator that could be turned on and off and on again in 40 femtoseconds.

While laser pulses as short as 5 fs have been demonstrated [4], making a device to operate at 25 THz rates would be technologically next to impossible: among other things, the heat generated as a by-product would in all likelihood cause the temperature to rise so much as to render the device unusable [5]. Therefore, a far easier and better method is multiplexing low-bit-rate signals before transmission over fibre, and demultiplexing them at the receiver end.

### 1.1.1 Multiplexing optical signals

Optical signals are commonly multiplexed in three ways: (1) in *time-division-multiplexing* (TDM) systems, signals are allotted different time slots, hence low-bit-rate signals are multiplexed into high-bit-rate signals (Fig. 1.2a); (2) in *wavelength-division-multiplexing* (WDM) systems, signals are allotted different wavelength channels, hence they may overlap in time, but not in wavelength (Fig. 1.2b); (3) in *code-division multiple access* (CDMA) systems, signals are encoded with different coding sequences in time- and/or wavelength-domain, hence they may overlap in both time and wavelength, but can be separated and recovered by decoding (Fig. 1.2c). Today's high-capacity long-haul transmission systems use exclusively WDM and/or TDM, primarily because they are straightforward to implement and less susceptible to noise and crosstalk than CDMA.

Although in theory (i.e. ignoring noise, fibre dispersion and nonlinearity), WDM and TDM have the same bandwidth efficiency, in practice, due to vast differences in their implementation, each technique has distinct advantages, but also creates unique problems. It has become more and more apparent that future high-capacity transmission systems will employ them both [1].

### 1.1.2 Ultrafast optical switching

High-capacity WDM-TDM systems require fast switching devices for time-domain demultiplexing. Studies on the physical limits of electronic devices show that their speed cannot be improved much beyond 10 GHz [6,7]. Although certain individual electronic devices can operate at  $\geq 10$  GHz, the resistance and capacitance of electronic interconnect severely limit the overall signal processing speed of an electronic chip. Integrating optical interconnects onto an electronic chip to improve speed has been proposed [8], but it is by no means clear that this constitutes a viable technology.

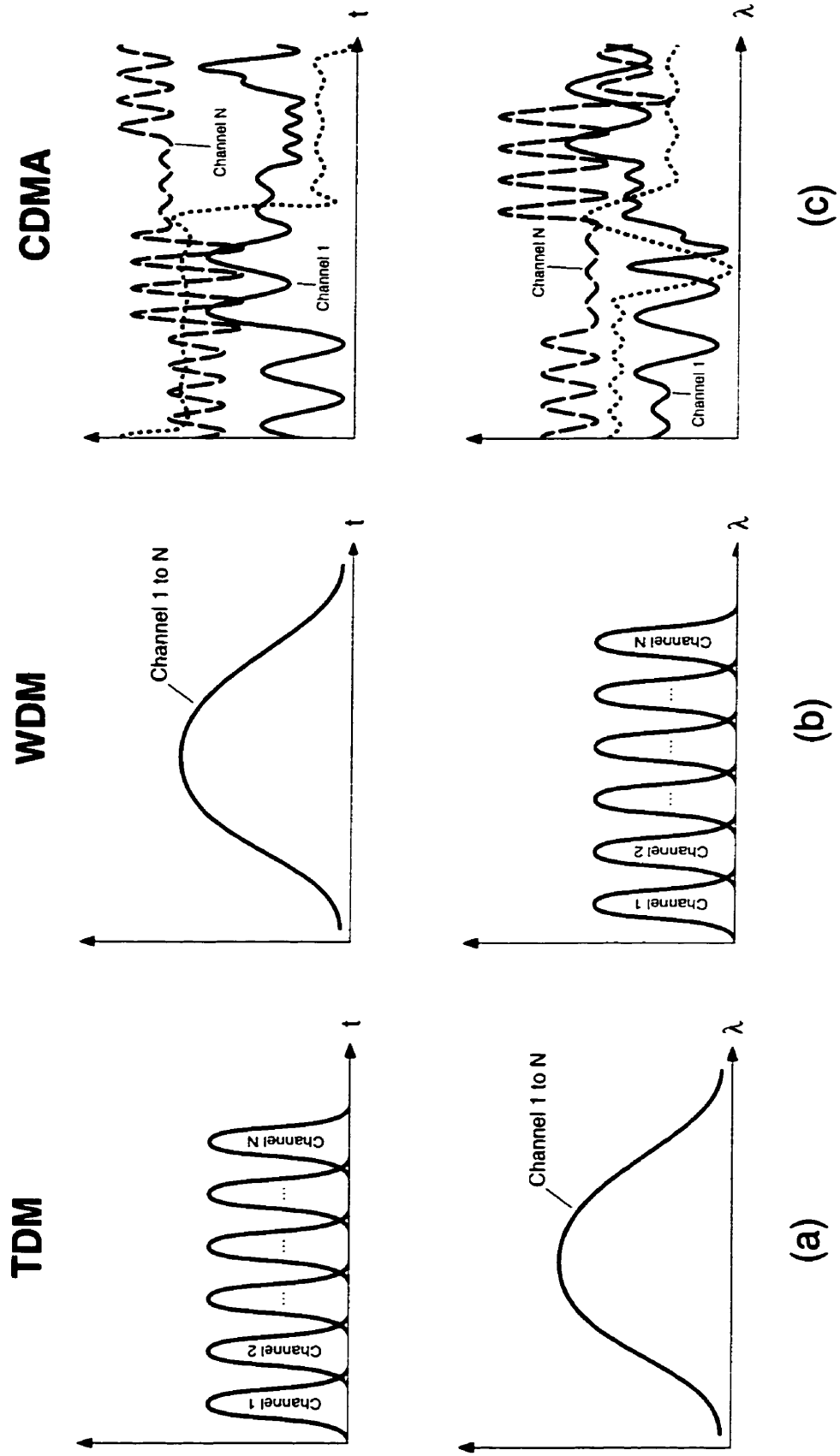
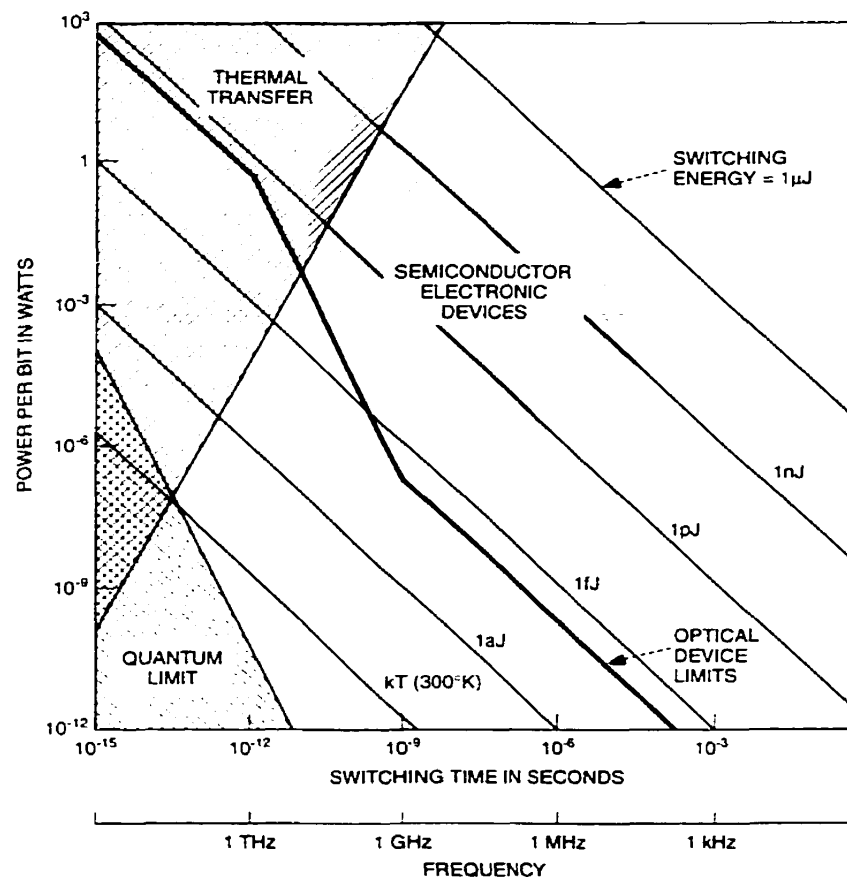


Figure 1.2 Schematics for (a) TDM, (b) WDM and (c) CDMA.

The physical limits of all-optical switching compared to electronic switching have been explored by Smith [9] ( Fig. 1.3). There are two ultimate limits: the quantum limit, beyond which no information can be transmitted by light, and the  $kT$  limit, beyond which switching devices at room temperature can randomly change states due to background thermal energy. Taking into consideration heat dissipation [9], a “thermal transfer” region sets a practical limit for switching devices (Fig. 1.3). However, this is not an absolute limit, as long as the switching device used for demultiplexing are not required to operate at a repetition rate equal to its switching rate. In fact, almost all ultrafast optical switching devices operate in this thermal transfer region. The “optical device limits” curve (Fig. 1.3) sets an approximate lower boundary for all-optical switching devices. Comparing this limit to the operation region of electronic devices (Fig. 1.3), it is clear that optical switching is superior to electronic switching when high speed and low switching energy are required.



**Figure 1.3** Physical limits of optical switching. After [9].

### 1.1.3 Current telecommunications systems in the laboratories and in the real world

Transmission capacity has been growing steadily over the decades (Fig. 1.4). Since 1994, the capacity of experimental systems has experienced a dramatic increase of growth rate, mainly due to the deployment of EDFAs, which eliminate the transmission bottleneck imposed by electrical amplification and regeneration [11]. Recently, the terahertz mark has been broken in several world's leading telecom laboratories (Table 1.1), all using WDM with very high bit rates ( $\geq 10$  GHz per channel).

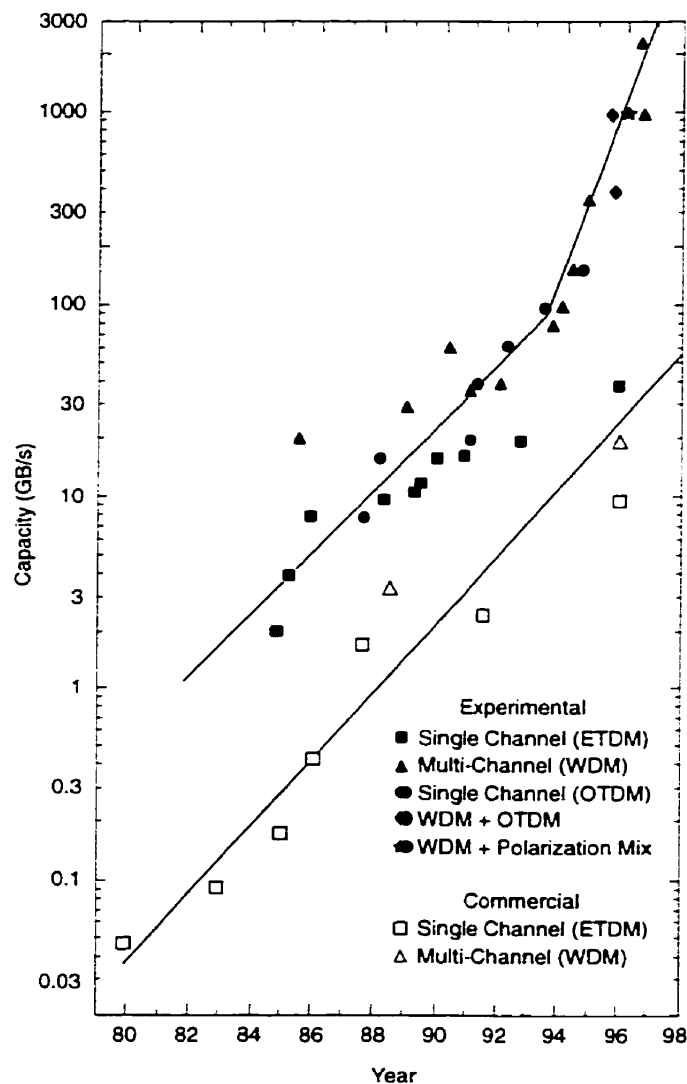


**Figure 1.4** The transmission capacity of optical fibre systems. After [10]

**Table 1.1 Terahertz transmission experiments**

AUTHORS	BIT RATE (Gbit/s)	CHANNEL SPACING (GHz)	TRANS. DISTANCE (km)	REF
H. Onaka <i>et al.</i> from Fujitsu Lab. Ltd.	55×20	75	150	[12]
A.R. Chraplyvy <i>et al.</i> from Bell Labs, Lucent Tech. & R.W. Tkachet <i>et al.</i> from AT&T Labs	50×20	100	55	[13]
T. Morioka <i>et al.</i> from NTT	10×100	200	40	[14]
Y. Yano <i>et al.</i> from NEC	132×20	33	120	[15]
S. Kawanishi <i>et al.</i> from NTT	7×200	600	50	[16]
A.K. Srivastava <i>et al.</i> from Bell Labs, Lucent Tech & AT&T	100×10	100	400	[17]
S. Aisawa from NTT	50×20	100	600	[18]
C.D. Chen <i>et al.</i> from Bell Labs & Lucent Tech.	30×40	125	85	[19]
C.D. Chen <i>et al.</i> from Bell Labs & Lucent Tech.	35×40	125	85	[20]

Although these researchers have surmounted great difficulties to achieve unprecedented terahertz transmission, none of their systems has fully exploited the usable bandwidth of fibre. The insatiable demand for information can only be met with more wavelength channels and higher bit rates per channel, which, in turn, demand faster and better switching technology.

## 1.2 MOTIVATION AND AIM OF THIS WORK

This work was motivated by the demand for ultrafast optical switching devices, especially those required by telecommunications systems. Development of optical switching devices involves, first and foremost, the development of suitable optical materials. Only when a detailed investigation is carried out on those materials, and a firm understanding of their relevant properties is acquired, can decisions be made on device configurations, can models be constructed for optimum design, and prototypes can be built for evaluation of device performance.

Our aims were to develop a suitable material for ultrafast optical switching, to characterize and tailor its material properties, and to use it to build a compact, ultrafast, all-optical switching device that meets practical system requirements.

### 1.3 MAIN CONTRIBUTION OF THIS WORK

One major difficulty of building compact, ultrafast, all-optical switching devices is the lack of materials with ultrafast *and* large optical responses. Semiconductor materials are, in many respects, ideal for optical switching. However, large nonlinearities associated with band gap resonance in conventional semiconductors are also accompanied by slow (nanosecond) carrier recombination, which prohibits the completion of the switching operation (on and off) in picosecond times.

The techniques developed to work around this limitation can be grouped into two categories. The first category achieves fast switching with slow semiconductor materials by employing two identical interfering devices, one to effect switching, the other to negate its effect, so that switching time is determined by the time delay between the two operations, rather than the time it takes for them to complete. The drawback of these devices, apart from their complex configuration, is that the switching repetition rate is still limited by the slow response time of the semiconductor. The second category speeds up the carrier recombination process to picoseconds, so that simple, straightforward switching devices can be based on these engineered materials. However, many techniques, although successful in reducing the recombination time, result in poor material quality, reduced response, and high loss, rendering the material unsuitable for practical switching. Before this work, two such engineered materials had been demonstrated to perform effective, high-speed all-optical switching: low-temperature-grown GaAs [21] and low-temperature-grown InGaAs/InAlAs multiple quantum wells [22]. However, the former does not exhibit resonant nonlinearities at the fibre communications wavelengths, and the latter exhibits narrow operation bandwidth. Moreover, both materials were produced by epitaxial growth at lower than the normal growth temperature, but this growth technique cannot produce ultrafast response in InGaAsP [23], a material commonly used for optical devices employed in communications systems because its resonance wavelength lies within the fibre transmission wavelength region.

Our approach to achieving semiconductor-based ultrafast switching falls in the second category, that is, we aim to speed up the material response through material engineering. We discovered that a new technique, helium-plasma-assisted molecular beam epitaxy, produced high quality semiconductors with picosecond to subpicosecond responses. Subsequently, we demonstrated, for the first time, compact ( $\mu\text{m}$ -sized), picosecond, polarization-independent, all-optical switching devices based on bulk semiconductor operating at the fibre communications wavelength [24].

Furthermore, we conducted the first-ever study on the optical properties of InGaAsP grown by HELium-Plasma-assisted epitaxy (HELP InGaAsP). The study reveals that, due to its unique optical properties, this novel material has many potential applications besides ultrafast switching, such as ultrafast detectors, modulators, saturable absorbers for mode-locked lasers, all in the realm of ultrafast photonics.

## 1.4 ORGANIZATION OF THE THESIS

The objective of this thesis is to provide readers with not only the complete details of our research, but also why this work is relevant and necessary, how this work is distinct from and related to other contemporary research, and how its results can be applied in the real world.

The remainder of the thesis is organized as follows. In Chapter 2, we discuss various mechanisms employed for all-optical switching, and review the contemporary and representative ultrafast all-optical switching devices, paying special attention to the strengths and limitations of each category of devices, with a view to identifying the major challenges faced by current devices in meeting practical system requirements. In Chapter 3, we begin with the origin of optical nonlinearities and their underlying physical processes, and discuss the existing means of obtaining and utilizing ultrafast optical nonlinearities in various material systems, with a view to demonstrating the difficulties in engineering a material with an ultrafast response *and* large nonlinearities. In Chapter 4, we introduce HELP InGaAsP material, present our detailed studies on its optical properties and our investigations of various factors that significantly influence these properties, revealing the unique coexistence of ultrafast response, large interband nonlinearity, and small band-tail absorption in this material, which makes this material particularly suitable for applications in ultrafast all-optical switching. In Chapter 5, we present our investigations of two types of switching devices based on this material, the nonlinear directional coupler and the asymmetric Fabry-Pérot (AFP) switch, with an emphasis on the design issues related to practical device requirements. We further demonstrate the operation of three prototype AFP devices, revealing the practical appeal of HELP-InGaAsP-based AFP switches for real-world systems. In Chapter 6, we highlight the main conclusions and original contributions of this study, and provide a brief outlook on future direction of improvement and implementation of this device.

---

# **Chapter 2**

## **ALL-OPTICAL SWITCHING: MECHANISMS AND DEVICE CONFIGURATIONS**

### **2.1 SWITCHING MECHANISMS**

All-optical switching is the process whereby the position, direction, or intensity of one optical beam is changed by another optical beam (or sometimes by itself) through interaction with materials. All-optical switching mechanisms are based on optical nonlinearity (i.e. nonlinear optical response) of materials. “Nonlinear” refers to the nonlinear relationship between the polarization induced in the material and the electrical field of the light which induces it. The origin of optical nonlinearities will be discussed in Chapter 3.

Most all-optical switching devices are based on third-order nonlinearities, i.e, intensity-dependent absorption and refractive index, which coexist and are related to each other by the Kramers-Krönig relations [25]. Depending on wavelength, either nonlinear absorption or nonlinear refraction can dominate. All-optical switching devices can be based on nonlinear absorption or on nonlinear refraction (Fig. 2.1), depending on which nonlinear effect dominates.

#### **2.1.1 Switching mechanisms based on nonlinear absorption**

In most absorptive materials, absorption can be saturated by an intense optical beam, as, for instance, in semiconductors at photon energies above the band gap energy. This intensity-dependent absorption can be used to modulate the intensity of another optical beam (Fig. 2.2). With feedback, such devices can exhibit optical bistability and can be used as optical flip-flops and other logic gates [26]. An efficient nonlinear-absorption-based switching device should exhibit large nonlinear absorption, i.e, large absorption at low intensities, and little absorption (or even gain) at high intensities. The asymmetric Fabry-Pérot switch we adopted in this work belongs mainly in this category (cf. Fig. 2.1).

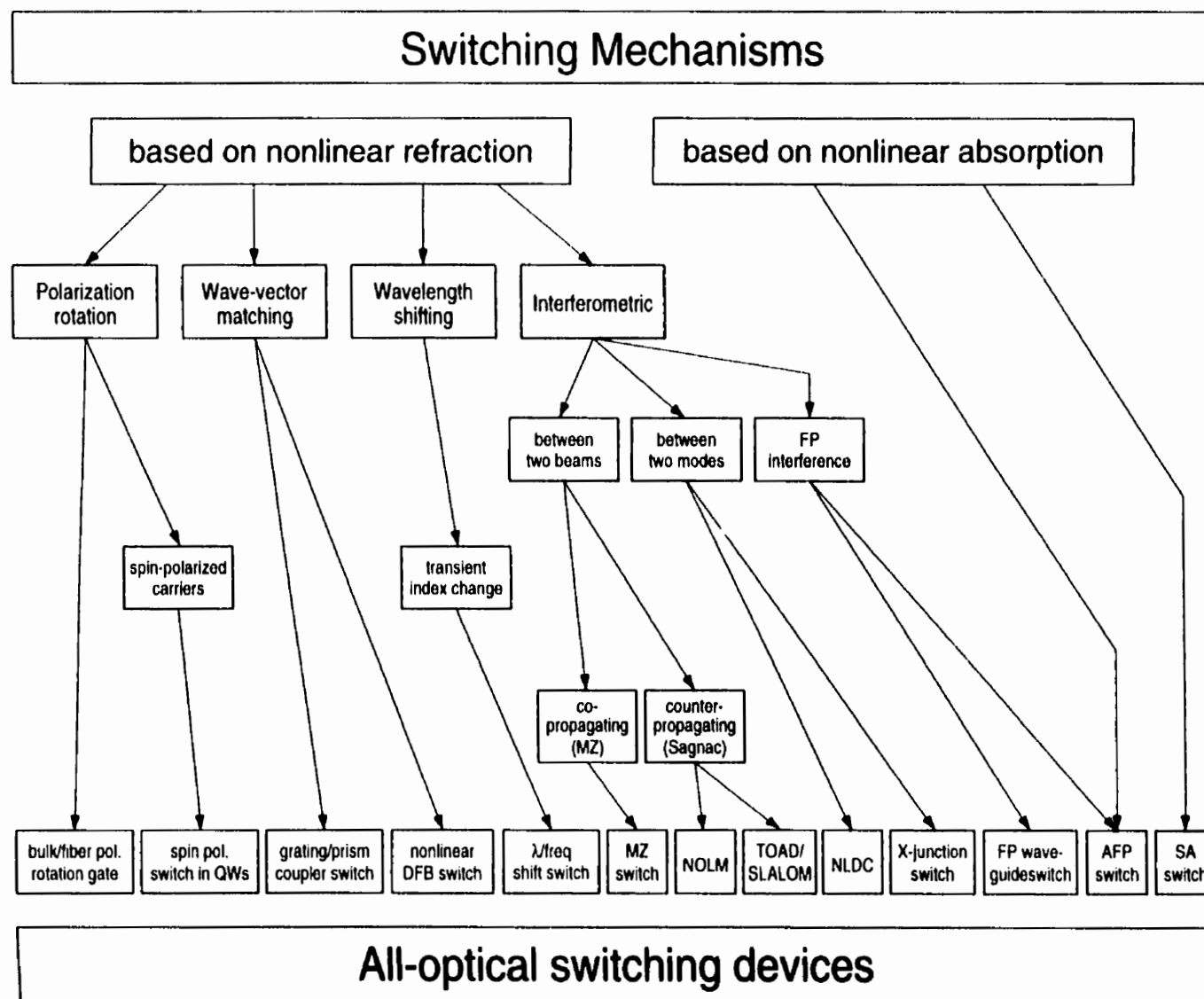


**Figure 2.1** Switching mechanisms and switching devices. FP: Fabry-Pérot; QW: quantum well; DFB: distributed feedback; MZ: Mach-Zehnder; NOLM: nonlinear optical loop mirror; TOAD: terahertz optical asymmetric demultiplexer; SLALOM: semiconductor laser amplifier in a loop mirror; NLDC: nonlinear directional coupler; AFP: asymmetric Fabry-Pérot; SA: saturable absorber.

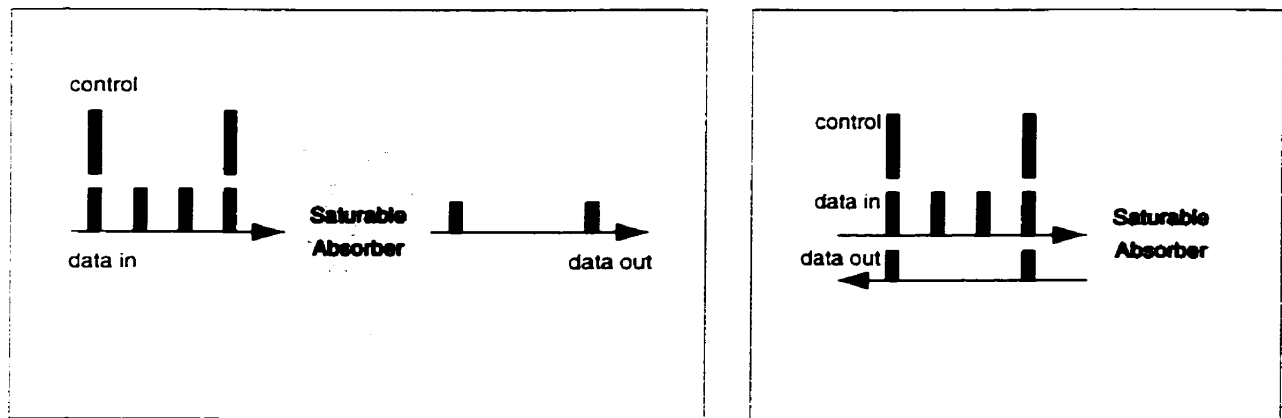


**Figure 2.2** Schematic diagram of switching based on nonlinear absorption

### 2.1.2 Switching mechanisms based on nonlinear refraction

Switching mechanisms based on nonlinear refraction can be roughly divided into four types: polarization rotation, wave-vector matching, wavelength shifting, and interferometric (Fig. 2.1).

#### 2.1.2.1 POLARIZATION ROTATION TYPE

The polarization rotation mechanism is used by perhaps the earliest of all-optical switching devices [27]. Such devices operate on the principle of light-induced birefringence, either through optical Kerr nonlinearity in bulk crystal or fibre [27, 28], or through carrier-induced index change in semiconductor multiple quantum well waveguides [29, 30]. In either cases, linearly polarized light is used to induce an index change larger in the direction of its polarization than in the direction perpendicular to it, making the material an optical retarder. Combining an appropriate length of this material with a polarizer yields an optical switching device (Figure 2.3a). Recently, spin-polarized carriers in quantum wells have been used for polarization rotation switch [31], because of their very fast relaxation times [32–35]. In such devices, a beam of circularly polarized light induces spin polarized carriers, and the index change associated with them affects only light with the same circular polarization, thus linearly polarized light passing through this medium experiences a polarization rotation (Fig. 2.3b).

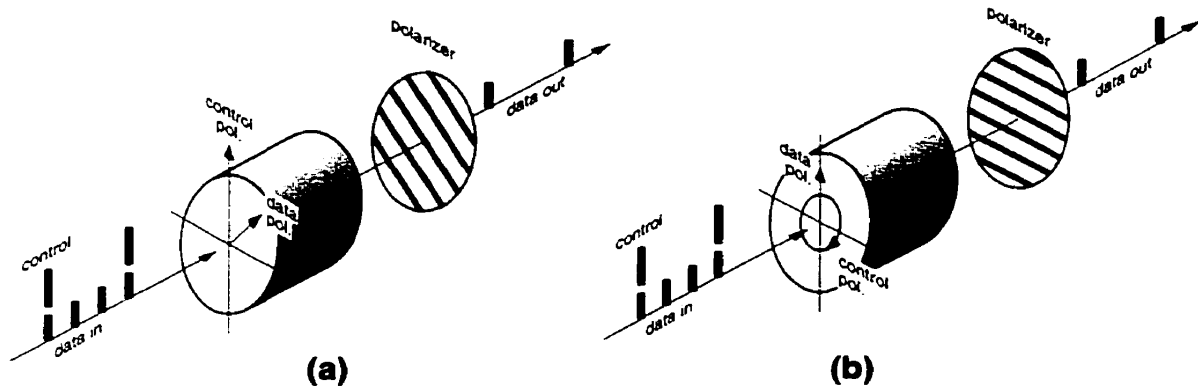


**Figure 2.3** Polarization rotation switch (a) based on Kerr medium, control is linearly polarized; (b) based on spin-polarization, control is circularly polarized.

### 2.1.2.2 WAVE-VECTOR MATCHING TYPE

Such devices use intensity-dependent field coupling in waveguides as the switching mechanism. To couple light into a waveguide from the side, the light wave-vector must match the wave-vector of one of the allowed modes of the waveguide. The latter depends on the index of the material, and thus, also on light intensity. Therefore, varying light intensity inside the waveguide can change the coupling condition and induce switching. Typical examples are the prism coupler switches [36] and the grating coupler switches [37]. Of these, devices utilizing distributed feedback gratings [38–42] make better use of the nonlinear index change than other types of couplers [43–46].

### 2.1.2.3 INTERFEROMETRIC TYPE

These devices are the most versatile and diverse; they can be further divided into three groups as illustrated in Figure 2.1.

In the first group of devices, light is split into two beams, which subsequently undergo different phase shifts because (a) nonlinear index change is only induced in one of the beam paths (Figure 2.4a), or (b) the amount of nonlinear material in the two paths is different (Fig. 2.4b). When the two beams are recombined, they can interfere either constructively or destructively in the direction of propagation depending on their relative phase shifts, causing the beam to be switched. A co-propagating configuration is referred to as a nonlinear Mach-Zehnder switch,

whereas a counter-propagating loop configuration is called a Sagnac switch. Examples of these devices will be given in Section 2.2.2.

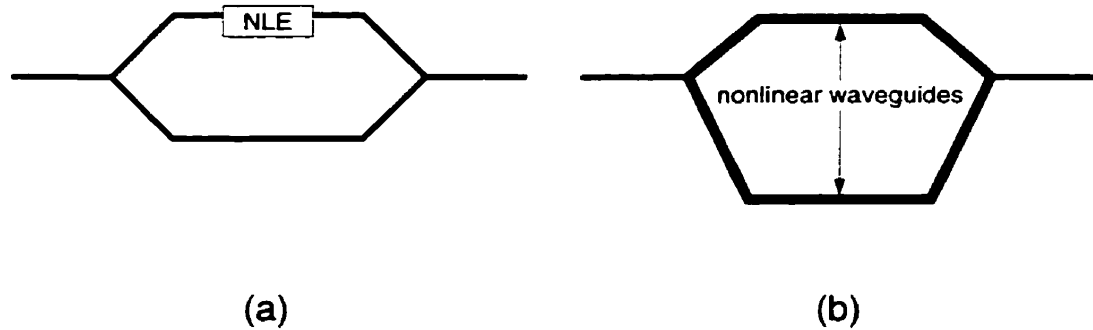


**Figure 2.4** Nonlinear Mach-Zehnder interferometer with (a) nonlinear element (NLE) only in one arm and (b) unequal nonlinear path lengths

In the second group of devices, the interference between two *modes* in a waveguide structure is used for switching. Since different modes have different field distribution and propagation constants, their interference results in spatial intensity variations. These spatial variations can be altered by introducing index changes in the waveguide structure, since both the field distribution and the propagation constant of a mode are functions of the refractive index. Typical examples are the nonlinear directional couplers (section 2.2.2.1) and X-junction switches [47–49].

The third group of interferometric switching devices uses Fabry-Pérot interference, i.e. the interference of multiple reflections from two surfaces of a nonlinear material or two facets of a nonlinear waveguide [50, 51]. This results in spectral transmission peaks at wavelengths where all multiple reflections are in phase, a condition determined by the index-length product of the medium. Hence, altering the medium's refractive index can shift these transmission peaks to different wavelengths, leading to change in the transmission intensity of a single-wavelength beam.

#### 2.1.2.4 WAVELENGTH SHIFTING TYPE

These devices [52] use the *transient* refractive index change to create a linearly *time-varying* phase shift, equivalent to a constant wavelength shift, and then switch the signal using a wavelength

filter. Therefore, wavelength shift is also introduced to the signal, which may be advantageous or disadvantageous depending on the specific application. Because of this particularity, and perhaps also because transient nonlinearity is difficult to control, this mechanism is rarely used for all-optical switching.

### **2.1.3 Switching mechanisms based on cascaded second-order nonlinearity**

Optical switching can also be based on second-order nonlinearity, which does not lead directly to intensity-dependent index or absorption change. But materials interacting with light through second-order nonlinearity can exhibit “effective third-order nonlinearity” caused by the cascading of two second-order processes under a slightly phase-mismatched condition [53–55]. Therefore, these materials can be used for all-optical switching in the same way as those exhibiting third-order nonlinearity. Furthermore, since many organic materials have high second-order nonlinearities, they can be candidates for ultrafast all-optical switching devices.

## **2.2 ALL-OPTICAL SWITCHING DEVICES**

### **2.2.1 Device requirements**

#### *Switching speed*

To compete with electronic switching devices, optical switching devices need to operate, at the very least, at speeds greater than 10 Gbit/sec, and preferably at 100 Gbit/sec. This is the speed at which the optical device opens and closes a gate. The required repetition rate of such a device is usually lower, depending on the number of time-division channels.

#### *Switching energy*

Switching energy is the energy required for the device to change state. For all-optical switching devices, this refers to the control pulse energy. Obviously, the switching energy should be kept as low as possible, especially when high repetition rates are required. The switching energy is limited chiefly by two factors: the output power of practical laser and amplifier systems, and device

heating. Currently, output power of both fibre amplifiers and semiconductor amplifiers can reach a few watts [56, 57], and pulse energies on the order of tens to hundreds of picojoules have also been demonstrated with both type of amplifiers operating at gigahertz repetition rates [58, 59]. Device heating depends on a host of factors: repetition rate, absorption of the control pulses, active volume and surface area of the device, and efficiency of the cooling equipment. All things considered, using currently available technology, a switching energy of tens of picojoules or less is desirable.

### *Throughput*

High throughput or low insertion loss is desirable for practical devices. Complex signal processing, requiring cascading of large chains of switching devices, can only be realized with high-throughput devices. Amplification is not always the solution for low throughput, since amplification is only useful where signal level is significantly higher than the noise level. Moreover, amplifiers necessarily introduce more noise<sup>1</sup>, so the fewer amplification stages used in the entire system, the better. However, recent advancements in high-gain optical amplifiers have considerably lowered the requirement for device throughput. With current fibre amplifier systems, an insertion loss of > 20 dB can sometimes be tolerated.

### *Contrast ratio*

Since noise is unavoidable in any practical system, high contrast ratio (or low cross-talk) between the switched signal and the leakage signal from unwanted channels is required to achieve a low bit-error-rate (BER). Since the required contrast ratio for a given BER depends on the noise level, and considerable noise is introduced in the amplification processes, the requirements for throughput and contrast ratio are often complimentary, i.e. higher throughput can lower the requirement for contrast ratio, and vice versa. In most systems, a contrast ratio of >10 dB is required.

---

<sup>1</sup> A 3 dB quantum noise is unavoidable in any phase-insensitive amplifiers. Phase-sensitive amplification, such as parametric amplification, does not introduce additional noise [60].

### *Bandwidth*

Future systems will likely employ both time-division and wavelength-division multiplexing schemes to fully utilize the fibre bandwidth. A switching device having a large operation bandwidth can be used to time-demultiplex several wavelength channels simultaneously. Therefore, increase in the bandwidth of a single device leads to fewer switching devices required, fewer control pulses required, and thus reduction in total switching energy.

### *Other requirements*

Other desirable features of a switching device include polarization independence, compactness, integration capability, signal routing capability, and capability to operate over a large temperature range. These features offer enormous advantages in system implementation, simplify system configuration, and ultimately lead to low cost, high efficiency, and flexibility.

## **2.2.2 Demonstrated all-optical switching devices**

### **2.2.2.1 NONLINEAR DIRECTIONAL COUPLERS (NLDC)**

Nonlinear operation of a directional coupler as an optical switch consisting two identical waveguides in close proximity was first proposed by Jensen [61]. Low intensity light launched into one guide is periodically coupled back and forth between the guides (Fig. 2.5), due to interference of the symmetric and antisymmetric modes supported by the coupler structure [62]. However, if the refractive index of one of the guides is changed by an intense optical excitation, coupling between the guides is frustrated. In principle, when a  $4\pi$  phase shift is achieved over one coupling length (Fig. 2.5), all the light energy can be preserved in the initial guide [63].

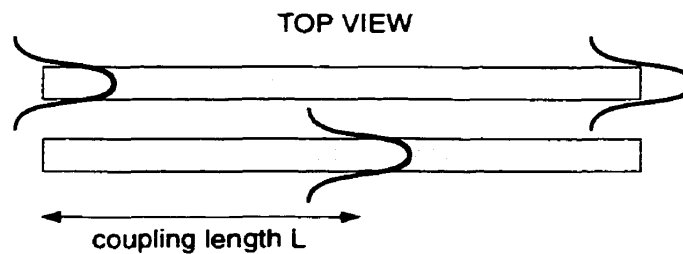


**Figure 2.5** Periodic power exchange between the two waveguides of a coupler

NLDCs are capable of performing versatile, multi-port, switching/routing functions. However, most demonstrated NLDCs, semiconductor-based or fibre based, exhibit low switching fraction and high insertion loss [64–72].

The low switching fraction can be largely attributed to two factors: (a) temporal pulse break-up—temporal wings of a pulse are not switched due to low intensity in the wings [66, 73], and (b) nonlinear index saturation and absorption, which are the major limiting factors in the operation of semiconductor-based NLDCs [74]. Such devices are usually operated in the wavelength region where nonlinearities are large, however, device length is limited due to the high absorption in this region. The limited nonlinear interaction length cannot always be compensated by increased intensity due to nonlinear saturation effects. Stegeman et al. have examined the effects of saturation and loss [63, 74–77] and arrived at a figure of merit ( $\Delta n_{sat} / \alpha \lambda$ , where  $\Delta n_{sat}$  is the saturated index change,  $\alpha$  is the absorption coefficient and  $\lambda$  the wavelength) for materials used in NLDCs [63].

It is obvious from this figure of merit that both low loss and large nonlinearities are important material requirements. For semiconductors, the figure of merit is highest at wavelengths just below the band edge and just below the half the bandgap [78]. Villeneuve et al. successfully demonstrated AlGaAs-based NLDC operating at below half the band gap [69, 73, 79, 80] with a switching time of <1 ps. However, because of the much reduced nonlinearity at below half the bandgap, switching energy on the order of  $10^{-10}$  J was required for their NLDCs.

Active NLDCs were proposed [72, 81] and demonstrated [70, 71] to reduce the switching energy, but they tend to have poor switching fraction ( $\leq 50\%$ ). Linear guides with nonlinear coupling medium [82, 83] were proposed to reduce loss, but experimental results were unsatisfactory [83].

In short, the main difficulties of implementing semiconductor-based NLDCs as ultrafast demultiplexers are poor contrast ratio and high loss (or high switching energy). Polarization dependence and bandwidth are other concerns with an NLDC switch.

#### 2.2.2.2 MACH-ZEHNDER (MZ) DEVICES

Recently, interest in all-optical MZ switches has revived, because they offer the possibility of achieving picosecond switching using conventional semiconductors with slow (nanosecond) nonlinear recovery times. Fast switching is achieved by inducing the same phase change in both

paths, but at slightly different times, so that only the data pulse passing through the device within the time interval experiences different phase changes in the two paths. This scheme can be implemented in three ways: (1) a symmetric MZ interferometer with two control pulses [84–87] (Figure 2.6a); (2) an asymmetric MZ interferometer [88, 89] (Figure 2.6b); and (3) an ultrafast nonlinear interferometer (UNI) [90–92] (Figure 2.6c).

These implementations have yielded very short switching windows, from a few picoseconds to 200 fs. However, the contrast ratios are less than ideal, typically about 1:5 or 1:4 [84–86, 88, 90, 91], due to the difficulty in achieving precise 50/50 signal splitting, and in achieving exactly  $\pi$  phase shift optically.

While low contrast seems to be a practical issue with these devices, which could be improved with better control and fabrication techniques, the inherent constraint of MZ devices is the repetition rate, which is limited by the nonlinear recovery time. To determine the maximum repetition rate in devices where index change is carrier-induced, we consider that, at steady-state, the number of induced carriers ( $N_{ind}$ ) for each switching operation should equal the number of recombined carriers over the time interval ( $1/R_{rep}$ ). Assuming the carrier lifetime ( $\tau$ )  $\gg 1/R_{rep}$ , then,

$$N_{ind} = \frac{N}{\tau R_{rep}} \quad (2.1)$$

where  $R_{rep}$  is the repetition rate, and  $N$  is the carrier density. The maximum carrier density is the saturation density  $N_{sat}$ , that is,

$$N_{ind} R_{rep} \tau \leq N_{sat} \Rightarrow R_{rep} \leq \frac{N_{sat}}{N_{ind}} \frac{1}{\tau} \quad (2.2)$$

If the linear approximation that  $N \propto \Delta n$  is used, where  $\Delta n$  is the carrier induced index change, then,

$$R_{rep} \leq \frac{\Delta n_{sat}}{\Delta n_{ind}} \frac{1}{\tau} \quad (2.3)$$

Additionally, since the required phase change is  $\pi$ ,  $\Delta n_{ind} L = \lambda/2$ . When net absorption ( $\alpha$ ) is present,  $L$  is limited by absorption:  $L \approx 1/\alpha$ , then  $\Delta n_{ind} = \alpha \lambda/2$ . Together with (2.3) we arrive at,

$$R_{rep} \leq \frac{2 \Delta n_{sat}}{\lambda \alpha \tau} \quad (2.4)$$

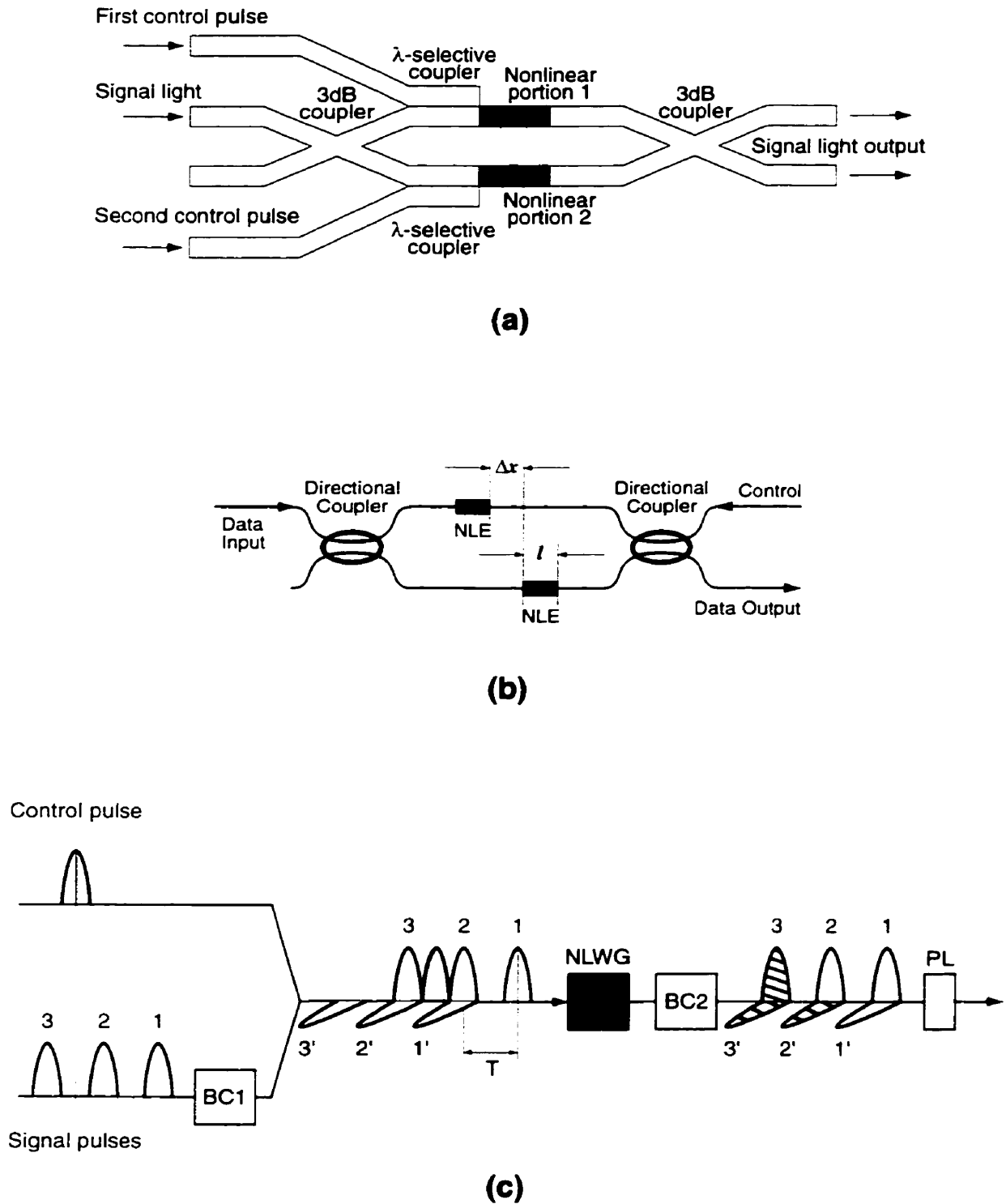


**Figure 2.6** Schemes of using slow nonlinear element to achieve fast switching: **(a)** A symmetric MZ interferometer with two control pulses, after [87]. **(b)** An asymmetric MZ interferometer, after [89]. **(c)** a UNI device, after [92].

If the typical values ( $\Delta n_{sat} = 0.01$ ,  $\alpha = 1 \text{ mm}^{-1}$ ,  $\lambda = 1.55 \text{ }\mu\text{m}$ ,  $\tau = 1 \text{ ns}$ ) are substituted into (2.4), then the maximum repetition rate  $R_{rep}$  is 12 GHz. It is perhaps for this reason that no one has yet demonstrated  $>10 \text{ GHz}$  rep rate with switches made of slow materials without employing other techniques to enhance the carrier recombination rate. It is interesting that the  $\Delta n_{sat}/\alpha\lambda$  ratio, defined by Stegeman as the figure of merit for NLDC materials, also affects the switching repetition rate for MZ switches employing slow nonlinear materials.

Apart from low contrast ratio and limited rep rate, all-optical MZ switches typically exhibit low throughput (unless current injection is used), polarization dependence, and narrow bandwidth.

### 2.2.2.3 NONLINEAR OPTICAL LOOP MIRRORS (NOLM)

The NOLM is the fibre implementation of a nonlinear anti-resonant ring interferometer [93, 94]. All-optical switching with NOLM was first analysed by Doran et al. [95], and was subsequently demonstrated by many groups [96–99]. A NOLM employs a 3 dB directional coupler connected to a fibre loop acting as a nonlinear medium (Figure 2.7). A data pulse sent into the loop is split by

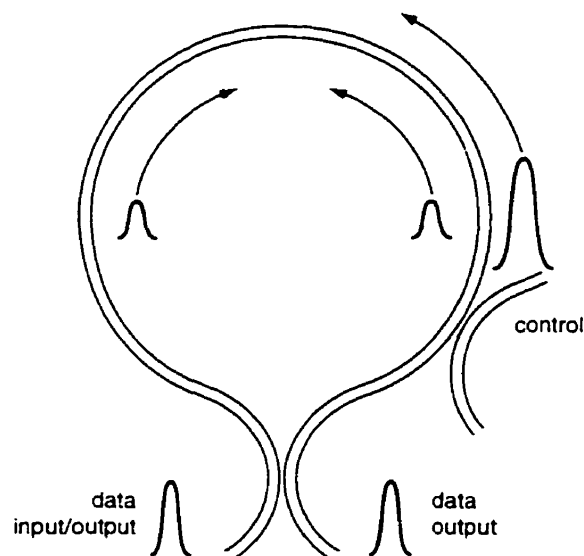


**Figure 2.7** Schematic of a NOLM

the coupler into two equal-intensity counter-propagating pulses which will recombine at the coupler and emerge out of the input port. Switching is achieved by injecting an intense control pulse into

the loop, which travels in synchronism with one of the data pulses and induces phase shift to this data pulse via cross-phase modulation. A  $\pi$  phase shift will cause the recombined data pulse to emerge out from the output port.

NOLMs present several advantages: (1) very fast switching time could be in principle achieved<sup>2</sup>, since the Kerr nonlinearity in fibre is virtually instantaneous; (2) stable operation can be maintained even for long fibre loops because thermal and vibrational disturbances, which typically act on a much longer time than the loop transit time, affect both interfering pulses equally; (3) low switching power can be achieved by lengthening the fibre loop.

The major challenges/drawbacks for NOLMs are (1) polarization dependence, (2) chromatic dispersion, (3) achieving high contrast, (4) latency, and (5) incompatibility with integrated optics.

Polarization dependence is due to birefringence induced by linearly polarized control pulse [100]. An elaborate polarization diversity scheme (Figure 2.8) employing two identical sections of birefringent fibre cross-spliced at the centre of the fibre loop, has been demonstrated to achieve polarization-insensitive switching [101–103]. Another recently developed polarization-insensitive NOLM uses a twisted fibre to emulate a circularly polarized fibre [104, 105], but the resultant throughput is reduced by more than 3 dB.

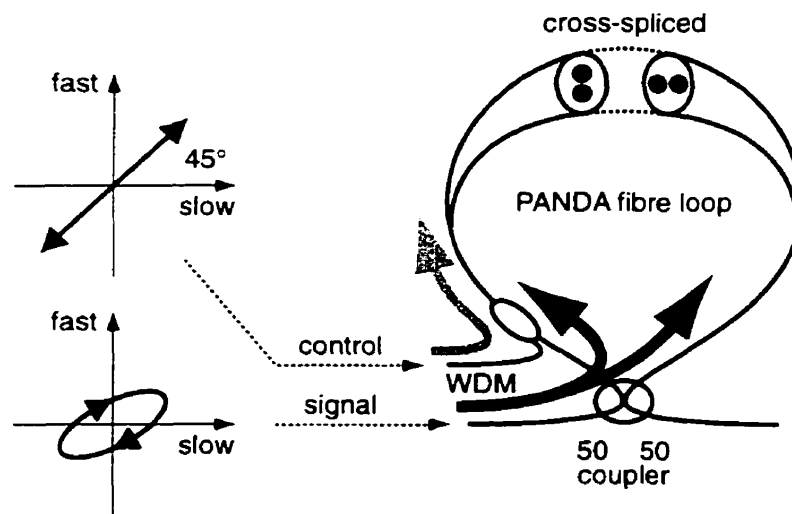


**Figure 2.8** Polarization-independent implementation of a NOLM using two identical, cross-spliced birefringent fibres. After [101].

<sup>2</sup> In practice, the switching window duration is limited by (a) group velocity dispersion between the control and data wavelengths, (b) polarization dispersion, and (c) control pulse broadening due to group velocity dispersion

To facilitate separation of control from signal after switching, the control is usually set at a different wavelength from the signal, hence chromatic dispersion in fibre has a number of undesirable consequences: (a) it limits interaction length, so that switching energy cannot always be reduced by lengthening the fibre; (b) it reduces the switching speed, since chromatic dispersion causes a broadening of the switching window [106]; (c) it limits the signal bandwidth [102].

Achieving high contrast ratio in many practical NOLMs represents another challenge because, (a) it requires a nearly perfect 50/50 split coupler; (b) the coupler is wavelength-dependent, hence high contrast ratio cannot be obtained over a large bandwidth; and, (c) contrast ratio deteriorates with increasing switching repetition rate. As the time interval between control pulses shortens, more control pulses are propagating in the loop at any given time, which introduce more unwanted phase shifts to the counter-propagating signals, causing incomplete cancellation of the unwanted channel at the transmission port.

Despite these drawbacks, NOLMs are promising for OTDM systems, and, apart from performing signal demultiplexing, NOLMs have been shown to perform wavelength conversion [107], optical rate conversion [108], and signal regeneration [109].

#### **2.2.2.4 NONLINEAR SEMICONDUCTOR ELEMENT IN A FIBRE LOOP MIRROR**

To eliminate the long latency problem of NOLMs, semiconductors with large resonant nonlinearity have been used to replace fibre as the nonlinear medium. This also brings other advantages, such as improved stability, reduced switching energy and the possibility of integration. Fast switching is achieved by using an asymmetric configuration (Figure 2.9), similar to the placing of nonlinear elements asymmetrically in a MZ switch (Section 2.2.2.2).

Devices employing a semiconductor laser amplifier (SLA) as the nonlinear element in a fibre loop have been demonstrated to perform various functions [110–115], the most notable being the SLALOM (SLA in a LOop Mirror) [112] and the TOAD (Terahertz Optical Asymmetric Demultiplexer) [115] which were used for demultiplexing high-bit-rate OTDM signals.

The major advantage of employing SLA in the loop, apart from low latency, is the very low switching energy required, typically about a picojoule: switching energy as low as 355 fJ was

reported [116]. This is due to: (a) the large nonlinearities in semiconductors, and (b) the usage of current-injected nonlinear elements (SLA) to provide gain as well as nonlinearity.

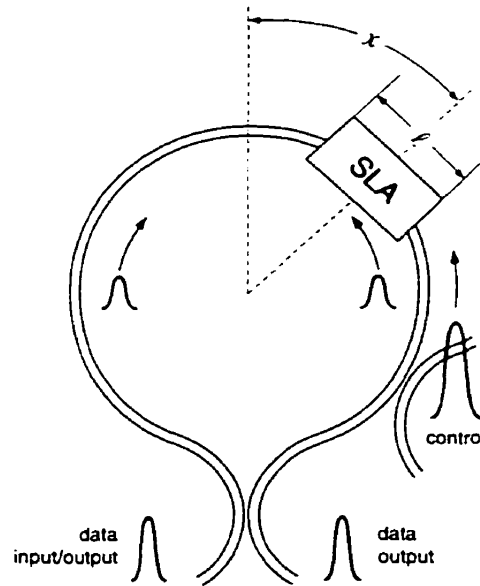


**Figure 2.9** Generic configuration for a nonlinear element in a loop mirror

Although integration is possible with this device, and a fully integrated version has been demonstrated [117], the integrated device is rather complex, consisting of passive loop waveguides, an active SLA, and a 3 dB directional coupler. Compared to passive integrated switches, such as NLDCs, this integrated device is bulky and its fabrication is considerably more complex.

The switching time of the TOAD or SLALOM is determined by the location  $x$  as well as the length  $l$  of the nonlinear element (Figure 2.9). The shortest switching time possible is twice the transit time of the nonlinear element. The length of the nonlinear element is determined by the SLA's nonlinear coefficient and the switching energy. It is typically several hundreds of microns, which limits the switching time to a few picoseconds<sup>3</sup>. The demultiplexing repetition rate, on the other hand, is still primarily limited by the SLA's carrier lifetime.

Major problems with SLA-based devices are amplified spontaneous emission (ASE) and gain variation, which degrade contrast ratio and introduce unwanted amplitude modulation to the

<sup>3</sup> Of course, the switching time is also limited by the control pulse width and the nonlinear "turn-on" time, but, in practice, both are much shorter than the transit time of the nonlinear element.

data signals. To alleviate these problems, signal wavelengths can be set far away from the gain bandwidth [118]. However, due to considerably reduced gain and free-carrier absorption, high insertion loss (18 dB) is experienced in such devices [119].

### 2.2.2.5 ASYMMETRIC FABRY-PÉROT DEVICES (AFP)

AFP devices, unlike those discussed above, are based mainly on nonlinear absorption. A generic AFP device (Figure 2.10) consists of an absorptive nonlinear material as the active layer, sandwiched between a low-reflection layer and a high-reflection layer. This arrangement results in extinction of reflected light through destructive interference of the two surface reflections under linear operation—the “off” state of the device. Under nonlinear operation, intense optical pulses saturate the absorption of the active layer, resulting in a much stronger reflection from the back surface, and thereby turning the device “on.”

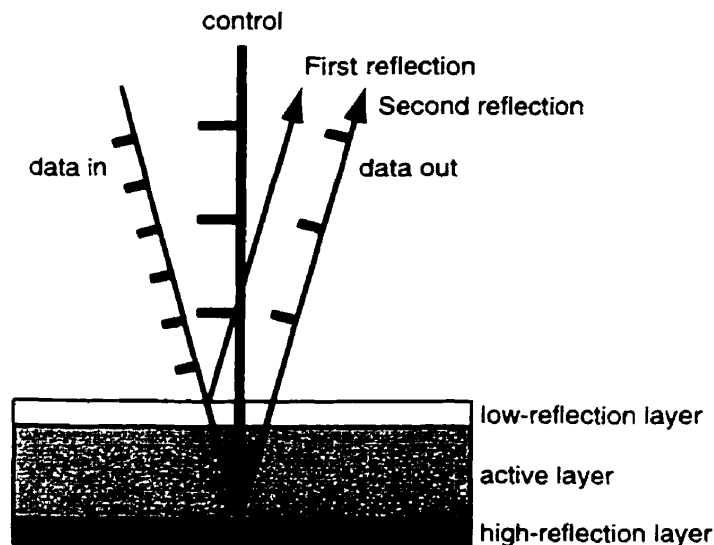


**Figure 2.10** Generic configuration of an AFP. Data beams drawn at an angle for clarity. They are in fact normal to the device to ensure polarization-independent operation.

The AFP device has evolved from the Fabry-Pérot (FP) switch, which is mainly a high finesse, nonlinear-refractive-index based switch [120, 121]. The FP switch’s output spectrum consists of narrow peaks at resonance wavelengths, which are determined by the index-length product of the étalon. Consequently, optical excitation, which changes the index of the étalon, can

drastically change the output at a wavelength near the resonance from low to high (or vice versa). Such a device requires a very high finesse to achieve high contrast ratio, and therefore, the bandwidth is very narrow.

An AFP device, on the other hand, achieves wide bandwidth *and* high contrast by using a *low* finesse étalon with asymmetric reflectances. Consequently, reflections from the two surfaces cancel out completely (or nearly completely) over a large wavelength region [122–124]. Because the finesse is much lowered, switching based on shifting the spectrum becomes impractical, since it would require a very large index change. However, if the nonlinear medium of the étalon is made of a saturable absorber, then switching can be carried out primarily by absorption saturation rather than index change, although any index change will also benefit the switching action. In other words, an AFP device combines the advantage of an interferometric device (high contrast) with the advantage of a nonlinear-absorption-based device (large bandwidth).

In addition to high contrast ratio and large bandwidth, AFP devices have very compact ( $\mu\text{m}$ ) sizes, and require low switching energy, because they use large interband nonlinearities in semiconductors. The normal incidence operation of an AFP device ensures polarization independence. In view of these desirable features, we have adopted the AFP configuration for demonstration of all-optical switching in this work.

The most important material requirement for an ultrafast AFP switch is the simultaneous presence of a large nonlinearity and a fast (picosecond) response. Developing such a material has become a major challenge. Prior to this study, two AFP switches had been demonstrated to achieve  $<10$  ps switching times, one developed by Takahashi et al. in NTT [22, 125, 126], and the other developed by Loka and Smith at the University of Toronto [21]. Herein we present a third ultrafast AFP device, which surpasses the former in bandwidth and ease of fabrication, and surpasses the latter in contrast ratio, in addition to the fact that it operates in the useful fibre communications wavelength range (see Chapter 5).

Takahashi's device [22, 125, 126] uses strained, Be-doped low-temperature-grown InGaAs/InAlAs MQWs (4  $\mu\text{m}$ -thick) as the active layer, gold coating as the high-reflection layer, and an InGaAs/InP distributed feedback reflector with a reflectivity of  $\sim 1\%$  as the low-reflection layer. The entire structure is grown on an InP substrate, and AR coating is applied to the substrate to create an input window. The MQW material offers large nonlinearity due to enhanced exciton

absorption, but the excitonic bandwidth is very narrow. The NTT group achieved fast switching by combining low-temperature growth and Be doping to produce MQWs with a subpicosecond response time [127]. However, the growth and doping processes flatten out the excitonic absorption peaks and consequently reduce the nonlinear absorption effect. The excitonic peaks can be, to a certain degree, recovered [22], and nonlinear absorption restored by carefully introducing 1% compressive strain to the MQW layers. Their initial device required a few picojoules of switching energy and had a contrast ratio of  $\sim 13$  dB [22].

Recently, the NTT team have achieved an overall contrast ratio of  $\sim 30$  dB by utilizing the spin polarization property of the material, and using a polarizer with a high extinction ratio (30 dB) to externally enhance the contrast ratio [126]. However, the resulting device is polarization sensitive. Polarization-independent operation of this device has been demonstrated using a highly elaborated polarization-diversity scheme consisting of two quarter-wave plates, two Wollaston prisms, a half mirror and a pinhole aperture [126]. The device has the drawback of a fourfold reduction in throughput, and it is very difficult to align, hence impractical for a real-world system.

Akiyama et al. introduced a coupled-cavity design [128] to lower the switching energy and increase the bandwidth of an AFP device based on a low-temperature InGaAs/InAlAs MQW material similar to Takahashi's. They demonstrated impressive low-energy switching (0.8 pJ), but the bandwidth of their device was still limited (the 10 dB bandwidth being 7 nm). The switching time is also very long,  $\sim 180$  ps, and thus not suitable for ultrafast OTDM demultiplexing.

The AFP device developed by Loka et al. is based on bulk low-temperature-grown GaAs [21], a material which exhibits picosecond to subpicosecond optical responses with large nonlinear absorption when subjected to a controlled amount of rapid thermal annealing [129]. However, in order to utilize the large interband nonlinear absorption, the device has to operate around 800 nm, making it incompatible with fibre communications systems.

#### **2.2.2.6 SUMMARY OF ULTRAFAST ALL-OPTICAL DEVICES**

Major advantages and disadvantages of various all-optical device configurations discussed in this section are summarized in Table 2.1, in view of the device requirements listed in Section 2.2.1. The various configurations are evaluated based on the performance of demonstrated devices (up to but not including this work). It is clear that no single existing device meets all the device

requirements (Section 2.2.1), and one of the objectives of this work is to demonstrate new, improved switching devices.

**Table 2.1 Comparison of Demonstrated Ultrafast All-Optical Devices  
(present study not included)**

NONLINEAR MATERIAL	DEMONSTRATED DEVICES	MAJOR ADVANTAGES	MAJOR DISADVANTAGES
fiber	NLDC NOLM	<ul style="list-style-type: none"> <li>● ultrashort switching time (&lt;1ps)</li> <li>● simple configuration</li> <li>● multiple port (add/drop)</li> </ul>	<ul style="list-style-type: none"> <li>● low contrast</li> <li>● polarization dependent (unless complex compensation is used)</li> <li>● latency</li> <li>● bulky</li> <li>● not integrable</li> </ul>
slow semiconductor with large nonlinearity	MZ TOAD SLALOM UNI	<ul style="list-style-type: none"> <li>● low switching energy<sup>1</sup></li> <li>● short switching time (ps)</li> <li>● multiple port (add/drop)</li> </ul>	<ul style="list-style-type: none"> <li>● complex structure</li> <li>● difficult to integrate</li> <li>● low repetition rate</li> <li>● low contrast</li> <li>● polarization dependent</li> </ul>
fast semiconductor with small nonlinearity	NLDC	<ul style="list-style-type: none"> <li>● simple structure</li> <li>● easy to integrate</li> <li>● multiple port (add/drop)</li> </ul>	<ul style="list-style-type: none"> <li>● high switching energy</li> <li>● low throughput</li> <li>● polarization dependent</li> </ul>
fast semiconductor (QW) with large nonlinearity	AFP	<ul style="list-style-type: none"> <li>● high contrast</li> <li>● low switching energy<sup>2</sup></li> <li>● simple structure</li> </ul>	<ul style="list-style-type: none"> <li>● only ON/OFF switching</li> <li>● structure does not allow planar integration</li> <li>● small bandwidth</li> <li>● polarization dependent (unless complex compensation is used)</li> </ul>
fast semiconductor (bulk) with large nonlinearity	AFP	<ul style="list-style-type: none"> <li>● low switching energy<sup>2</sup></li> <li>● simple structure</li> <li>● polarization independent</li> <li>● large bandwidth</li> </ul>	<ul style="list-style-type: none"> <li>● operating wavelength not at 1.55<math>\mu</math>m</li> <li>● only ON/OFF switching</li> <li>● structure does not allow planar integration</li> </ul>

<sup>1</sup> Only applies to active devices, i.e. devices with electrical current injection

<sup>2</sup> Compared to other passive devices, AFPs show remarkably low switching energy due to their extremely small volume. In fact, the switching energies of passive AFPs are similar to switching energies of many active devices, such as the TOAD and SLALOM.

## Chapter 3

### MATERIALS FOR ULTRAFAST ALL-OPTICAL SWITCHING

All-optical switching devices employ materials that exhibit optical nonlinearity. Although all materials exhibit a certain degree of nonlinearity when optical excitation is sufficiently high, developing materials suitable for practical, efficient optical switching remains a major challenge. Although a variety of nonlinear processes are known to occur in semiconductors, few will enable devices to meet all necessary requirements (cf. Section 2.2.1). A great deal of effort has been spent on material engineering (such as making quantum well structures and intentionally introducing defects) to improve the nonlinear optical properties of materials, making them suitable for all-optical switching in the picosecond to femtosecond domain.

One of the major contributions of this work is developing a suitable semiconductor material for all-optical switching, but prior to discussing it, an overview on the various nonlinear processes in semiconductors and a comparison of various material engineering techniques are necessary to justify our work and to show the uniqueness of our approach.

#### 3.1 OPTICAL NONLINEARITIES

Light, a travelling wave of oscillating electromagnetic fields, interacts with the outer electrons and inner ion cores of atoms in a material. The wave equation for the electric field of light in a non-magnetic dielectric medium, which follows from Maxwell's equations, can be written as:

$$\nabla \times \nabla \times \mathbf{E} = -\frac{1}{c^2} \frac{\partial}{\partial t^2} \mathbf{E} - \mu_0 \frac{\partial}{\partial t^2} \mathbf{P} \quad (3.1)$$

where  $\mathbf{P}$  is the induced polarization. In the traditional framework of nonlinear optics, far away from any resonances,  $\mathbf{P}$  is expressed as a power series of the driving electrical field  $\mathbf{E}$  of the lightwave:

$$P_i = \epsilon_0 \left( \sum_j \chi_{ij}^{(1)} E_j + \sum_{j,k} \chi_{ijk}^{(2)} E_j E_k + \sum_{j,k,l} \chi_{ijkl}^{(3)} E_j E_k E_l + \dots \right) \quad (3.2)$$

where  $\epsilon_0$  is the permittivity of vacuum,  $\chi^{(1)}$  is the linear susceptibility, and  $\chi^{(2)}$  and  $\chi^{(3)}$  are the second- and third-order susceptibilities, respectively. For a weak driving field, only the linear

term in (3.2) is significant. Therefore,  $\mathbf{P}$  oscillates with the same frequency as the incident light beam, and two light beams crossing each other in the material will not interact. But, for a strong driving field (i.e. field strength comparable to the atomic field), the second- and third-order terms become significant. Consequently, the nonlinear interaction between a light beam and matter can be used to alter the behaviour of another light beam (or itself). This is the basis for all-optical switching.

Although both second- and third-order nonlinearities can be used for all-optical switching, utilization of the third-order nonlinearity is more straightforward, since it reflects an intensity-dependent susceptibility, which is obvious when the polarization is expressed as:

$$P = \epsilon_0(\chi^{(1)} + \chi^{(3)}|E|^2)E = \epsilon_0\chi(I)E \quad (3.3)$$

where  $\chi(I)$  is the intensity-dependent susceptibility. For simplicity, scalar form is used and the second-order term is neglected here. Since absorption and refractive index of a material are associated with the imaginary and real part of  $\chi$ , respectively, third-order nonlinearity is manifested as intensity-dependent absorption and refractive index.

Although Eq. (3.2) is a general expression for optical nonlinearities, it is mostly used to describe nonresonant optical nonlinearities, i.e. optical nonlinearities induced at frequencies far removed from any resonant frequencies in the system. In such cases, the nonlinearities arise from virtual electronic transitions, and polarization of the medium responds to the *instantaneous* amplitude of the incident field.

It was discovered by the late 1970s that nonlinear effects in semiconductors can be enhanced by exploiting the resonance close to the fundamental absorption edge. The resulting nonlinear effects are orders of magnitude larger (typically  $10^4\times$  larger) than nonresonant nonlinearities due to real carriers (electrons and holes) being created by optical excitation. However, carrier-induced nonlinearities cannot be calculated within the framework of conventional nonlinear optics described by Eq (3.2). In contrast, nonlinear optical properties of a semiconductor close to the band edge are often calculated by linear response theory for the interaction between the electronic system and the applied light field [130], i.e.:

$$P = \epsilon_0\chi(N)E \quad (3.4)$$

where  $N$  stands for the number of electron-hole pairs.  $N$  depends on the carrier generation rate and

on the carrier decay rate. The former is a function of intensity, while the latter is affected by various carrier trapping and recombination mechanisms. Therefore, effectively,  $\chi(N)$  is also intensity-dependent.

Resonant nonlinearities arise from carrier redistribution (either inter- or intra-band), which modifies the physical system in a much more dramatic way than the virtual electronic transitions associated with nonresonant nonlinearities. Thus resonant nonlinearities are usually considerably larger, but their recovery times are longer, due to the finite carrier decay times. The magnitude and response times of these nonlinearities depend on the material and on the physical processes involved. For example, in conventional semiconductors, the radiative recombination time of carriers is on the order of 1 nanosecond, consequently band to band nonlinearities recover on nanosecond time scales. Some intraband processes, such as carrier thermalization and spin relaxation, are femtosecond processes, but the nonlinearities they induce are also significantly weaker than interband nonlinearities.

In short, the two types of intensity-dependent nonlinearities differ in several respects. Nonresonant nonlinearity is induced instantaneously through a third-order nonlinear process which does not involve real transitions from one electronic state to another, but merely induces dipole polarization in atoms interacting with the light beam. Therefore, the induced nonlinear effect is conceivably small. Resonant nonlinearity involves real transitions of some quasiparticles with finite lifetimes, the nonlinear effect is enhanced by the resonance, but the recovery time of the nonlinear effect is limited by the lifetime of the quasiparticles involved.

### 3.2 MATERIAL REQUIREMENTS

The material requirements for ultrafast all-optical switching are determined primarily by the device requirements, as well as by the particular device configuration adopted (Fig. 3.1). Material requirements can sometimes be relaxed by using special device configurations. As mentioned previously (Section 2.2.2), picosecond switching times can be achieved by devices (e.g. the TOAD device) made of materials with nanosecond recovery time. However, apart from more complex device configurations and stringent fabrication requirements, the switching repetition rates of these devices are limited by the slow recovery time of the material. Materials with fast nonlinear recovery times are still the preferred choice for ultrafast all-optical switching.

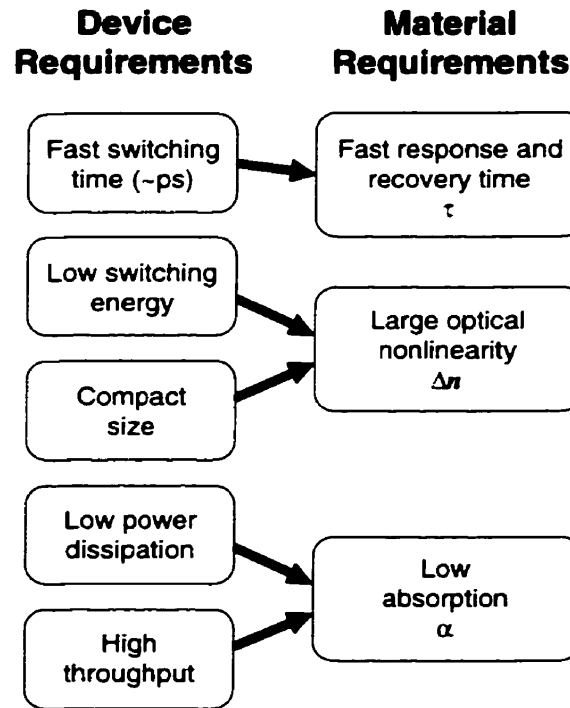


**Figure 3.1** Material requirements for ultrafast all-optical switching deriving from device requirements.

Requirements for nonlinearity and absorption also vary depending on device configurations. For example, in most waveguide devices where intense light can be confined to a small region over a long distance, light-matter interaction length can be increased to compensate weak index change, but the absorption has to be very low. In fact, it is the ratio between nonlinear refraction and absorption that needs to be high (Stegeman's criterion [43]). Because absorption variation and index change variation as a function of wavelength differ, one can determine certain wavelength regions where this ratio is highest. In semiconductors, such regions lie just below the fundamental band edge and just below half of the band gap [73]. Semiconductor devices operated at just below the band edge are required to have an absorption spectrum with a sharp band edge and a low absorption band tail.

While nonlinear-refraction-based switching devices require relatively large index changes and low absorption, nonlinear-absorption-based devices, such as asymmetric Fabry-Pérot switches, require mainly large absorption changes. Semiconductors are the most suitable material in this case because the large band edge absorption can be easily saturated optically.

In general, for semiconductor materials used for ultrafast all-optical switching, the most desirable properties are ultrashort nonlinear response and recovery times, large nonlinearities, and low band-tail absorption.

### 3.3 FAST NONLINEAR PROCESSES IN SEMICONDUCTORS

Some optical processes are inherently fast, such as the carrier thermalization process or the exciton ionization process. Some processes, such as carrier recombination process, are inherently slow in conventional semiconductors, but can be accelerated by tailoring the material, e.g., by intentionally introducing defects in the material. Moreover, nonlinearities induced by different processes vary considerably in magnitude. All the nonlinear processes discussed here have been considered for all-optical switching.

#### 3.3.1 Fast nonlinear phenomena in conventional semiconductors

##### *Carrier thermalization, carrier heating and relaxation*

When “hot” carriers are optically generated in a narrow spectral region high up in the band through band-to-band or free-carrier absorption, carrier-carrier scattering causes the “hot” carriers to reach a new thermalized distribution. If there are carriers lower in the band, carrier-carrier scattering also causes the “hot” carriers to give up their excess energy and heat the rest of the distribution. The entire carrier distribution will eventually cool back to lattice temperature via phonon emission through carrier-phonon scattering process. The carrier-carrier scattering process takes place typically within 100 fs [131, 132], and the carrier-phonon scattering process typically takes hundreds of femtoseconds [133].

These intraband processes lead to subpicosecond gain and index nonlinearities which were observed experimentally [70, 134–137]. However, to be used for ultrafast switching, these processes need to be separated from the slow interband process, i.e. only intraband carrier redistribution should take place and interband carrier population changes should be avoided. This can be achieved by biasing the material at transparency through current injection. There are three drawbacks to using the intraband processes for switching: (1) very limited bandwidth, because the device has to

operate at the transparency wavelength; (2) difficulty of implementation, due to simultaneous presence of many processes leading to comparable but opposite index changes (e.g., free-carrier absorption, two-photon absorption, carrier heating, carrier thermalization, stimulated emission) [134, 138]; (3) small overall nonlinear effect relative to interband nonlinearities. Measurements by Hall et al. of optical nonlinearities in current-injected semiconductors [134] indicate that the induced index changes are significantly higher for higher intensity pulses even though the pulse energy is kept constant, which suggests that these carrier-induced nonlinearities are similar in magnitude to nonresonant nonlinearities.

#### *Exciton bleaching and ionization*

Excitonic resonance just below the band edge leads to significantly enhanced optical nonlinearities (see [139] and references therein). Although at room-temperature, due to screening of excitons by free carriers, the excitonic effect is reduced relative to that at lower temperatures, it can be enhanced in quantum-well structures due to the increased binding energy of the confined excitons. In fact, excitonic nonlinearities can be larger than interband nonlinearities in quantum-well structures.

When excitons are created by a short light pulse at a wavelength resonant with the excitonic transition, excitonic absorption is rapidly bleached (within  $\sim 200$  fs) because of phase-space filling [140]. As excitons ionize via phonon interactions, absorption initially recovers with a time constant of  $\sim 300$ – $400$  ps (at room temperature) [140, 141], but this absorption recovery is incomplete due to free-carrier screening of excitons, and the large residual absorption gradually recovers on a nanosecond time scale due to the long carrier lifetime.

Because of the high linear exciton absorption, exploiting the index change associated with the excitonic resonance for switching is not practical. In contrast, exciton-related nonlinearities seem to be more suitable for nonlinear-absorption-based devices (cf. Section 2.1.1). Takahashi et al. have demonstrated an asymmetric Fabry-Pérot switch using the large nonlinear excitonic absorption [22, 126]. However, because excitonic effects are always accompanied in conventional semiconductors by slow carrier recombination time, ultrafast all-optical switching cannot be carried out unless other methods of speeding up the carrier recombination process are applied. Another drawback of the excitonic effects is the limited excitonic bandwidth.

### Spin polarization relaxation

Photons of right or left circularly polarized light have angular momentum of  $+\hbar$  or  $-\hbar$ , respectively. Angular momentum conservation requires the total spin of the electron and hole created by absorption of a photon to be equal to the angular momentum of the photon. Spin distribution of photo-excited electrons and holes is determined by the polarization of light, the type of optical transitions involved, and the selection rules dictated by the band structure of the semiconductor (Figure 3.2). Circularly polarized light can generate carriers with an average spin orientation. The spin orientation will eventually disappear due to various relaxation processes.

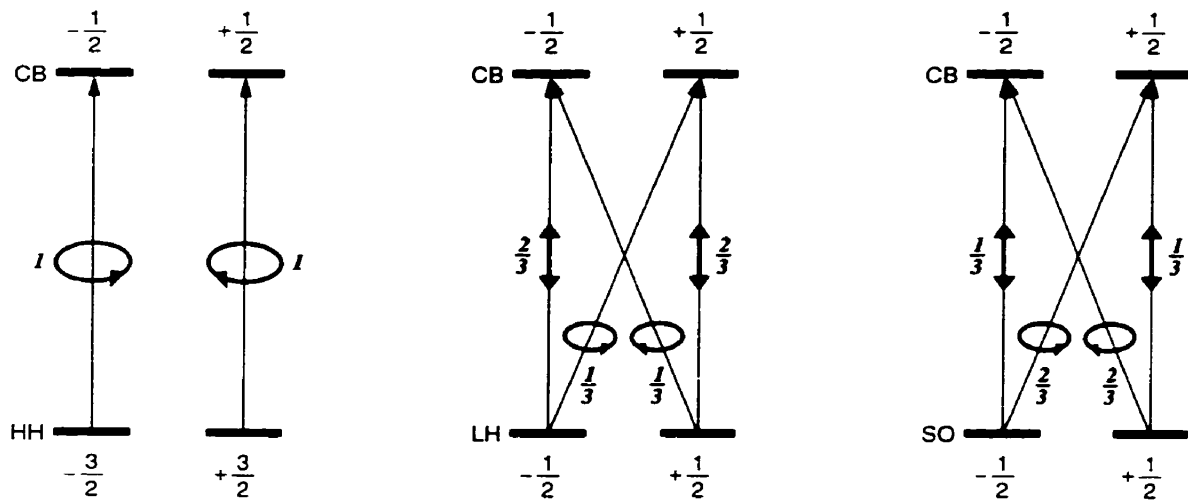


**Figure 3.2** Optical selection rules and transition probabilities for transitions occur at the centre of the Brillouin zone (G-point). The numbers near the arrows representing the transition probabilities. After [142]

The average spin orientation of the carriers results in circular-polarization-dependent nonlinearities, which can be used to devise polarization switches. The switching speed of such devices is determined by the spin relaxation time, which is mainly influenced by three spin relaxation mechanisms: (1) the D'yakonov-Perel' (DP) mechanism, which affects crystals without inversion symmetry, where for  $k \neq 0$ , the spin-orbit coupling leads to spin splitting of the conduction band; (2) the Elliott-Yafet (EY) mechanism, a result of spin-orbit interaction, which causes electron spin to become disoriented through the process of momentum scattering; (3) the Bir-Aronov-Pikus (BAP) mechanism, which is due to electron-hole exchange interaction [143]. Comparing

the efficiency of the three mechanisms based on theoretical analysis and experimental measurements under various conditions, Pikus and Titkov [143] found that for medium-gap crystals, like GaAs or GaSb, DP and BAP mechanisms dominate, resulting in spin relaxation times of  $\sim 10^{-10}$  second at room temperature. For narrow-gap crystals, like InGaAs, EY mechanism becomes more efficient, and spin relaxation times become shorter, about tens of picoseconds. Recent studies have shown that spin relaxation time can also be significantly reduced in quantum well structures [32, 35], and picosecond all-optical switching based on spin-polarization has recently been demonstrated in quantum well devices [31, 126, 144].

A major drawback of using spin-polarization for switching is polarization dependence. Apart from this, spin relaxation process does not lead to a full recovery of the nonlinearities induced by spin-polarization, because the average spin orientation of the carriers does not reverse, but rather randomizes. A complete nonlinear recovery is again limited by the slow carrier recombination process. Although differential method can be used for switching with only partial nonlinear recovery [144], the throughput is low and the switching repetition rate is still limited by the long carrier lifetime.

### *Carrier tunnelling*

Carrier tunnelling process in coupled multiple quantum well structures (Fig. 3.3) has been used [145, 146] to remove carriers from the central well to adjacent wells in order for the carrier-induced nonlinearity to recover quickly in the central well. Carrier tunnelling is assisted by the LO-phonon-carrier scattering [147, 148], a process which depends critically upon the degree of mismatch between the energy level in the central well and those in the adjacent wells, as well as upon the barrier thickness. Resonant tunnelling yields the fastest mechanisms, on the order of  $10^{-13}$  s [149], while for mismatched energy levels, the tunnelling time constant increases exponentially with barrier thickness [147].

Although Tackeuchi et al. [145] has shown that electron tunnelling time can be reduced to 1 ps by using a very thin (1.7 nm) barrier layer (Fig. 3.3a), hole tunnelling remains a very slow process ( $>1$  ns), due to its large effective mass. Another problem arises from absorption by the adjacent wells, because the band gap of the central well is larger than that of adjacent wells (Fig. 3.3a). A type II tunnelling quantum well structure (Fig. 3.3b) [146] is used to remedy this

problem. However, because hole tunnelling is no longer possible in this structure, slow residual absorption saturation problem becomes more severe, limiting the device performance. Apart from these problems, excitonic nonlinearity is decreased due to reduced barrier thickness [145], and switching repetition rate is limited by carrier accumulation in adjacent wells.

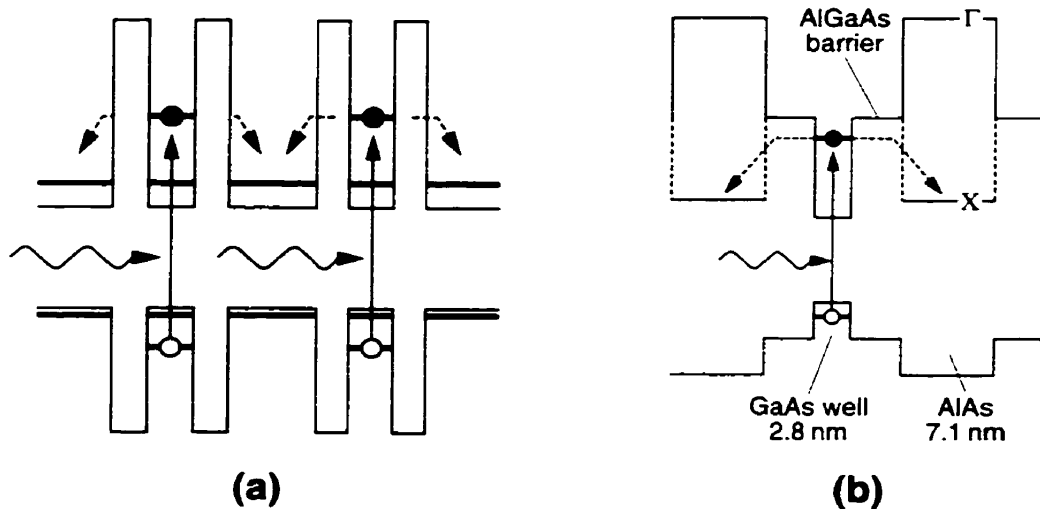


**Figure 3.3** Carrier tunnelling in quantum well structures. **(a)** Tunnelling in type I quantum wells. After [145] **(b)** Tunnelling in type II quantum wells, where the first excited state in the well is lower than the conduction band bottom of the barrier layer at G-point, but higher than that at the X-point. After [146].

#### *Field effects—carrier sweeping*

A fast nonlinear recovery can be obtained by electrically “sweeping out” the carriers [150–152]. Such devices usually have a p-i-n structure where a reverse DC bias can be applied for carrier sweeping. The field strength is generally at least  $10^4$  V/cm in order to accelerate carriers rapidly to the saturated drift velocity of  $\sim 10^7$  cm/s and sweep carriers out of the active region in tens of picoseconds. When this method is applied to quantum well structures, it speeds up two additional processes which assist the fast removal of carriers: carrier tunnelling and carrier thermionic emission, both due to reduced barrier heights [150]. Although tunnelling times for holes are usually long ( $>1$  ns), thermal emission time of the holes can be made much shorter (tens of picoseconds)

by reducing the barrier heights for the valence band. So the combination of field effects and carrier tunnelling are much more effective.

While this method improves the response of the material, it also reduces absorption saturation due to dc electroabsorption [152, 153]. Furthermore, the shortest response time it can achieve is limited to tens of picoseconds due to space charge effects and saturation drift velocities of carriers.

#### *Stimulated emission/absorption*

Free carriers can be removed (or replenished) through stimulated emission (or absorption) by employing a cw holding beam at the transparency wavelength of a current-injected semiconductor. Optical excitation at a different wavelength introduces either gain or absorption changes by depleting or creating more carriers, respectively. With the holding beam, stimulated absorption or emission at the holding beam wavelength takes place; without it, carrier population will recover at the rate of carrier recombination. Since the stimulated transition rate is proportional to the holding beam intensity, nonlinear recovery rate can be accelerated by using an intense holding beam.

Experimental nonlinear recovery times using this method are in the range of tens of picoseconds to more than 100 ps [154, 155], showing moderate improvement with respect to natural carrier lifetimes. The major drawbacks are: (1) the requirement for high intensity holding beams, and (2) considerable reduction of the nonlinear effect. According to the theoretical analysis performed by Manning et al. on a 500  $\mu\text{m}$  long InGaAsP waveguide (assuming waveguide effective area of only 0.2  $\mu\text{m}^2$ ), a 1 W cw holding beam is required to achieve a 3.4 ps carrier lifetime, and the nonlinear phase change is reduced a hundredfold compared to the case when the holding beam is absent [156].

### **3.3.2 Semiconductors with ultrafast carrier lifetimes**

As discussed above, in conventional semiconductors, many ultrafast nonlinear phenomena (e.g., hot carrier effects, exciton effects, spin polarization effects) are accompanied by the slow carrier recombination process. Carrier recombination can be accelerated, for instance, by electrical field sweeping or by stimulated transitions, but such means do not effectively reduce nonlinear recovery

time (limited to the tens of picoseconds range), while resulting in significantly degraded nonlinearities.

Consequently the long carrier recombination time is the major obstacle to ultrafast all-optical switching in semiconductors. The radiative emission rate  $R(\nu)d\nu$  at light frequency  $\nu$  can be calculated by balancing absorption and emission processes at thermal equilibrium [157]:

$$R(\nu)d\nu = \frac{8\pi}{c^2} \frac{\nu^2 n^2 \alpha(\nu)}{\exp(h\nu / kT)} d\nu \quad (3.5)$$

where  $c$  is the speed of light in vacuum,  $n$  is refractive index of the material,  $\alpha$  is absorption coefficient, and  $kT$  is thermal energy. Obviously, for semiconductors, the band gap energy  $h\nu \gg kT$ , resulting in very long carrier recombination lifetimes, on the order of nanoseconds. In addition, non-radiative recombination is not likely, for it requires an immediate imparting of the band gap energy to lattice vibrations, which can only be carried out by emission of an enormous number of phonons simultaneously. However, any possibility of energy emission in parts during the recombination process, i.e. recombination via intermediate states, causes a sharp increase in recombination probability. In fact, the probability increases exponentially with the decreasing number of phonons required: hence, the most effective single intermediate state for reducing recombination lifetime is in the middle of the band gap, where both electron trapping and hole trapping can take place efficiently.

Defects and impurities in semiconductors often create electronic states in the band gap region, therefore, they can serve as carrier trapping and recombination centres and thus effectively reducing carrier lifetime. This reduction in carrier lifetime is obtained not without cost, however. Large concentrations of defects or impurities can significantly disturb the long range order of the crystalline structure, and thereby reduce the large resonant nonlinearity of semiconductors. Additionally, defects typically create band tail states, which results in increase of band tail absorption, an adverse effect for all optical switching devices. For efficient, ultrafast all-optical switching, we need to develop an appropriate method of introducing defects in semiconductors which reduces carrier lifetime effectively with minimal side-effects.

### *Naturally-occurring defects*

Defects and impurities are created unintentionally by standard epitaxial growth techniques, but their concentrations are usually negligible. Nevertheless, large amounts of defects exist at the surface and interfaces of different materials, due to breaking of material's structural continuity at the surface/interface, which results in chemical bonds very different from those in the bulk of the material. Consequently fast recombination processes occur at the surface/interface of materials.

Fast surface recombination has been observed by Lee et al. in windowless GaAs (GaAs with no top AlGaAs layer) étalon optical gates, obtaining 30 ps optical recovery time with a 0.135  $\mu\text{m}$ -thick sample [158]. They measured a linear reduction of response time with decreasing sample thickness, which suggests that surface recombination is the dominant mechanism. Even shorter lifetimes ( $\sim 10$  ps) were observed by Pelouch et al. in a 300 nm InGaAs layer grown on GaAs substrate with a 4.6% lattice mismatch, where high density of dislocations is present at the InGaAs/GaAs heterojunction [159].

The drawback of using surface and interface defects to obtain fast nonlinear recovery is that very thin ( $< 1$   $\mu\text{m}$ ) layers of material have to be used, hence the significantly reduced nonlinearity due to the defects cannot be compensated by large interaction volume. In Pelouch's experiment, only  $\leq 0.1\%$  transmission change was observed for a high carrier density of  $2.4 \times 10^{18} \text{ cm}^{-3}$  [159].

### *Doping*

Shallow dopants, as those normally used for n- or p-doping, do not result in ultrafast carrier lifetimes, because their states are very close (in energy) to one of the bands, making them efficient in trapping one type of carriers, but very inefficient in trapping the other type. Only dopants that create defect states near the middle of the band gap may be efficient in trapping both carriers. Both Cr dopants [160] and Er dopants [161] have been used in GaAs to produce picosecond carrier lifetimes. Among the more unusual dopants, hydrogen sulfide and diethylzinc have been applied to InGaAs, resulting in  $\sim 25$  ps carrier lifetime [162]. In these materials, doping concentration of  $> 10^{19} \text{ cm}^{-3}$  are required to achieve the picosecond lifetimes. Although absorption and nonlinear effects are not mentioned in these studies, it is conceivable that, with such high concentrations of deep-level dopants, absorption is high and nonlinear effects are greatly reduced.

### *Ion implantation*

Ion implantation is another established technique to introduce defects and thus enhance the carrier recombination rate in semiconductors. Proton bombardment has been used to reduce the absorption saturation response time in GaAs/AlGaAs multiple quantum wells down to 150 ps without much degradation of excitonic properties [163]. Subpicosecond carrier lifetimes of GaAs have been obtained using heavy dose ( $10^{12} - 10^{16} \text{ cm}^{-2}$ ) of high energy (200 keV), large ions ( $\text{As}^+$ ), but the estimated reduction in refractive index nonlinearity due to implantation is more than tenfold [164]. Ion implantation on InGaAs/InAlAs multiple quantum wells has been reported to produce lifetimes of a few picoseconds [165]. Although some exciton features were preserved after implantation, large damage trails were observed leading to large increase in absorption at band tail [165]. Annealing after implanting can improve the nonlinearity and reduce band tail absorption to some degree, but carrier lifetime is increased as well [166].

From a practical point of view, ion implantation is an additional device processing step, and it is normally applied before growing more layers. Therefore, this technique is not practical for growing heterostructure devices.

### *Low-temperature molecular beam epitaxial growth*

Low-temperature (LT) growth refers to epitaxial growth at a substrate temperature lower than normal growth temperature. LT-grown GaAs after controlled annealing exhibits high resistivity and ultrafast carrier lifetimes (subpicosecond to picoseconds), and various defects in LT-grown-GaAs have been extensively studied (see review by Melloch et al. [167] and the special issue on low-temperature grown materials in *Journal of Electronic Materials* vol. 22 (12), 1993). Recently, Loka et al. have demonstrated 3 ps all-optical switching using LT-grown GaAs at 850 nm [21]. Other LT-grown materials and quantum wells with relatively large band gap energies, such as InAlAs/InP [168], AlAs/GaAs [169], and GaInP [170], have also shown ultrafast lifetimes. However, LT growth of InGaAs/InAlAs produces relatively long carrier lifetimes (about 100 ps),

and only when used in conjunction with Be doping, can subpicosecond carrier lifetimes be obtained [127, 171, 172].

Although LT-growth combined with Be-doping has successfully produced InGaAs/InAlAs multiple quantum well material with subpicosecond response and large exciton nonlinearity<sup>1</sup>, LT-growth of bulk Be-doped InGaAsP having band gap wavelength of 1.55  $\mu\text{m}$  has produced very poor crystalline quality with no identifiable band edge [23].

Annealing can affect the LT-grown material response drastically. Consequently, it is usually employed to “tailor” the material to yield the desired properties. However, this makes LT-grown materials unsuitable for heterostructure devices, where subsequent layers are required to be grown at normal growth temperature.

#### *Helium-plasma-assisted molecular beam epitaxial growth*

The He-plasma-assisted molecular beam epitaxial growth (HELP growth in short) refers to growth under standard conditions with the material being exposed to a high-energy helium plasma flow generated by an Electron Cyclotron Resonance (ECR) source during growth [173]. It is a unique growth technique, never before been used to produce ultrafast lifetimes in semiconductors.

HELP growth was first used to produce highly resistive InP ( $10^5 \Omega\text{cm}$ ) by Mitchell et al. at McMaster University [174, 175]. HELP-grown InP (HELP InP in short) showed much reduced free carrier density and carrier mobility, and emitted very little photoluminescence. All these traits indicated the presence of deep-level carrier traps, yet, despite these very unusual material characteristics, double crystal x-ray diffraction indicated that the material was not strained and material surface exhibited the same morphology as a standard material. Hence it appeared that high crystalline quality was preserved despite the defects, which suggested that large band-gap nonlinearity may also have been maintained. Thereupon we suggested applying the growth technique to an InGaAsP material whose band gap wavelength was at 1.55  $\mu\text{m}$ , the telecommunications wavelength.

---

<sup>1</sup> LT-growth and Be-doping significantly weaken the exciton feature in InGaAs/InAlAs multiple quantum wells, but the nonlinear exciton absorption can be restored to a certain degree by straining the quantum wells [22].

As subsequent experiments have shown (Chapter 4), this unique growth technique produced high quality InGaAsP having picosecond carrier lifetimes. Furthermore, when we applied Be doping in conjunction with HELP growth, we further shortened the carrier lifetime to the subpicosecond range, without introducing a significant band tail absorption. We have demonstrated ultrafast all-optical switching devices based on this material ([24] and Chapter 5).

HELP growth can be easily implemented. The gas-source Molecular Beam Epitaxy (MBE) facility at McMaster University integrates the ECR chamber with the main MBE growth chamber (Fig. 3.4), enabling instant on-off control of the He-plasma flow during growth. In addition, as will be shown in Chapter 4, this growth technique produces the desired material properties at the standard growth temperature. Therefore, unlike ion-implantation and low-temperature growth, it is particularly convenient for growing heterostructures.

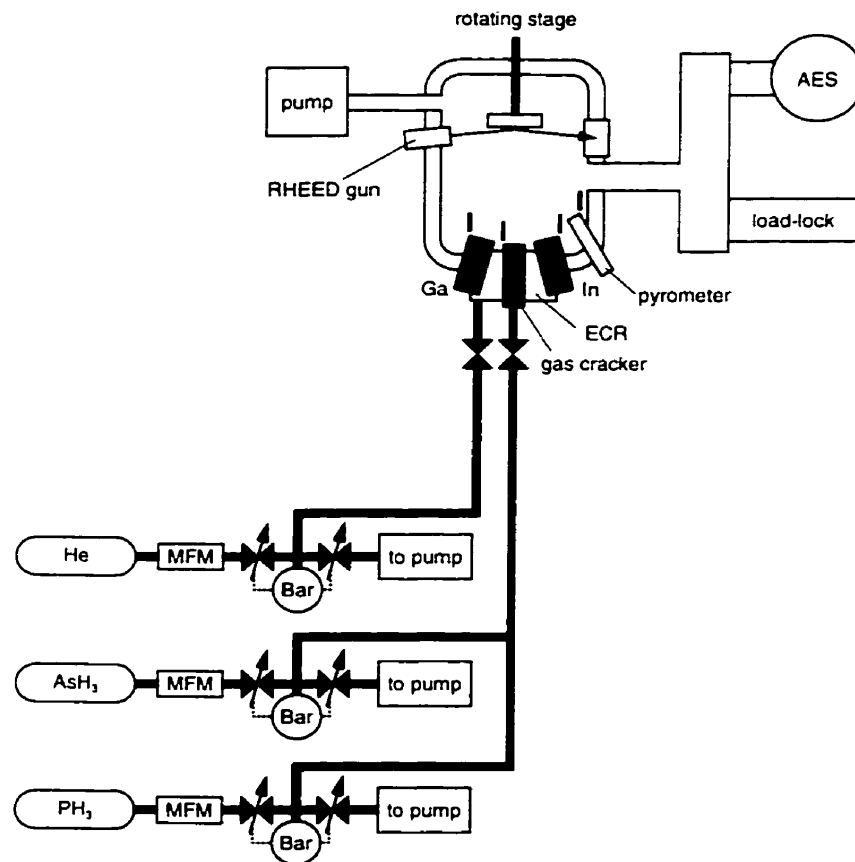


**Figure 3.4** Gas-source Molecular Beam Epitaxy (MBE) system at McMaster University, equipped with the Electron Cyclotron Resonance (ECR) chamber for plasma-assisted growth. MFM: mass flow meter; AES: Auger electron spectroscopy; RHEED: reflection high-energy electron diffraction. After [173].

### 3.4 SUMMARY

Among the two types of intensity-dependent nonlinearities in semiconductors, resonant nonlinearities are in general significantly larger than the nonresonant nonlinearities, and therefore offer the possibility of compact, low-energy all-optical switching.

Large nonlinearities arise from interband transitions recover only in nanosecond time scales due to the slow carrier recombination process in conventional semiconductors. Various intraband processes can induce ultrafast nonlinearities, but they all result in incomplete nonlinear recovery, followed by the slow carrier recombination process. Intraband nonlinearities are also considerably weaker compared to the interband nonlinear effects. To fully utilize the large nonlinearities in semiconductors for ultrafast switching, techniques must be developed either to remove carriers quickly from the active region or to speed up the carrier recombination process.

We have surveyed existing methods for fast carrier removal (tunnelling, electric field sweeping, and stimulated transitions) and techniques of introducing defects (doping, ion implantation, low-temperature growth) to reduce the carrier recombination time. We conclude that, in comparison with all existing techniques, the He-plasma-assisted growth technique produces unique material properties that are better suited for ultrafast all-optical switching.

---

## **Chapter 4**

# **OPTICAL CHARACTERIZATION OF HELP InGaAsP**

This chapter comprises our detailed studies on the optical properties of HELP InGaAsP, with a view to assessing the suitability of this material for ultrafast all-optical switching in future fibre communications systems.

### **4.1 DIAGNOSTIC TOOLS AND TECHNIQUES**

The optical characterizations of HELP InGaAsP we carried out include measurements on optical response times, optically induced index changes, and absorption spectra around the band edge. We performed the measurements using the pump-probe technique, the Z-scan technique, and FTIR (Fourier Transform InfraRed) spectroscopy, respectively. A home-built optical parametric oscillator (OPO) was used as the laser source for all measurements involving short-pulse excitation. The interpretation of the results depends on experimental conditions and techniques, therefore we include below a brief description of the characteristics of the OPO and discussions on the principles of the techniques employed and their limitations.

#### **4.1.1 Optical parametric oscillator**

Assessing the suitability of HELP InGaAsP for ultrafast switching devices in high-speed fibre communications systems required from our laser source the essential characteristics demanded by such systems, i.e. (1) tunable wavelength in the range of 1.5–1.6  $\mu\text{m}$ , (2) short output pulses ( $\sim 1$  ps), (3) narrow-bandwidth, preferably transform-limited, pulses, and (4) sufficient pulse energy for nonlinear switching operation.

We built the OPO [176] (Fig. 4.1) specifically to satisfy these requirements: its signal output has a large tuning range from 1.46  $\mu\text{m}$  to 1.64  $\mu\text{m}$  (Fig. 4.2), its output pulses are  $\sim 1$  ps and transform-limited, and its pulse energy can reach  $\sim 1.5$  nJ. In addition, it has a second pulsed output, the idler, also in the 1.5  $\mu\text{m}$  wavelength region, but generally at a different wavelength from the signal (Fig. 4.2). The idler pulses are perfectly synchronized to the signal pulses by

virtue of the parametric process. The signal and idler have orthogonal polarizations—the signal is horizontally polarized (parallel to the optical table), and the idler is vertically polarized—which allows easy separation and recombination of the two beams. The dual-wavelength function of the OPO enabled us to investigate the material response at a wavelength different from the excitation wavelength, and thereby assess the suitability of HELP InGaAsP for all-optical switching devices utilizing dual-wavelength operation.

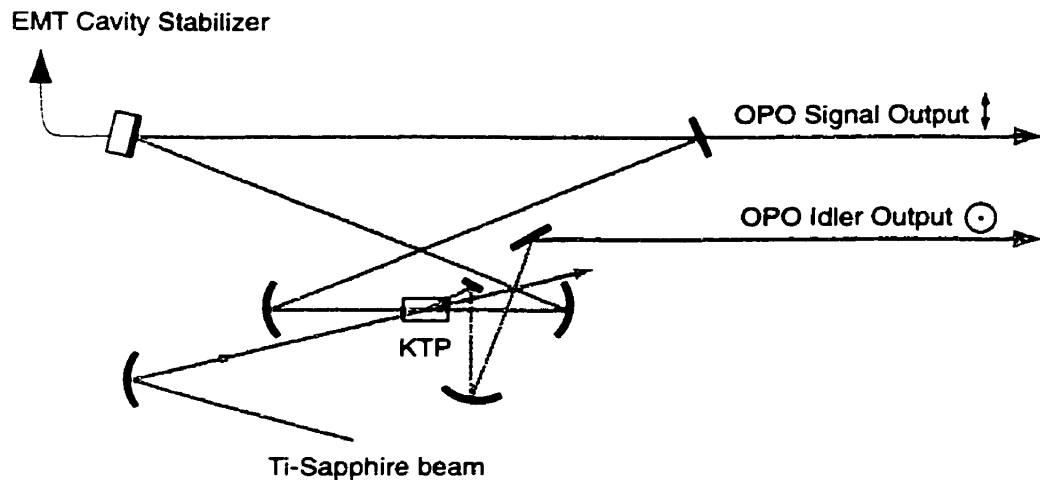


**Figure 4.1** Schematic of the optical parametric oscillator (OPO). The gain medium, KTP ( $\text{KTiOPO}_4$ ), is pumped by a tunable mode-locked Ti-sapphire laser. The laser cavity is stabilized by an EMT (electromechanical transducer). The signal output is taken from the resonating cavity. The idler is not resonated and it is taken directly after the parametric generation. The signal and idler have orthogonal polarizations.

Although the OPO has a low repetition rate of 82 MHz, which did not allow us to test the material response under high-rep-rate excitation in the usual sense, optical excitation by two pulses in fast succession was made possible by splitting the low-rep-rate pulse train into two and multiplexing them with an appropriate time delay in between. Thus, by using two closely spaced pulses, we mimicked the high-rep-rate operation. Although this arrangement does not replicate high-rep-rate operation in every respect, it does offer some insight into the dynamics of material response under high-rep-rate excitation.

The OPO offers extremely large tuning range, short pulse duration, high pulse energy, and coherent, synchronized, dual-wavelength output, and, aside from its low rep rate, it proved to be a versatile tool for our studies on the ultrafast nonlinear response of HELP InGaAsP.

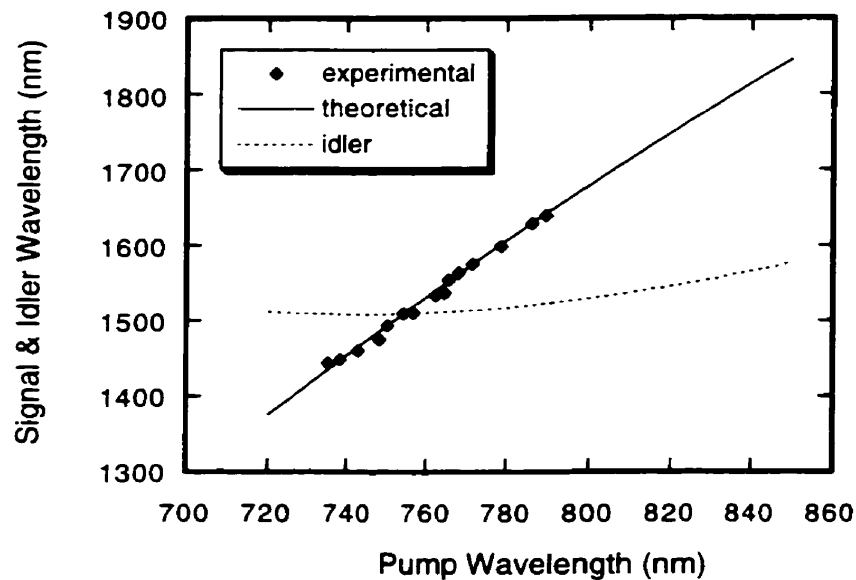


**Figure 4.2** Tuning ranges of the OPO signal and idler outputs, obtained by tuning the Ti-sapphire wavelength. Signal tuning is limited to  $1.46\ \mu\text{m}$ – $1.64\ \mu\text{m}$  by the bandwidth of the cavity mirrors. Symbols represent measured data, lines are calculated. After [176].

#### 4.1.2 Pump-probe technique for measuring material response times

The standard pump-probe technique is commonly employed to measure the ultrafast material response to optical excitation. An intense pump pulse train is used to excite the material optically and alter its optical properties (absorption or index). At the same time, the transmission or reflection of a weak probe pulse train, also directed at the material, is monitored as a function of the time delay (or path difference) between pump pulses and probe pulses. The change in probe transmission (or reflection) reflects the dynamic change in material properties. By this technique, we can measure extremely fast changes, since the time resolution is limited only by the pulse duration.

Specifically, we measured the transient transmission responses of InGaAsP samples optically excited at wavelengths in the absorption band edge region. Probe transmission is affected by sample absorption, which is dictated by band-filling and Coulomb screening effects [139], and therefore varies as a function of electron and hole concentrations. Consequently, when pump pulses and probe pulses overlap in time, the probe pulses experience a sharp transmission increase (or absorption saturation) due to carriers induced by the pump pulses. As the probe pulses are delayed relative to the pump pulses, the probe transmission experiences a recovery, because, during

the delay interval, carriers decay through radiative or non-radiative recombination or trapping. Therefore, the recovery time of probe transmission gives indication to carrier lifetimes. However, the relationship is a complex one (see discussion below), and throughout this thesis, we will use the term “optical response time” loosely to denote the probe recovery time ( $\tau$ ).

In materials where non-radiative carrier trapping by mid-gap defect levels is the dominant carrier decay mechanism, as is the case with HELP InGaAsP, electron trapping rates are in general different from hole trapping rates. The difference in electron and hole trapping rates leads to  $\tau$  variation with (1) probe wavelength and (2) induced carrier density (or pump pulse energy).

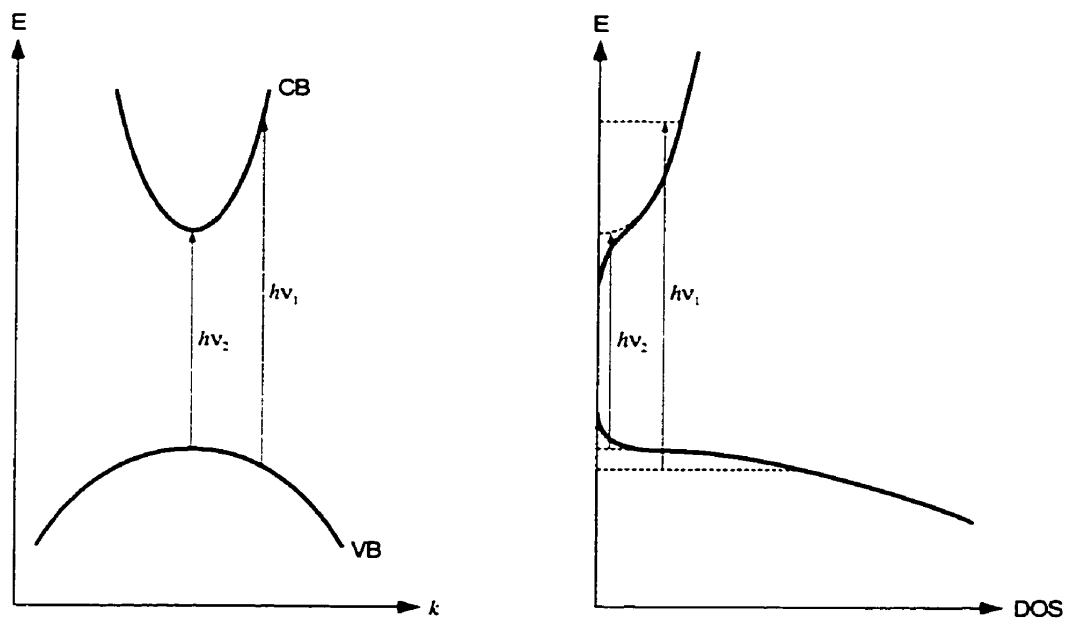


**Figure 4.3** Above-band absorption ( $h\nu_1$ ) versus band-tail absorption ( $h\nu_2$ ). The left diagram illustrates that absorption obeys the  $k$ -selection rule, the right diagram shows the Density Of States (DOS) involved in these transitions. For above-band transitions, valence band DOS is much higher than conduction band DOS, whereas for band-tail transitions, the DOS's are comparable.

The variation in  $\tau$  with probe wavelength can be explained as follows. Because of the large difference in the density of states of the conduction and valence bands (Fig. 4.3), the transient absorption at an above-band wavelength ( $h\nu_1$  in Fig. 4.3) is dominated by conduction band filling. Therefore, pump-probe experiments conducted with an above-band probe are more sensitive to conduction-band electron population than to valence-band hole population, and  $\tau$  reflects mainly the electron lifetime. On the other hand, absorption at a longer probe wavelength ( $h\nu_2$  in Fig. 4.3)

occurs only between the band-tail states, where densities of states are comparable in conduction band and valence band (Fig. 4.3). In this case, the probe transmission change reflects both electron and hole trapping times, and  $\tau$  can differ considerably from the above-band case.

The variation in  $\tau$  with induced carrier density can be caused by limited trap (defect) density, a phenomenon we refer to here as the “bottleneck” effect. For instance, when the electron trapping rate is much higher than the hole trapping rate, trap levels tend to be “filled” with electrons because the “trap emptying” process (hole trapping) is slower than the “trap filling” process (electron trapping). Trap filling in turn slows down electron trapping due to the reduction of available electron states in the trap levels. When the initial carrier density is much lower than the trap density, electron trapping will not be significantly affected because “trap filling” does not occur; however, when the initial carrier density is of the same order or higher than the trap density, the “bottleneck” effect will slow down the initially fast electron trapping process, until electron and hole trapping rates are balanced.

Therefore, in order to gain more insight into carrier trapping dynamics, we performed pump-probe experiments at various probe wavelengths and under a range of carrier densities. Our experimental setup (Fig. 4.4) allows for both single-wavelength and dual-wavelength pump-probe measurements, and the probe, being the signal output of the OPO, can be tuned over a wide wavelength range (1.46–1.64  $\mu\text{m}$ ). The pump and probe beams are focused onto the same spot on the sample, and probe transmission is measured by lock-in detection as a function of pump-probe time delay, registered by the computer which controls the delay stage. Lock-in detection increases the sensitivity of the measurements and ensures that only pump-induced changes are measured. Probe power is monitored to correct errors introduced by power fluctuations of the OPO. Single-wavelength pump-probe experiments are carried out by blocking either the signal or the idler beam before the polarization beam splitter (PBS1 in Fig. 4.4). The pump-to-probe power ratio can be easily controlled by inserting a half-wave plate (labelled as  $\lambda/2$  plate 1 in Fig. 4.4) between PBS1 and PBS2. Dual-wavelength pump-probe experiments require both signal and idler beams. The manual translation stage is adjusted to ensure overlap of pump and probe pulses at PBS 1. This allows easy conversion of a single-wavelength pump-probe experiment to a dual-wavelength one, or vice versa. In addition, dual-pulse pump-probe experiments, with either

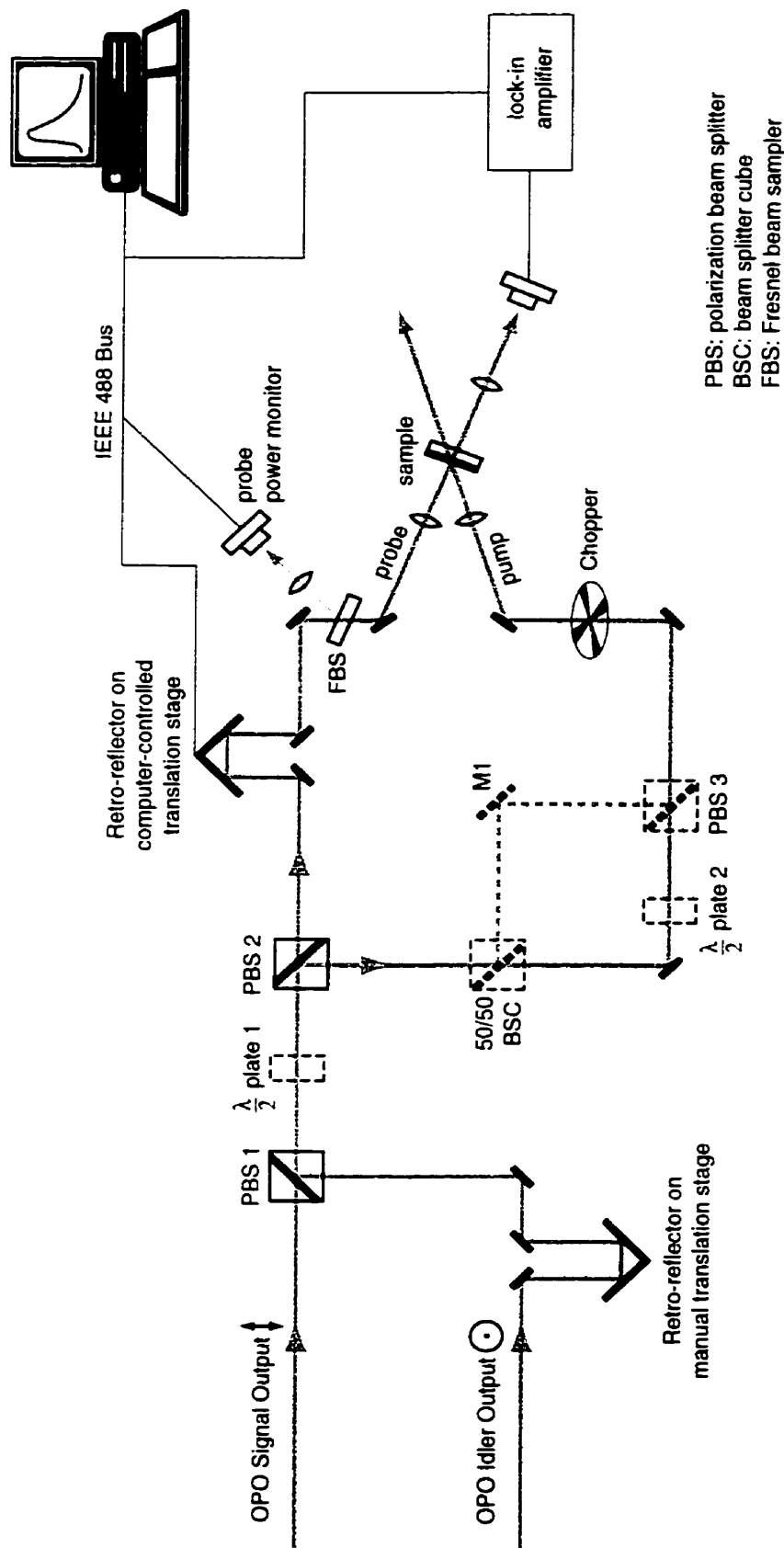


**Figure 4.4** Schematic diagram of the pump-probe experiment. This set up allows for easy conversion between single-wavelength and dual-wavelength operation, as well as between single-pulse and dual-pulse operation.

single- or dual-wavelength configuration, can be carried out by creating an additional path with proper optics (dotted lines in Fig. 4.4).

### 4.1.3 Z-scan technique for measuring light-induced index change

We employed the standard Z-scan technique [177] to measure light-induced refractive index changes. When an intense Gaussian beam passes through a layer of nonlinear material, the beam experiences self-focusing or defocusing caused by the intensity-dependent index change induced in the material. If an aperture smaller than the beam cross-section is placed after the sample, the amount of light transmitted through the aperture will depend on the position of the sample relative to the waist position of the Gaussian beam. During a Z-scan, the transmitted power is recorded as the sample is moved along the  $z$ -axis ( $z$  being the direction of beam propagation) across the focal region. A simple relationship can be derived between the index change induced at the beam waist centre and the maximum change in normalized transmission. (See Appendix A for a more detailed, quantitative account of the Z-scan technique and its underlying assumptions.)

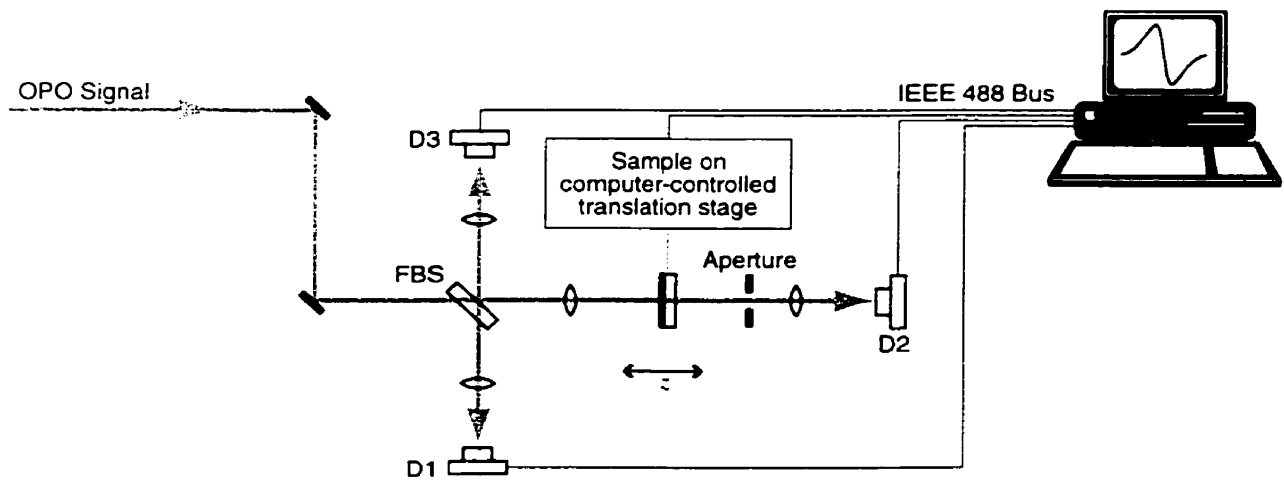


**Figure 4.5** Schematic diagram of the Z-scan experiment which measures the average index change in the sample induced by pulses from the OPO over the pulse duration ( $\sim 1$  ps)

Our Z-scan setup is shown in Fig. 4.5. Detector 1 (D1) monitors the incident light power, so that any power fluctuation from the source can be corrected. Detector 2 (D2) measures power transmitted through the aperture to determine light-induced index change in the sample. An

additional detector (D3) can be added to measure power reflected from the sample, hence, this setup can also be used to measure absorption. Several factors contribute to the change in signal received by D2 as the sample is moved along the  $z$ -axis: (1) self-focusing or defocusing of the beam caused by light-induced index change in the sample, (2) carrier-induced absorption saturation, and (3) beam scattering caused by sample surface inhomogeneities. To eliminate contributions from (2) and (3), four scans—two Z-scans and two open-aperture scans performed under high intensity and low intensity—are required, thus light-induced index change can be measured in the presence of absorption saturation and surface inhomogeneities (Appendix A). An important requirement of Z-scan measurement is that the beam should be Gaussian. We confirmed this during our experiments by observing the beam cross-section over the scanning range with a beam profiler, which we also used to measure the beam waist size.

#### 4.1.4 Fourier transform infrared spectroscopy for measuring absorption spectra

Fourier transform spectroscopy is based on the principle that the spectral density  $S(\nu)$  of any light signal is the Fourier transform of its auto-correlation function  $G(\tau)$ , also known as the Wiener-Khinchin theorem:

$$S(\nu) = \int_{-\infty}^{\infty} G(\tau) e^{-j2\pi\nu\tau} d\tau \quad (4.1)$$

The auto-correlation function can be obtained by a Michelson interferometer with a scanning arm (Fig. 4.6), and the spectrum can be extracted by performing Fourier transform.

We used a commercial FTIR spectroscopy system (Bomem MB157) [178] to measure the absorption spectra of our HELP samples near the band edge. FTIR spectrometers do not require dispersive elements, have large spectral ranges and high sensitivity. The Bomem system has the added advantage of maintaining permanent interferometer alignment [178].

The samples were placed at the main focus point shown in Fig. 4.7. Since this system only measures the transmission spectrum, and our samples were not antireflection coated, Fabry-Pérot fringes were visible in the low-loss region of the spectrum. Our main purpose was to verify whether the material exhibited a sharp band edge without a significant band tail absorption, hence in most cases we did not attempt to remove the Fabry-Pérot effect.

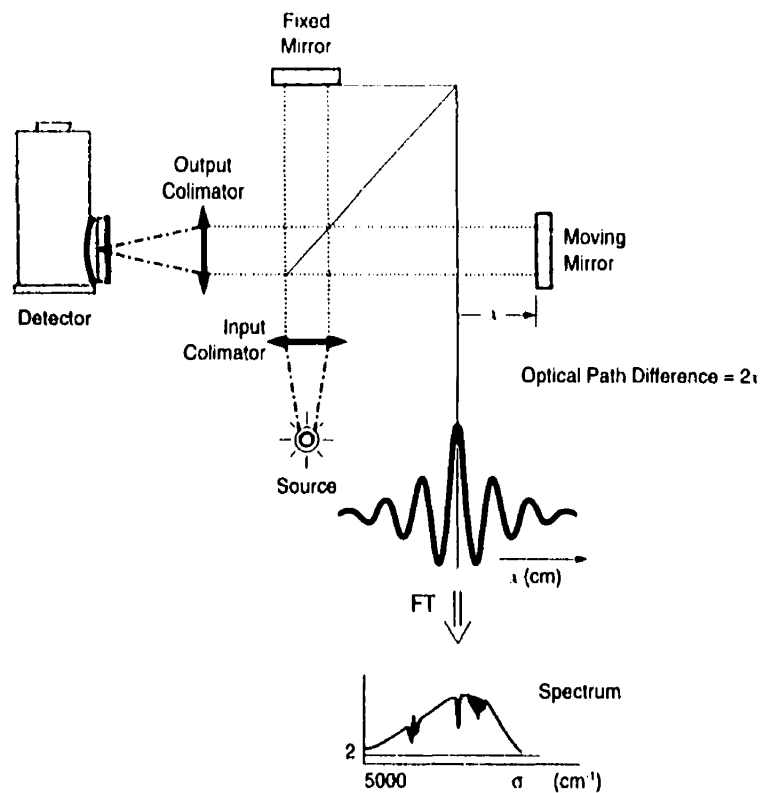


**Figure 4.6** Principle of operation of an FTIR spectrometer based on a Michelson interferometer (After [3]). The spectrum of the “source” is obtained by performing a Fourier Transform on its auto-correlation signal, detected at the output of the Michelson interferometer.

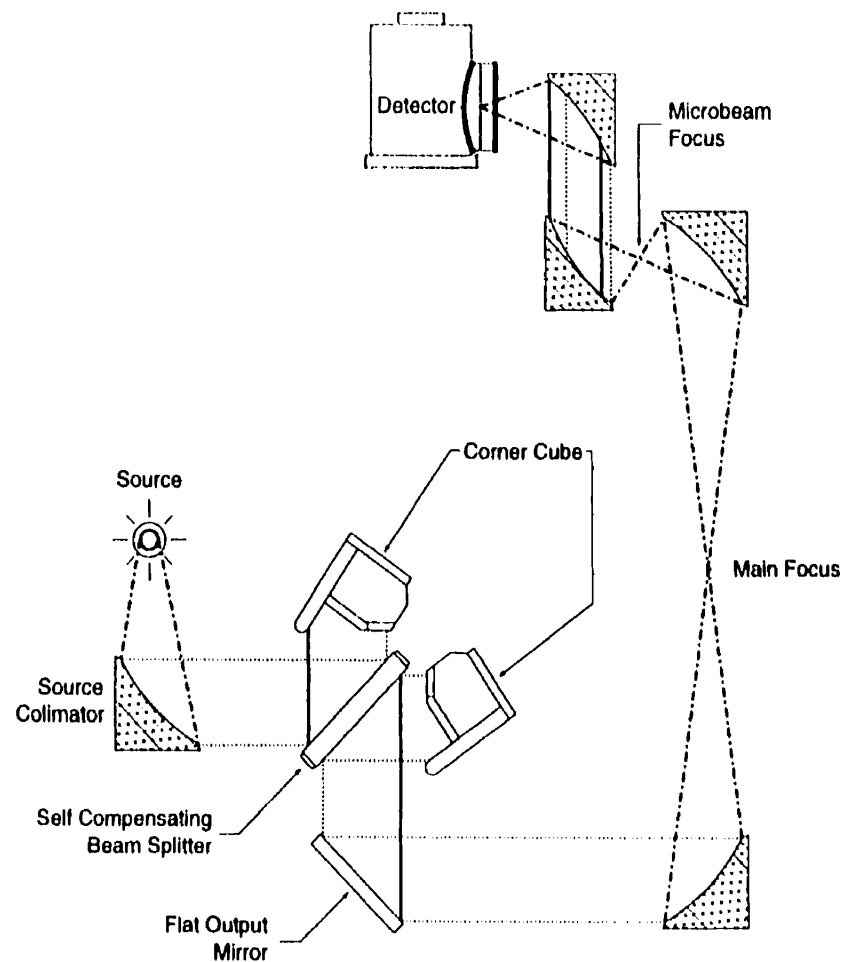


**Figure 4.7** Schematic diagram of the Bomem Michelson spectrometer. The test sample is placed at the “main focus.” After [3]

## 4.2 INITIAL STUDIES ON CARRIER-INDUCED INDEX CHANGE, RESPONSE TIME, AND ABSORPTION

Our objectives were to utilize the large interband resonant nonlinearity in InGaAsP for optical switching and to speed up this nonlinear recovery by introducing defects in the material by HELP growth. As stated previously (Section 3.3.2), defects usually lead to poor crystalline quality, reduced nonlinearity, and additional absorption at the band tail due to disruption of the long range order of the crystalline structure. Therefore, we needed to investigate not only the response time of HELP InGaAsP, but also its nonlinear index change, as well as its absorption band edge (as a measure of its crystalline quality), in order to determine if the material is suitable for waveguide devices operating at the band tail.

**Table 4.1 Samples and measurements performed in the initial studies**

Sample ID	Sample Description	Growth condition	Measurements		
1639	standard InGaAsP	conventional gas source MBE at 435° C (standard)	pump-probe	FTIR	Z-scan
1640	HELP InGaAsP	He-plasma-assisted gas source MBE at 435° C (standard + He-plasma)	pump-probe	FTIR	Z-scan
1641	low-temperature-grown InGaAsP	conventional gas source MBE at 200° C		FTIR	

For quantitative comparison of material properties, we requested growth of three InGaAsP samples at McMaster University (Table 4.1). Sample IDs correspond to growth log numbers used for their MBE system. All samples have a nominal band-edge wavelength of  $\sim 1.57 \mu\text{m}$  and a nominal thickness of  $2 \mu\text{m}$ . Each sample was grown on top of a  $\sim 300 \mu\text{m}$  semi-insulating InP substrate with a  $500 \text{ \AA}$  InP buffer layer and a  $500 \text{ \AA}$  of InP cap layer. The substrates were polished but not removed, because they were transparent at the wavelengths of interest ( $1.5\text{--}1.6 \mu\text{m}$ ).

### 4.2.1 Optical response times

The single-wavelength pump-probe experiment at 1.55  $\mu\text{m}$  (above-band) shows a 15 ps response time in sample 1640 (HELP sample) (Fig. 4.8). The response time in sample 1639 (standard sample) is too long to be determined accurately with this technique, but it is estimated to be on the order of 1 ns. Therefore, HELP growth reduces the material response time by two orders of magnitude.

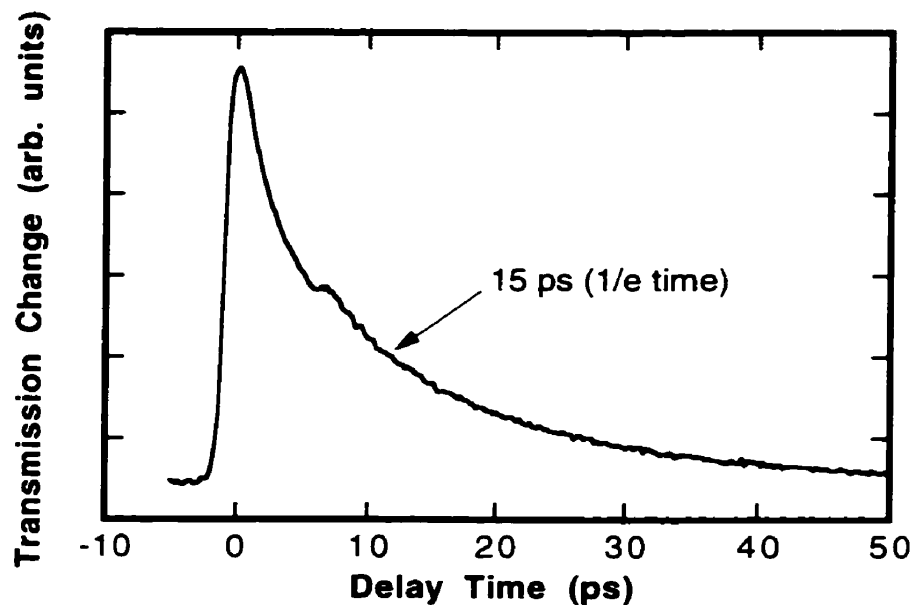


**Figure 4.8** Change in transmission measured by single-wavelength pump-probe technique in sample 1640 (HELP sample) using 1 ps pulses at 1.55  $\mu\text{m}$ , showing a 15 ps optical response time.

We attribute the drastic reduction in response time to the defects introduced by HELP growth which serve as effective carrier traps and recombination centres. Two findings [179] from the electrical characterizations of the HELP InGaAsP material support our attribution:

(1) Room-temperature Hall effect measurements on the HELP InGaAsP indicate a  $\sim 10\times$  reduction in free carrier concentration and a  $\sim 3\times$  reduction in carrier mobility relative to those of the standard sample. The reduced free carrier concentration implies effective carrier trapping by deep-level defects (thermal excitation energies  $\gg kT$ ), and the reduced mobility suggests significant carrier scattering by impurities.

(2) HELP InGaAsP does not emit any detectable photoluminescence signal, indicating that non-radiative carrier decay processes are favoured over the radiative decay process.

Thus, it is reasonable to assume that these deep-level defects trap carriers through non-radiative carrier decay processes (multi-phonon-assisted or Auger processes). Since non-radiative carrier trapping by deep-level defects are generally orders of magnitude more efficient than radiative carrier recombination (Section 3.3.2), we conclude that these non-radiative processes result in picosecond carrier lifetimes and ultrafast recovery of light-induced nonlinearity in the HELP InGaAsP material.

#### 4.2.2 Light-induced index changes

Following successful reduction of optical response time by the introduction of effective carrier-trapping defects in the material, we proceeded to determine whether these defects affect the magnitude of the nonlinear response. We measured the average index change induced by a 1 ps Gaussian pulse as a function of fluence at three different wavelengths, corresponding to different amounts of detuning from the band edge (Fig. 4.9). An average index change of as much as -0.077 was observed in sample 1640 (HELP sample) at zero detuning. Under high photon fluence and at zero detuning, the nonlinear index change in this sample was comparable to that of sample 1639 (standard sample), yet its response time was reduced a hundredfold. At 40 nm detuning, we obtained an average index change of -0.03 in sample 1640, larger than that of sample 1639. This larger index change, however, may not be an advantage, because it is obtained in the wavelength region where absorption is also slightly larger than that of sample 1639 (Section 4.2.3). Obviously, the larger index change is associated with this larger absorption, which is primarily due to absorption between the band tail states resulted from the perturbation of the band edge by defects.

The fact that HELP growth maintains the large nonlinearity similar to that of the standard material implies that long range order of the crystalline structure is preserved; and, despite the defects introduced, the predominant absorption process is still band-to-band. This implication is verified next by absorption spectra measurements around the band edge.

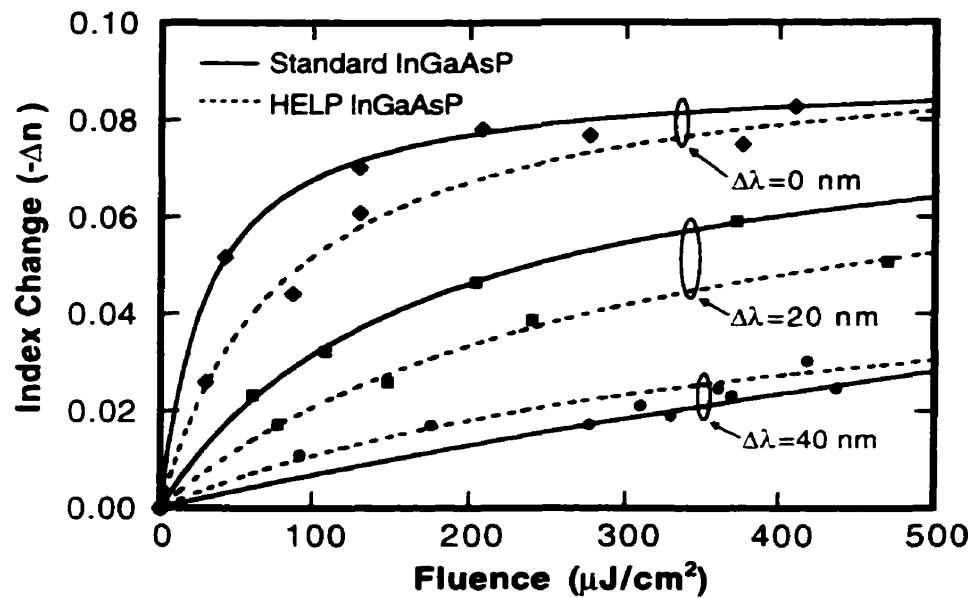
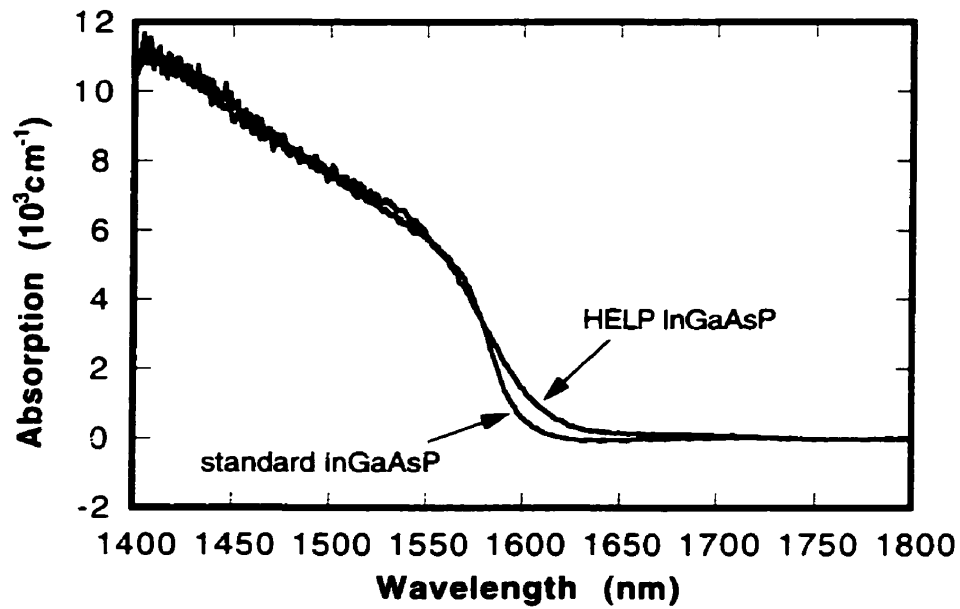


**Figure 4.9** Comparison of index changes induced in sample 1640 (HELP InGaAsP) and sample 1639 (standard InGaAsP) by 1 ps pulses of varying intensity and at a series of wavelengths detuned from the band edge. Points are actual data; curves are guides for the eye.

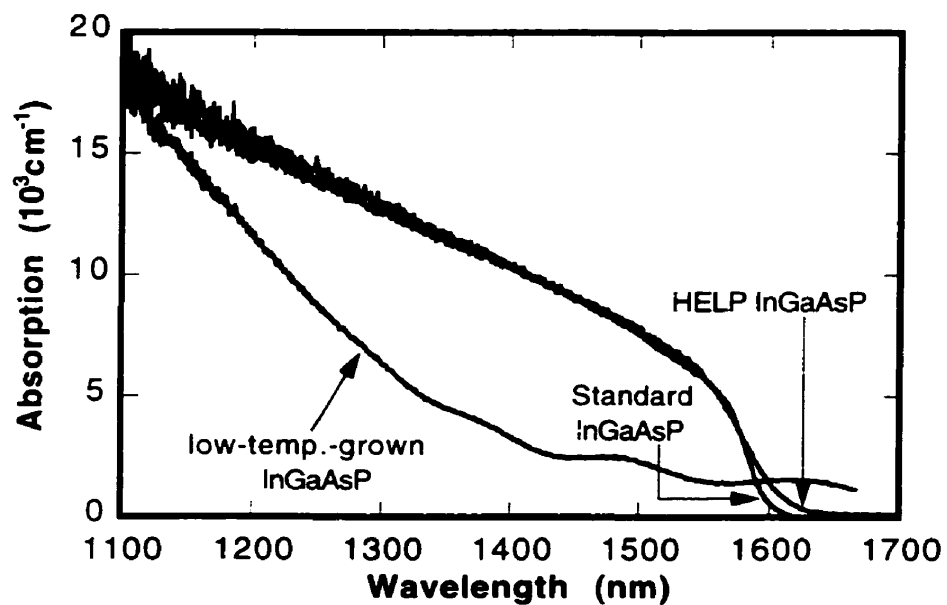
### 4.2.3 Absorption spectra around band edge

Defects and impurities in semiconductors introduce “tails” of states, which extend the bands into the energy gap through several mechanisms [180]:

- (1) A single shallow impurity can bind an electron (or a hole) and form a discrete level just above the valence band (or just below the conduction band). The binding energy is usually smaller than  $kT$ . As the impurity concentration increases, the electron wavefunctions at the impurity level overlap, resulting in the formation of a band of states merging with the valence band (or conduction band).
- (2) Randomly distributed charged impurities perturb the band edges by Coulomb interactions with free carriers, resulting in a number of local conduction-band states (or valence-band states) at lower (or higher) potentials relative to the unperturbed band edge.
- (3) Defects and impurities create mechanical strain, which locally increases or decreases the energy gap depending on whether the strain is compressional or dilational. These perturbations also result in tail states.



(a)



(b)

**Figure 4.10** Absorption spectra of InGaAsP samples around band edge illustrating the major advantage of HELP growth over low-temperature growth. Comparison between the HELP sample and the standard sample (a) indicates that high crystalline quality is maintained in the HELP sample. The lack of an identifiable band edge in the low-temperature-grown sample (with Be doping) (b) indicates a poor crystalline quality. (Data for the standard and HELP samples have been modified to compensate for the Fabry-Pérot effects.)

The absorption tail resulting from absorption between the tail states is known as the Urbach tail. Generally, the higher the defect concentration, the larger the tail. But the size of the tail also depends on the type of defects and their host material. For optical device applications, materials with small absorption tails are desirable.

We have measured the absorption spectrum of sample 1640 (HELP InGaAsP) by FTIR spectroscopy; like that of sample 1639 (standard InGaAsP), it has a sharp band edge and its absorption tail is only slightly higher ( Fig. 4.10a), indicating high crystalline quality. In contrast, there is a marked difference between the spectra of sample 1639 and 1640 and that of sample 1641 (low-temperature-grown InGaAsP) (Fig. 4.10b). Remarkably, compared to the well-known low-temperature growth technique, HELP growth produces much sharper band edges, which highlights one of the major advantages of HELP growth in device applications: large nonlinearity can be obtained at a relatively low absorption level.

### **4.3 DOPING, ANNEALING AND OTHER CONDITIONS AFFECTING MATERIAL PROPERTIES**

The next step in our investigations was the study of methods of enhancing the optical properties of HELP InGaAsP, particularly with a view to further reducing the material response time, while maintaining a sharp absorption band edge (and hence the large nonlinearity). Specifically, we investigated effects on material properties by (1) beryllium doping, (2) varying helium plasma conditions, (3) annealing at various temperatures, and (4) varying induced carrier concentration.

#### **4.3.1 Effects of Be doping**

There were a number of reasons why we considered Be doping as a possible means to further reduce the response time of HELP InGaAsP. First, several authors have shown that, while low-temperature growth (LTG) alone can reduce carrier lifetimes only down to ~100 ps in InGaAs materials, Be doping can be used in conjunction with LTG to reduce effectively lifetimes to subpicosecond in these materials [127, 171, 172]. One plausible explanation for the lifetime reduction by Be dopants, suggested by Jodawlkis et al., is that Be doping helps to form Be-As

defect complexes in LTG InGaAs which serve as effective carrier traps [171]. Second, Haiml et al. reported that, in contrast to undoped LTG GaAs where ultrafast response is only obtained at the expense of reduced nonlinearity, Be-doped LTG maintains relatively high nonlinearity, while reducing the response time to subpicosecond [181]. Third, electrical characterization of HELP InP material revealed that p-type doping (Be) maintains the high resistivity ( $>10^4 \Omega\text{cm}$ ) found in undoped HELP InP, and the material remains weakly n-type even with  $3 \times 10^{18} \text{ cm}^{-3}$  Be doping [175]. Both the high resistivity and the fact that high Be doping does not result in high free hole concentration suggest the presence of effective free carriers traps. Evidently, Be doping significantly affects the defect-related optical and electronic properties of InGaAs and InP. Because InGaAsP is similar in composition to InGaAs and InP, we would expect Be doping to play a significant role in the carrier dynamics of HELP InGaAsP as well.

**Table 4.2 Description of samples used for study of Be-doping effects**

Sample ID	Growth condition	Doping concentration
1968	standard	undoped
1969	standard + He-plasma	undoped
1970	standard + He-plasma	$3 \times 10^{17} \text{ cm}^{-3}$
2001	standard + He-plasma	$1 \times 10^{18} \text{ cm}^{-3}$
2002	standard + He-plasma	$6 \times 10^{18} \text{ cm}^{-3}$
2460	standard	$6 \times 10^{18} \text{ cm}^{-3}$
2461	standard + He-plasma	$6 \times 10^{18} \text{ cm}^{-3}$

We used HELP InGaAsP samples with various Be doping concentrations ( $0\text{--}6 \times 10^{18} \text{ cm}^{-3}$ ) (see Table 4.2) to study the effects of Be doping on material response time and absorption band edge. For the purpose of comparison, we also included in our study two samples grown under the standard growth conditions (without He plasma): one undoped (1968), the other doped with  $6 \times 10^{18} \text{ cm}^{-3}$  Be (2460). All samples have nominal band edge wavelengths of  $\sim 1.52 \mu\text{m}$ , (small

variations in wavelength for each sample may be present, due to unintentional change in growth conditions<sup>1</sup>). All samples are ~2 μm thick, grown on lattice-matched semi-insulating InP substrates, each with a 500 Å InP buffer and a 500 Å InP cap layer. The substrates are transparent in the wavelength region of interest, and their back surfaces were polished to facilitate transmission experiments.

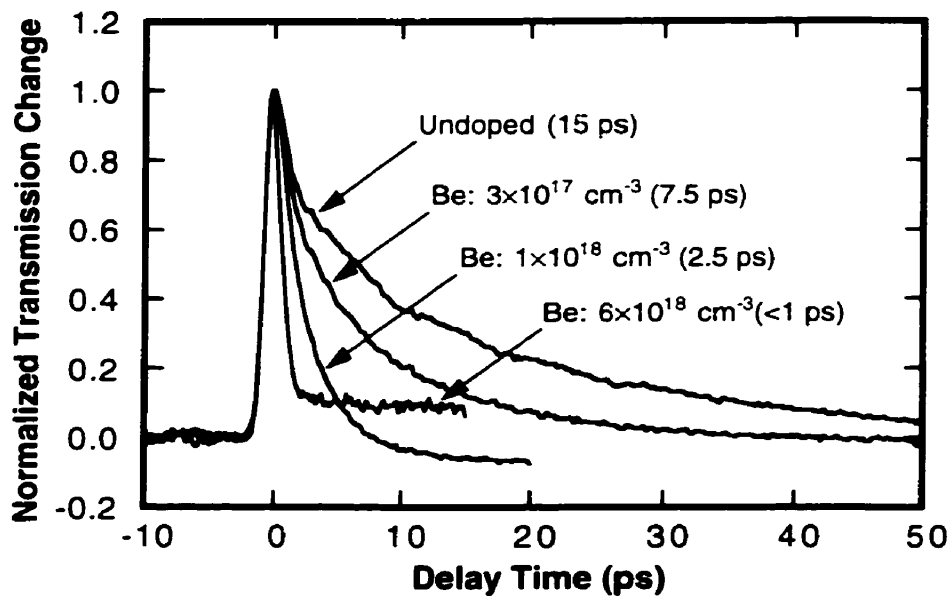
#### 4.3.1.1 MATERIAL RESPONSE TIMES OF BE-DOPED HELP InGaAsP

We measured material response times of the four HELP samples (1969, 1970, 2001, 2002) by standard pump-probe technique at an above-band wavelength (1.50 μm), under two different pump pulse energies. In both cases, the material response times decrease progressively as Be doping concentration increases (Fig. 4.11). At the lower pump-pulse energy (0.1 nJ), the response time drops from 15 ps in sample 1969 (undoped) to 0.8 ps in sample 2002 ( $6 \times 10^{18} \text{ cm}^{-3}$  Be doped). (The measured value of 0.8 ps is limited by the resolution of the experiment). At the higher pump pulse energy (0.6 nJ), the reduction in response time by Be doping is more dramatic: from ~25 ps in sample 1969 to 1 ps in sample 2002. (The longer response times obtained under the higher pump energy is due to the “bottleneck” effect, which will be discussed in Section 4.3.4.) Additionally, we have verified that Be doping alone does not lead to ultrafast response times in InGaAsP, as the pump-probe measurement on sample 2461 revealed a 325 ps response time (Fig. 4.12). Therefore, a three-order-of-magnitude reduction in optical response time in InGaAsP can be achieved by HELP growth combined with Be doping.

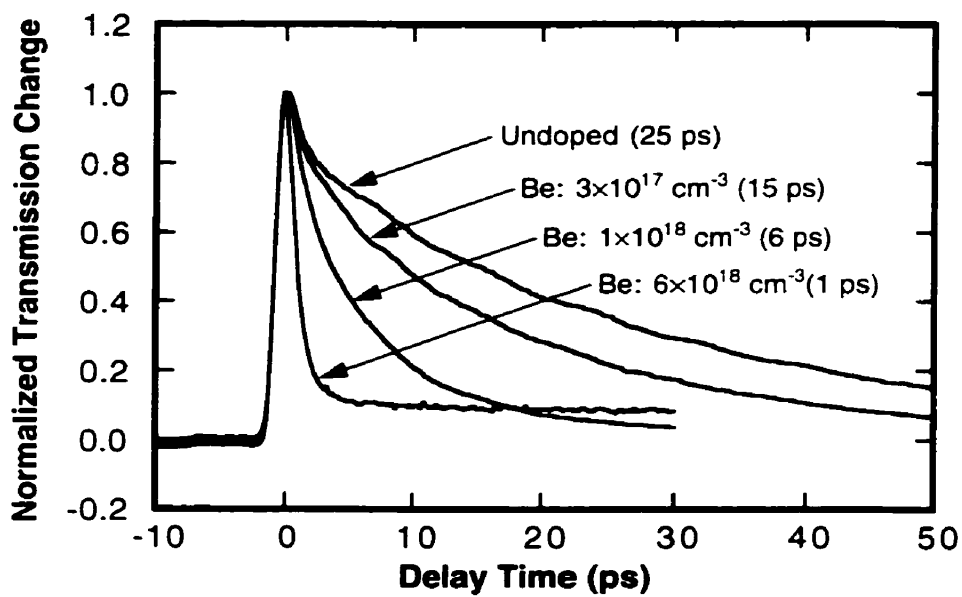
Since the measurements were carried out at an above-band wavelength, the probe transmission transients were dominated by the conduction-band electron population. Hence, short response times indicate fast conduction-band electron decay. As discussed above (Section 4.2.1), HELP InGaAsP materials comprise efficient carrier traps which are responsible for the fast carrier decay processes. The electron decay rate  $dN_e/dt$  ( $N_e$  being the conduction-band electron

---

<sup>1</sup> Samples with consecutive ID numbers were grown consecutively, so they are likely to have nearly identical growth parameters, including material composition, growth temperature, and growth rate.

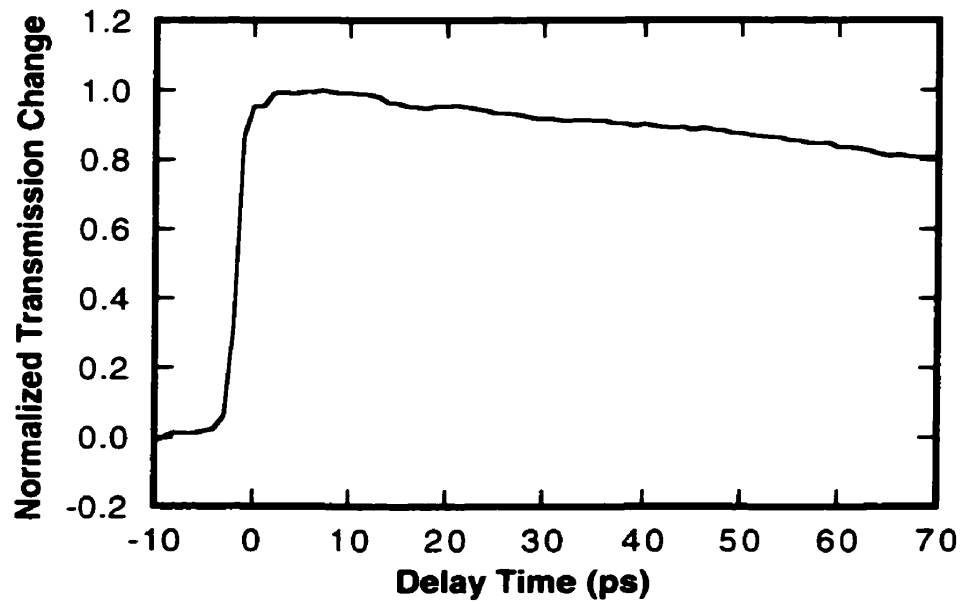


(a)

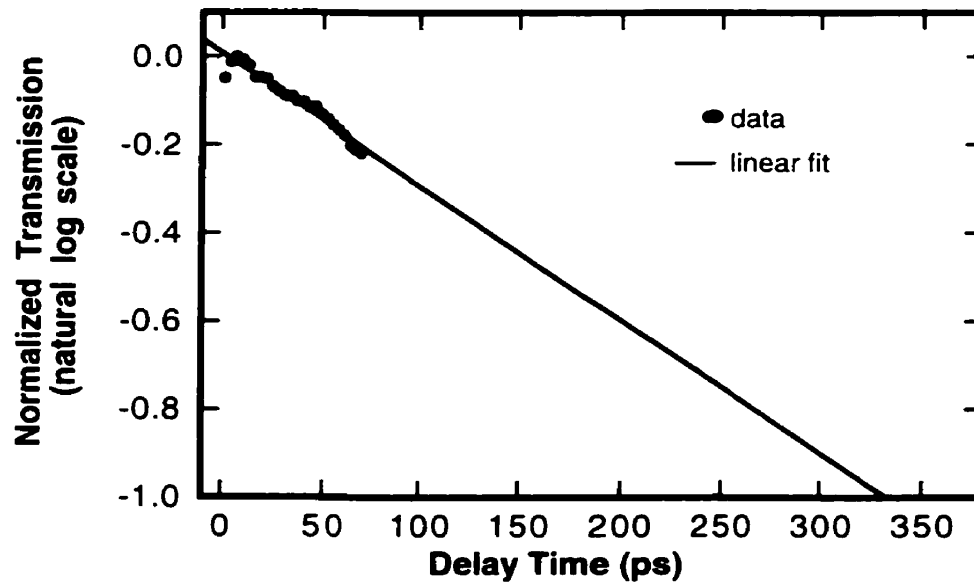


(b)

**Figure 4.11** Optical response times of HELP InGaAsP samples with various Be doping concentrations, measured by single-wavelength pump-probe technique at  $1.50 \mu\text{m}$  for pump pulse energies of (a) 0.1 nJ and (b) 0.6 nJ.



(a)



(b)

**Figure 4.12** (a) Optical response of sample 2460 (standard InGaAsP doped with  $6 \times 10^{18} \text{ cm}^{-3}$  Be), measured by single-wavelength pump-probe technique at  $1.50 \mu\text{m}$ . (b) Linear fit of the data in (a) on a natural log scale yields a response time of 325 ps.

concentration) is proportional to the electron capture coefficient ( $\beta$ ) of the traps, the concentration of available electron traps (empty traps)  $N_m$ , and  $N_e$ :

$$\frac{dN_e}{dt} = -\sum_i \beta_i N_{mi} N_e, \quad i = 1, 2, 3, \dots \quad (4.2)$$

where each term in the summation corresponds to a defect level  $i$ . Furthermore, the concentration of the empty traps ( $N_m$ ) depends, in turn, on electron trapping rate ( $dN_e/dt$ ), as well as on hole trapping rate ( $dN_h/dt$ ). That is,

$$\frac{dN_m}{dt} = -\beta_i N_{mi} N_e + \gamma_i (N_{ti} - N_m) N_h, \quad i = 1, 2, 3, \dots \quad (4.3)$$

where  $\gamma_i$  is the hole capture coefficient associated with trap level  $i$ ,  $N_{ti}$  is the total trap concentration of level  $i$ , and  $N_h$  is the valence-band hole concentration.

Equation (4.2) and (4.3) indicate that the conduction-band electron decay rate varies with the following parameters: free electron and hole concentrations, electron and hole capture coefficients, and the concentrations of empty and filled traps of every effective trap level (i.e. mid-gap level or deep level). Therefore, the enhancement of the electron decay rate subsequent to Be doping can be caused by one or more of the following possibilities: (a) higher free electron concentration, (b) higher free hole concentration, (c) larger electron capture coefficients, (d) larger hole capture coefficients, (e) higher empty deep-level trap concentration, and (f) higher filled deep-level trap concentration.

Since the above possibilities involve carrier and trap concentrations, we can gain more insight into the role of beryllium and narrow down the causes by examining the electrical behaviour of the material. First, beryllium atoms, with two valence electrons, act as acceptors in standard InGaAsP material. Second, room-temperature Hall measurements indicate that undoped HELP InGaAsP is weakly n-type, but its carrier concentration is much lower than that of the standard material (without He-plasma) [182]. Third, Hall measurements also show that, for doping concentrations up to about  $1 \times 10^{18} \text{ cm}^{-3}$ , Be doping results in increased resistivity, and decreased carrier mobility and free carrier concentration; but for doping concentration of  $2 \times 10^{18} \text{ cm}^{-3}$ , the Fermi level suddenly drops to just above the valence band (the material becomes p-type). Further increase in Be concentration only results in ionization of the additional Be dopants and a corresponding increase in free hole concentration [179].

The fact that undoped HELP InGaAsP is n-type *and* has a low carrier concentration suggests the presence of deep-level filled traps above the middle of the band gap. Be doping initially *decreases* carrier concentration and *increases* resistivity, implying that Be dopants are compensating for the filled trap states, resulting in more empty states and lowering of the Fermi level towards the middle of the band gap. Increasing Be concentration to  $2 \times 10^{18} \text{ cm}^{-3}$  causes the material to change from n-type to p-type, indicating all filled traps above the middle of the band gap are compensated. Further Be doping only contributes to free hole concentration, which implies that Be dopants, rather than forming new deep-level defects, act only as shallow acceptors. This implication is consistent with our observation that Be doping alone does not lead to ultrafast response times.

Since Be dopants are shallow acceptors, possibilities (a) and (f) outlined above can be ruled out as causes for the reduced response time. Since Be doping does not introduce new deep-level defects, possibilities (c) and (d) are also not likely. Consequently, in samples doped with  $< 2 \times 10^{18} \text{ cm}^{-3}$  Be (e.g., 1970 and 2001), (e) is the major cause of response time reduction, whereas in the heavily doped material, both (e) and (b) are major contributors to the reduction of the response time. In other words, Be doping enhances the electron trapping rate by emptying filled deep-level states, and it enhances the hole trapping rate (which in turn enhances the electron trapping rate) by contributing to free hole concentration.

Apart from the fast decay, we also observed incomplete recovery, indicated by either a positive “tail” in the heavily doped sample, or a negative “tail” in the medium doped sample. In fact, the long tail was observed in all samples, doped or undoped, which suggests that there are traps associated with a very slow hole-capturing process, a subject we will discuss in detail in Section 4.5.2. Nevertheless, we will show that this slow process has negligible effect on the ultrafast switching operation using this material (Section 4.6).

#### 4.3.1.2 ABSORPTION SPECTRA OF BE-DOPED HELP InGaAsP

The absorption spectra around the band edge of the four HELP InGaAsP samples (1969, 1970, 2001, and 2002) and the standard InGaAsP sample (1968), obtained by FTIR measurements, are compared in Fig. 4.13. The band edge slope shows little variation from sample 1968 to 1970. In

fact, sample 1970 has the same absorption edge as sample 1969, yet the response time is reduced by half by doping with  $3 \times 10^{17} \text{ cm}^{-3}$  Be. When doped with  $1 \times 10^{18} \text{ cm}^{-3}$  Be, the sample (2001) shows an absorption edge slightly shifted in wavelength with respect to previous samples (probably because of slight change in composition due to variation in the growth condition), but the steepness of the band edge remains unchanged. Even with  $6 \times 10^{18} \text{ cm}^{-3}$  doping (sample 2002), there is an identifiable band edge. Compared to other material systems with subpicosecond response, such as the low-temperature-grown GaAs [129], the band tail in HELP InGaAsP material is significantly smaller.

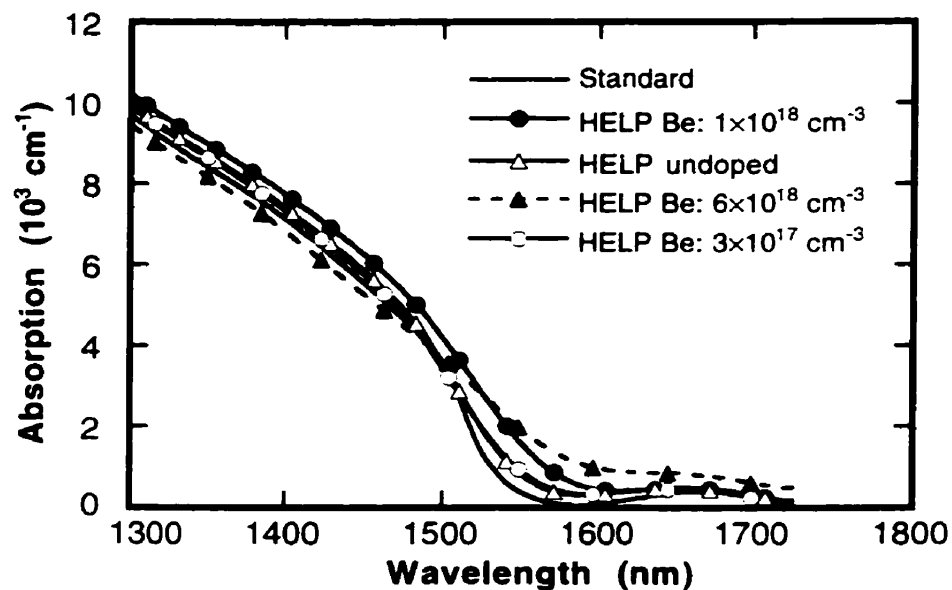


**Figure 4.13** Absorption spectra of the InGaAsP samples around the band edge, obtained by FTIR measurements. The steepness of the absorption edge is maintained in the HELP samples with doping concentration up to  $1 \times 10^{18} \text{ cm}^{-3}$ , indicating good crystalline quality. Even with  $1 \times 10^{18} \text{ cm}^{-3}$  doping, there is still an identifiable band edge. The samples are not antireflection coated, so small Fabry-Pérot fringes are seen in the low absorption region.

The fact that light to medium Be doping hardly alters the band tail absorption is consistent with our theory that Be doping, rather than introducing more deep-level defects, simply compensates for defects already created by the HELP growth. Of course, Be doping does introduce shallow acceptor levels just above the valence band, which can result in increase in band tail absorption. However, this is true for standard InGaAsP material as well. To verify that the smearing of the band edge in the heavily doped material (Fig. 4.13) is indeed due to Be doping and not HELP

growth, we measured the band edges of two heavily doped ( $6 \times 10^{18} \text{ cm}^{-3}$ ) samples (2460 and 2461), grown under similar conditions except for the presence and absence of the He plasma, respectively. Comparison of their band edge absorption (Fig. 4.14) shows that HELP growth causes little additional absorption at the band tail.

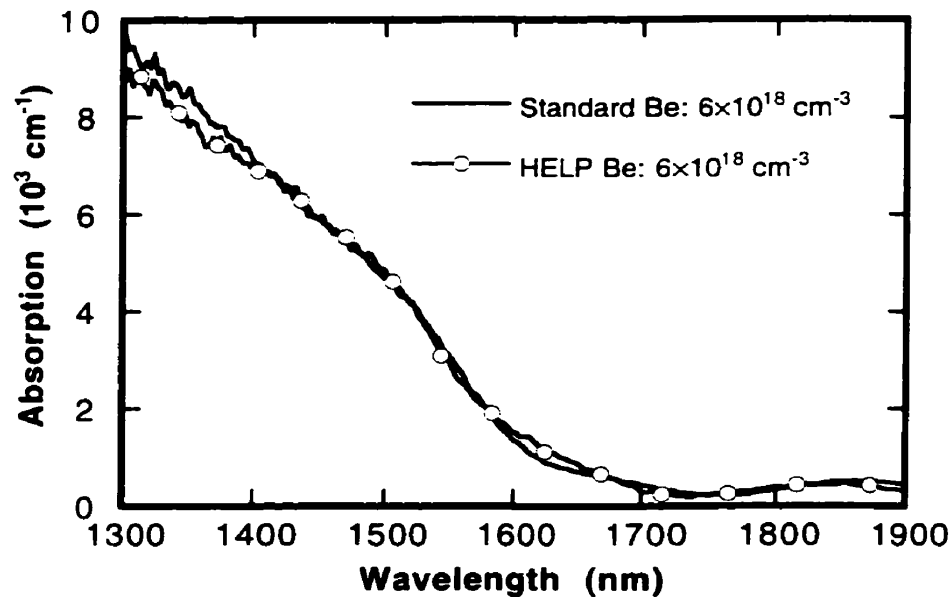


**Figure 4.14** Comparison of band edge absorption spectra of a heavily-doped HELP sample and a heavily-doped standard sample indicates that HELP growth introduce little additional absorption at the band tail.

### 4.3.2 Effects of helium plasma condition during growth

Since HELP growth was a newly developed technique and we were still in the exploratory stage of using this technique to produce fast optical materials, we needed to determine empirically the helium plasma conditions—helium flow rate and microwave power of the plasma generation chamber—which produce the shortest material response time.

We used for this study undoped and doped HELP InGaAsP samples grown under various helium plasma conditions (Table 4.3). Other growth parameters (e.g., growth rate, temperature) were kept constant for these samples. A helium flow rate of 7 sccm and an estimated absorbed microwave power of 100–150 W were chosen prior to our investigation to be the standard plasma

condition, because under these conditions HELP growth produces the most resistive undoped HELP InGaAsP.

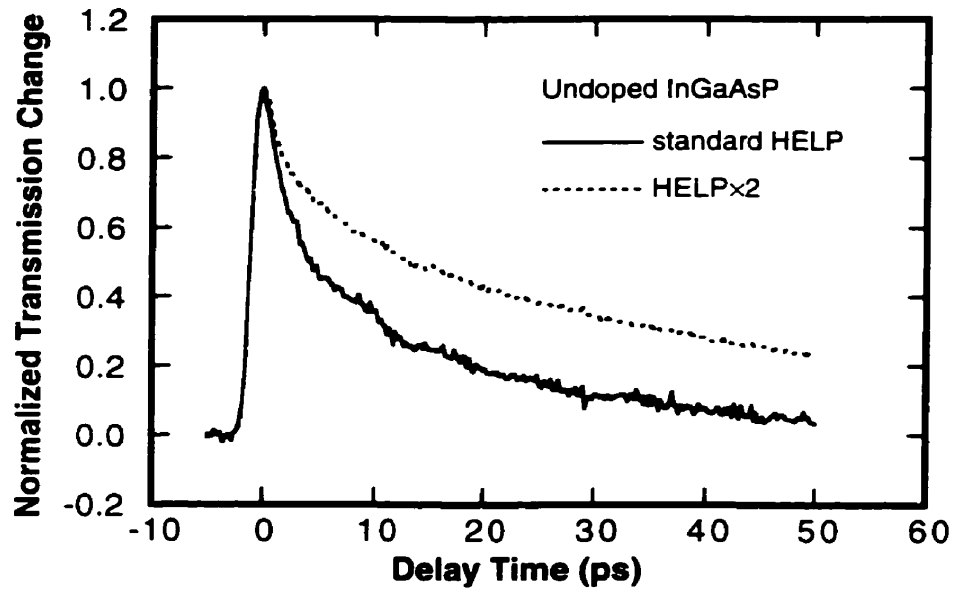
**Table 4.3 Samples used to determine optimal He-plasma conditions**

Sample ID	Sample description	Helium flow rate to ECR chamber	Absorbed microwave power	Be doping concentration
1969	undoped HELP	standard (7 sccm)	standard (100–150 W)	undoped
1971	undoped HELP × 2	double	double	
1970	lightly doped HELP	standard	standard	$3 \times 10^{17} \text{ cm}^{-3}$
1973	lightly doped HELP × 1/2	half	half	

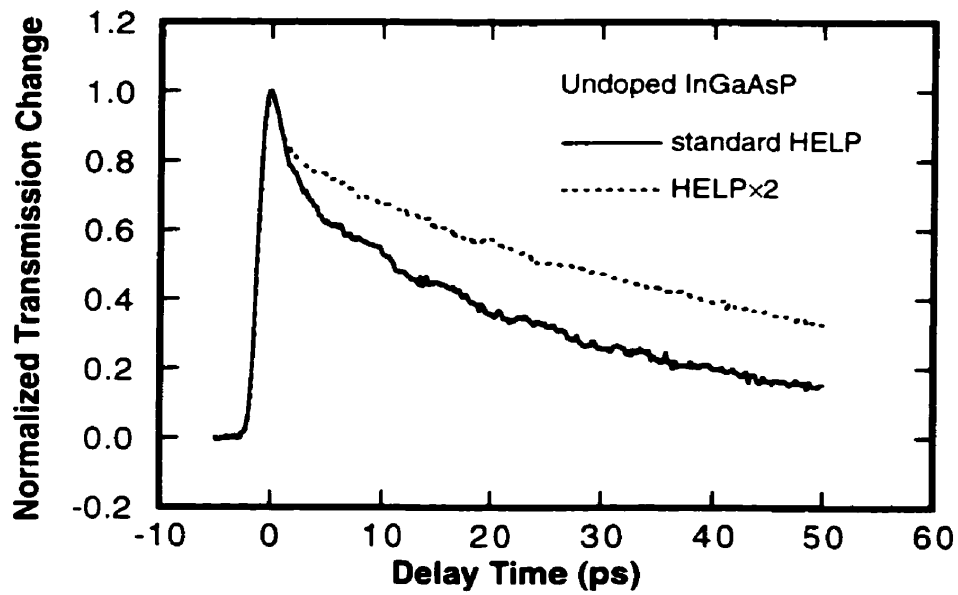
The optical responses of sample 1971 are considerably slower than those of sample 1969 (Fig. 4.15), indicating that increasing helium flow and microwave power leads to a decrease in carrier trapping rate. The slower response is consistent with the increase in carrier mobility (from  $1200 \text{ cm}^2/\text{Vs}$  in sample 1969 to  $2000 \text{ cm}^2/\text{Vs}$  in sample 1971) and the increase in free electron concentration (from  $1.2 \times 10^{14} \text{ cm}^{-3}$  in sample 1969 to  $4.1 \times 10^{14} \text{ cm}^{-3}$  in sample 1971) [183]. The former observation suggests a lower concentration of charged impurities in sample 1971, the latter suggests a lower electron trap concentration or a smaller electron trapping coefficient associated with traps in sample 1971.

The effect on the optical response time produced by reducing the helium flow rate and the microwave power was examined by comparing the optical responses of samples 1970 and 1973. At a lower pump pulse energy (0.14 nJ), the two response times are similar (Fig. 4.16a), but when the energy is increased to 0.35 nJ, sample 1973 shows a slower response (Fig. 4.16b), indicating that this sample experiences a more pronounced “bottleneck” effect (Section 4.3.4), therefore the hole trapping rate in this sample is lower than that of 1971.

The standard helium flow rate and microwave power constitute the optimum condition for producing the fast optical response in HELP InGaAsP.

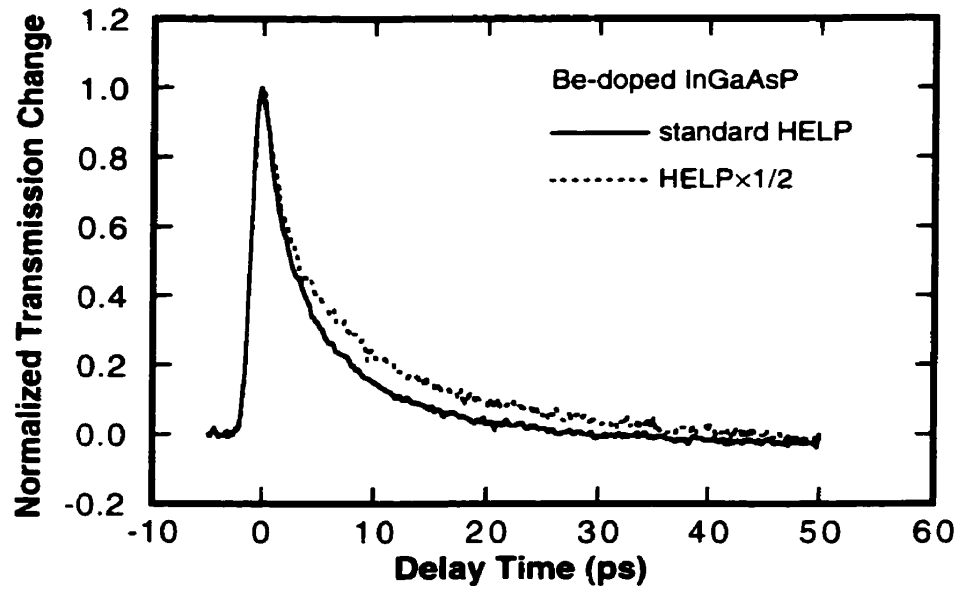


(a)

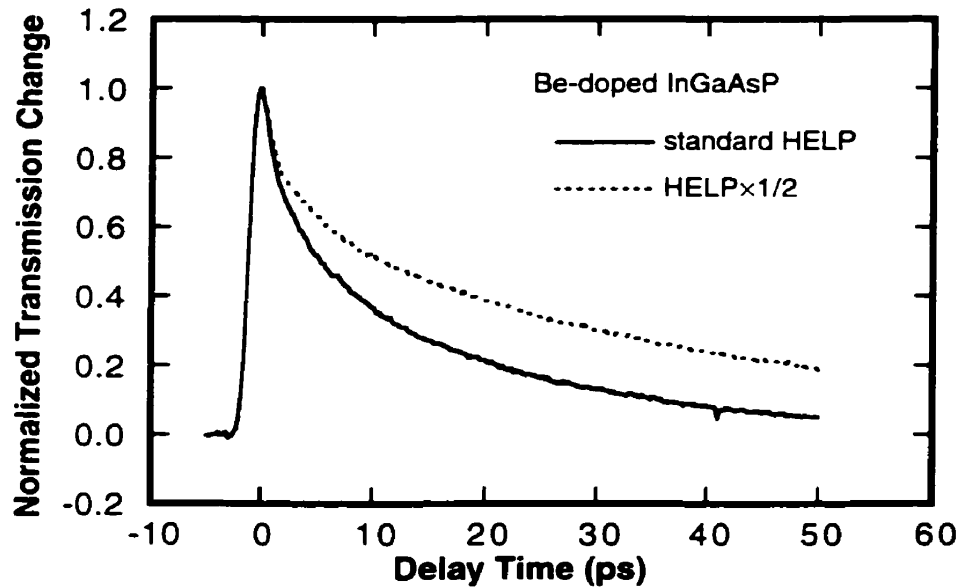


(b)

**Figure 4.15** Comparison of optical response times of two undoped HELP InGaAsP samples, one grown under the standard plasma conditions (1969), the other under doubled helium flow rate and doubled microwave power (1971). Response times are measured at  $1.50 \mu\text{m}$  (above band) with pump pulse energies of (a) 0.14 nJ and (b) 0.55 nJ.



(a)



(b)

**Figure 4.16** Comparison of optical response times of two Be-doped ( $3 \times 10^{17} \text{ cm}^{-3}$ ) HELP InGaAsP samples, one grown under the standard plasma conditions (1970), the other under half the helium flow rate and half the microwave power (1973). Response times are measured at  $1.50 \mu\text{m}$  (above band) with pump pulse energies of (a) 0.14 nJ and (b) 0.35 nJ.

### 4.3.3 Effects of annealing

Annealing at sufficiently high temperatures can alter or remove defects in semiconductors, due to defects gaining enough thermal energy to diffuse towards other defects or the surface and escape.

**Table 4.4 Samples used in annealing study**

Sample ID	Growth condition	Doping concentration	Annealing temperature ( $\pm 10^\circ\text{C}$ )
1969	standard + He-plasma	undoped	no anneal
1969A	standard + He-plasma	undoped	500° C for 10 sec
1969B	standard + He-plasma	undoped	550° C for 10 sec
1969C	standard + He-plasma	undoped	600° C for 10 sec
1970	standard + He-plasma	$3 \times 10^{17} \text{ cm}^{-3}$	no anneal
1970A	standard + He-plasma	$3 \times 10^{17} \text{ cm}^{-3}$	500° C for 10 sec
1970B	standard + He-plasma	$3 \times 10^{17} \text{ cm}^{-3}$	550° C for 10 sec
1970C	standard + He-plasma	$3 \times 10^{17} \text{ cm}^{-3}$	600° C for 10 sec
2001	standard + He-plasma	$1 \times 10^{18} \text{ cm}^{-3}$	no anneal
2001A	standard + He-plasma	$1 \times 10^{18} \text{ cm}^{-3}$	500° C for 10 sec
2001B	standard + He-plasma	$1 \times 10^{18} \text{ cm}^{-3}$	550° C for 10 sec
2001C	standard + He-plasma	$1 \times 10^{18} \text{ cm}^{-3}$	600° C for 10 sec
2002	standard + He-plasma	$6 \times 10^{18} \text{ cm}^{-3}$	no anneal
2002A	standard + He-plasma	$6 \times 10^{18} \text{ cm}^{-3}$	500° C for 10 sec
2002B	standard + He-plasma	$6 \times 10^{18} \text{ cm}^{-3}$	550° C for 10 sec
2002C	standard + He-plasma	$6 \times 10^{18} \text{ cm}^{-3}$	600° C for 10 sec
2155	standard	undoped	no anneal
2155C	standard	undoped	600° C for 10 sec

Thus, annealing is commonly used to remove point defects and restore the crystalline quality of semiconductors with intentionally-induced defects, such as low-temperature-grown materials and ion-implanted materials [129, 184-187]. It has been very successful in reducing the large absorption tail and restoring the absorption band edge in low-temperature-grown GaAs [129]. Since annealing removes some defects in the material, it usually leads to an increase in optical response time. It was therefore necessary for us to examine the effects of annealing on the material's absorption band edge, as well as on the response time, in order to determine if annealing can enhance the optical properties useful for all-optical switching.

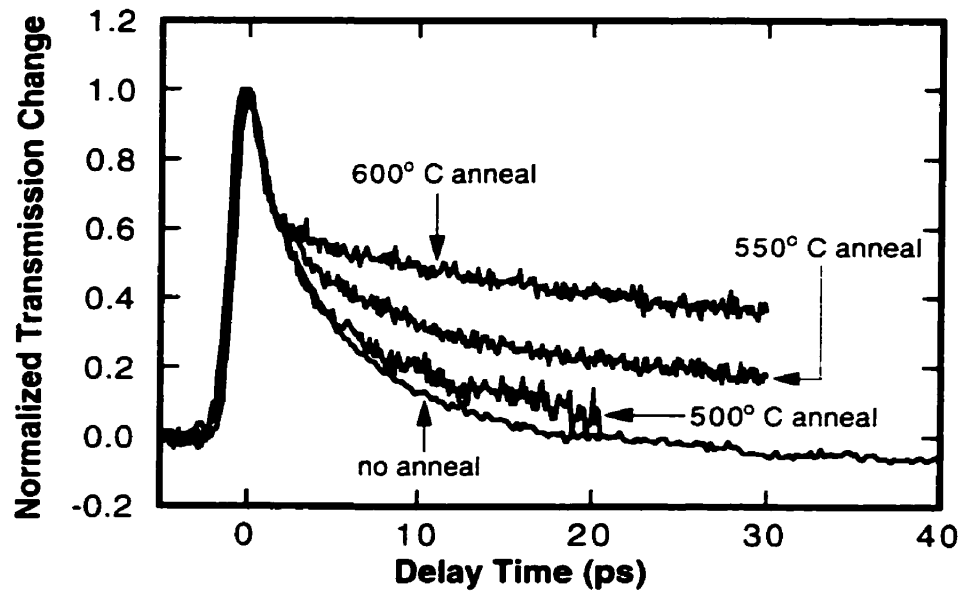
We studied the effects of annealing on undoped as well as doped HELP InGaAsP materials, subjected to rapid thermal anneal over 10 seconds at various temperatures (Table 4.4). Rapid thermal annealing was performed inside a quartz furnace chamber, and the sample, capped with a piece of n-InP wafer to prevent phosphorus loss from the sample surface, was rapidly heated (temperature ramp rate was 100° C/second) by banks of halogen lamps situated above and below the chamber. After the desired anneal time elapsed, the lamps were automatically shut off and the sample was left to cool to room temperature before removal. Because annealing was carried out rapidly, dopant diffusion and quartz contamination was minimized.

#### 4.3.2.1 MATERIAL RESPONSE TIMES OF ANNEALED HELP InGaAsP

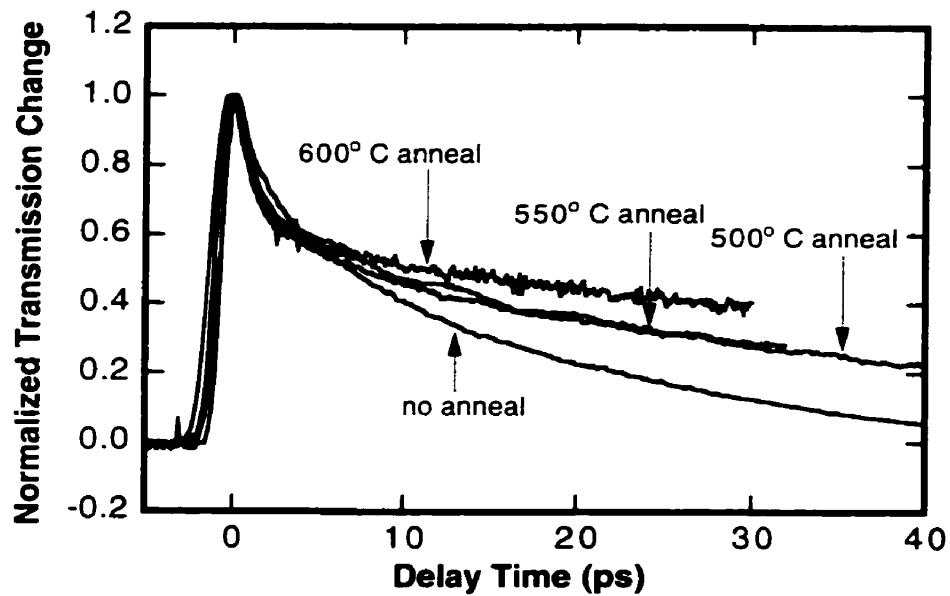
##### *Undoped samples*

The material responses of the undoped samples, measured at a low induced carrier density, show initially a small, but fast (<5 ps) decay, independent of annealing temperature. There follows a second decay, strongly affected by annealing: from 5 ps (sample 1969, as-grown) to ~80 ps (sample 1969C, 600° C anneal) (Fig. 4.17a). At a higher induced carrier density, the initial fast decay remains the same as before for all samples, but, the second decay is slower (~30 ps) than in the low-carrier-density situation for sample 1969 (as-grown), while it remains the same (~80 ps) for sample 1969C (600° C anneal) (Fig. 4.17b).

The slowing down of the second decay with increasing annealing temperature suggests that either the electron trap concentration, or the electron capture coefficient is reduced by annealing (cf. Eq. 4.2). The initial fast decay excludes the latter, therefore, annealing must cause a reduction



(a)



(b)

**Figure 4.17** Optical response times of the undoped HELP samples of various anneals measured at  $1.50 \mu\text{m}$  (above-band) for carrier densities of (a)  $7 \times 10^{16} \text{ cm}^{-3}$  and (b)  $2 \times 10^{17} \text{ cm}^{-3}$ .

in electron trap concentration, which, together with the presence of “bent” decay curves (most obvious for sample 1969C) indicates that the trap concentration is smaller than the induced carrier concentration, and that traps have an electron capture coefficient significantly larger than the hole capture coefficient. Thus, fast decay takes place due to fast electron trapping until all traps are filled with electrons, and then follows the slow decay.

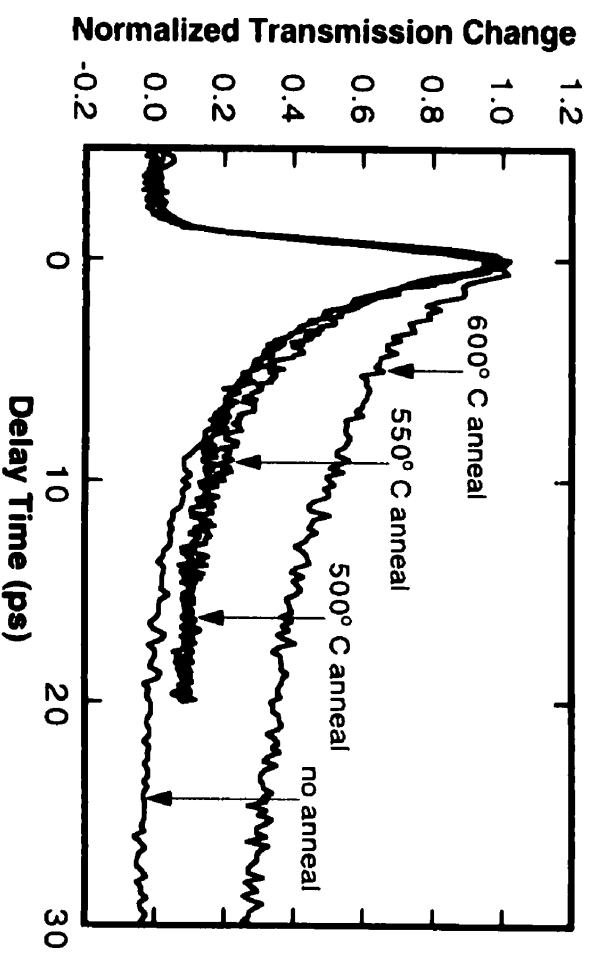
Our qualitative explanation is consistent with the results from the study of the electrical properties of annealed HELP InGaAsP [188]. We consider the two mid-gap trap levels identified in the study to be primarily responsible for the non-radiative carrier decay. According to the study, in undoped materials, the upper mid-gap level is empty (ready to trap electrons), and the lower mid-gap level is filled (ready to trap holes). The trap concentration in the upper mid-gap level remains steady at  $5 \times 10^{17} \text{ cm}^{-3}$  for anneals at  $\leq 550^\circ \text{ C}$ , and then drops to  $\sim 3 \times 10^{17} \text{ cm}^{-3}$  for  $600^\circ \text{ C}$  anneal, whereas in the lower mid-gap level, trap concentration drops almost linearly with annealing temperature, from  $1.2 \times 10^{18} \text{ cm}^{-3}$  for as-grown samples, to  $4 \times 10^{17} \text{ cm}^{-3}$  for  $550^\circ \text{ C}$  anneals, to a negligibly small value for  $600^\circ \text{ C}$  anneals. Our observation of the slowing down of the second decay process after anneal is therefore consistent with the reductions in defect concentration derived from the study.

Furthermore, if we apply these results (i.e. that in samples annealed at  $600^\circ \text{ C}$  only upper-level traps are left) to our sample 1969C, then the “bent” decay it exhibited (Fig. 4.17a and 4.17b) implies that upper-level traps have a large electron capture coefficient (yielding a 5 ps decay) and a small hole capture coefficient (yielding an  $\sim 80$  ps decay). This implication is later verified by our two-trap-level rate equation model (Section 4.5).

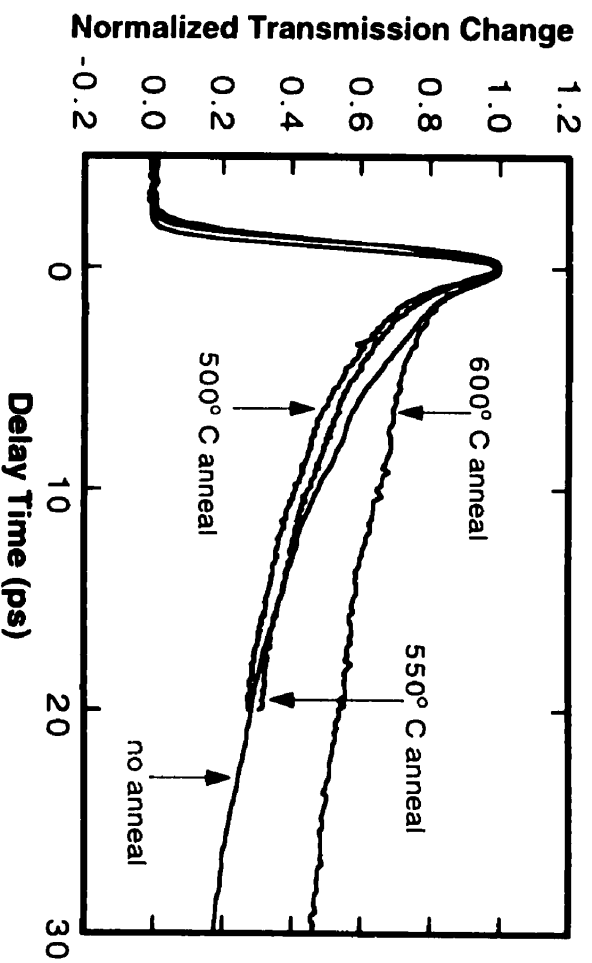
#### *Doped samples*

For samples with doping concentrations from  $3 \times 10^{17} \text{ cm}^{-3}$  to  $6 \times 10^{18} \text{ cm}^{-3}$ , annealing at  $\leq 550^\circ \text{ C}$  has little effect on material’s response time (Fig. 4. 18–20). However, as the annealing temperature is raised to  $600^\circ \text{ C}$ , drastic slowing down in decay process is observed for all doped samples (Fig. 4.18–20).

For samples annealed at  $\leq 550^\circ \text{ C}$ , according to the results from the electrical study quoted above, the filled trap concentration (lower-level) is  $\geq 4 \times 10^{17} \text{ cm}^{-3}$ . Therefore, in these samples,

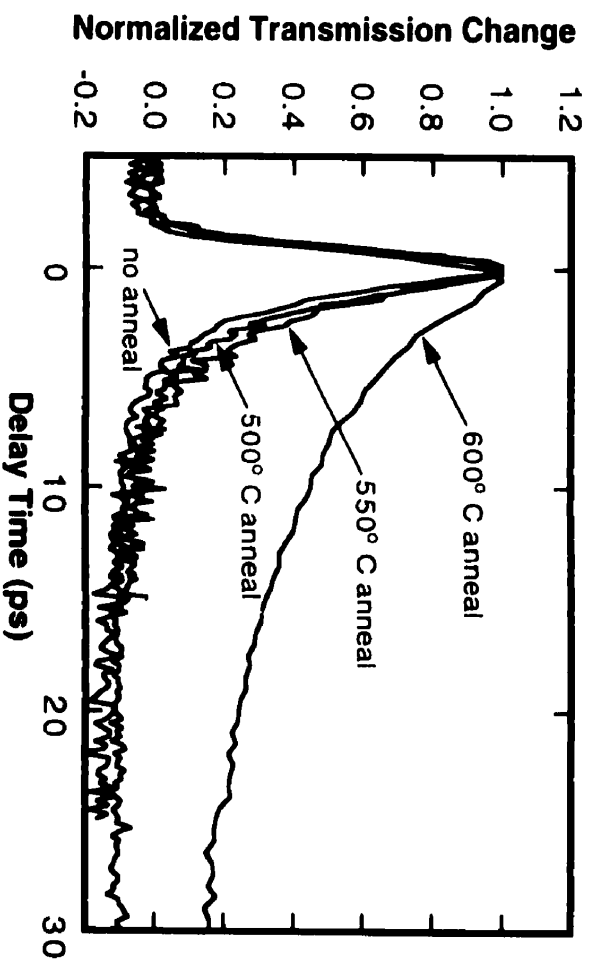


(a)

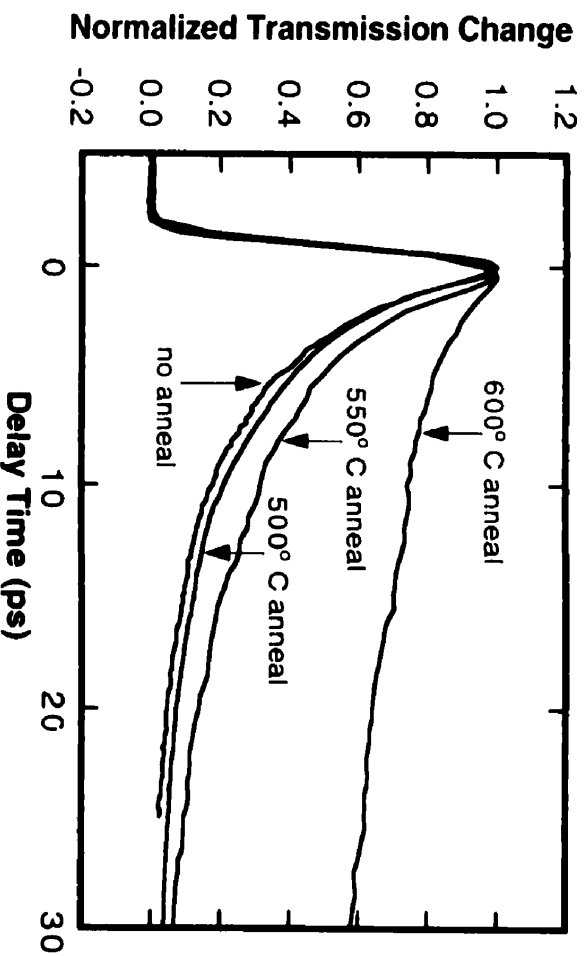


(b)

**Figure 4.18** Optical response times of the lightly Be-doped ( $3 \times 10^{17} \text{ cm}^{-3}$ ) HELP samples of various anneals, measured at  $1.50 \mu\text{m}$  (above-band) for carrier densities of **(a)**  $8 \times 10^{16} \text{ cm}^{-3}$  and **(b)**  $5 \times 10^{17} \text{ cm}^{-3}$ .



(a)



(b)

**Figure 4.19** Optical response times of the medium Be-doped ( $1 \times 10^{18} \text{ cm}^{-3}$ ) HELP samples of various anneals measured at  $1.50 \mu\text{m}$  (above-band) for carrier densities of **(a)**  $8 \times 10^{16} \text{ cm}^{-3}$  and **(b)**  $7 \times 10^{17} \text{ cm}^{-3}$ .

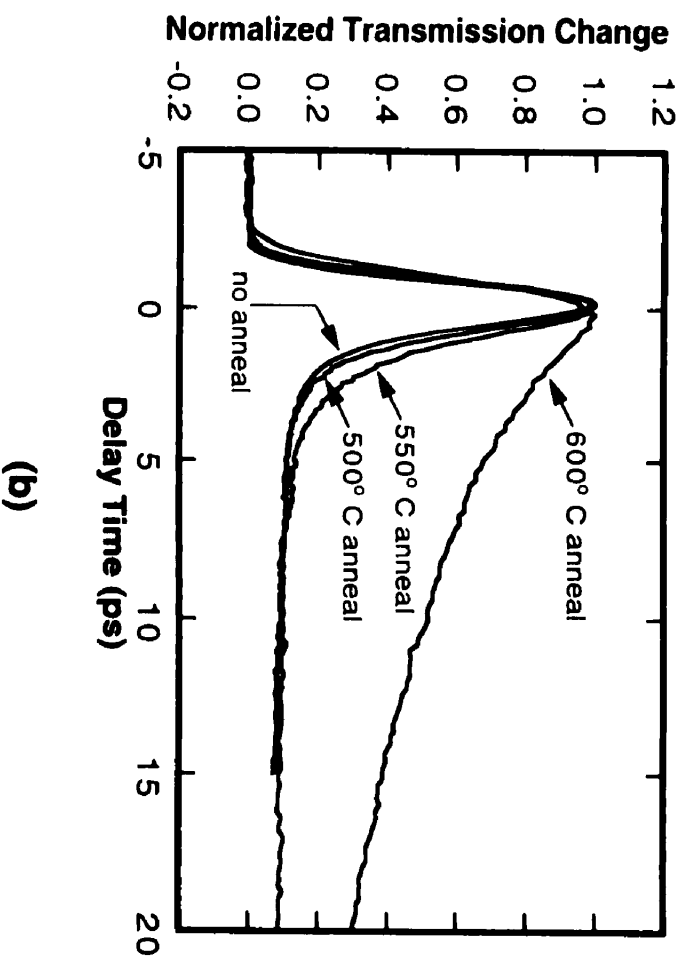
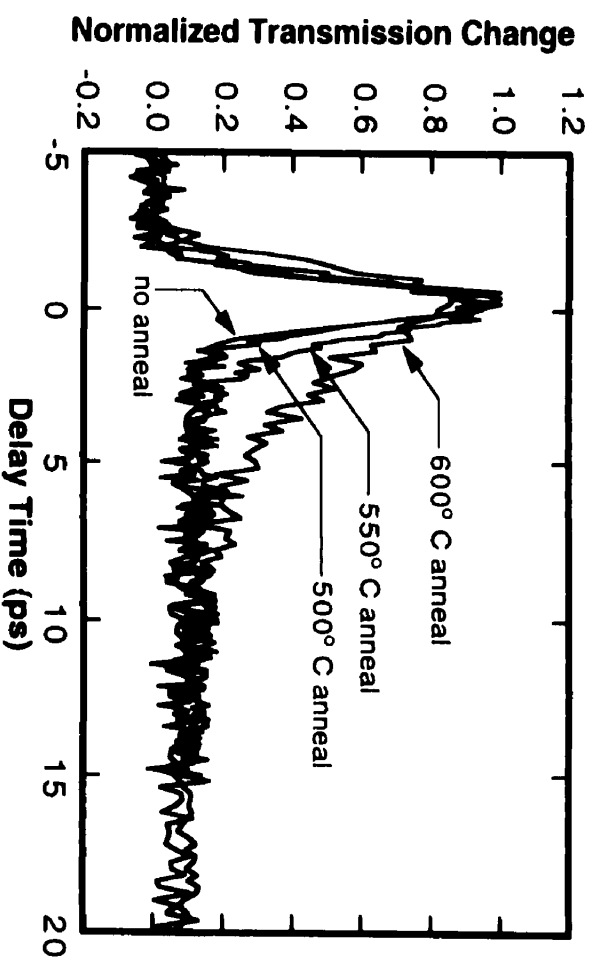


**Figure 4.20** Optical response times of the heavily Be-doped ( $6 \times 10^{18} \text{ cm}^{-3}$ ) HELP samples of various anneals measured at  $1.50 \text{ } \mu\text{m}$  (above-band) for carrier densities of **(a)**  $8 \times 10^{16} \text{ cm}^{-3}$  and **(b)**  $5 \times 10^{17} \text{ cm}^{-3}$ .

Be doping can significantly increase the empty trap concentration by compensating for the filled lower-level traps. As a result, the total empty trap concentrations (including the upper-level) in all doped samples annealed at  $\leq 550^\circ\text{C}$  are greater than the induced carrier densities ( $5\text{--}7 \times 10^{17}\text{ cm}^{-3}$ ) used in our measurements. Hence, the reduction in trap concentrations in samples annealed at  $\leq 550^\circ\text{C}$  has very little effect on the response times, as observed (Fig. 4.18–20).

For samples annealed at  $600^\circ\text{C}$ , however, results from the electrical study show that trap concentrations in both levels experience drastic reductions: the upper-level trap concentration drops to  $3 \times 10^{17}\text{ cm}^{-3}$  and the lower-level trap concentration diminishes to a negligible value. The drastic reduction in trap concentrations leads to the significantly slower material responses in these samples (Fig. 4.18–20). In addition, since the lower-level trap concentration is negligible, Be doping does not result in any increase in empty trap concentration, therefore sample 1969C (undoped), sample 1970C ( $3 \times 10^{17}\text{ cm}^{-3}$  doping) and sample 2001C ( $1 \times 10^{18}\text{ cm}^{-3}$  doping) have similar response times (compare Fig. 4.17b, 4.18b and 4.19b). Sample 2002C ( $6 \times 10^{18}\text{ cm}^{-3}$  doping,  $600^\circ\text{C}$  anneal) shows a slightly faster response (Fig. 4.20) relative to samples with lower doping concentrations, mainly due to its much higher free hole concentration, which enhances the hole trapping rate.

In conclusion, annealing leads to reduced trap concentration and increased material response time. We can qualitatively explain our observed response times of annealed materials using results obtained from Pinkney's study on the electrical properties of the materials.

#### 4.3.2.2 ABSORPTION SPECTRA OF ANNEALED HELP InGaAsP

Annealing improves the band edge steepness of the undoped HELP material only slightly (Fig. 4.21). A more noticeable effect of annealing on the absorption band edges of the undoped material is the blue shifts exhibited by all undoped annealed samples (1969A–C). The largest shift, 30 nm or 16 meV, is found in sample 1969C, annealed at  $600^\circ\text{C}$  (Fig. 4.21). For comparison, we measured the absorption edges of two undoped samples grown without He plasma, one without annealing (2155), one annealed at  $600^\circ\text{C}$  (2155C). The lack of a blue shift in the absorption band edge of sample 2155C relative to that of sample 2155 (Fig. 4.22) suggests that the blue shifts observed in Fig. 4.21 are indeed associated with HELP growth.

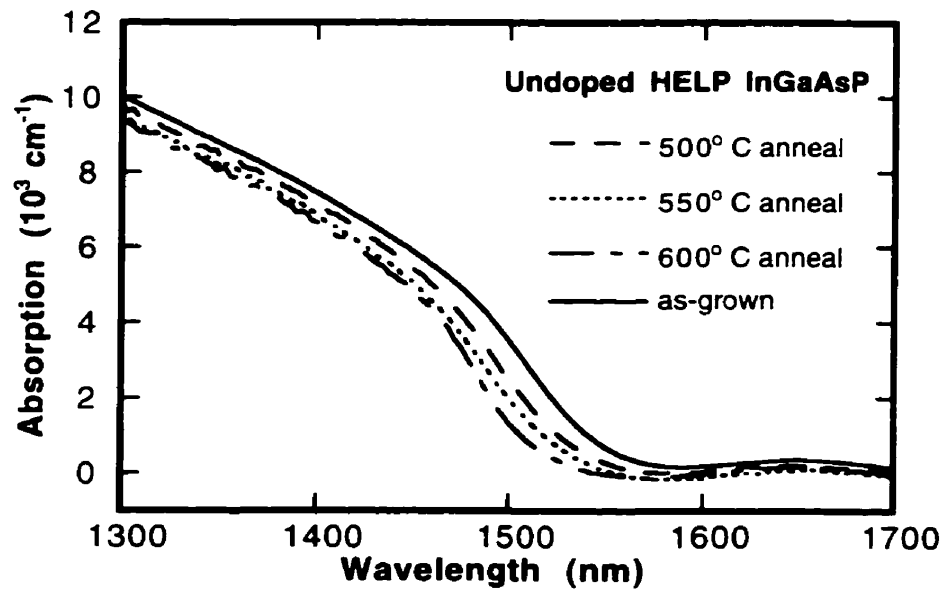


**Figure 4.21** Absorption spectra of undoped HELP InGaAsP of various anneals around the band edge. A blue shift of ~30 nm is observed between the as-grown material and the 600° C annealed material.

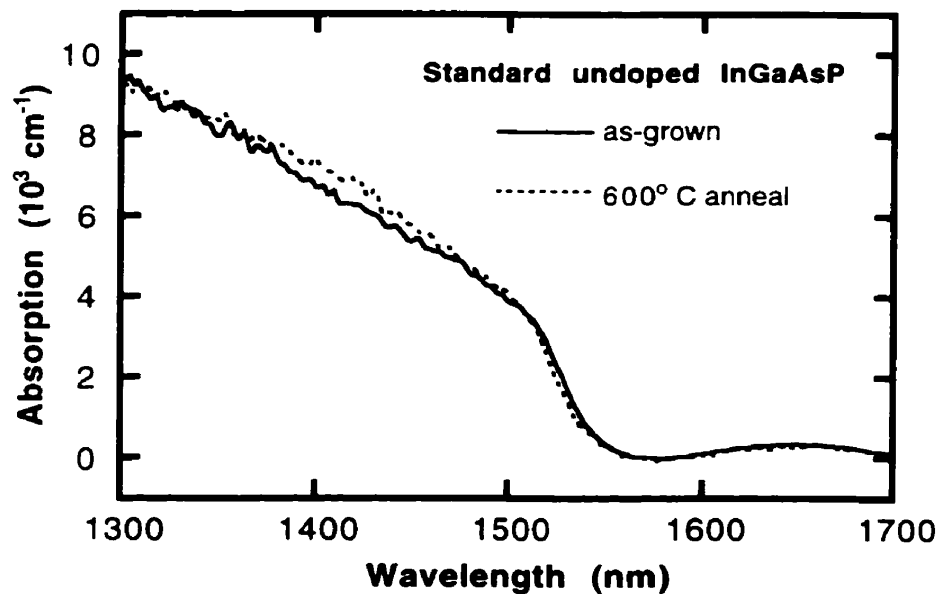


**Figure 4.22** Absorption spectra of two standard undoped InGaAsP (as grown and 600° C annealed) around the band edge. No band edge blue shift is observed, indicating that the blue shift observed in Figure 4.21 is due to HELP growth.

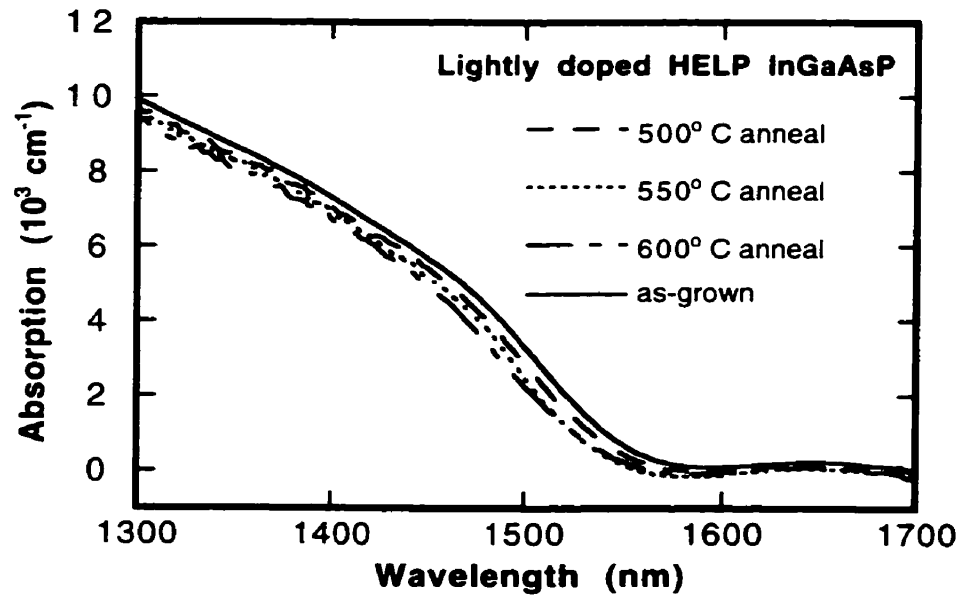


**Figure 4.23** Absorption spectra of lightly Be-doped ( $3 \times 10^{17} \text{ cm}^{-3}$ ) HELP InGaAsP of various anneals around the band edge. Slight band edge blue shifts with increasing annealing temperature are observed.

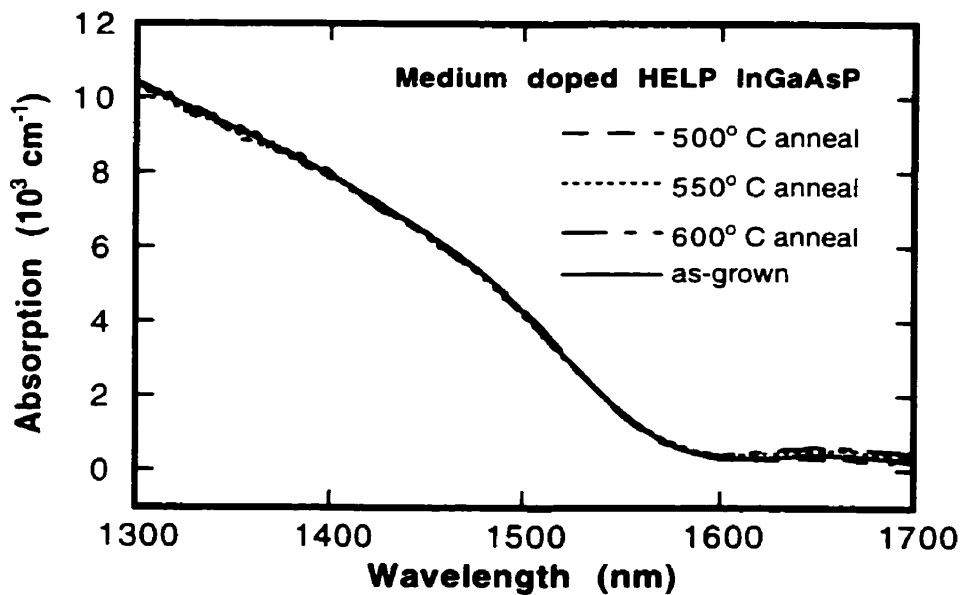


**Figure 4.24** Absorption spectra of medium Be-doped ( $1 \times 10^{18} \text{ cm}^{-3}$ ) HELP InGaAsP of various anneals around the band edge. Annealing does not alter the band edge absorption.

In the lightly-doped annealed samples (1970A–C), there is less blue shift than in the undoped samples for all anneals, however, there is little improvement in the steepness of the band edge (Fig. 4.23). Annealing does not alter the absorption edge of the medium-doped material (sample 2001A–C) (Fig. 4.24), while, in the heavily-doped material (sample 2002A–C), annealing causes neither a change in the band tail absorption, nor any blue shift of the band edge, but it lowers the absorption in the region above the band edge (Fig. 4.25).

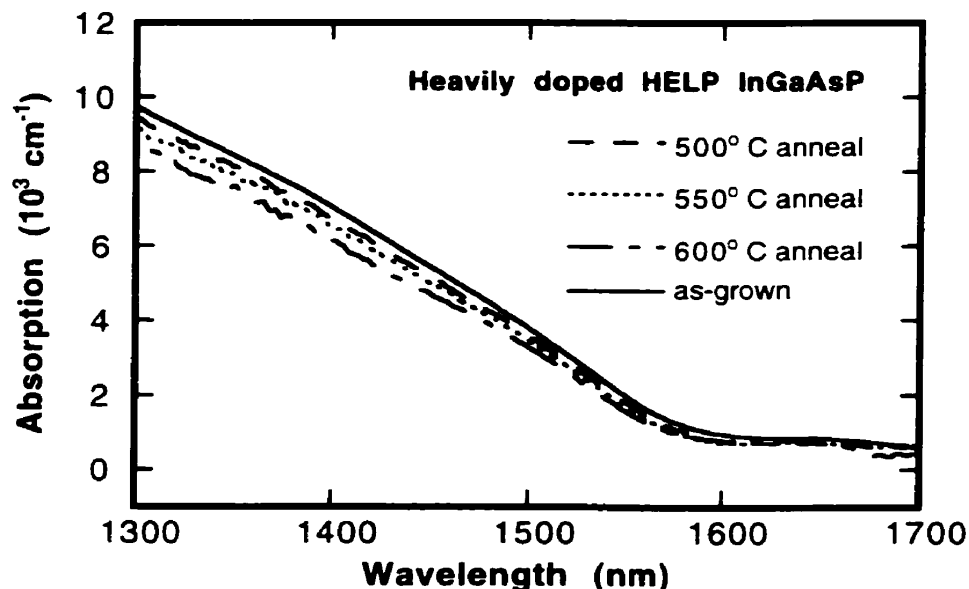


**Figure 4.25** Absorption spectra of heavily Be-doped ( $6 \times 10^{18} \text{ cm}^{-3}$ ) HELP InGaAsP of various anneals around the band edge. Annealing does not result in improved band edge, but only reduces the above-band absorption.

The blue shifts observed by us may be linked to an increase in the normalized S parameter observed in the positron annihilation experiments by Pinkney [179], who used this technique to detect open-volume defects (vacancies) in HELP samples. Pinkney observed a significant increase in the normalized S parameter<sup>1</sup> with annealing temperature in the undoped HELP sample. She postulates that mono- or di-vacancies in the as-grown sample migrate to form large vacancy clusters after annealing. It is possible that the blue shift of the absorption band edge is caused by

<sup>1</sup> In positron annihilation experiments, an increase in the normalized S parameter indicates the presence of vacancy defects. Larger increase in the S parameter generally implies larger vacancy size. The normalized S parameter is not sensitive to positively-charged vacancies.

the forming of large vacancy clusters. The amount of increase in the normalized S parameter reduces with increasing doping concentration [179], which correlates well with the decreasing blue shifts of absorption band edges observed by us (cf. Fig. 4.21, 4.23 and 4.24).

Since neither the absorption band edge (Fig. 4.24) nor the material response time (Fig. 4.19) of the medium-doped ( $1 \times 10^{18} \text{ cm}^{-3}$ ) HELP InGaAsP material is significantly altered by annealing at temperatures  $\leq 550^\circ \text{ C}$ , this material can be used in devices where annealing (at temperatures up to  $550^\circ \text{ C}$ ) is required, for example, to improve the optical or electrical properties of other parts of the device.

#### 4.3.4 Response time variation with carrier density

Even when annealing conditions, helium plasma conditions, and doping concentrations are fixed, material response time can still vary with induced carrier density. The variation is a result of the dependence of the carrier decay rate on the carrier density and on the density of available traps (cf. Eq. 4.2 and Eq. 4.3). The latter also varies with carrier density when the electron capture coefficient associated with the traps is different from the hole capture coefficient. Consequently, by investigating the response time variation with carrier density, we can gain more insight into the properties of traps (density and carrier capture coefficients) responsible for the fast carrier decay in HELP InGaAsP.

We investigated the material response time variation with induced carrier density in four HELP InGaAsP samples (1969, 1970, 2001, 2002 listed in Table 4.2) with different doping concentrations. In samples 1969, 1970 and 2001, the response time increases with carrier density, but there is less increase at higher doping concentration (Fig. 4.26–28). In the most heavily-doped sample (2002), no increase in response time was observed over a large range of carrier densities (Fig. 4.29a). However, after rapid thermal annealing at  $600^\circ \text{ C}$ , the sample exhibits response time variation with carrier density just as the other samples (Fig. 4.29b).

Since our measurements were carried out at an above-band wavelength, the observed material response times reflect mainly the electron decay times. The increase in material response times (Fig. 4.26–28) therefore indicates a slowing down of the electron decay processes when the induced carrier density is increased. The reduced electron decay rate is a clear indication of the “bottleneck”

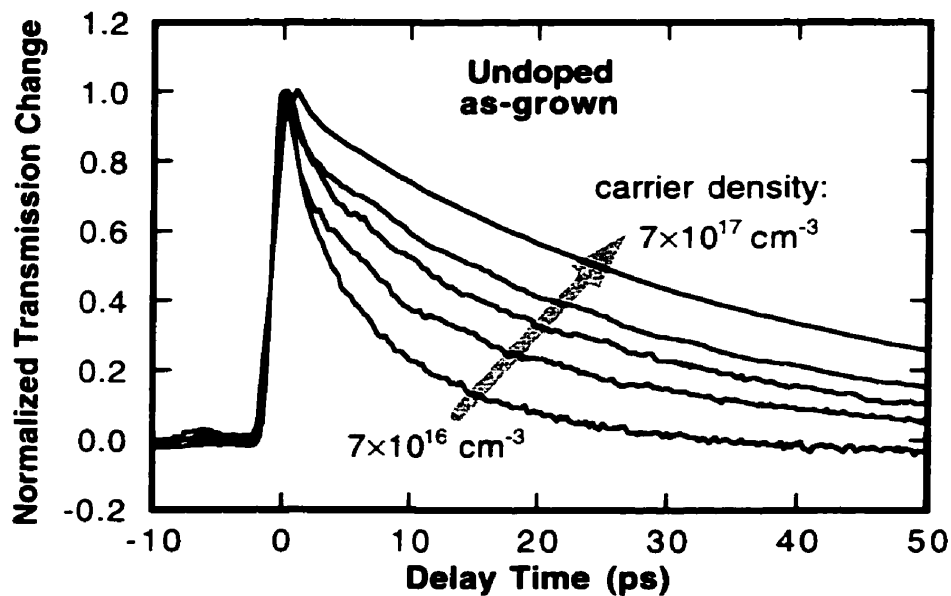


**Figure 4.26** Optical response times of undoped as-grown HELP InGaAsP measured by above-band single-wavelength ( $1.50 \mu\text{m}$ ) pump-probe technique under various carrier densities, clearly showing the “bottleneck” effect.

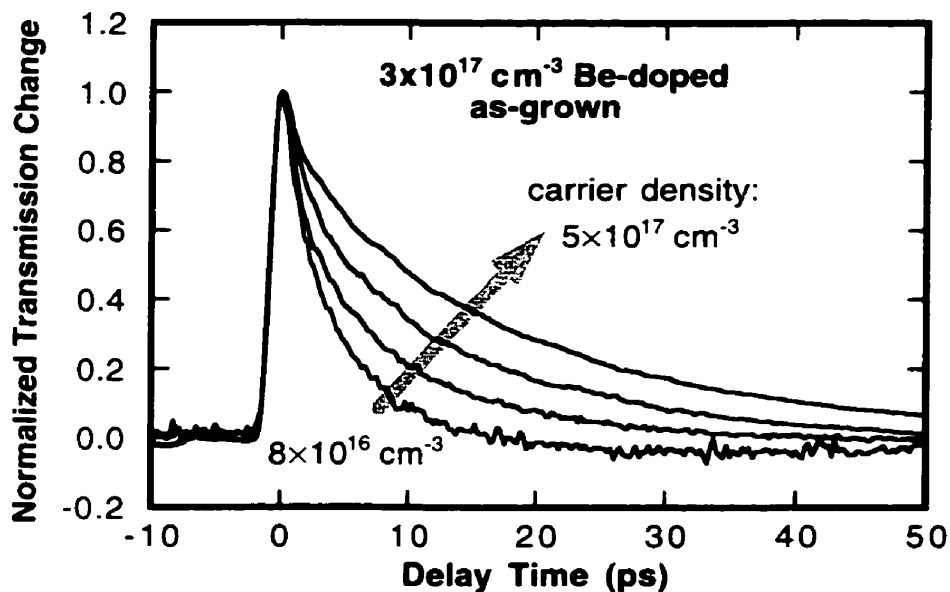


**Figure 4.27** Optical response times of lightly Be-doped as-grown HELP InGaAsP measured by above-band single-wavelength ( $1.50 \mu\text{m}$ ) pump-probe technique under various carrier densities. A slightly smaller “bottleneck” effect is observed here than in the undoped case, due to increase in empty trap concentration.

effect (Section 4.1.2), caused by the reduction of available electron traps (empty traps) as a result of trap filling, which occurs when the electron trapping coefficient of the traps is larger than the hole trapping coefficient. The “bottleneck” effect is more severe in the undoped sample than in doped samples, indicating a lower density of empty traps in the undoped material, consistent with our theory that Be dopants compensate for filled traps (Section 4.3.1.1). The absence of the “bottleneck” effect in the heavily doped sample for carrier densities up to  $6 \times 10^{17} \text{ cm}^{-3}$  (Fig. 4.29a) suggests that the density of empty traps in this sample is significantly higher than  $6 \times 10^{17} \text{ cm}^{-3}$ , which will be verified in Section 4.5.2. The reappearing of the bottleneck effect after  $600^\circ \text{ C}$  anneal (Fig. 4.29b) indicates that the density of empty traps is greatly reduced by annealing, consistent with the conclusion of Section 4.3.3.1.

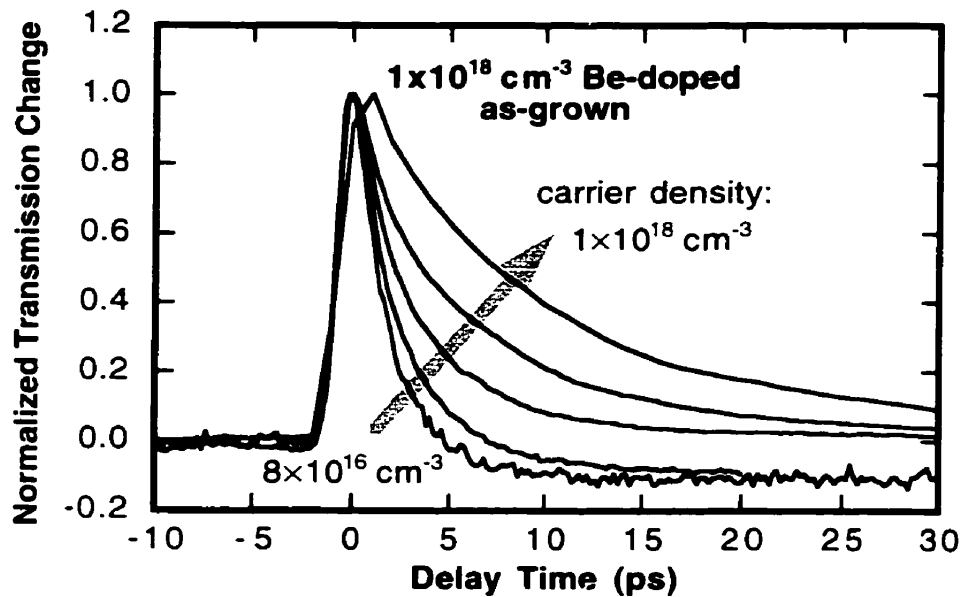
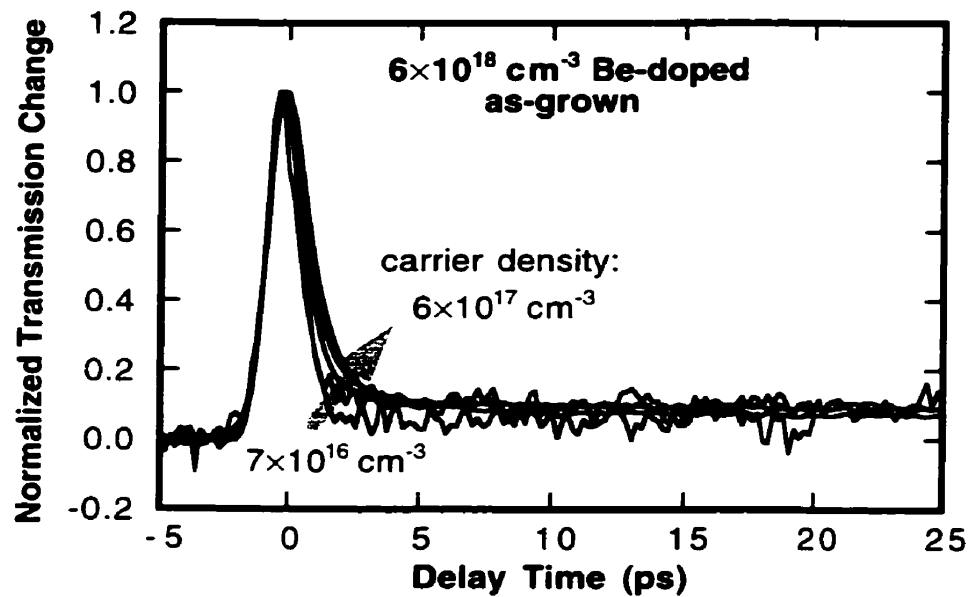
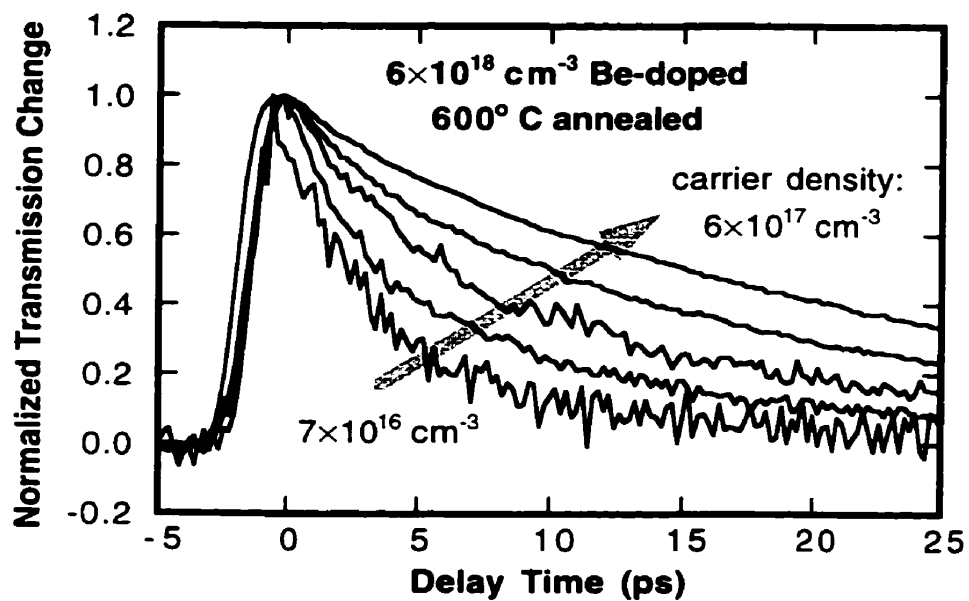


**Figure 4.28** Optical response times of medium Be-doped as-grown HELP InGaAsP measured by above-band single-wavelength ( $1.50 \mu\text{m}$ ) pump-probe technique under various carrier densities. The bottleneck effect observed here is smaller than in the undoped and lightly doped cases, due to increase in empty trap concentration.



(a)



(b)

**Figure 4.29** Optical response times of heavily Be-doped as-grown HELP InGaAsP measured by above-band single-wavelength (1.50  $\mu\text{m}$ ) pump-probe technique under various carrier densities. No obvious "bottleneck" effect is observed in the as-grown sample (a), due to increase in empty trap concentration as well as increase in hole concentration. However, the "bottle-neck" effect appears in the 600° C-annealed sample (b), due to drastic decrease in trap concentration by annealing.

## 4.4 DUAL-WAVELENGTH STUDY ON MATERIAL RESPONSE TIMES

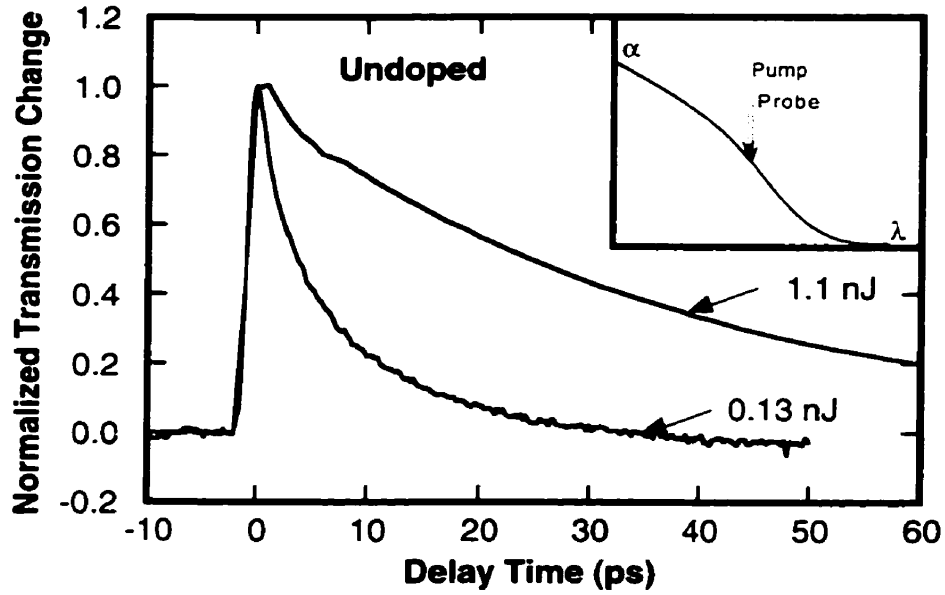
The wavelength region around the band edge, characterized by drastic changes of optical properties and large variations in nonlinearity and absorption, is the preferred region of operation for a variety of all-optical switching devices. Nonlinear-absorption-based devices (Section 2.1.1) can take advantage of the large nonlinear absorption at wavelengths just above the band edge; nonlinear-refraction-based devices (Section 2.1.2) can operate at wavelengths in the band tail region or just below the band edge to avoid large absorption, while still taking advantage of the relatively large nonlinear refraction. In addition, when implementing optical switching, it is advantageous to set control pulses at a shorter wavelength than that of data pulses, allowing for efficient absorption of control pulses to actuate switching, while minimizing loss for the data pulses.

To further assess the suitability of HELP InGaAsP for devices utilizing dual-wavelength switching operation, we performed dual-wavelength pump-probe measurements in the wavelength region around the band edge, and investigated the material response times for probe wavelengths just above the band edge, in the band tail region, and just below the band edge.

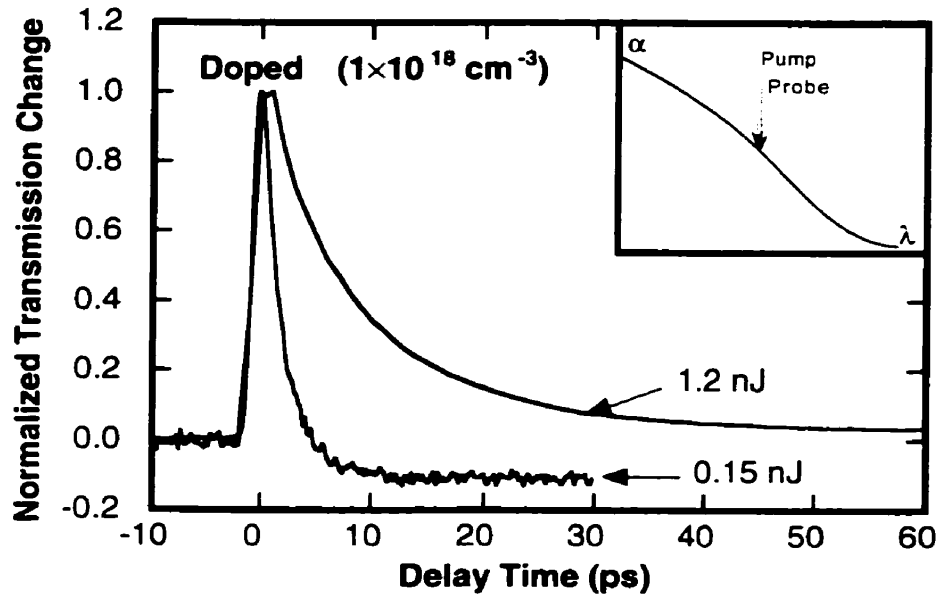
We used the OPO's idler beam as pump, and its signal beam as probe. Three sets of wavelength pairs—1510 nm and 1513 nm, 1516 nm and 1550 nm, and 1523 nm and 1600 nm—were used for the pump and probe, respectively. We used the undoped (1969) and the medium-doped (2001) as-grown samples for this study.

### 4.4.1 Probe wavelength above the band edge

With the probe wavelength above the band edge, we observed response times (Fig. 4.30) similar to those exhibited in the above-band single-wavelength pump-probe experiments (Section 4.3.1). The absorption saturation is dominated by conduction band filling, due to the smaller conduction-band density of states relative to the valence-band density of states. Hence the measured response times reflect primarily conduction band electron lifetimes, which, due to deep-level defects introduced by the HELP growth and the large number of empty electron traps made available by Be doping, are about 100–1000× shorter than that of the standard InGaAsP material. The bottleneck effects, less pronounced in the doped sample (2001) than in the undoped sample (1969),

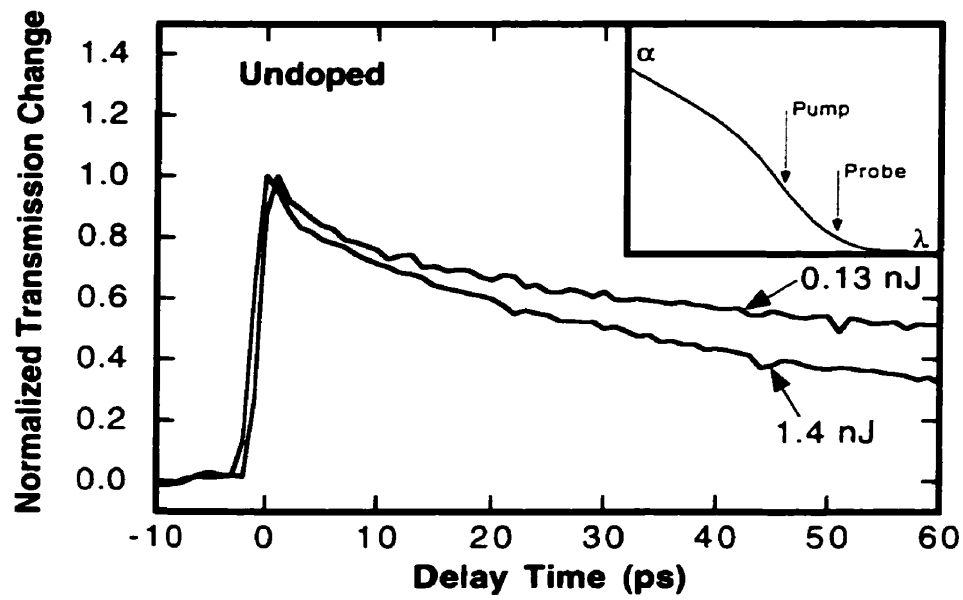


(a)

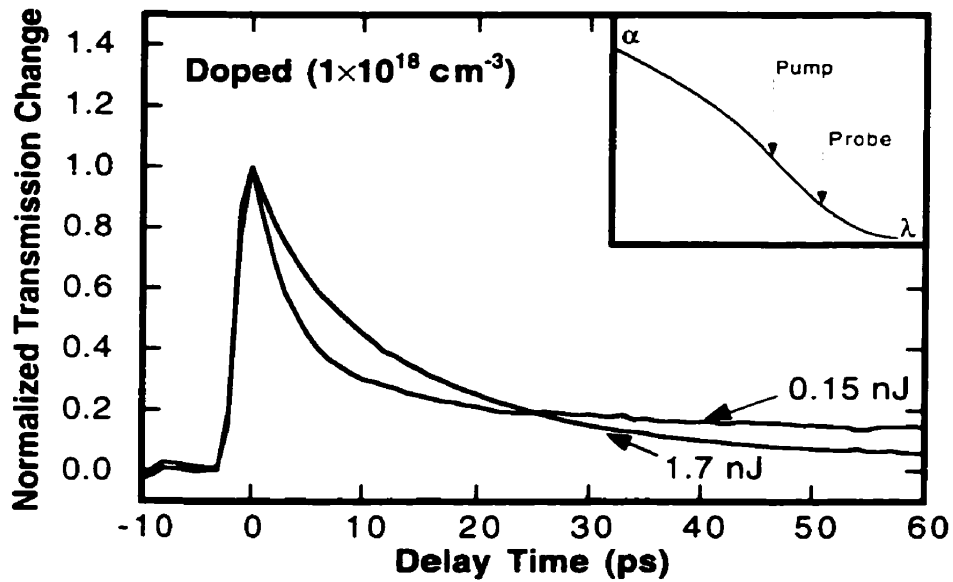


(b)

**Figure 4.30** Optical response times obtained by dual-wavelength pump-probe technique on (a) undoped and (b) Be-doped ( $1 \times 10^{18} \text{ cm}^{-3}$ ) HELP InGaAsP, under different pump pulse energies. Pump and probe wavelengths are 1510 and 1513 nm, respectively. The inset shows their position relative to the absorption edge.



(a)



(b)

**Figure 4.31** Optical response times obtained by dual-wavelength pump-probe technique on (a) undoped and (b) Be-doped ( $1 \times 10^{18} \text{ cm}^{-3}$ ) HELP InGaAsP, under different pump pulse energies. Pump and probe wavelengths are 1516 and 1550 nm, respectively. The inset shows their position relative to the absorption edge.

indicate limited electron trap concentrations and smaller hole capture coefficients than electron capture coefficients.

#### 4.4.2 Probe wavelength in the band tail

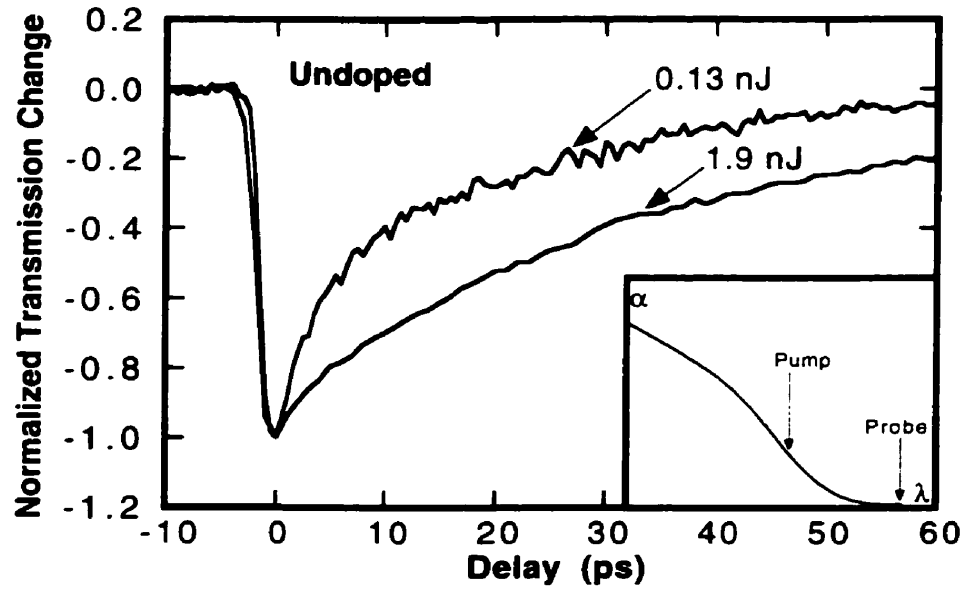
With the probe wavelength in the band tail region, absorption is expected to take place primarily between band-tail states. Consequently, the measured response time can be dominated by either electron trapping time, or hole trapping time, or both, depending on the densities of states (DOS) in the band tails.

Response times of the undoped sample (1969) observed here ( $>70$  ps) are much longer than those obtained with the probe wavelength above the band edge (cf. Fig. 4.31a and Fig. 4.30a), indicating that the response times reflect mainly the long hole trapping times ( $>70$  ps). This implies that the DOS is higher in the conduction band tail than in the valence band tail. The long hole trapping times measured here are the cause of the bottleneck effect discussed above (Section 4.4.1). The hole trapping time is even longer at a lower pump pulse energy (Fig. 4.31a), because the hole trapping rate is proportional to the hole density in the valence band (cf. Eq. 4.3), which decreases with the lowering of the pump pulse energy.

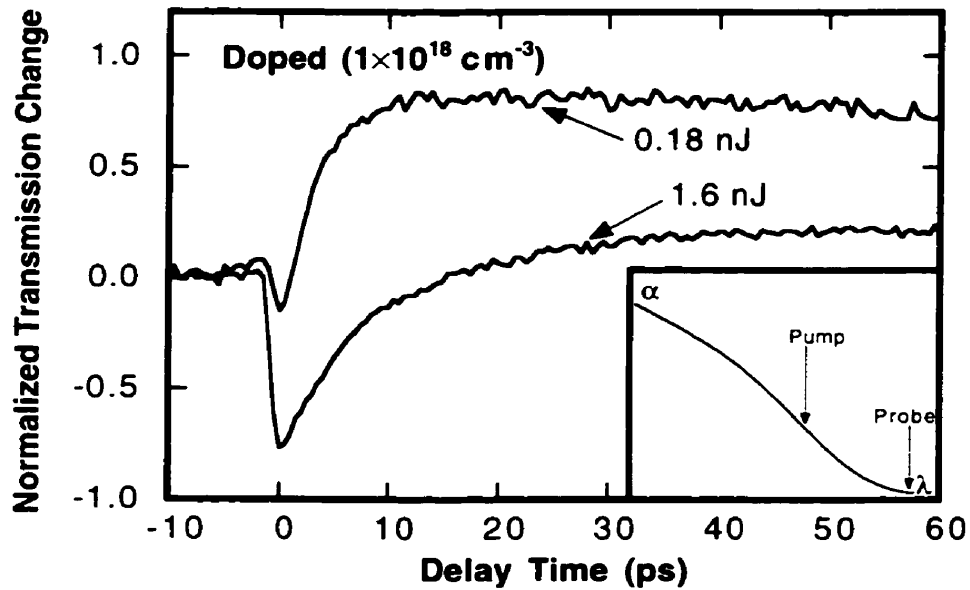
In the doped sample (2001), a fast, nearly complete absorption saturation recovery ( $\sim 10$  ps) is followed by a residual slow decay ( $>70$  ps) (Fig. 4.31b), indicating apparent contributions from both electron trapping and hole trapping, which is expected, since Be doping increases the DOS in the valence band tail. The residual “tail” of the decay curve is smaller for the higher pump energy than for the lower pump energy (Fig. 4.31b), which cannot be explained by invoking only one type of traps. Instead, it suggests that there are different types of traps, and that only a small portion of them have small hole capture coefficients, an inference supported by independent studies based on Hall measurements and Fermi statistics modelling [188].

#### 4.4.3 Probe wavelength below the band edge

With the probe wavelength below the band edge, we observed in the undoped sample an absorption increase, rather than absorption saturation (Fig. 4.32a), which we attributed to pump-induced



(a)



(b)

**Figure 4.32** Optical response times obtained by dual-wavelength pump-probe technique on (a) undoped and (b) Be-doped ( $1 \times 10^{18} \text{ cm}^{-3}$ ) HELP InGaAsP under different pump pulse energies. Pump and probe wavelengths are 1523 and 1600 nm, respectively. The inset shows their position relative to the absorption edge.

free-carrier absorption in the conduction band, i.e. free-electron absorption<sup>1</sup>. Therefore, the measured response time is the electron trapping time, which, due to the “bottleneck” effect, is faster at low pump pulse energy than at high pump pulse energy. In the doped sample, the free-electron absorption recovery is also followed by absorption saturation (Fig. 4.32b), which is likely associated with transitions between the valence band and the empty traps, and it is therefore more pronounced in the doped sample at a lower pump pulse energy.

## 4.5 RATE EQUATION MODELLING

We have shown ample evidence that the material response time is directly affected by the presence of traps. Ultimately, the response time can be determined by: (1) the concentrations of empty and filled traps at all trap levels responsible for non-radiative carrier decay, and (2) the carrier capture coefficients associated with all trap levels. However, given the complex nature of the quaternary system, theoretical calculations or direct measurements of defect concentrations and capture cross-sections prove very difficult, and usually trap parameters cannot be obtained by optical measurements alone. Nevertheless, we have developed a rate equation model to describe phenomenologically the material transient response, based partly on results from our pump-probe measurements, and partly on results from electrical characterizations of HELP material [188].

### 4.5.1 Defect levels in HELP InGaAsP

Identification and characterization of deep defect levels in semiconductors have always been difficult, especially in quaternary systems, for a number of reasons:

- (a) Defects take many forms: antisites, interstitials, various types of vacancies, or defect complexes; so there can be scores of possible defects in a quaternary system.
- (b) Some defects can have several charge states, each charge state corresponding to a different energy level.
- (c) Even when the defects are identified, theoretical energy-level calculations of deep-level defects are formidable. Due to the short-range nature of the potentials associated with

---

<sup>1</sup> See Appendix B for a more detailed discussion of this attribution.

these defects, the defect wavefunction must include contributions from all k-space and from many bands. The calculation will then require methods akin to band-structure calculations.

- (d) Experimental determination of deep-level defects is also difficult. Excitation energies of defects are commonly measured optically and thermally, but their interpretation is not obvious due to the large number of possible transitions involved.

HELP quaternaries, relatively new materials developed at McMaster University only a few years ago, have been little studied so far. But a comprehensive study of the electrical properties of HELP InGaAsP as functions of doping and annealing has been carried out by Heidi Pinkney in Dr. D. A. Thompson's group at McMaster University [188]. Her positron annihilation studies of vacancy-related defects and Hall effect measurements of majority carrier densities and mobilities are particularly relevant to defect identification and characterization. By developing a Fermi-Dirac statistics model to fit the Hall measurement data, she identified four defect levels and obtained the approximate energy levels and concentrations of these defect levels. We have already used some of her results in our previous discussions in Section 4.3, and showed that her results, derived independently from the study of the electrical properties of HELP InGaAsP, correspond very well with our observations.

Among the four defect levels identified in the study [188], two are near the middle of the band gap, and we believe, contribute significantly to non-radiative carrier trapping and recombination. Therefore they are responsible for the carrier dynamics observed in our pump-probe experiments. The other two levels do not contribute significantly to carrier trapping, because one trap level situates at an energy level higher than those of the free electrons optically generated, and therefore does not interact significantly with carriers: the other trap level lies just above the valence band, and can be considered as part of the band tail, because transitions between this level and the valence band can take place easily through thermal excitation. Hence, we incorporate only the two mid-gap levels in our phenomenological rate-equation model to describe the transient response of the material.

Fermi levels corresponding to undoped and doped materials are also identified through Hall effect measurements [179], which we use to determine the initial trap conditions in our model.

### 4.5.2 Two-trap-level rate equation modelling

Our two-trap-level rate equation model incorporates two trap levels with different electron and hole trapping rates (Figure 4.33).

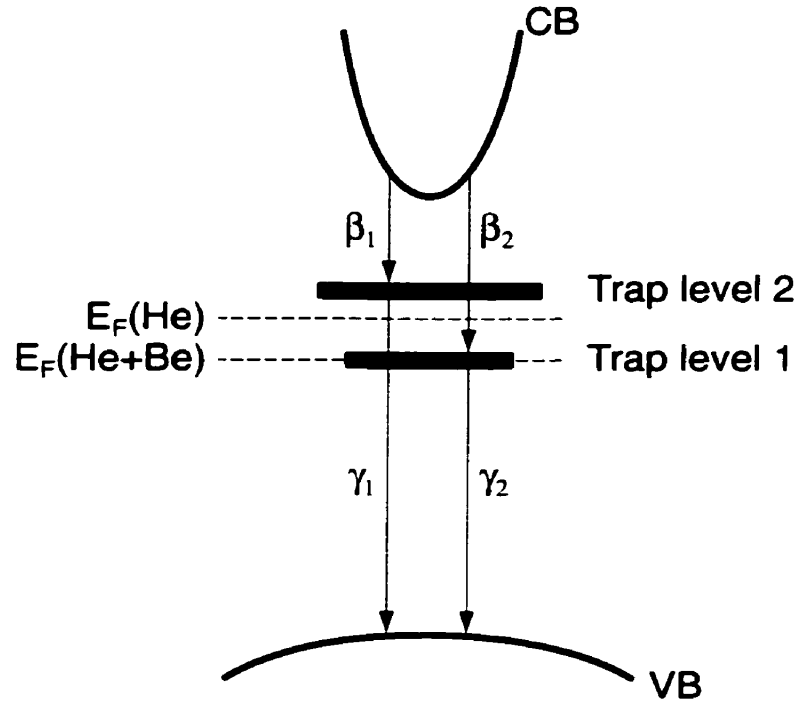


**Figure 4.33** Schematic energy band diagram for the two-trap-level rate equation model,  $E_F(\text{He})$  indicating the Fermi level of the undoped material, and  $E_F(\text{He+Be})$  indicating that of the doped material.

We assume no transition takes place between the two levels, because, generally, deep-level defects have relatively localized fields, and they are physically too distant from one another for direct transitions between them to be probable. Therefore, similar to Eqs (4.2) and (4.3), the rate equations for electron densities in the conduction band ( $N_e$ ), in trap level 1 ( $N_{1e}$ ), in trap level 2 ( $N_{2e}$ ), and hole densities in the valence band ( $N_h$ ), can be written as:

$$\frac{dN_e}{dt} = -\beta_1 N_e (N_1 - N_{1e}) - \beta_2 N_e (N_2 - N_{2e}), \quad (4.4)$$

$$\frac{dN_{1e}}{dt} = \beta_1 N_e (N_1 - N_{1e}) - \gamma_1 N_{1e} N_h, \quad (4.5)$$

$$\frac{dN_{2e}}{dt} = \beta_2 N_e (N_2 - N_{2e}) - \gamma_2 N_{2e} N_h, \quad (4.6)$$

$$\frac{dN_h}{dt} = -\gamma_1 N_{1e} N_h - \gamma_2 N_{2e} N_h, \quad (4.7)$$

where  $N_1$  and  $N_2$  are the trap densities,  $\beta_1$  and  $\beta_2$  are the electron capture coefficients, and  $\gamma_1$  and  $\gamma_2$  are the hole capture coefficients. The capture coefficients,  $\beta_i$  and  $\gamma_i$ , are related to the capture cross-sections,  $\sigma_{ei}$  and  $\sigma_{hi}$ , by  $\beta_i = \sigma_{ei} v_{th}$  and  $\gamma_i = \sigma_{hi} v_{th}$ , respectively, where  $v_{th}$  is the thermal velocity of the electrons or holes.

Since our model (Eqs. 4.4–4.7) calculates the electron and hole decay transients, in order to use this model to fit the data obtained in our pump-probe measurements, we need to consider the relationship between carrier densities and probe transmission changes. The probe transmission change is, to the first order approximation, proportional to the absorption coefficient change  $\Delta\alpha$ . The relationship between carrier density and  $\Delta\alpha$  varies, depending on the dominant transitions taking place at the probe wavelength.

For probe wavelengths above-band or at band tail (Section 4.4.1 and 4.4.2), band-to-band transitions dominate. Although the transient carrier-density-dependent absorption may be calculated quantum mechanically by the Green's function technique [189], it involves complex calculations and require material parameters difficult to obtain either by experiment or calculation.

For probe wavelengths below the band (Section 4.4.3), on the other hand, free-carrier absorption dominates, which we attribute mainly to free-electron absorption (Appendix B). Since free-electron absorption is proportional to conduction band electron density, its recovery rate also represents the decay of conduction band electrons. Therefore, we can measure the recovery transients of the free-electron absorption of samples with different doping concentrations under various pump pulse energies, and use our rate equation model to fit these decay curves directly to determine the electron and hole capture coefficients in Eqs. 4.4–4.7.

Recovery transients of free-electron absorption in three samples, undoped (1969), lightly-doped (1970) and medium-doped (2001), were measured under various induced carrier densities (Fig. 4.34). Initial empty and filled trap concentrations were determined by the Fermi level and Be doping concentration. The fitting parameters were then obtained by fitting the measured decays

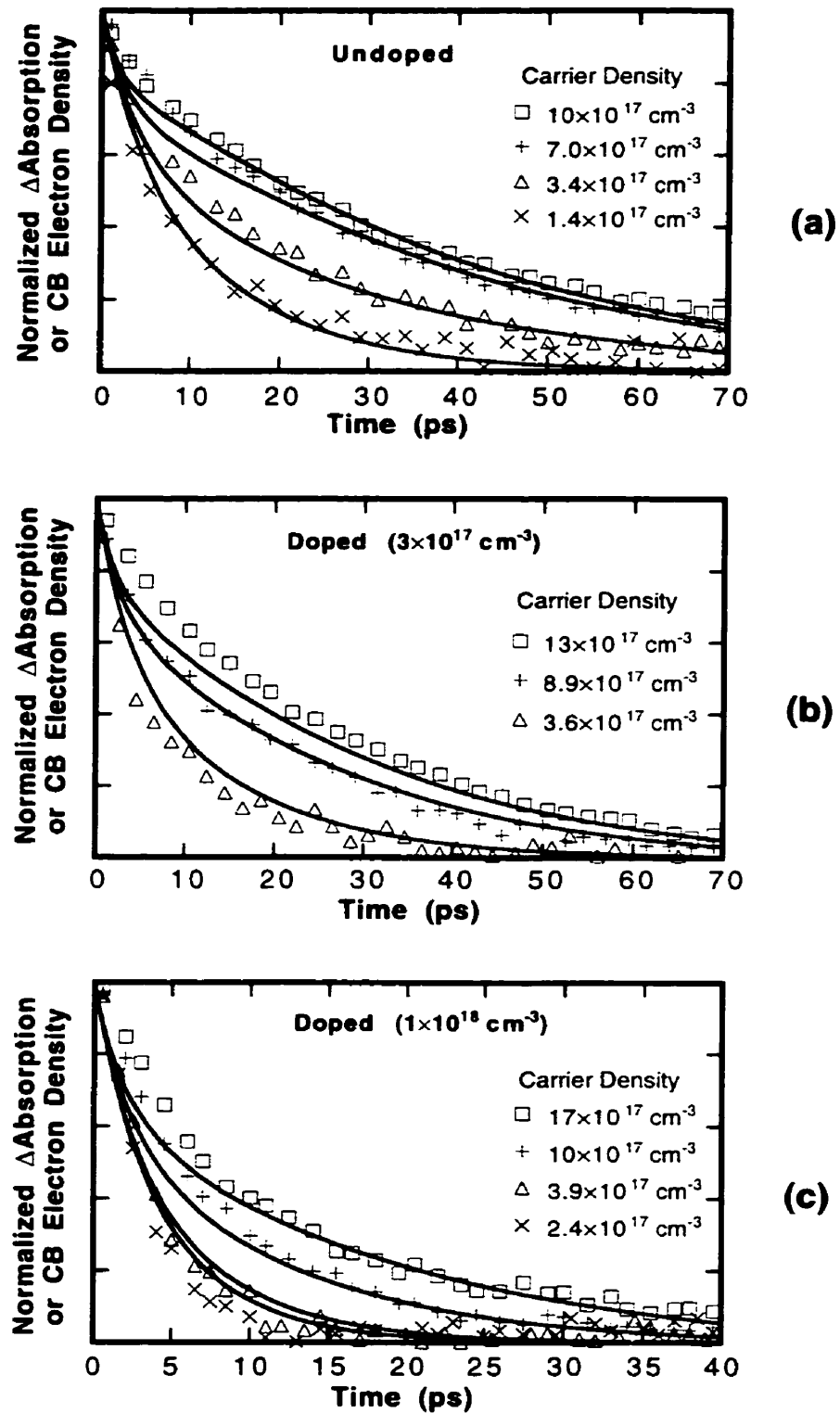


**Figure 4.34** Normalized conduction-band electron density ( $N_e$ ) decay curves for HELP InGaAsP samples of various doping concentrations. The symbols represent the decay curves of free-electron absorption ( $\alpha_{\text{fea}} \propto N_e$ ) obtained by dual-wavelength pump-probe measurements with the probe wavelength below the band edge.

(symbols in Fig. 4.34) with the calculated conduction-band electron decays (solid lines in Fig. 4.34):  $(2.5 \pm 0.4) \times 10^{17} \text{ cm}^{-3}$  and  $(12 \pm 2) \times 10^{17} \text{ cm}^{-3}$  for  $N_1$  and  $N_2$ , respectively;  $(12 \pm 3) \times 10^{-15} \text{ cm}^2$  and  $(2.8 \pm 0.5) \times 10^{-15} \text{ cm}^2$  for the electron capture cross-section  $\sigma_{e1}$  and  $\sigma_{e2}$ , respectively; and  $(1.4 \pm 0.8) \times 10^{-16} \text{ cm}^2$  and  $(1.8 \pm 0.4) \times 10^{-15} \text{ cm}^2$  for hole capture cross-sections  $\sigma_{h1}$  to  $\sigma_{h2}$ , respectively. The conduction-band electron decay rates calculated using these parameters closely resemble the experimental decay rates.

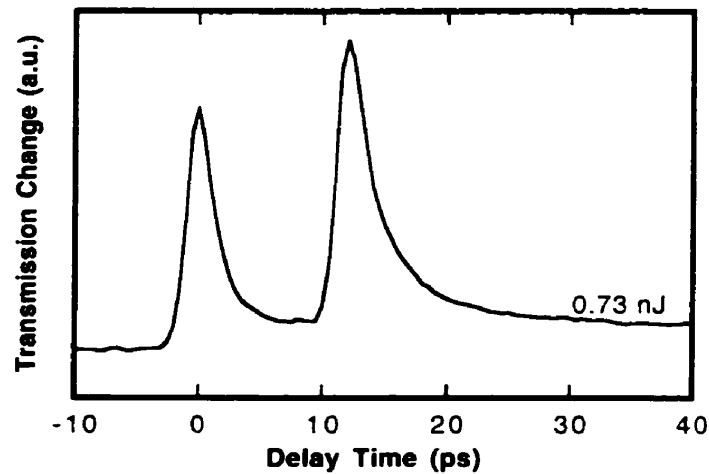
Furthermore, the trap densities we obtained agree, within a factor of 2, with those obtained by Hall measurements and Fermi statistics modelling [188]. Such an agreement is remarkable, considering that one study used optical measurements and modelling, while the other used electrical measurements and modelling. The transition cross-sections obtained here are similar to those reported on low-temperature GaAs [167, 190]. The hole capture cross-section of trap 1 ( $\sigma_3$ ) is more than one order of magnitude smaller than the others, indicating a slow hole-capture rate, which explains the slow decay “tails” observed in our pump-probe experiments.

#### 4.6 DUAL-PULSE EXPERIMENTS

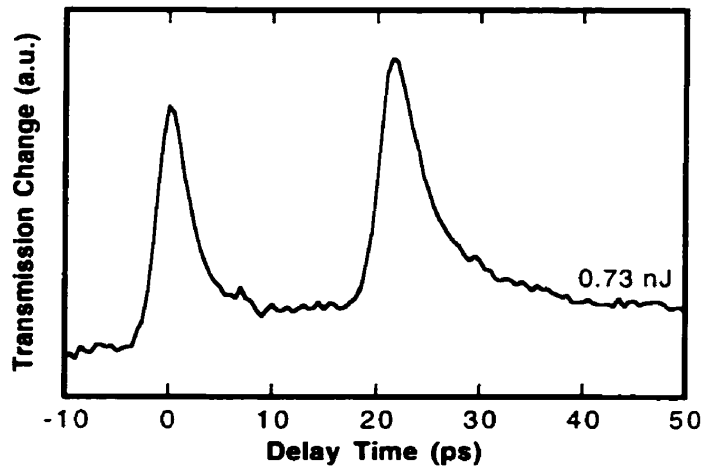
When implementing optical switching devices, high-repetition-rate switching operation is sometimes desirable, for instance, in high-speed optical signal processing and logic circuits, and in hybrid TDM/WDM systems where there are a small number of high-speed, large-bandwidth TDM channels. High-repetition-rate operation usually requires fast and complete recovery from optical excitation. However, our rate equation model reveals that, while three of the four carrier capture processes are ultrafast, one hole capture process is  $\sim 10\times$  slower, which leads to incomplete nonlinear recovery accompanied by a residual signal with a long decay. On the other hand, the slow hole capture is only associated with a small concentration of traps ( $2.5 \times 10^{17} \text{ cm}^{-3}$ ), whereas the concentration of the traps associated with the relatively fast hole capture can be increased, by Be-doping, up to  $12 \times 10^{17} \text{ cm}^{-3}$ . Therefore, we expect that the impact of the slow hole-capture trap level on the repetition rate will not be significant for heavily doped HELP materials.

We performed dual-pulse pump-probe measurements on a heavily-doped HELP InGaAsP sample (2002) to assess the impact of the slow hole capture process on the high-repetition-rate switching operation. In the dual-pulse pump-probe experiment (Fig. 4.4), two pump pulses closely separated in time (10–20 ps) are used to simulate high-repetition-rate operation. For probe

wavelengths above the band edge or at band tail, the response of the sample shows an incomplete recovery after the first excitation due to the slow hole trapping rate, but the residual “tail” does not accumulate after the second pump pulse, and near complete recovery is observed after the second excitation (Fig. 4.35). Therefore, this material can, in principle, be used in switching devices operating at 50–100 GHz rep rates.



(a)



(b)

**Figure 4.35** Response times of the heavily Be-doped ( $6 \times 10^{18} \text{ cm}^{-3}$ ) HELP InGaAsP sample (2002) obtained by dual-wavelength dual-pulse pump-probe technique for (a) probe wavelength above the band and (b) probe wavelength at band tail, indicating that fast, high-repetition-rate switching with this material is possible.

## 4.7 CONCLUSIONS

HELP InGaAsP has the unique advantage of simultaneously exhibiting picosecond optical response, large optical nonlinearity, and excellent crystalline quality. The picosecond response time is associated with high resistivity, low carrier concentration and mobility, and lack of photoluminescence. These optical and electrical properties of HELP InGaAsP indicate that, during HELP growth, high-energy helium plasma generates deep-level defects in the material. These deep-level defects, situated near the middle of the band gap, capture carriers efficiently through multi-phonon (non-radiative) decay process, resulting in ultrafast recovery of interband resonant nonlinearity. Contrary to defects introduced by many other methods, the defects in HELP material have minimal impact on the long range order of the crystalline structure, do not lead to reduced optical nonlinearity, and do not introduce large absorption tails.

Be doping in HELP material further reduces the material response time by more than one order of magnitude, and does not introduce significant band tail absorption. The reduction in material response time is attributed to the increase in empty electron traps, made available by Be dopants compensating for the filled deep-level traps. Be doping does not create new deep-level defects but only shallow acceptor levels, which leads to only slight increase in band-tail absorption. These effects of Be doping make HELP InGaAsP valuable for ultrafast all-optical switching.

Annealing results in a significant increase in the response time of the undoped material, and, at temperatures beyond 550° C, it also leads to a considerable increase in the response time of the doped material. The increase in the response time results from the removal by annealing of the mid-gap defects responsible for carrier trapping. Annealing also causes a blue shift of the band edge in the undoped material, which may be associated with the formation of large vacancy clusters. In the doped material, annealing does not cause blue shift, but it does not lessen the band tail absorption either. From the optical switching point of view, annealing does not offer any major advantages. However, our study on annealing effects indirectly verified some of the results of the electrical characterizations of HELP InGaAsP, and indicated that Be-doped (concentration  $\sim 1 \times 10^{18} \text{ cm}^{-3}$ ) HELP InGaAsP exhibits annealing-stable properties at temperatures  $\leq 550^\circ \text{ C}$ , which can be potentially useful to its application in optical devices.

The optical response time of HELP InGaAsP varies not only with doping concentration and annealing temperature, but also with carrier density and wavelength. Detailed studies of response times under various carrier densities and at various wavelengths across the band edge, together with results from electrical studies of the material system, reveal that two mid-gap defect levels are chiefly responsible for carrier trapping. Trap concentrations and carrier capture cross-sections were determined by fitting a two-trap-level rate equation model, and trap concentrations derived from this model agree well with those derived independently from the electrical study of the material.

Based on our studies on the optical properties of HELP InGaAsP, we conclude that this material is suitable for ultrafast all-optical switching applications.

---

# **Chapter 5**

## **ALL-OPTICAL SWITCHING DEVICES**

### **BASED ON HELP InGaAsP**

We demonstrate the possibility of HELP-InGaAsP-based ultrafast all-optical switching devices, specifically the nonlinear directional coupler and the asymmetric Fabry-Pérot switch, both of which can take advantage of the fast and large nonlinearity provided by HELP InGaAsP.

#### **5.1 NONLINEAR DIRECTIONAL COUPLER**

Semiconductor-based nonlinear directional couplers (NLDCs) offer a simple and elegant way of performing optical switching/routing. They are also highly desirable because they can be made compact and can be easily integrated with other semiconductor components. However, they require relatively large nonlinear phase changes to perform switching, for example, double those of Mach-Zehnder devices [191]. In order to use the large resonant nonlinearities in semiconductors to reduce switching energy and device size, the operation wavelength can be set at the spectral vicinity of the band edge. However, absorption near the band edge is also high, hence only the band tail region is potentially useful for operation if resonant nonlinearity is to be utilized [78]. Consequently, a very low band-tail absorption is an essential material requirement for an NLDC.

We discuss below the design issues concerning a HELP-InGaAsP-based NLDC, including device geometry, switching energy, operation wavelengths, polarization dependence, and throughput. Our discussion will be based on results obtained through numerical modelling and experimental measurements on a single waveguide structure.

##### **5.1.1 Theoretical considerations**

###### **5.1.1.1 PRINCIPLE OF OPERATION**

The structure of a NLDC consists of two identical, closely-spaced, single-mode waveguides (Fig. 5.1). It supports an even and an odd mode (Fig. 5.2), each with a slightly different propagation constant. If the coupler structure does not vary in the  $z$ -direction, then the two modes travel

independently (without coupling) along the  $z$ -direction. The coupler can support any arbitrary superposition of the two modes. If the modes have equal amplitude, then, when they are in phase, the energy is concentrated in one guide; when they are out of phase by  $\pi$ , the energy is concentrated in the other guide. Interference of the two modes (beating) as they propagate along the structure leads to periodic energy exchange between the two guides (Fig. 5.1). The beat length is  $2\pi/(\beta_e - \beta_o)$ , where  $\beta_e$  and  $\beta_o$  are the propagation constants of the even and odd mode, respectively. The half beat length ( $L$ ) is called the *coupling length* (Fig. 5.1).

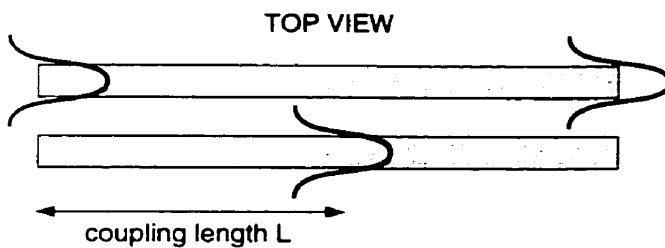


**Figure 5.1** A coupler consisting of two closely-spaced identical waveguides. The coupling length  $L$  is the distance over which one complete energy exchange takes place. (Same as Figure 2.5, redrawn here for convenience)

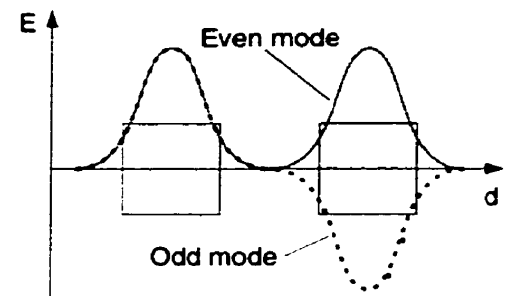


**Figure 5.2** Cross-section of a coupler and the field amplitudes of the even and odd modes.

Under nonlinear operation, when the light field intensity becomes high enough to induce significant index change in the guiding material, the two guides become dissimilar, because the intensity distribution is not the same in both at all times. This change brings about changes in field distribution, as well as in propagation constants, for both even and odd modes, resulting in, (1) a different coupling length  $L'$  due to different  $\beta_e'$  and  $\beta_o'$ , and (2) incomplete energy exchange between the guides, because of the asymmetry introduced by the index change. Under certain conditions [61], at one coupling length  $L$  away from the entrance of the coupler, almost all the light launched into one guide will emerge from the same guide, instead of being completely coupled into the other guide. For a lossless NLDC of length  $L$  (one coupling length), the cumulative phase change required for switching to occur is  $4\pi$  [63], corresponding to a required index change of  $4\pi/(k_o L)$ , where  $k_o$  is the free-space propagation constant. For a lossy NLDC, the intensity decreases as the beam propagates; however, as long as the index change is relatively uniform along the guide, the required phase change is still  $\sim 4\pi$ .

The operation of an NLDC was first described by Jensen [61], using the coupled-mode equations, which were later adopted and modified by Stegeman et al. [75]:

$$-i \frac{\partial}{\partial z} a_1(z) = \beta_1 a_1(z) + \kappa a_2(z) + \Delta n_1 k_0 a_1(z) + i \alpha a_1(z) \quad (5.1)$$

$$-i \frac{\partial}{\partial z} a_2(z) = \beta_2 a_2(z) + \kappa a_1(z) + \Delta n_2 k_0 a_2(z) + i \alpha a_2(z) \quad (5.2)$$

where  $a_1$  and  $a_2$  are the amplitudes of the two modes propagating along the two guides,  $\beta_1$  and  $\beta_2$  are their propagation constants,  $\kappa$  is the linear coupling constant, related to coupling length  $L$  by  $\kappa = \pi/2L$ ,  $\Delta n_1$  and  $\Delta n_2$  are the index changes induced in the two guides, and  $\alpha$  is the absorption coefficient of the guiding material.

Although widely used to model the behaviour of NLDCs, the coupled-mode method has the following limitations:

- (1)  $\beta_1$  and  $\beta_2$  in equations (5.1) and (5.2) are approximated by the propagation constants of the guides in isolation, whereas, strictly speaking, they should be calculated from the compound coupler structure, i.e. from  $\beta_e$  and  $\beta_o$ . The approximation becomes less reliable when the guide separation becomes small [62]. Since coupler behaviour can be completely described by the even and odd modes of the compound structure, if they can be solved, there is no need for equations (5.1) and (5.2). The coupled-mode method is only helpful when  $\beta_e$  and  $\beta_o$  are much more difficult to solve than the propagation constants for guides in isolation, and when the two guides are relatively far apart.
- (2) In the coupled equations (5.1) and (5.2), the linear term and nonlinear term are isolated. This description obtains only for index changes  $\Delta n_1$  and  $\Delta n_2$  so small that the modal field distribution is not significantly altered from the linear case, which may not apply to semiconductor waveguides using resonant nonlinearities, where relatively large index changes can be induced.
- (3) Under pulsed operation, if both pulse width and the nonlinear recovery time of the guide are so short that the guide index exhibits rapidly varying  $z$ -dependence, then, strictly speaking, the field distribution cannot be described by waveguide modes. Instead, nonlinear beam propagation method is more appropriate.

Therefore, under conditions of high intensity, short pulse excitation of couplers with very closely-spaced waveguides, which are the conditions of interest here, the coupled-mode method can, at best, offer only qualitative insight into the operation of an NLDC. In fact, an accurate numerical model for an NLDC would be extremely complex, because nonlinear absorption and index changes constantly modify the field distribution of the compound structure, which, in turn, changes the material absorption and index. Furthermore, nonlinear absorption and index changes in semiconductors are dictated by complex carrier dynamics and interactions. It is thus beyond the scope of this work to develop a quantitative model for the operation of a semiconductor-based NLDC. However, there exist several modelling tools we can use to acquire a qualitative understanding of the operation of an NLDC, and to assist us in device design.

### 5.1.1.2 MODELLING TOOLS

#### *Fwave IV electromagnetic wave solver*

Fwave IV is a freeware waveguide simulation program based on a finite difference implementation of the vector electromagnetic wave equations [192]. It explicitly solves for the horizontal and vertical (TE and TM) components of the electric field for a given structure, which can be a single waveguide or a coupler. It also calculates the effective index of a given mode, so it can be used to find the propagation constants  $\beta_e$  and  $\beta_o$  of a coupler, and hence the coupling length. A typical Fwave IV output window displays the field contour lines of a mode and its effective index value (Fig. 5.3). Because Fwave IV directly solves for the odd and even modes of the coupler structure, it is not necessary to use the coupled-mode equations (5.1) and (5.2).

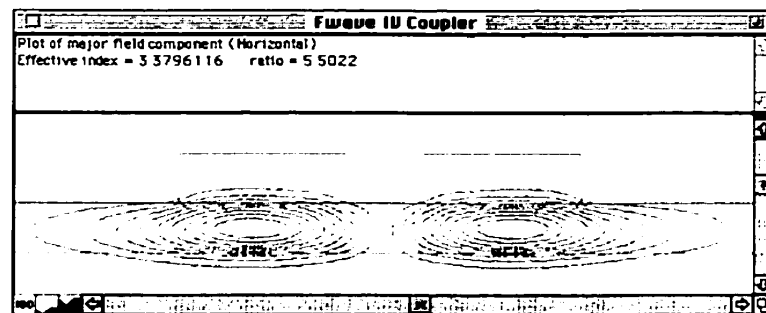


**Figure 5.3** A typical Fwave IV output window: Coupler structure and field contour lines of a mode are shown in the lower panel. The upper panel gives the value of the effective index of this mode and indicates it is a quasi-TE mode (Horizontal).

### *The Bányai-Koch model and the Kramers-Krönig relation*

The Bányai-Koch model [193] is a well-known model, based on a partly phenomenological theory developed to describe the nonlinear absorption of semiconductors under optical excitation in the wavelength region around the band edge. The absorption coefficient is calculated explicitly as a function of electron-hole-pair concentration.

The theory of Bányai and Koch is based on the linear response theory for the dielectric susceptibility of semiconductors, considering only transitions between the valence band and the conduction band. The theory takes into account three major contributions to the nonlinear absorption process: (1) band filling, which decreases the transition probability as the available states are being filled; (2) exciton screening, which weakens the attractive interaction between electrons and holes as the carrier concentration increases; (3) band gap renormalization, which reduces the photon energy required to create an electron-hole pair, due to the polarization cloud in the plasma. The rather involved formulation of the Bányai-Koch model is presented in Appendix C.

We developed a FORTRAN program (BK) to calculate the nonlinear absorption of InGaAsP based on the Bányai-Koch model, while another computer program (KK) is used to calculate the index change from the absorption change using the Kramers-Krönig relations [25]. Input parameters to program BK, e.g., band gap energy, electron and hole masses, conduction to valence band

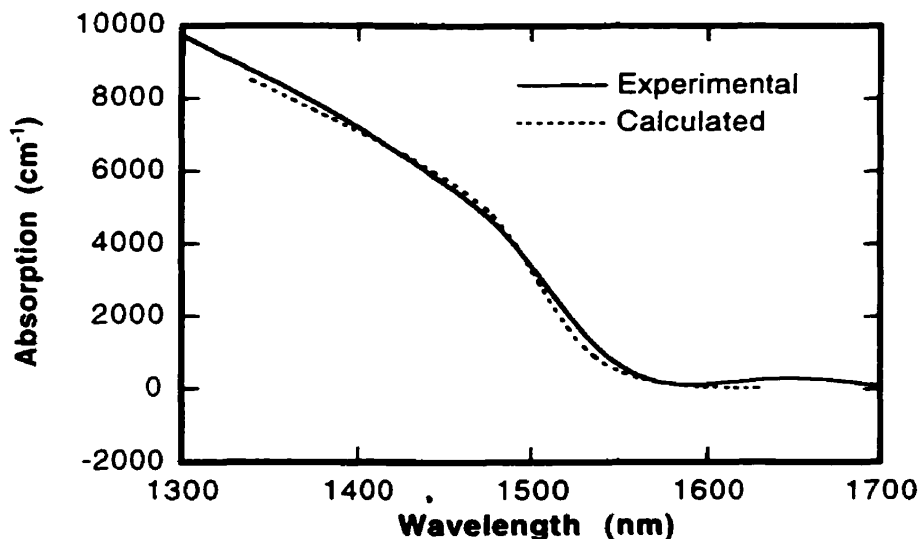


**Figure 5.4** Experimental and calculated absorption spectra of  $\text{In}_{0.60}\text{Ga}_{0.40}\text{As}_{0.84}\text{P}_{0.16}$ . The experimental spectrum is measured by FTIR spectrometer on an undoped HELP InGaAsP; the calculated spectrum is obtained by program BK, with two input parameters (transition strength and broadening parameter) adjusted to yield a good fit with the experimental spectrum.

transition strength, exciton broadening parameter, were chosen for the InGaAsP material system according to reported values [194] and experimental measurements. The transition strength and the broadening parameter are adjusted to yield a good fit between the calculated absorption spectrum and the measured spectrum (Fig. 5.4). An example of the absorption and index changes calculated by programs BK and KK as functions of wavelength and carrier density is given in Figure 5.5.

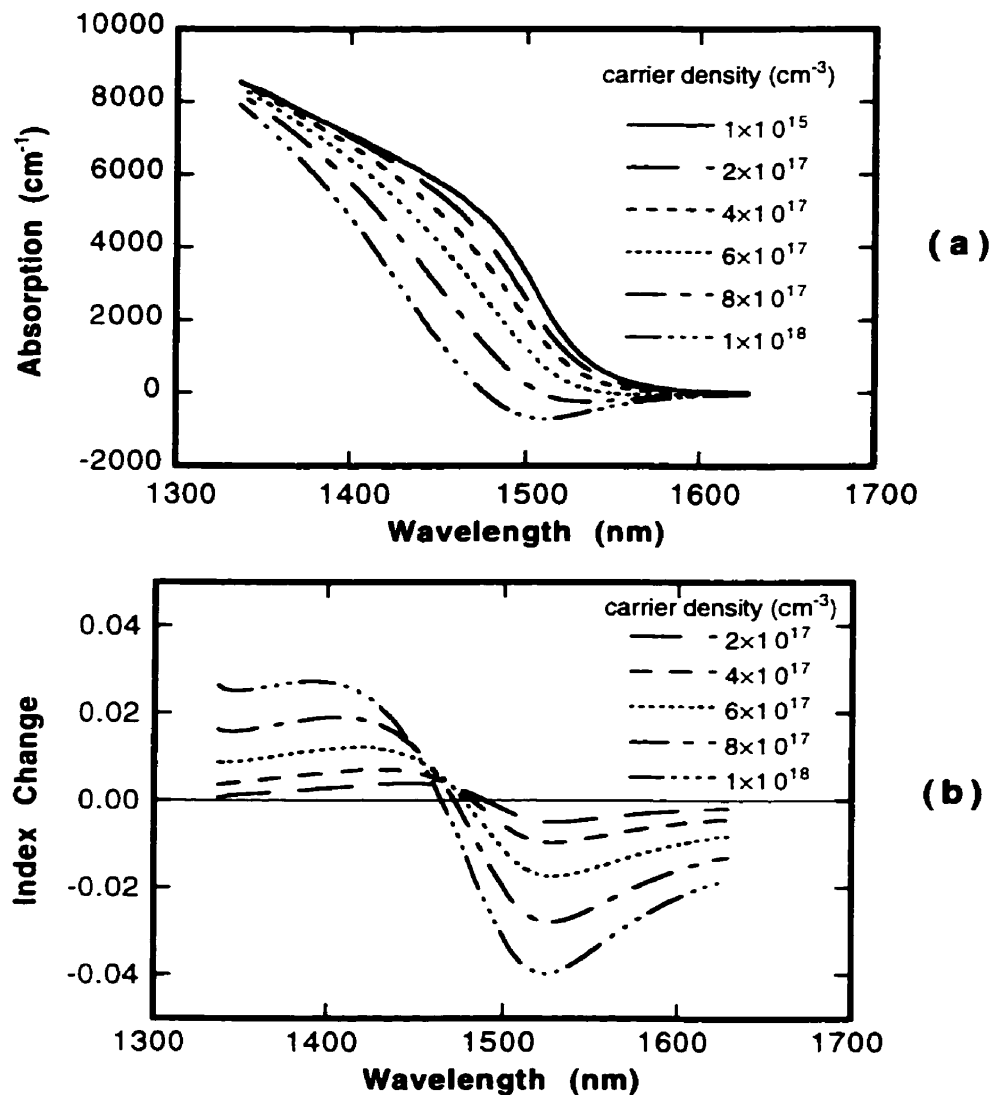


**Figure 5.5** (a) Band edge absorption as a function of carrier density, calculated with the Bányai-Koch model. (b) Index change as a function of carrier density, calculated from (a) using Kramers-Krönig relation.

The Bányai-Koch model applies, strictly speaking, to semiconductor materials without defects, since it does not include any defect contribution to the nonlinear absorption. Our experimental

results show that HELP InGaAsP has a sharp band edge (Fig. 4.10a) and maintains the large nonlinear index changes found in standard InGaAsP (Fig. 4.9), both of which indicate that the predominant absorption process in HELP InGaAsP is still interband, despite the defects introduced by HELP growth. Therefore, the Bányai-Koch model can still be used to provide a good approximation for the calculation of nonlinear absorption and index as functions of carrier concentration in HELP InGaAsP.

#### *Calculation of pulse-induced index change along a waveguide*

We developed a computer program (PP) to calculate the index change induced by a Gaussian pulse propagating in a waveguide as a function of time and position along the waveguide. The program takes into account the pulse-induced absorption saturation (calculated by BK) and the finite carrier lifetime of the waveguide material. It is intended to generate a qualitative description of how index change along the waveguide may be affected by pulse energy and wavelength, with a view to obtaining appropriate design parameters, such as wavelengths for control and data pulses, and estimating required switching energy.

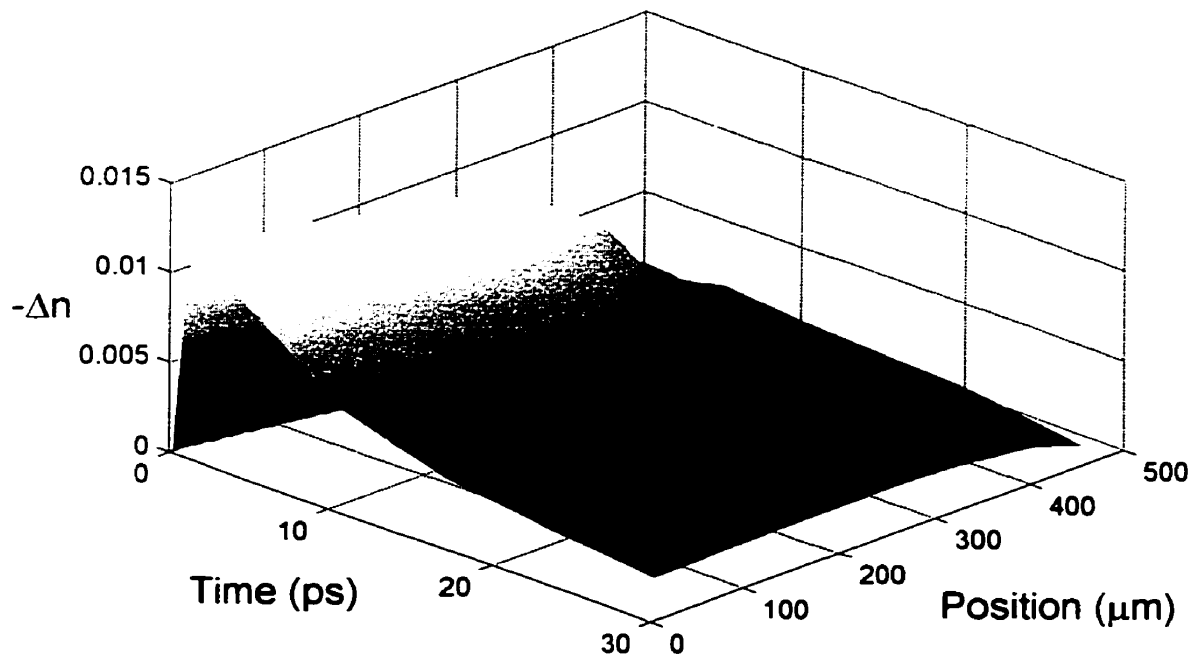


**Figure 5.6** An example of numerical simulation of the index change as a function of time and position along a waveguide. This type of graph can be used to determine the distance over which uniform index is induced along the waveguide, and the accumulated phase change in the waveguide.

For example, let us consider a simulation on a sample with the following parameters:

- composition:  $\text{In}_{0.60}\text{Ga}_{0.40}\text{As}_{0.84}\text{P}_{0.16}$  (1.50  $\mu\text{m}$  band gap wavelength)
- carrier lifetime: 15 ps
- control pulse: 2 ps Gaussian, wavelength = 1.54  $\mu\text{m}$ , peak intensity = 2  $\text{GW}/\text{cm}^2$
- data wavelength = 1.57  $\mu\text{m}$

According to the simulation (Fig. 5.6), the index change (calculated at the data wavelength) induced along the waveguide remains relatively constant for approximately 300  $\mu\text{m}$ . Along this distance, the control pulse is absorbed gradually from its front end, saturating the absorption. As long as there is enough energy left in the control pulse to saturate the absorption while it is propagating, the index change remains relatively uniform. Eventually, all of the control pulse will be absorbed, and the index change drops gradually (Fig. 5.6). Consequently, this particular combination of control pulse intensity, control and data wavelengths, and material properties should be suitable for a 300  $\mu\text{m}$ -long NLDC device. We can also determine the cumulative phase change experienced by the data pulse propagating along with the control pulse,  $-4\pi$  in this case, which is enough for switching.

### 5.1.1.3 DESIGN PARAMETERS

Although the numerical modelling tools described above do not simulate the complete operation of an NLDC, they can be used to determine several key design parameters, i.e. coupler cross-section geometry, device length, switching energy, and operation wavelengths.

#### *Coupler cross-section geometry*

Buried ridge waveguides (Fig. 5.7) are the most common structures in NLDC design. The ridges provide lateral mode confinement, while the thickness of the active layer provides vertical confinement. Several factors should be considered in the design of the cross-section geometry. First, each waveguide, when isolated, should be single mode, to avoid higher-order multi-mode interference in the coupler structure. Second, the modal field distribution should be concentrated as much as possible in the active layer, so that the large nonlinearity and fast response of the material is fully utilized. Third, it is also desirable that the mode should have a more “rounded”

shape for high coupling efficiency to and from an optical fibre. Taking into account these factors, we designed a coupler with a cross-section geometry as illustrated in Fig. 5.8.

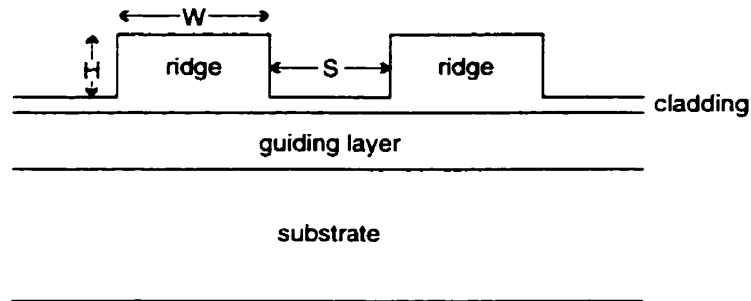
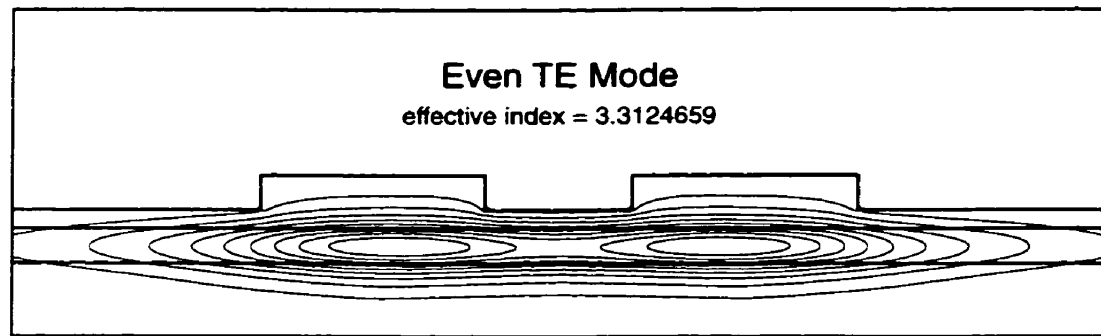


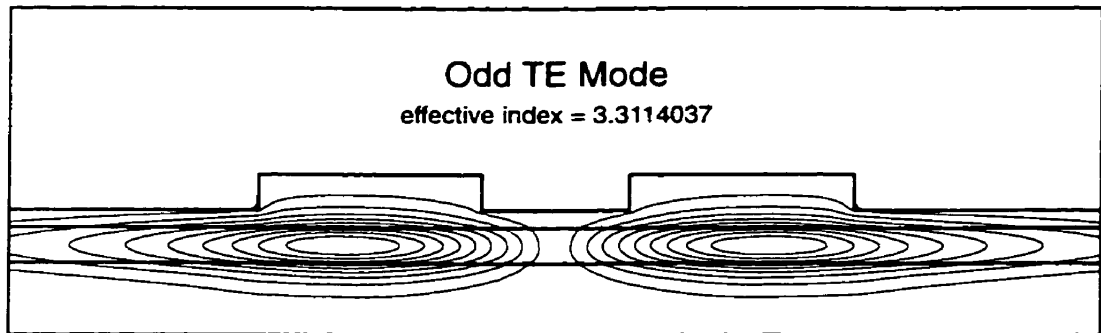
**Figure 5.7** Cross-section of a NLDC consisting of buried ridge waveguides.  $W$ : ridge width,  $H$ : ridge height,  $S$ : guide separation.

In addition, the cross-section geometry affects coupling length (and thus device length and throughput) and polarization sensitivity of the device. There are three polarization-dependent factors: (1) polarization mode dispersion, due to the different effective indices experienced by the two polarization modes; (2) polarization-dependent coupling efficiency, due to the difference in mode shape and area for different polarizations; and (3) polarization-dependent coupling length, due to different propagation constants ( $\beta_e$  and  $\beta_o$ ) for the TE and TM modes. (As discussed in Section 5.1.1.1, the coupling length  $L$  is equal to  $\pi/(\beta_e - \beta_o)$ , where  $\beta_e$  and  $\beta_o$  are the propagation constants of the even and odd mode, respectively.)

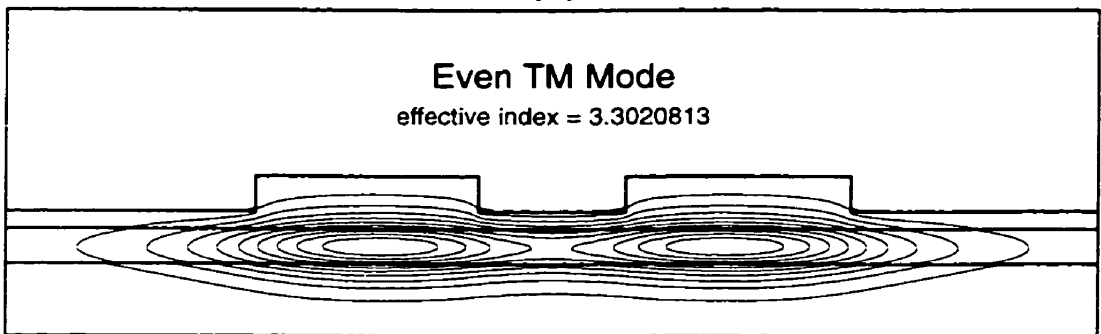
Fwave IV can be used to calculate the field distributions and effective indices of the TE and TM modes (Fig. 5.8), from which propagation constants and the coupling lengths for the different polarizations can also be calculated. We can neglect the polarization mode dispersion effect since the typical device length is very small ( $<1$  mm). For example, for the structure illustrated in Fig. 5.8, the maximum difference in effective index only leads to a temporal walk-off of  $<2\%$  of the total pulse width (assuming 1 ps pulse width, and 500  $\mu\text{m}$  device length). The difference in coupling efficiency for the TE and TM modes results in a polarization-dependent loss, although not calculated by Fwave IV, can be roughly estimated from the field distributions to be 1 dB. The difference in coupling lengths for the two polarizations, on the other hand, results in polarization-dependent contrast ratio, which can be more limiting than polarization-dependent loss in many practical systems. From the calculated coupling lengths for different ridge widths and guide separations



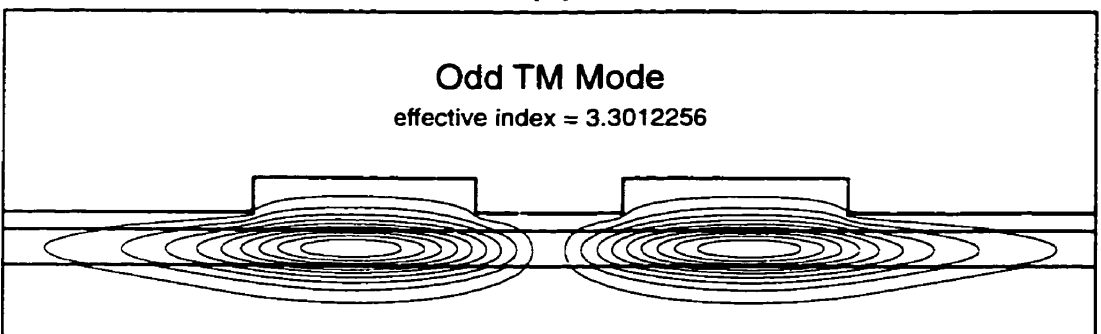
(a)



(b)



(c)



(d)

**Figure 5.8** Effective indices and field contours in an NLDC, as calculated by Fwave IV. The parameters used for calculation are:  $W = 3 \mu\text{m}$ ,  $H = 0.5 \mu\text{m}$ ,  $S = 2 \mu\text{m}$ , cladding thickness =  $0.75 \mu\text{m}$ , cladding and substrate index = 3.17, guiding layer thickness =  $0.5 \mu\text{m}$ , guiding layer index = 3.42, wavelength =  $1.55 \mu\text{m}$ . (a) Even TE mode, (b) Odd TE mode, (c) Even TM mode, (d) Odd TM mode.

(Table 5.1), it is apparent that the polarization dependence of the coupling length can be affected by varying the cross-section geometry of the coupler.

**Table 5.1 Coupling lengths ( $L_{TE}$  and  $L_{TM}$ ) calculated by Fwave IV for three coupler geometries with the layer structure illustrated in Figure 5.8**

	ridge width W	separation S	$L_{TE}$	$L_{TM}$	% difference in L
Coupler 1	2 $\mu\text{m}$	1 $\mu\text{m}$	278 $\mu\text{m}$	271 $\mu\text{m}$	~3%
Coupler 2	3 $\mu\text{m}$	1 $\mu\text{m}$	451 $\mu\text{m}$	403 $\mu\text{m}$	11%
Coupler 3	3 $\mu\text{m}$	2 $\mu\text{m}$	730 $\mu\text{m}$	906 $\mu\text{m}$	22%

Fwave IV simulation indicates that the difference between the coupling lengths for TE and TM modes grows dramatically when the guide separation increases or when the ridge width increases (Fig. 5.9). Consequently, polarization dependence of coupling length can be essentially eliminated by using narrow, closely spaced waveguides. However, making such waveguides and coupling light into them involve several technical difficulties. First, as waveguides and their spacing become smaller, tolerances on dimensions and on the straightness of the ridge walls become

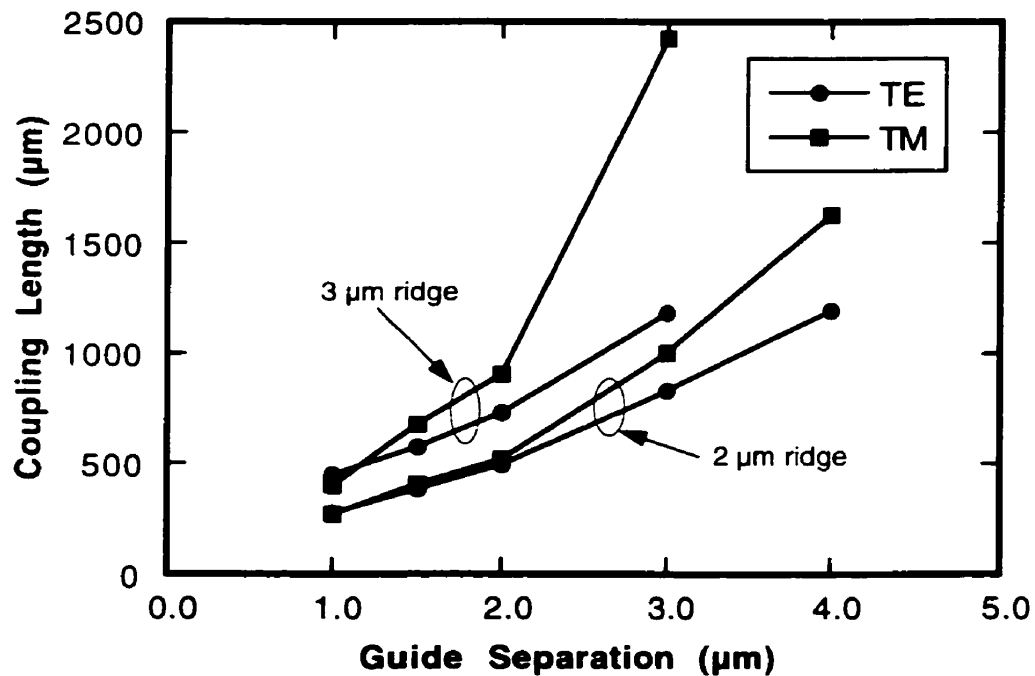


**Figure 5.9** Coupling length as a function of guide separation for couplers with 2  $\mu\text{m}$  and 3  $\mu\text{m}$  ridge widths. Simulation for the same structure as in Figure 5.8.

tighter, and coupling efficiency drops. Second, to allow easy coupling of light into and out of one guide only, the waveguides have to gradually branch away from each other on both sides of the coupler. The closer the spacing, the longer the branches, which may lead to considerable absorption of the control pulse before it reaches the coupler (control pulse pre-absorption).

The tolerance on the percentage of difference in coupling length is limited by the minimum contrast ratio required. The power transfer of a linear, lossless directional coupler varies gradually with distance (Fig. 5.10) [195]. Hence, if a 10:1 contrast ratio is required between the cross and the bar states, the difference between device length and coupling length should be within approximately 20%. Therefore, all three couplers listed in Table 5.1 can achieve 10:1 contrast ratio under linear operation. However, under nonlinear operation, the contrast ratio (switching fraction) is usually much lower, due to pulse breakup and nonlinear saturation (Section 2.2.2.1); consequently, the difference in coupling length should be kept to about a few percent.

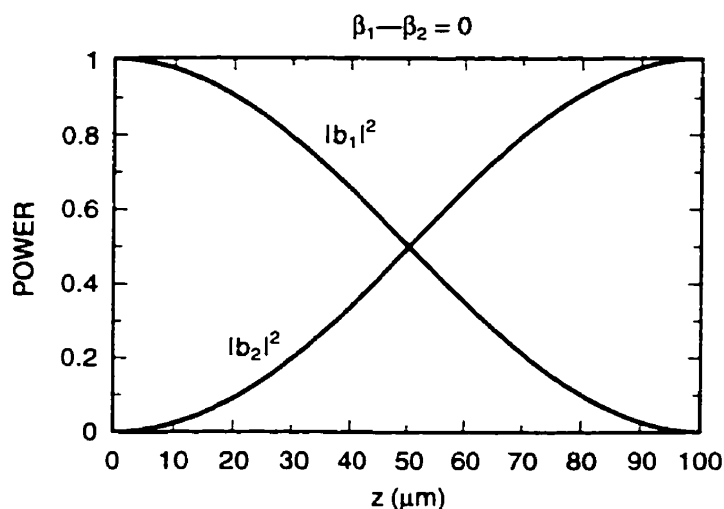


**Figure 5.10** Power exchange along a linear directional coupler with a coupling length of 100  $\mu\text{m}$ . After [195].

### *Device length*

Device length is usually one coupling length, the latter can be set to any desired value by altering the coupler geometry. In lossy couplers, device length is limited by absorption of the guiding material and by how much insertion loss the system can tolerate. As a rule of thumb, the length should be about one absorption length of the guiding material, i.e.  $\alpha^{-1}$ , where  $\alpha$  is the linear

absorption coefficient. The absorption length of undoped HELP InGaAsP near the band tail, where sufficient index change can be obtained, is on the order of hundreds of microns. Measurements on the waveguide absorption coefficient will be presented below (Section 5.1.2.3), and they will be used to determine the appropriate device length.

#### *Switching energy and operation wavelengths*

Switching energy is affected by the nonlinear index and the nonlinear absorption of the guiding material, both of which are wavelength-dependent. On one hand, switching energy can be lowered by setting the control pulse at a wavelength where absorption is high, thereby facilitating efficient absorption of the control pulse. On the other hand, absorption at the control wavelength should be low enough to allow relatively uniform absorption of the control pulse along the waveguide. This is particularly important when long waveguide branches precede the coupler, where control pulse pre-absorption may occur.

The choice of data wavelength should also be carefully considered. At a longer wavelength below the band edge, data pulses experience less loss. Additionally, switching time is shorter at a wavelength below the band edge than at the band tail. (As discussed in Section 4.4, material response at band-tail wavelengths is relatively slow, due to slow hole capture, whereas the response at a longer wavelength, below the band, is fast, because absorption is dominated by free-electron absorption). However, the induced index change is also smaller at the longer wavelength, thus higher switching energy is required.

Our simulation program (PP) can be used to determine the appropriate control and data wavelengths and to calculate the required switching energy. For a waveguide of length 450  $\mu\text{m}$  (corresponding to coupler 2 in Table 5.1), the simulation shows that, setting the control at too short a wavelength (1500 nm, above band) can cause the pulse to be completely absorbed only half way into the waveguide (Fig. 5.11), whereas setting the control at a longer wavelength (1540 nm) induces uniform index change along the waveguide (Fig. 5.12), although the switching energy required is slightly higher (100 pJ versus 80 pJ). Note that the *data* wavelength used was 1570 nm, longer than in the previous case, which means the insertion loss in this case was smaller as well. The cumulative phase change of the data pulse was approximately  $6\pi$ , more than that required for switching operation.

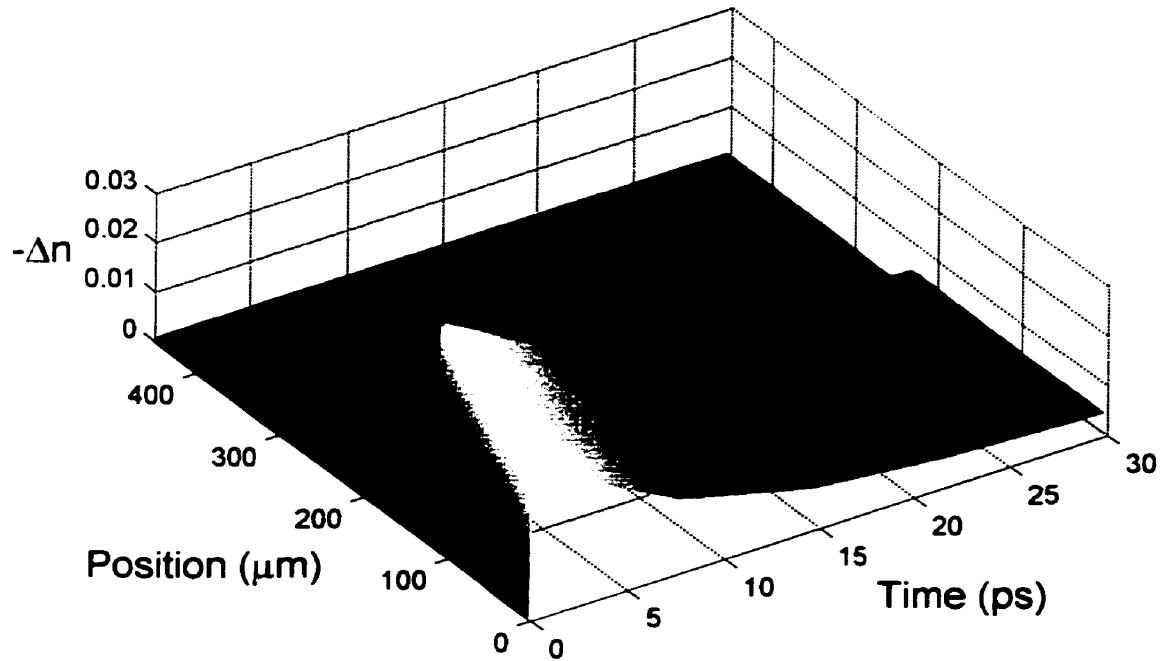


**Figure 5.11** Calculated induced index change at 1550 nm as a function of time and waveguide position. Control pulse: 2 ps Gaussian, peak intensity = 2 GW/cm<sup>2</sup>, wavelength = 1500 nm. Waveguide material: InGaAsP, band edge = 1500 nm, carrier lifetime = 15 ps. Applying this result to coupler 2 in Table 5.1, one obtains ~80 pJ switching energy.

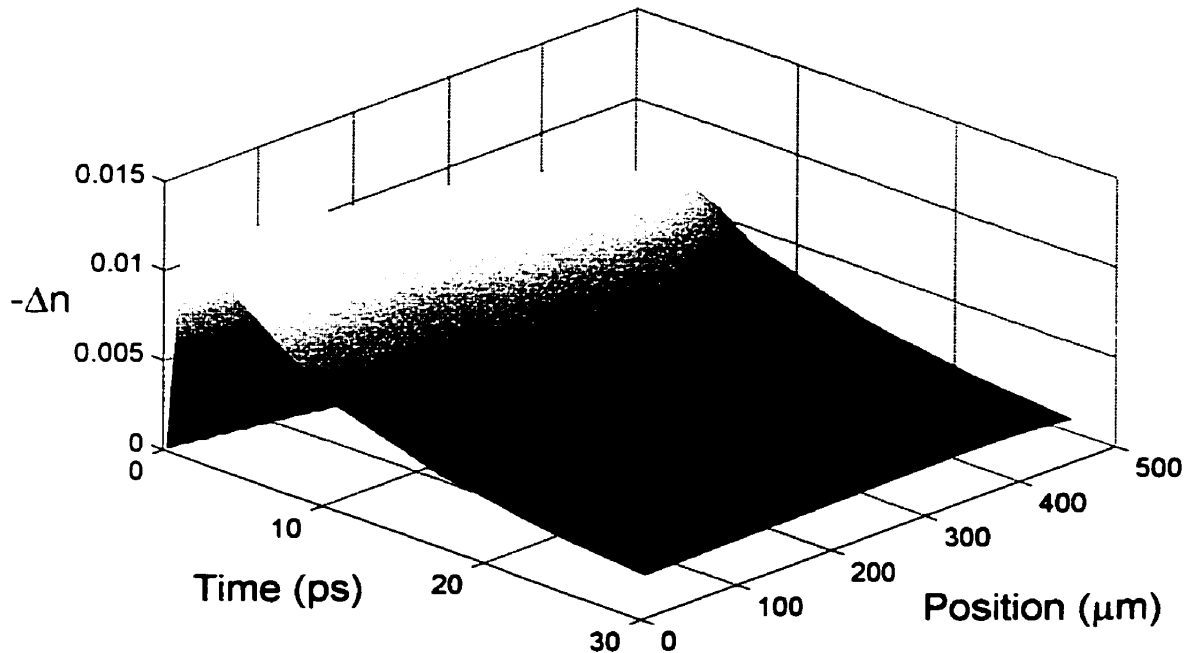


**Figure 5.12** Calculated induced index change at 1570 nm as a function of time and waveguide position. Control pulse: 2 ps Gaussian, peak intensity = 2.5 GW/cm<sup>2</sup>, wavelength = 1540 nm. Waveguide material parameters as in Figure 5.11. Applying this result to coupler 2 in Table 5.1, one obtains ~100 pJ switching energy.

The switching energy can be reduced significantly by using couplers with smaller ridge widths because, (1) waveguide volume is smaller, due to smaller mode size and shorter coupler length (see Fig. 5.9), therefore, lower energy is required to induce nonlinear index change; and, (2) shorter control wavelengths can be used, because uniform index change is required over a shorter distance, and shorter control wavelengths lead to more efficient absorption of the control pulse. For example, for a waveguide of length  $275\ \mu\text{m}$  (corresponding to coupler 1 in Table 5.1), by setting the control wavelength at  $1530\ \text{nm}$ , and the data wavelength at  $1570\ \text{nm}$ , only  $40\ \text{pJ}$  is required to induce uniformly along the waveguide sufficient index change for switching (Fig. 5.13).

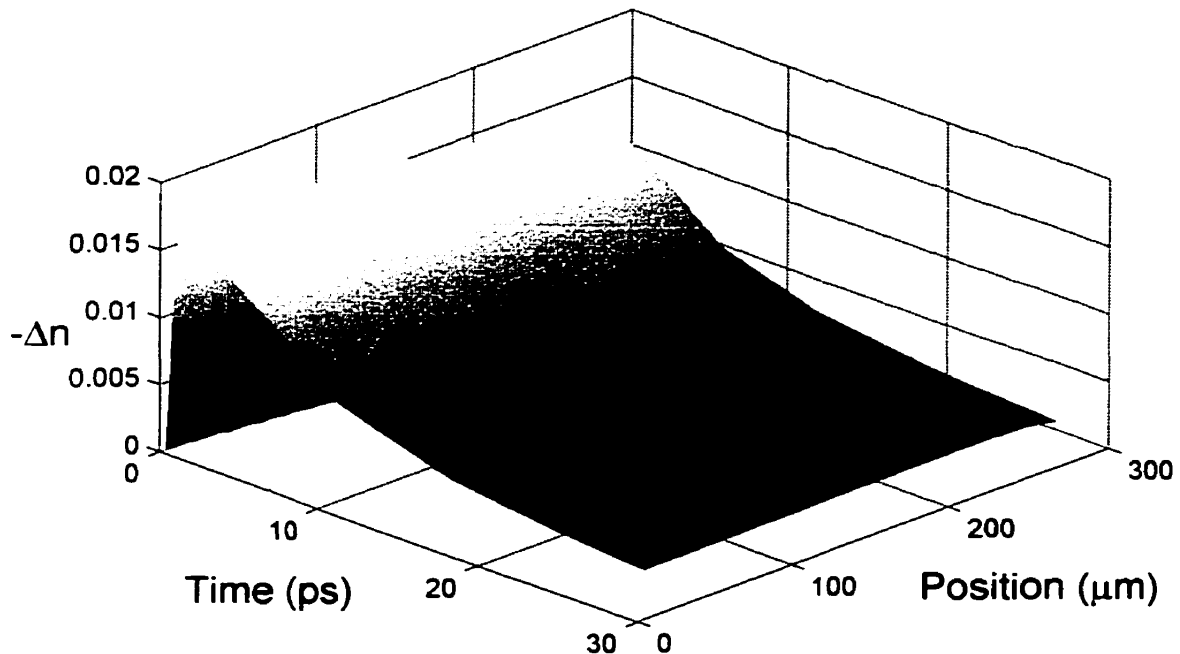


**Figure 5.13** Calculated induced index change at  $1570\ \text{nm}$  as a function of time and waveguide position. Control pulse:  $2\ \text{ps}$  Gaussian, peak intensity =  $2.0\ \text{GW}/\text{cm}^2$ , wavelength =  $1530\ \text{nm}$ . Waveguide material parameters as in Figure 5.11. Applying this result to coupler 1 in Table 5.1, one obtains  $\sim 40\ \text{pJ}$  switching energy.

Compared to the previous case (Fig. 5.12), a 60% reduction in switching energy is achieved as a result of using a shorter coupler ( $275\ \mu\text{m}$ ) and a smaller ridge width ( $2\ \mu\text{m}$ ). However, as mentioned before, smaller waveguide makes coupling and fabrication much more difficult. In practical implementations, switching energy may also be several times higher than the estimation given here, due to coupling losses. Our calculated switching energies for both the  $2\ \mu\text{m}$ -ridge and

3  $\mu\text{m}$ -ridge couplers are 40 pJ and 100 pJ, respectively, which compare favourably to values reported for passive NLDCs by Jin et al. (400 pJ) [68], and Villeneuve et al. (236 pJ)<sup>1</sup> [80].

### *Summary of NLDC design*

The design of HELP-InGaAsP-based NLDC devices resulted from the above discussions are summarized here: For a coupler cross-section structure as illustrated in Fig. 5.8, (1) the suitable coupler length should be in the range of 250–500  $\mu\text{m}$ , in order to yield a reasonable throughput; (2) the waveguides should be 2–3  $\mu\text{m}$  wide, and their separation should be 1–2  $\mu\text{m}$ , in order to minimize polarization dependence and to produce a coupling length of 250–500  $\mu\text{m}$ ; (3) the control pulse should have a wavelength 30–50 nm longer than the band edge wavelength, in order to be efficiently absorbed, and to induce large enough nonlinear index change for switching, while avoiding control pulse pre-absorption and maintaining a uniform index change along the waveguide; (4) the data pulse should have a wavelength  $\sim$ 70 nm longer than the band edge wavelength in order to minimize loss as well as to achieve a short switching time, while still taking advantage of the large nonlinearity near the band edge; (5) the switching energy required depends largely on the waveguide geometry and on the operation wavelengths: for the device parameters and operation wavelengths mentioned above, switching energy of 40–100 pJ is required, without taking into account of coupling and reflection losses.

### **5.1.2 Single waveguide experiments**

The modelling tools presented above (Fwave IV, BK, KK, and PP programs) are useful for device design, but they cannot predict many practical problems associated with NLDCs. For example, perfectly straight waveguide walls may not be attainable by etching; cleaving very short waveguides may be difficult; coupling from fibre to waveguide may result in large coupling loss, difficult to estimate; scattering losses due to non-ideal etching and contamination may be significant. To investigate these potential problems, and particularly, to measure the waveguide loss, we ex-

---

<sup>1</sup> Estimated by us, using the authors' values for input intensity (5 GW/cm<sup>2</sup>) [80, Figure 4a], waveguide dimensions (5  $\mu\text{m}$  × 1.5  $\mu\text{m}$ ), and pulse width (0.63 ps).

perimented with several single waveguide structures with undoped HELP InGaAsP as the guiding material.

### 5.1.2.1 WAVEGUIDE STRUCTURES: GROWTH AND PROCESSING

Two structures, A and B, were grown and processed into waveguides of a series of ridge widths: 2  $\mu\text{m}$ , 3  $\mu\text{m}$ , 4  $\mu\text{m}$ , 5  $\mu\text{m}$ , 6  $\mu\text{m}$ , 7  $\mu\text{m}$ , and 10  $\mu\text{m}$  (Fig. 5.14). The guiding layer of the two structures

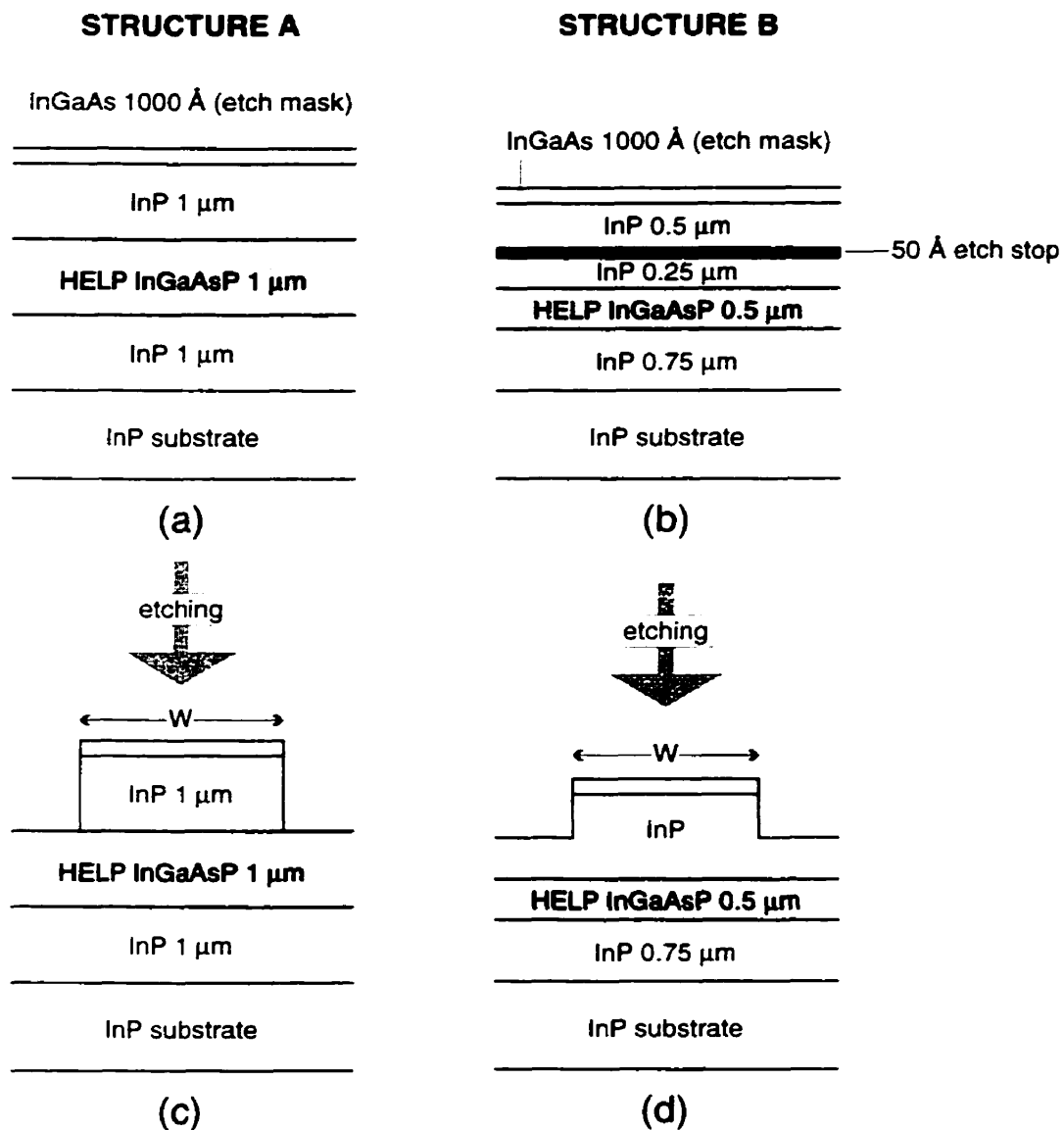


**Figure 5.14 (a) & (b)** Schematic representations of structures A and B, respectively **(c) & (d)** Waveguides processed by etching. Structure A has a thicker guiding layer for better coupling; structure B is the same as that analyzed by Fwave IV (see Figures 5.8 & 5.9) and the simulation program PP (see Figures 5.11–5.13).

are made of undoped HELP InGaAsP with band edge wavelength at 1.50  $\mu\text{m}$ . Structure B has been numerical characterized by Fwave IV (Fig. 5.8 and 5.9) and by simulation program PP (Fig. 5.11–5.13). Structure A has a thicker guiding layer than that of structure B, and therefore a higher coupling efficiency.

Growth and processing were performed at McMaster University by Dr. Brad Robinson and Dr. Heidi Pinkey, respectively. Both Reactive Ion Etching (RIE) and wet etching were used to process the waveguides. Wet etching is fast and requires little preparation, and it usually leaves smoother surfaces, but it sometimes results in undercutting the mask, and the side walls may not be vertical. RIE, on the other hand, is much slower, and therefore, theoretically, more controllable; it is also less affected by undercutting. However, RIE tends to cause rough surfaces, and therefore, it is usually followed by a quick wet etch for smoothness. After etching, the waveguides were cleaved into bars, each of which contains several series of  $\sim 500$   $\mu\text{m}$ -long waveguides. The cleaving was done manually by Heidi Pinkey, and the shortest length that could be cleaved successfully was around 500  $\mu\text{m}$ .

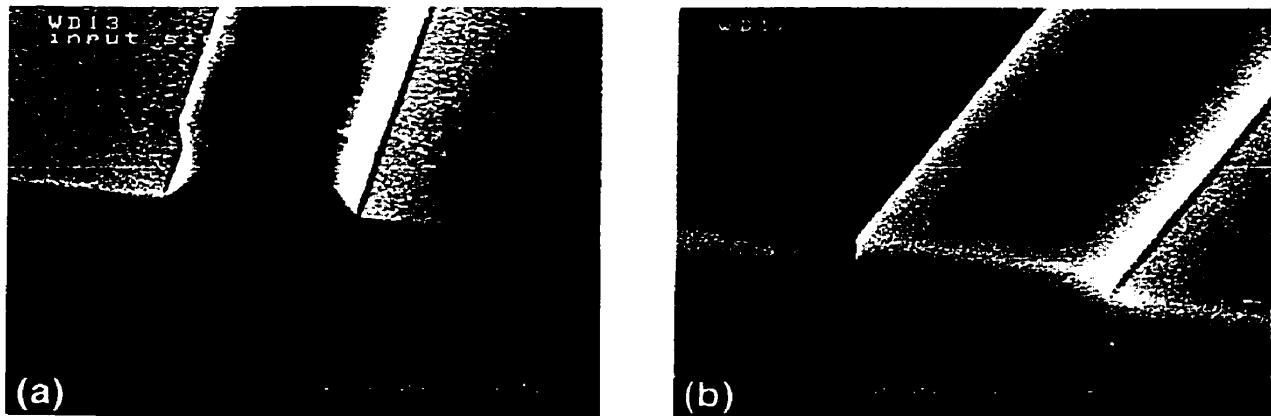


**Figure 5.15** SEM images of wet-etched waveguides, showing smooth surfaces and relatively vertical walls. **(a)** Structure A. **(b)** Structure B.

We examined some samples under a Scanning Electron Microscope (SEM), which revealed several significant features of these waveguides: (1) the wet-etched waveguides had a much smoother finish (Fig. 5.15), and they showed no significant undercutting; (2) RIE produced rough surfaces (Fig. 5.16), and, in waveguide structure B, large pedestals on both sides of the ridge (Fig. 5.16b); (3) large contaminants were found along or near the side walls of both RIE-processed

(Fig. 5.17a) and wet-etched waveguides (Fig. 5.17b); (4) many waveguide facets show some kind of mechanical damage (Fig. 5.18), most likely due to handling and/or cleaving.

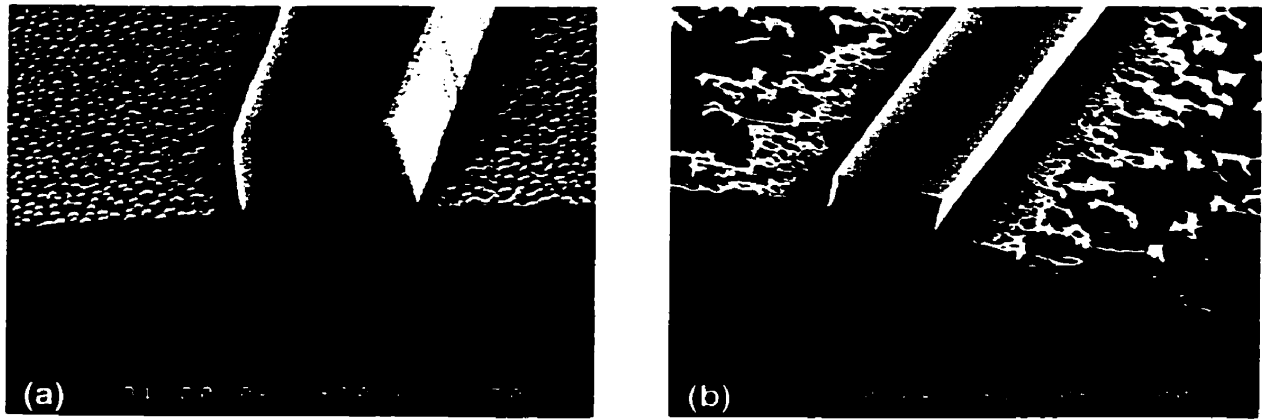


**Figure 5.16** SEM images of RIE-processed waveguides. (a) Structure A (note rough top surface of the guiding layer). (b) Structure B (note large, rough pedestals).

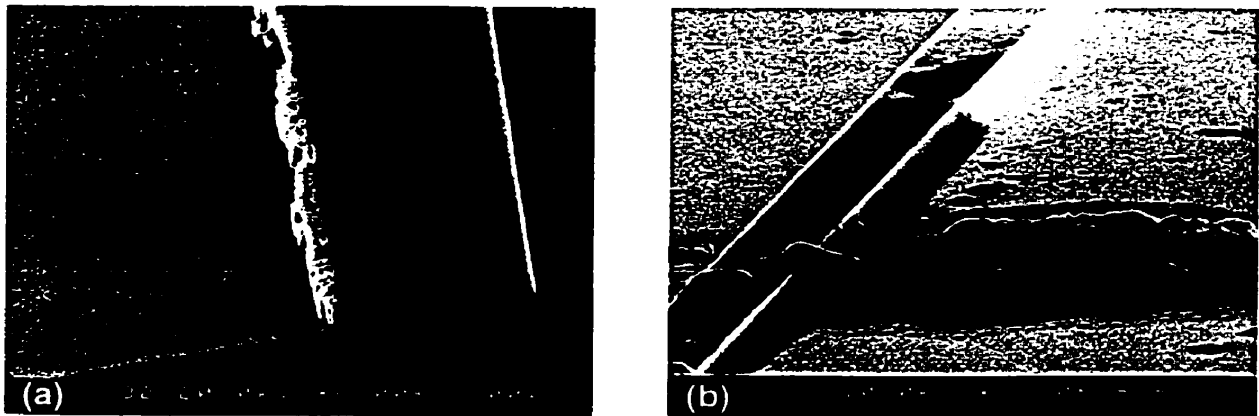


**Figure 5.17** SEM images showing large contaminants found in waveguides. (a) RIE-processed sample. (b) Wet-etched sample.

These imperfections and contaminants were primarily responsible for the large coupling and scattering losses experienced in later experiments.

### 5.1.2.2 IMAGING THE OUTPUT FACET AND THE OUTPUT MODES

Coupling light into such tiny waveguides is no trivial task, and, when the waveguides are extremely short, the output field image can be easily confused with the input image. To insure that we

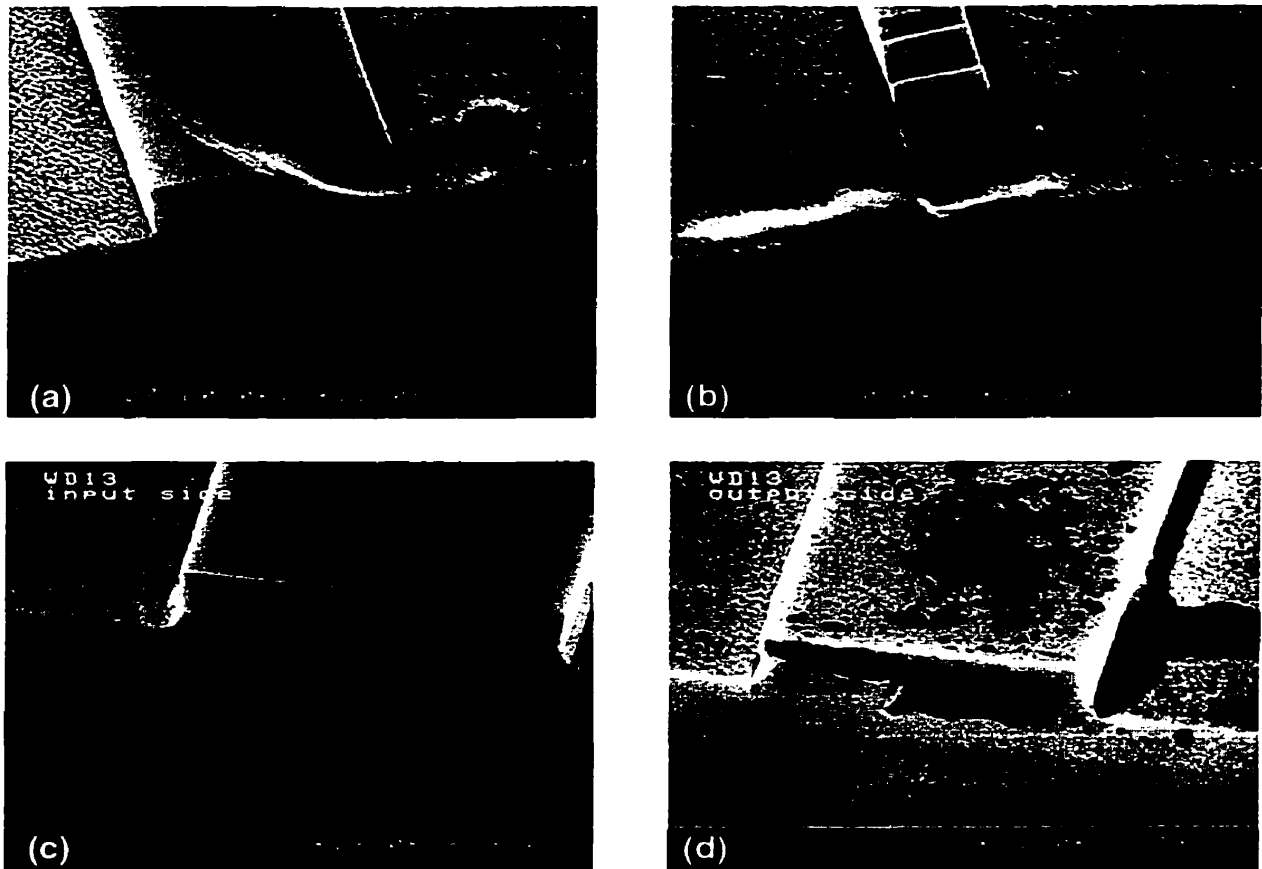


**Figure 5.18** Various types of mechanical damage found in waveguides. **(a), (b)** RIE-processed waveguides. **(c), (d)** Wet-etched waveguides.

coupled light into the waveguides, and to view the output field, we first imaged the output facet. (See Fig. 5.19 for the schematic diagram of the experimental setup.)

The OPO output was coupled into a single mode fibre, part of which was wound into a fibre polarization controller. Half of the light was directed to Detector 1, which monitors the power, while the other half was coupled into a fibre with a lensed tip (tapered fibre) at the other end, to facilitate light coupling into the waveguide sample. We used a microscope objective ( $f \approx 3\text{mm}$ ) to collect the output light from the waveguide sample. The fibre tip, the waveguide bar, and the microscope objective were mounted on a Newport UltraAlign translation stage set, which offered movement of submicron accuracy. While aligning for waveguide coupling, the waveguide bar and the fiber tip were observed under a microscope installed above the UltraAlign assembly.

To image the output facet of the waveguide sample, we used a beam splitter cube to reflect the imaging light (white light) to the output facet through the microscope objective, which, together

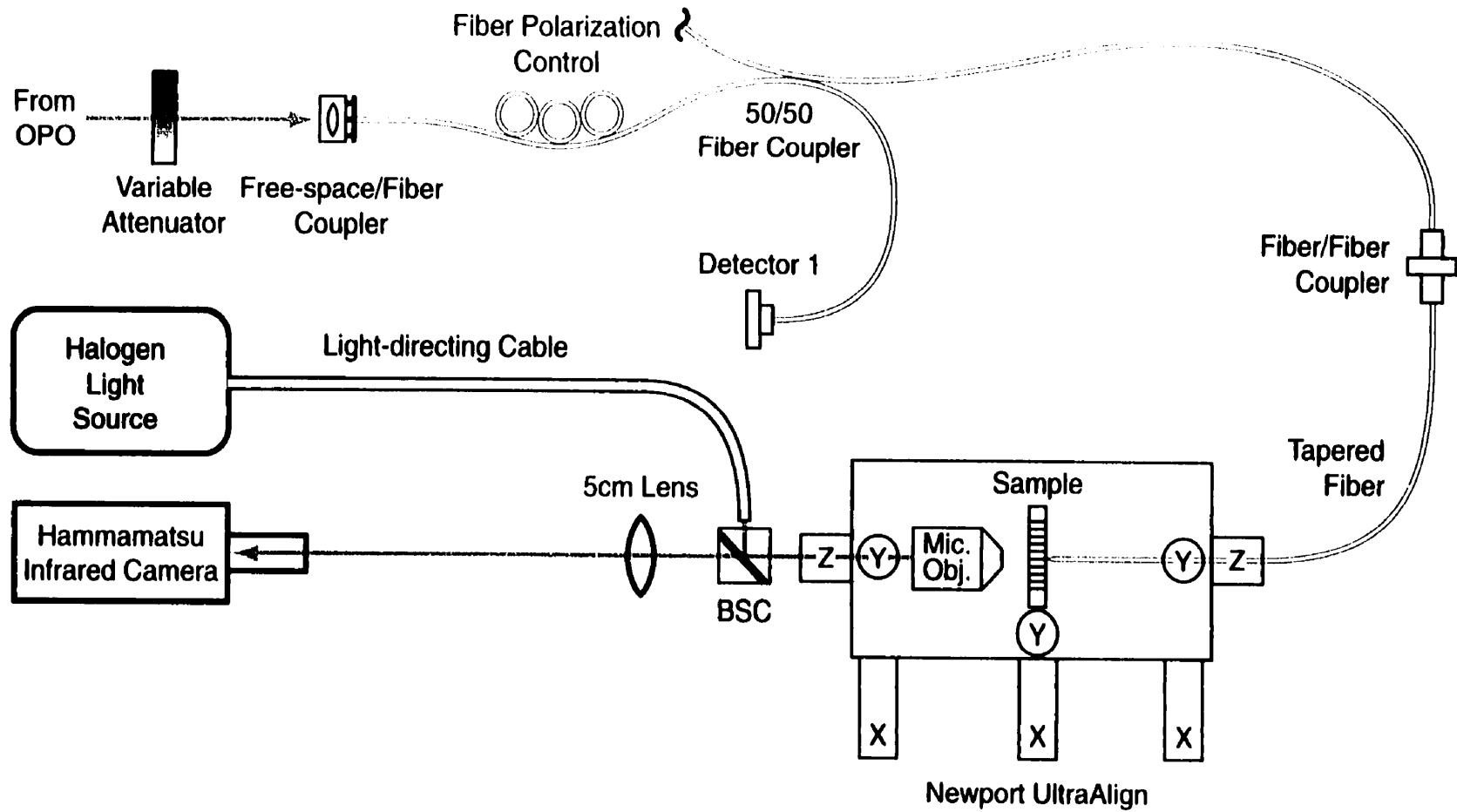


**Figure 5.19** Schematic diagram of the experimental setup for coupling light from fiber to waveguide, and for imaging the output sample facet, and the output waveguide mode.

with the 5 cm-focal-length lens, formed a magnified image of the output facet onto a Hamamatsu IR camera (also sensitive to visible light). The waveguide's output mode was also imaged and magnified via the microscope objective and the 5 cm-focal-length lens onto the camera. The magnification of the facet image is limited by the illumination level of the white light source. Images recorded by the IR camera were viewed on an monochrome monitor and recorded photographically. Note the image quality was influenced by various settings of the IR camera and the monitor, as well as by photographic processing, and therefore, the intensity of the recorded images might not accurately represent the actual intensity.

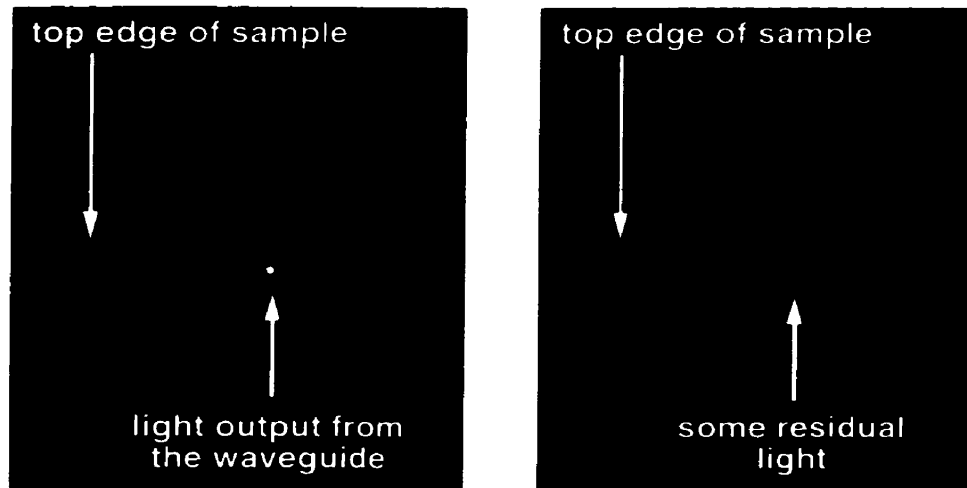


**Figure 5.20** Output facet images. **(a)** With light output from a waveguide, when the tapered fiber tip is aligned with it. **(b)** Without light output, when the waveguide is moved laterally away from the fibre tip. The magnification of the image is not high enough to resolve the ridges of the waveguides.

The output mode could be clearly seen from the recorded output facet images (Fig. 5.20a), although the individual waveguide ridges could not be resolved due to limited illumination. After translating the waveguide laterally away from the fiber tip, we observed a much reduced intensity (Fig. 5.20b), which indicated that the stronger light was indeed from the waveguide. The weak residual light was probably due to stray light or scattered light collected by the microscope objective. Since the white light source and the OPO had very different wavelengths, the lenses could not bring both images into sharp focus due to chromatic aberration, consequently, the image obtained by the camera may be distorted and may display a certain degree of parallax effect.

To obtain a higher magnification of the output mode profile, we removed the beam splitter and replaced the lens with a 2.5 cm-focal-length lens for higher magnification. Some recorded

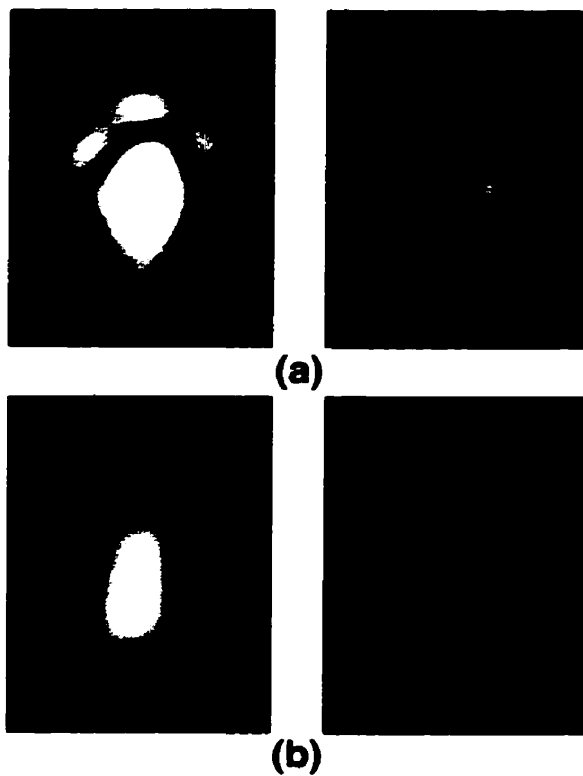


**Figure 5.21** Left: Output mode image of a  $4\ \mu\text{m}$ -wide waveguide of structure A. Right: Image obtained when the tapered fiber tip is moved away from the waveguide. Input light is (a) TE polarized, and (b) TM polarized.

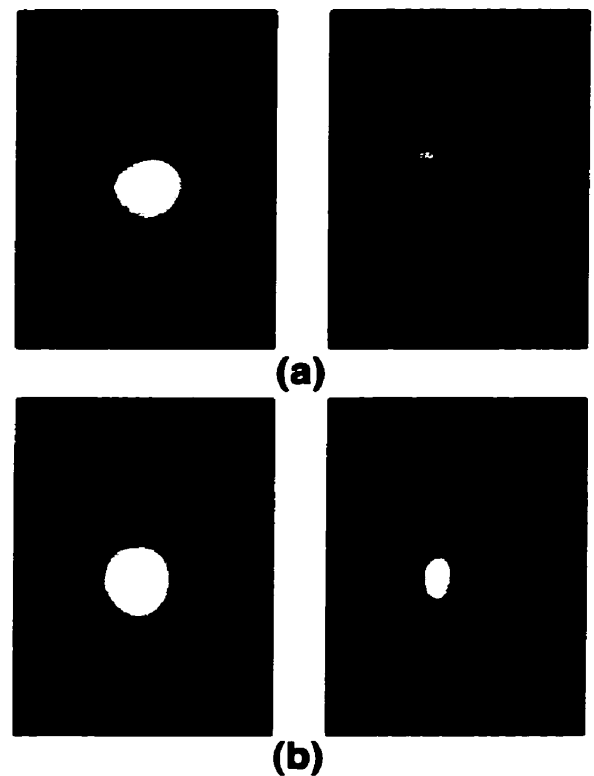


**Figure 5.22** Left: Output mode images of (a) a  $5\ \mu\text{m}$ -wide waveguide and (b) a  $4\ \mu\text{m}$ -wide waveguide of structure B. Right: Images obtained when the tapered fiber tip is moved away from the waveguide.

images of the output light from waveguides of structures A and B are shown in Fig. 5.21 and 5.22, respectively. The spots surrounding the mode seen in some of these images may be caused by the scattered light from imperfect ridges or large contaminants. We observed a much higher output mode intensity from structure A than that from structure B, which was expected due to higher coupling efficiency of structure A. The more elongated mode shape of structure A (Fig. 5.21)

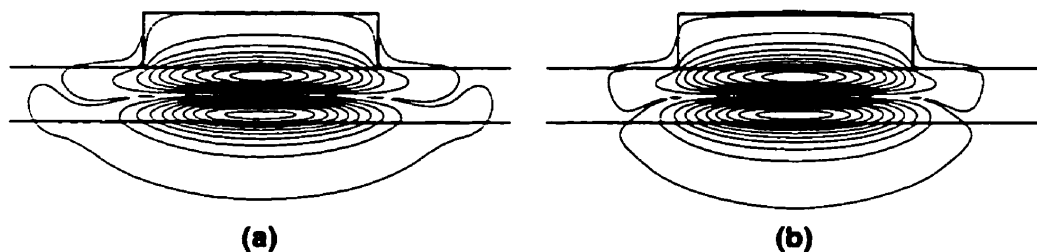


**Figure 5.23** Field contours of higher-order modes in a  $4\ \mu\text{m}$ -wide waveguide of structure A, calculated by Fwave IV. The largest contour is the 1% field contour, others are field contours from 10% to 90% at an increment of 10%. (a) TE mode. (b) TM mode.

suggests that this structure supports higher-order modes in the vertical direction. Indeed, there is some degree of resemblance between the observed mode images and the higher-order mode field contours calculated by Fwave IV (Fig. 5.23).

### 5.1.2.3 ABSORPTION MEASUREMENTS ON SINGLE WAVEGUIDE STRUCTURES

The extremely short absorption length of the waveguide material rendered the usual cut-back method for measuring waveguide absorption inapplicable. Instead, one can use the modulation depth of Fabry-Pérot fringes in transmission or reflection, resulted from multiple reflections at the two parallel facets of the waveguide, to derive the absorption coefficient [196]. The Fabry-Pérot fringes can be obtained by varying wavelength or waveguide temperature. We chose to measure the waveguide transmission versus wavelength, since it is easy to implement (Fig. 5.24).

We chose as laser source the INTUN 1500, a commercial fiber pig-tailed diode laser, because of its fine tunability, high wavelength stability, and computer interface capability. Detector 1 was used to monitor the input light power, and tapered fiber was used for light coupling into the waveguide (Fig. 5.24). Initially, we used the IR camera to ensure that the output light was indeed from the waveguide, and to optimize the coupling. Then we measured the output light power by inserting an aperture, a lens, and detector 2 after the 2.5 cm lens (Fig. 5.24). The aperture was used to filter out stray light and scattered light not coming from the waveguide but nevertheless collected by the microscope objective. The wavelength was then scanned, and the normalized transmission was plotted against it, showing the Fabry-Pérot fringe pattern. We determined the waveguide absorption coefficient by fitting the experimental data with the theoretically calculated Fabry-Pérot transmission curves. The theoretical fit was based on the following expression for the Fabry-Pérot transmission:

$$\left| \frac{E_t}{E_o} \right|^2 = t^4 \gamma^2 \left| \frac{e^{i\delta}}{1 - \gamma^2 r^2 e^{i2(\delta+\pi)}} \right|^2 \quad (5.3)$$

where  $E_t$  and  $E_o$  are the electric fields of the transmitted and the incident beam respectively,  $t$  and  $r$  are the amplitude transmission and amplitude reflection coefficients, respectively,  $\gamma$  is the single-pass amplitude loss coefficient, and  $\delta$  is the single-pass phase shift. The latter is related to the

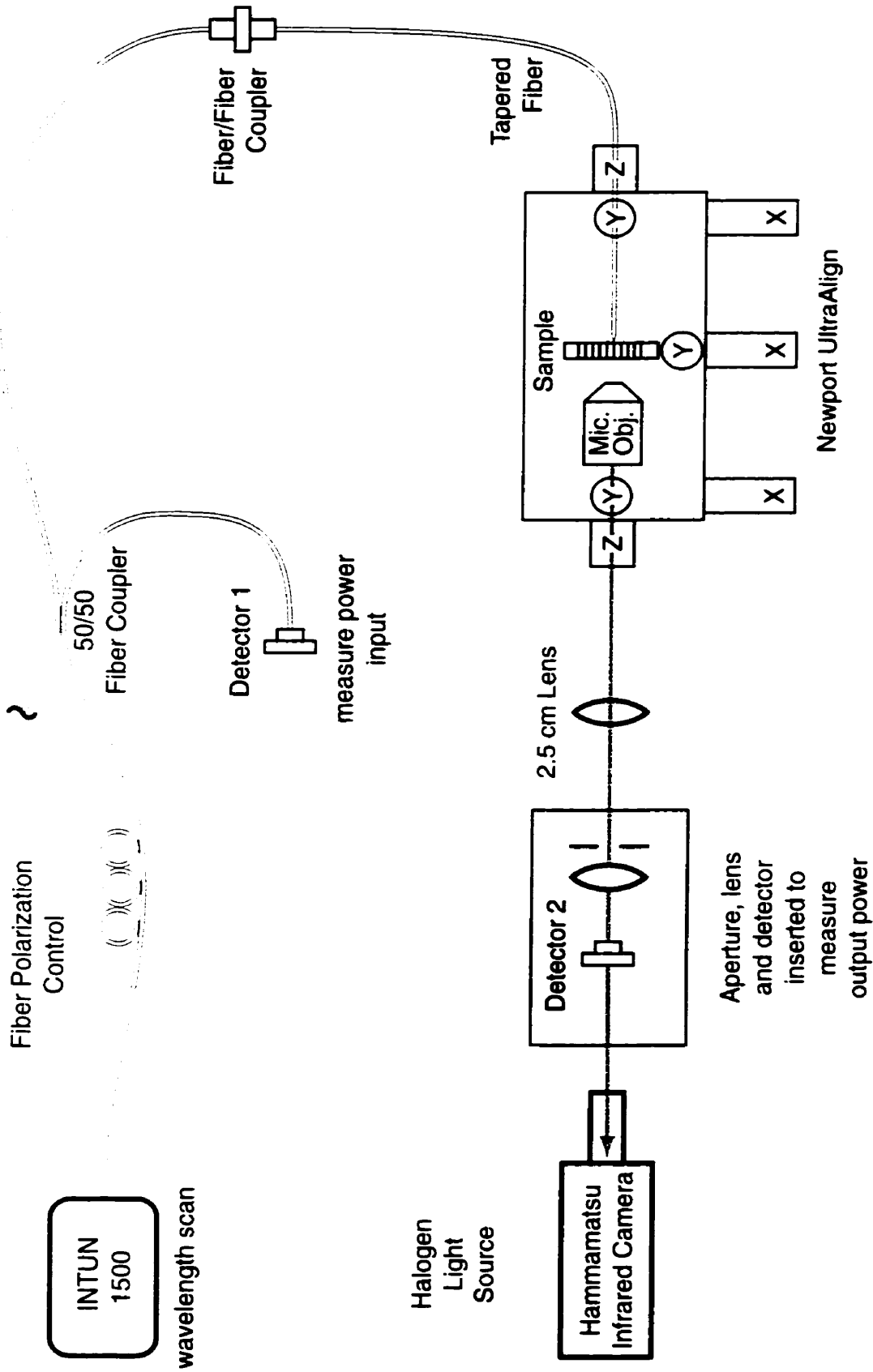


**Figure 5.24** Schematic diagram of the experimental set up for measuring the absorption coefficient of the waveguide material.

change in wavelength  $d\lambda$  by:

$$\frac{d\delta}{d\lambda} = -\frac{2\pi nL}{\lambda_0^2} \quad (5.4)$$

where  $n$  is the refractive index of the material,  $L$  is the length of the waveguide and  $\lambda_0$  is the central wavelength.

Since the waveguide facets are not anti-reflection coated, the reflection and transmission coefficients ( $R$  and  $T$ ) can be calculated from the refractive index of the guiding material, which is taken to be 3.4 [197]:

$$R = |r|^2 = \left(\frac{n-1}{n+1}\right)^2 = 0.295 \Rightarrow r = 0.54 \quad (5.5)$$

$$T = |t|^2 = 1 - R = 0.705 \Rightarrow t = 0.84 \quad (5.6)$$

It follows that the only fitting parameters are  $L$  and  $\gamma$ . The former is used to fit the *period* of the intensity modulation, and the latter the *modulation depth*. The absorption coefficient can then be calculated by:

$$\alpha = -\frac{\ln(\gamma^2)}{L} \quad (5.7)$$

The fitting of several sets of measured data obtained from waveguides of structure A gave a consistent absorption coefficient of  $35 \pm 4 \text{ cm}^{-1}$  at  $1.57 \text{ }\mu\text{m}$  (Fig. 5.25–5.27). Fitting of the data obtained from the RIE-processed waveguide structure B (e.g. Fig. 5.28), however, yielded a larger absorption coefficient of  $47 \pm 8 \text{ cm}^{-1}$  at  $1.57 \text{ }\mu\text{m}$ . The Fabry-Pérot fringes in Fig. 5.28 were less obvious than those in Fig. 5.25–5.27, and thus the error associated with the fitting is larger. The larger absorption coefficient obtained from RIE-processed waveguide structure B may very possibly be due to the additional scattering loss caused by the rough pedestals on both sides of the ridge (cf. Fig. 5.16b). The measurements were mainly limited by the very low ( $<1 \text{ }\mu\text{W}$ ) output power from the waveguides, as a result of low coupling efficiency. Other factors, such as the unfiltered scattered light, imperfect facets, and power instability of the laser source, also contributed to uncertainties in the data.

The measurements indicated large loss (absorption and scattering) in these waveguide structures, which, together with losses due to facet reflections, coupling, and imperfection/damage

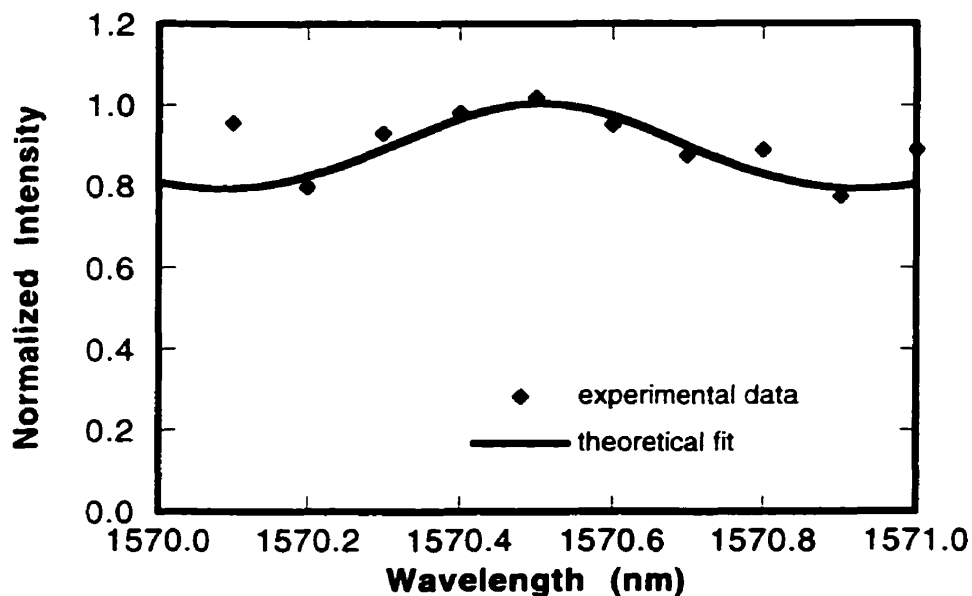


**Figure 5.25** Normalized transmission of TM polarized light through a 3  $\mu\text{m}$ -wide waveguide of structure A (wet-etched) as a function of wavelength. Parameters used for theoretical fitting are  $L=430 \mu\text{m}$ ,  $\gamma=0.45$ . Absorption coefficient obtained from fitting is  $37 \text{ cm}^{-1}$ .

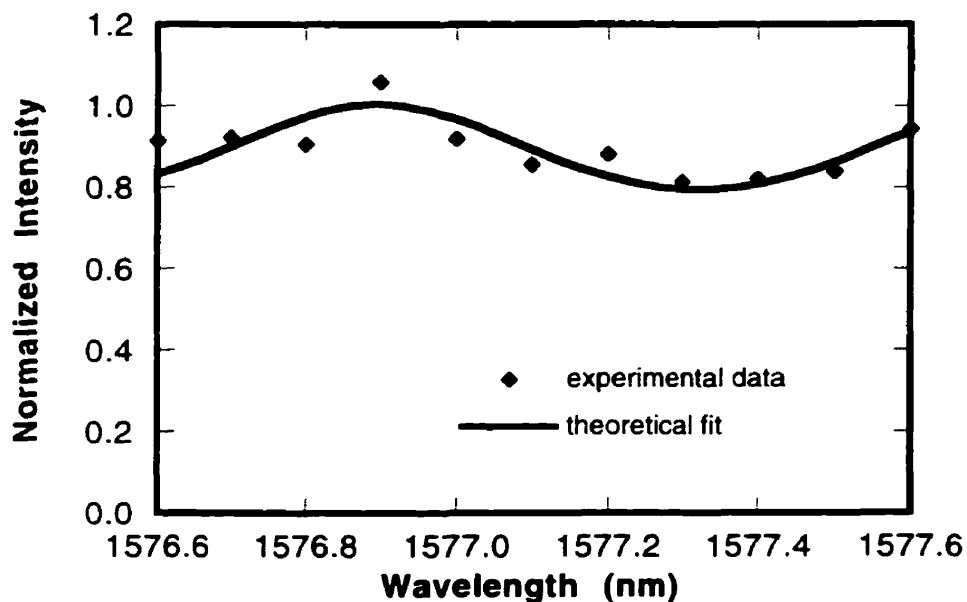


**Figure 5.26** Normalized transmission of TE polarized light through a 3  $\mu\text{m}$ -wide waveguide of structure A (wet-etched) as a function of wavelength. Parameters used for theoretical fitting are  $L=430 \mu\text{m}$ ,  $\gamma=0.45$ . Absorption coefficient obtained from fitting is  $37 \text{ cm}^{-1}$ .

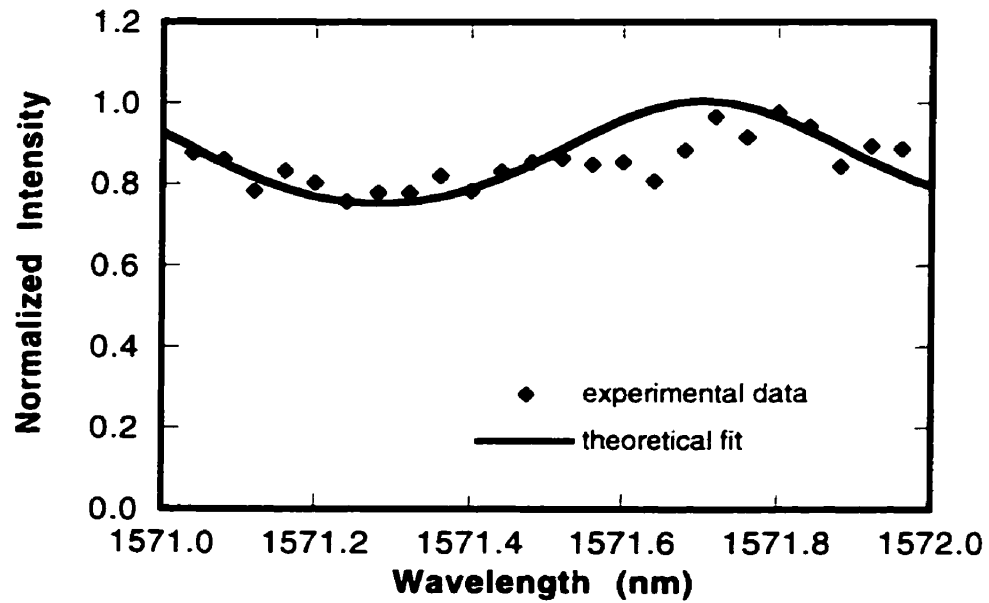


**Figure 5.27** Normalized transmission of TM polarized light through a 6  $\mu\text{m}$ -wide waveguide of structure A (wet etched) as a function of wavelength. Parameters used for theoretical fitting are  $L=430 \mu\text{m}$  and  $\gamma=0.5$ . Absorption coefficient obtained from fitting is  $32 \text{ cm}^{-1}$ .

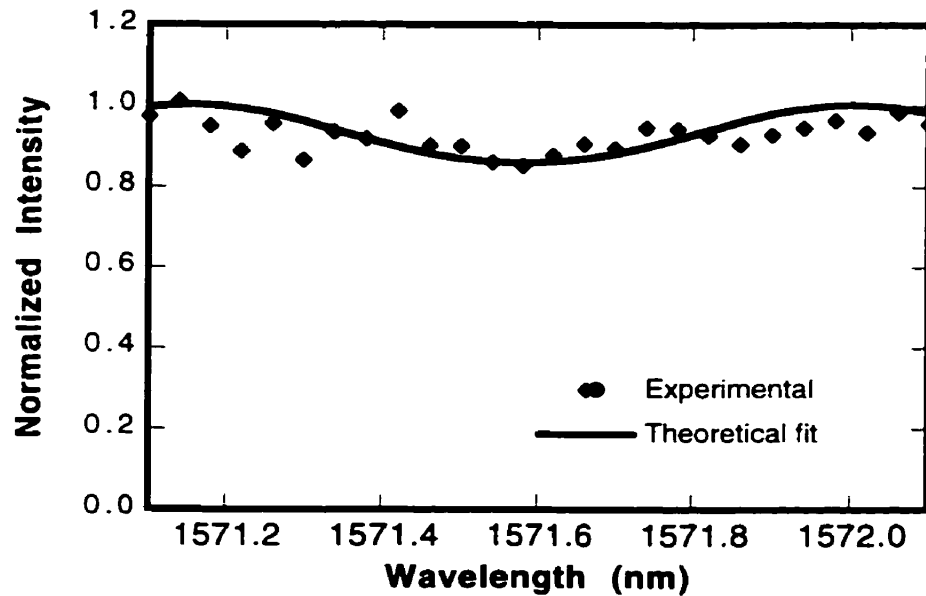


**Figure 5.28** Normalized transmission of TM polarized light through a 5  $\mu\text{m}$ -wide waveguide of structure B (RIE-etched) as a function of wavelength. Parameters used for theoretical fitting are  $L=430 \mu\text{m}$ ,  $\gamma=0.365$ . Absorption coefficient obtained from fitting is  $47 \text{ cm}^{-1}$ .

of the waveguides, resulted in total losses of ~20 dB for structure A and ~24 dB for structure B. Consequently, measurements of absorption coefficients at shorter wavelengths were not attempted, due to the expected higher losses, which would result in an even smaller modulation depth of the fringes. Measurements at longer wavelengths were not possible due to the tuning range limitation of laser sources available to us. Be-doped HELP InGaAsP has a higher band-tail absorption than undoped material, and it is therefore less suitable for waveguide devices, and thus not studied here.

### 5.1.3 Possible problems in the practical implementation of NLDC devices

Experimental results lead us to the conclusion that HELP-InGaAsP-based NLDCs with small, closely-spaced waveguides require relatively low switching energies (40–100 pJ). Moreover, according to measurements described previously (sections 4.4 and 5.1.2), switching times of tens of picoseconds and absorption losses of 4–8 dB for coupler lengths of 250–500  $\mu\text{m}$  could be achieved with such devices<sup>1</sup>. All these parameters fall within practical system tolerance, but the practical implementation of NLDCs has three major challenges to overcome.

- (1) Large coupling losses. It is evident from our single waveguide experiments that coupling from fiber to waveguide and vice versa can result in high loss. The estimated one-end coupling loss in our experiments is about 6–8dB, which is similar to those reported for most waveguide devices [51, 68, 70]. However, coupling loss has much more serious consequences in passive all-optical NLDC devices than in other waveguide devices (e.g., active devices, electro-optical devices), because it not only causes a low throughput for the data pulses, but also reduces the control pulse energy into the waveguide. As a result, higher switching energy is required to compensate for coupling losses, which imposes higher system requirements and increases the probability of optical damage to waveguide facets.

---

<sup>1</sup> Although these values are higher than those obtained in other devices, e.g. active semiconductor devices or fibre-based devices, other factors render the implementation of NLDCs desirable, if possible. For a detailed discussion, see Chapter 2.

Large coupling loss is mainly due to the difference in spot sizes of the fiber mode and the waveguide mode. Even with tapered fiber, the coupling efficiency is still low because a waveguide mode is typically elongated, making mode matching difficult. One solution for this problem is to use a InGaAsP-InP based “spotsize converter” [198], which utilizes tapered waveguide technology. Though promising, this technology is still in the experimental stage, and the reduction in coupling loss demonstrated is only ~1 dB.

- (2) Low contrast ratios. Here the contrast ratio refers to the ratio of output power of the two waveguides, and since NLDC devices operate in both linear (low power) and nonlinear (high power) regimes, there are also two contrast ratios. Experimentally obtained linear-regime contrast ratios reported in the literature are typically ~10 dB for submillimeter NLDCs [67–70, 199], although higher contrast ratios (18 dB) have been reported for other types of compact waveguide couplers [200]. The nonlinear-regime contrast ratio, sometimes called the switching fraction, is poor (a few dBs at best) for almost all demonstrated NLDCs [64–72].

The linear-regime contrast ratio is limited by the accuracy of device fabrication. The coupling length of an actual device is usually different from the theoretically calculated value due to discrepancy between actual and designed coupler geometry. Optimizing device length by trial-and-error method is usually difficult and impractical. Furthermore, polarization-dependent coupling length excludes the possibility of optimizing contrast ratios for both polarizations.

The main cause of the low nonlinear-regime contrast ratio is pulse breakup—the wings of the pulse experience low nonlinearity and are coupled to the adjacent waveguide while the centre of the pulse remains in the original waveguide. Pulse breakup is avoided either by using wider control pulses (several times wider than data pulses), or by employing a walk-through scheme [80]. The former significantly increases the switching energy, whereas the latter cannot be implemented over a short coupler length.

- (3) Control pulse pre-absorption. Because it is difficult to couple light into just one of the waveguides when the guides are very closely spaced, practical implementation of a NLDC device will require the two guides be branched away from each other at the two ends of the coupler (as illustrated in Figure 5.29). However, since control pulses are at

a more absorbing wavelength, long waveguide branches can lead to a large absorption of the control pulse before it reaches the coupler (pre-absorption). To avoid pre-absorption, a material of different composition, with lower absorption at the control wavelength, must be used as guiding material for the branches. It is still a challenge to fabricate waveguides of different compositions on the same plane. While research on quantum well intermixing [201–203] and selective area epitaxial growth [204–206] has shown some promise in this direction, this problem still remains to be fully addressed.

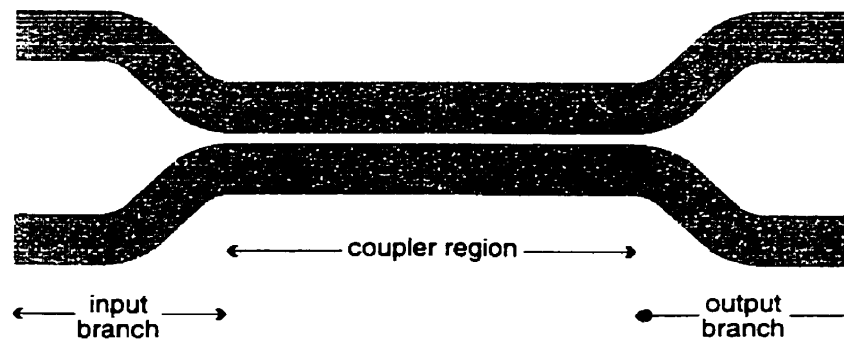


**Figure 5.29** NLDCs with input and output waveguide branches to facilitate coupling light into and out of individual waveguides.

In addition, passive NLDCs also suffer from high absorption loss. A major attraction of the NLDC configuration is that it offers add/drop, as well as signal routing capability. Therefore, theoretically, cascading NLDCs, which can be integrated on a semiconductor substrate, could enable complex signal processing tasks. However, high absorption loss (typically around 5dB for passive NLDCs), prohibits the cascading of a large number of NLDCs. The inherent absorption of passive NLDCs is due to the inevitable association of nonlinear index change with absorption/gain change. Gain being absent in passive devices, absorption becomes unavoidable.

Because of the practical difficulties and limitations of passive NLDCs, we did not conduct further experimental research on these devices. Since limitations such as coupling loss and high switching energy are common to passive, all-optical, semiconductor waveguide devices, it became clear that if we wanted to demonstrate a switching device that meets practical system requirements, we need to adopt a device configuration other than waveguides.

## 5.2 ASYMMETRIC FABRY-PÉROT DEVICE

Optical switching with asymmetric Fabry-Pérot (AFP) devices (cf. Chapter 2) is based mainly on nonlinear absorption, rather than on nonlinear index change, and it is carried out in a vertical layered structure, rather than in a waveguide, thus eliminating coupling loss and polarization dependence. Because large changes in absorption coefficient—on the order of thousands per centimeter—can be obtained in the band edge region of a semiconductor, AFP devices can be made very small, hence requiring a very low switching energy. Moreover, high contrast ratio can be easily achieved in an AFP device, because layer thicknesses can be precisely controlled during device fabrication to cancel out (by interference) unwanted signals.

In addition, the AFP device configuration is more suitable than the NLDC configuration for devices employing HELP InGaAsP materials, because (a) the operation wavelength is above band, where faster material response time is observed, rather than at band tail, and (b) Be doping can be applied to further reduce switching time, while the device performance is not limited by the increased band tail absorption due to Be doping.

The all-optical AFP configuration was first explored by Takahashi et al. [22] who used InGaAs/InAlAs quantum wells (QW) as the active layer, where switching was achieved by the saturation of exciton absorption. Although the enhanced excitonic nonlinearities in QW materials can be utilized for efficient switching, bulk HELP-InGaAsP-based AFPs have several advantages over QW-based devices: (a) bulk materials have inherently large operation bandwidths compared to the narrow exciton bandwidths of quantum well materials; (b) the control wavelength for bulk-material-based devices is not restricted to the excitonic wavelength region, allowing efficient absorption of the control pulse and easy separation of the control from the signal after switching; and, (c) the fabrication process of bulk HELP-InGaAsP-based devices is simpler and more reliable than that of the low-temperature-grown strained-QW devices used by Takahashi et al..

### 5.2.1 Theoretical considerations

#### 5.2.1.1 DEVICE CONFIGURATION AND PRINCIPLE OF OPERATION

AFP devices consist of an active nonlinear absorption layer sandwiched in between a low-reflection front layer and a high-reflection back mirror (Fig. 5.30). The control pulse is usually set at a

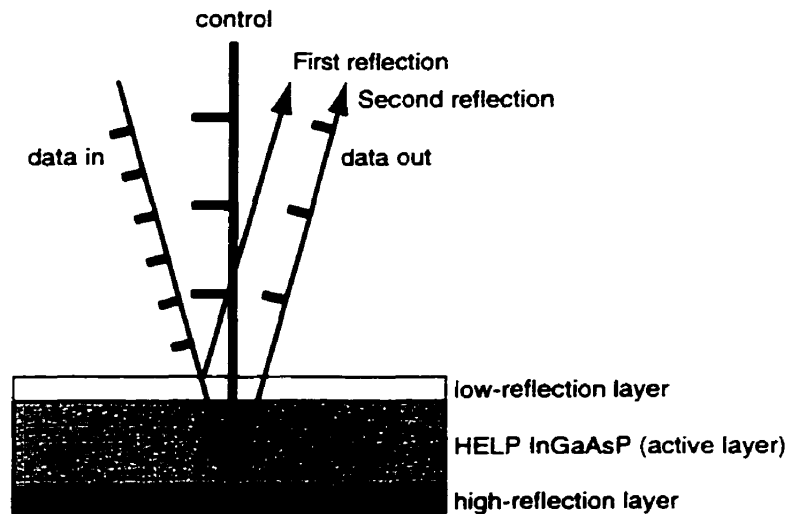


**Figure 5.30** All-optical asymmetric Fabry-Pérot switching device configuration using HELP InGaAsP as active medium. For clarity, the data beams shown are not normal to the device, but normal incidence is used in actual implementation to ensure polarization-independent switching.

highly absorbing wavelength above the band; the data pulse is set at the wavelength region where absorption saturation is highest, which is usually just above the band edge (Fig. 5.31). When the control pulse is absent, data pulses experience large absorption losses at the active layer, hence the second reflected wave (reflected by the back mirror), after going through the active layer twice, has the same intensity (by design) as the first reflected wave (reflected by the front layer) (Fig. 5.30). The thickness of the active layer and the reflectivities of the front and back layers are

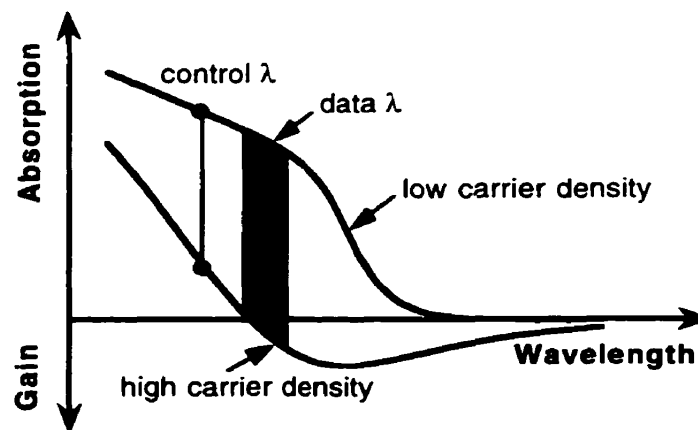


**Figure 5.31** Absorption spectra of InGaAsP at low and high carrier densities, with relation to control and data wavelengths.

designed to put the two reflected waves  $\pi$  out of phase, leading to their complete cancellation, and resulting in zero total reflection at the wavelength of interest. (Due to the large absorption of the active layer, and due to the low reflectivity of the front surface, other multiple reflections can be neglected). When an intense control pulse is applied, it saturates the absorption of the active layer (and it may even provide gain at the data wavelength, cf. Fig. 5.31), resulting in a much more intense reflection from the back mirror. In addition, the phase of this reflected wave is modified by induced index change in the active layer. Consequently, the first and second reflections are no longer completely out of phase, and one is much more intense than the other, resulting in data pulses being reflected with small loss, or even with gain (cf. Fig. 5.30).

### 5.2.1.2 DEVICE MODELLING

We developed a simulation program (FD) to calculate the reflection (throughput) of the device as a function of data wavelength over a specified time period, during which a user-defined control pulse induces nonlinear absorption and index changes in the device. The program simulates the device behaviour in steps of small time intervals, which correspond to the light propagation time in the active layer. At each time interval, the program calculates the overall reflectivities over a range of data wavelengths, taking into account of the multiple reflections from the front and back surfaces, the carrier-density-dependent index and absorption changes, and the carrier recombination over the time interval. An example of the simulation results is given in Fig. 5.32.

The carrier-density-dependent absorption and index changes of the active layer were calculated with the Bányai-Koch model (cf. Section 5.1.1.2), assuming nonlinear absorption and refractive index were similar to those of standard InGaAsP material. However, this assumption is expected to result in an overestimation of the nonlinearity in Be-doped HELP InGaAsP, because (1) defects in the material may cause some degradation in nonlinearity not accounted for in the model; and (2) the Bányai-Koch model assumes quasi-steady-state carrier densities, and this assumption becomes less applicable when material response time is similar to, or shorter than, the excitation pulse width, as is the case for Be-doped HELP InGaAsP materials. Nonetheless, the simulation program FD, incorporating the Bányai-Koch model for calculation of the carrier-density-dependent index and absorption changes, offers a qualitative description of the effects of various

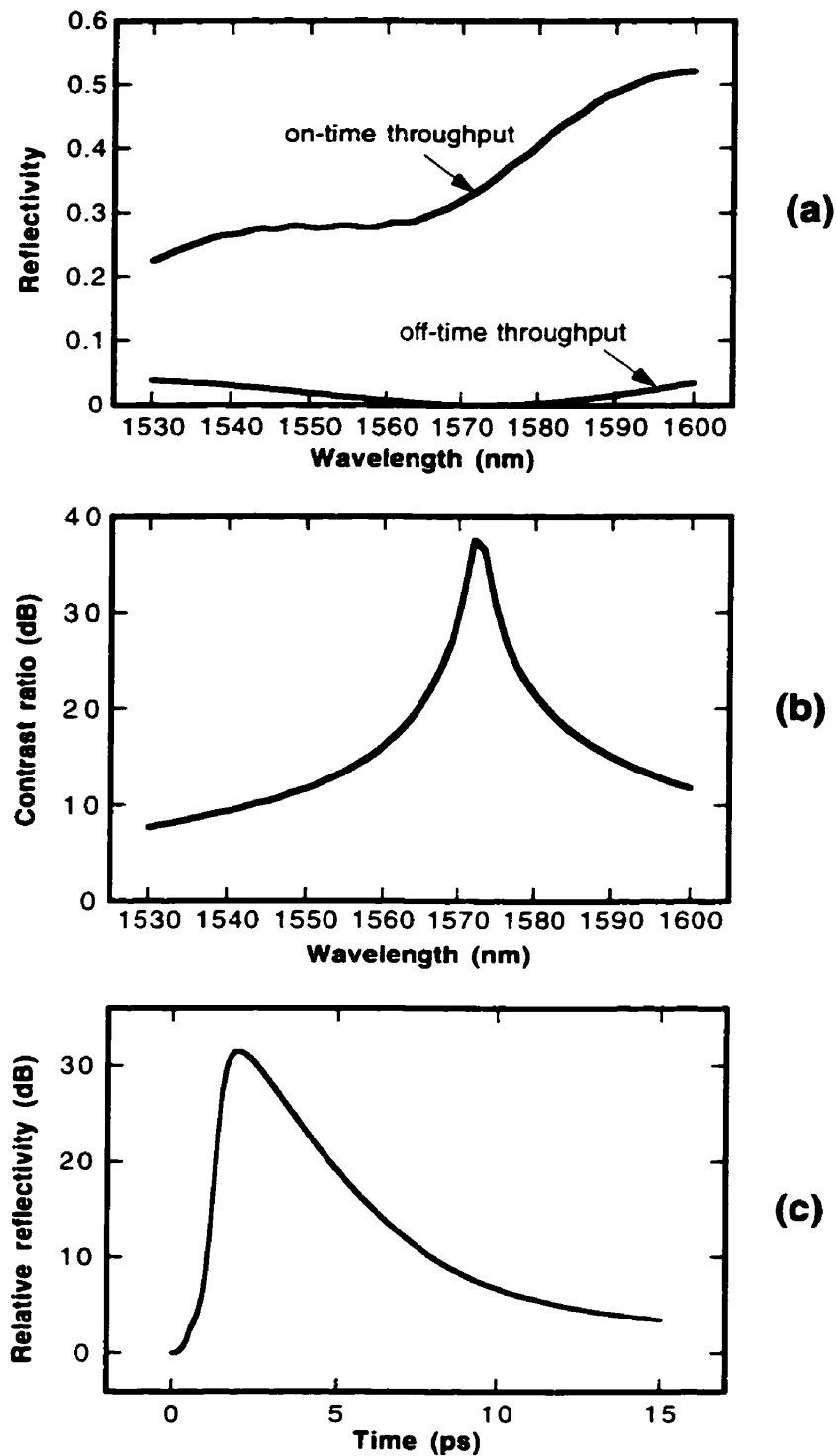


**Figure 5.32** Simulation results of an AFP device. Parameters used in simulation: Front layer = SiON, thickness = 241 nm,  $n = 1.73$ ; Active layer =  $\text{In}_{0.55}\text{Ga}_{0.45}\text{As}_{0.96}\text{P}_{0.04}$ , thickness = 3.13  $\mu\text{m}$ , carrier lifetime = 3 ps; Back mirror = 12 pairs of  $\lambda/4$   $\text{In}_{0.67}\text{Ga}_{0.33}\text{As}_{0.7}\text{P}_{0.3}$ /InP; Control pulse = 1 ps Gaussian pulse at 1520 nm, peak intensity = 0.2  $\text{GW}/\text{cm}^2$ . **(a)** Off-time and on-time throughput. **(b)** Contrast ratio. **(c)** Switching window (relative reflectivity as a function of time).

design parameters on device performance, and it can therefore be used to assist device design. However, the performance of the device should be evaluated experimentally.

### 5.2.1.3 DESIGN PARAMETERS

Device parameters for our prototype devices include front and back reflections, and the thickness, composition and doping concentration of the active layer. Device parameter values have to be set to yield optimal performance parameters (contrast ratio, bandwidth, throughput, switching energy and switching time). Not all performance parameters can be optimized simultaneously, and compromises have to be made between them, on the basis of device simulation and of experimental trials.

#### *Contrast ratio, bandwidth, throughput*

For bulk-material-based devices, the operation bandwidth is dictated mainly by the bandwidth over which the off-time reflectivity is low. When the control pulse is absent, the device is a low finesse Fabry-Pérot structure. By lowering the finesse of the structure (i.e. lowering the reflectivities of the front and back layers, and increasing the absorption of the active layer), it is possible to obtain larger bandwidth—at the cost of reduced on-time throughput. For example, a combination of 4% front layer reflection, 2.5  $\mu\text{m}$  of active layer, and 70% back reflection produces the off-time throughput, the on-time throughput, and contrast ratio spectra as shown in Figure 5.33a. By reducing the reflections of the front and back layer to 0.3% and 20%, respectively, and accordingly increasing the active layer thickness to 4.03  $\mu\text{m}$ , one can improve the bandwidth and the contrast ratio (Fig. 5.33b right). However, the on-time throughput is reduced significantly as a result (Fig. 5.33b left). Alternatively, one can sacrifice the peak contrast ratio to improve the overall contrast ratio over a large bandwidth and achieve significantly more throughput, as illustrated in Fig. 5.33c. The drawback here is that a thicker active layer has to be used, and the thickness is limited by the growth method.

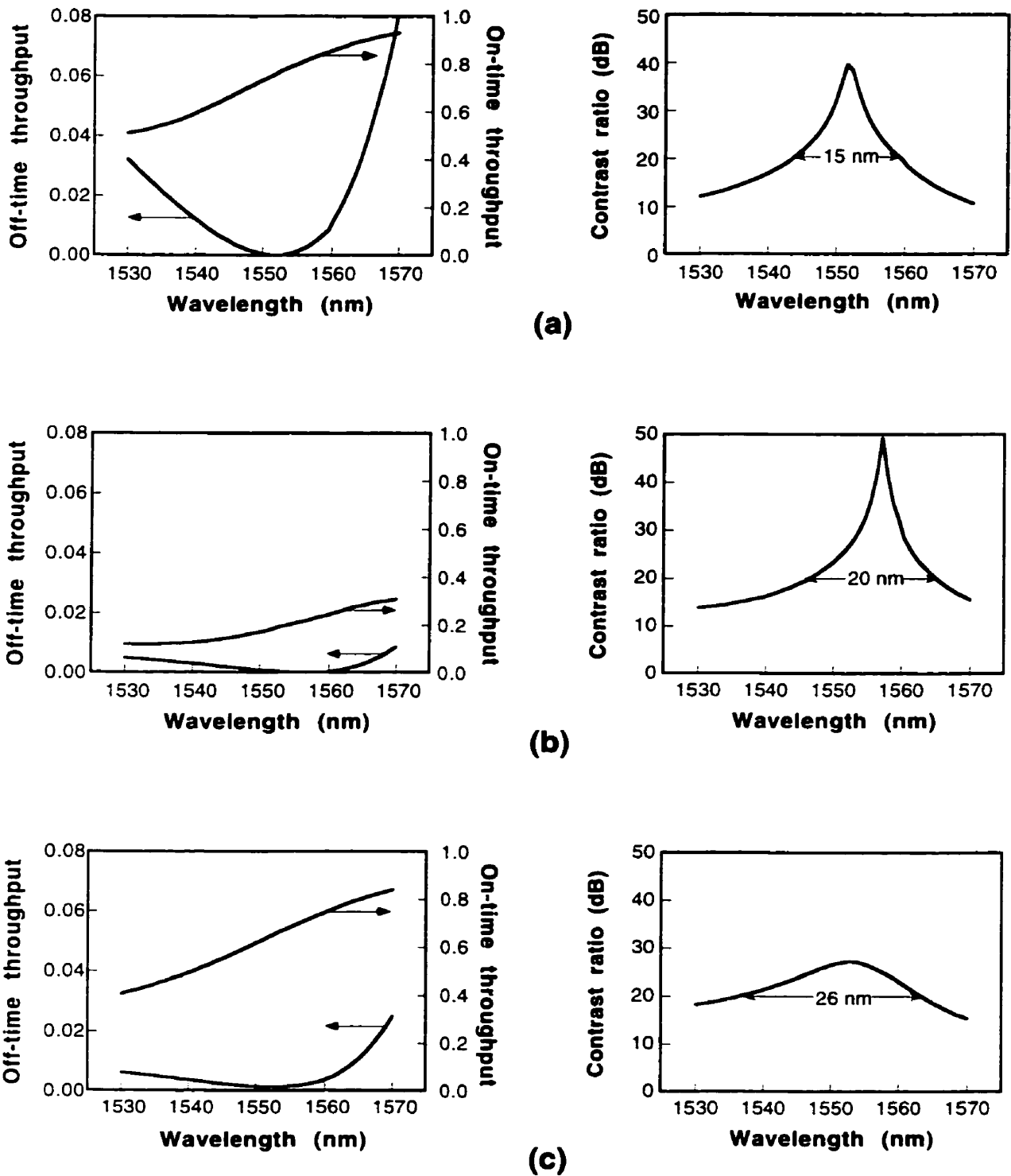


**Figure 5.33** Simulation results for off-time and on-time throughputs and contrast ratio spectra of three AFP devices with different parameters. **(a)** Front reflection = 4%, back reflection = 70%, thickness of active layer = 2.5  $\mu\text{m}$ , Finesse=0.72 **(b)** Front reflection = 0.3%, back reflection = 20%, thickness of active layer = 4.03  $\mu\text{m}$ , Finesse=0.18 **(c)** Front reflection = 0.3%, back reflection = 60%, thickness of active layer = 4.25  $\mu\text{m}$ , Finesse=0.22. Switching energy is the same for all three cases.

### *Control pulse shape, switching gate and switching energy*

The control pulse “opens” the switching gate by creating sufficient carriers to saturate the absorption, and it holds the gate open by compensating for carriers lost in the recombination process. For a specified switching gate and material response time, the temporal shape of the control pulse can be tailored to minimize switching energy. If the control pulse has the same rise time as the gate, a certain minimum peak power is required to open the gate, but, if the control pulse rise time is slower, a higher peak power is necessary, in order to generate sufficient carriers to open the gate within the rise time. To maintain the gate open, the control pulse has to generate enough carriers to compensate for recombined carriers. Since the power required to open the gate and that to keep the gate open are not necessarily the same, the former being much higher than the latter in most cases, the switching energy can be lowered by using a tailored pulse shape with a high-power leading edge, and a low-power tail.

For example, simulation results (by program FD) show that, in order to obtain a >20 dB contrast ratio for 5 ps in an active layer with a 5 ps carrier lifetime, one could use (1) a Gaussian pulse of 1 ps (FWHM) with a peak intensity of 0.6 GW/cm<sup>2</sup>, totalling 3.2 pJ/μm<sup>2</sup> (Fig. 5.34a, left), or (2) a trapezoid-shaped pulse with peak intensity of 0.08 GW/cm<sup>2</sup> totalling 1.4 pJ/μm<sup>2</sup> (Fig. 5.34b, left), or (3) a specific tailored pulse shape (Figure 5.34c, left) totaling 0.6 pJ/μm<sup>2</sup>. The much reduced switching energy, in addition to relaxing amplifier requirements, also leads to shorter switching times, due to reduced optical response times of HELP InGaAsP at lower carrier densities (cf. Section 4.3.4).

Control pulse shaping can also offer a more uniform on-time reflectivity. In the case of a Gaussian pulse or of a trapezoid-shaped pulse, the contrast ratio varies significantly with time (Fig. 5.34a and 5.34b, right). Therefore, any time jitter in the data pulses will translate into power variation. A tailored pulse shape can generate a flat-top time-gate (Fig. 5.34c, right), which may be more desirable.

The fall time of the switching gate is limited by the longer of two factors—control pulse fall time and the material response time. Material response time is usually the more limiting. Therefore, a shorter gate fall time requires a faster carrier recombination, which means higher switching energy.

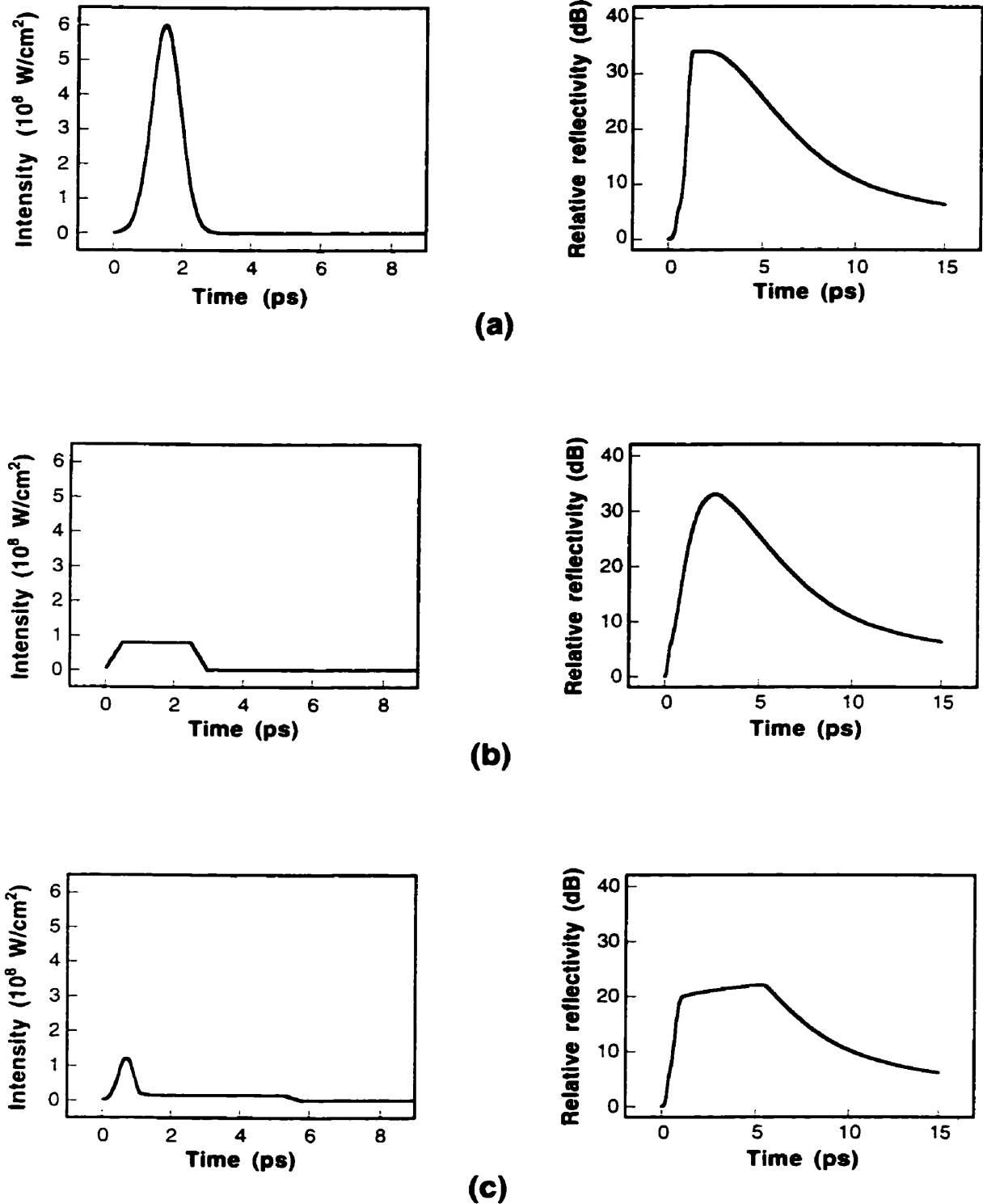


**Figure 5.34** Simulations of switching windows produced by three different control pulse shapes, assuming a 5 ps carrier lifetime. Control pulses are at left, resulting windows at right. **(a)** Gaussian pulse. **(b)** Trapezoidal pulse. **(c)** Tailored-shape pulse. All three pulses yield a >20 dB contrast ratio for 5 ps, but the switching energy of (a) is 5x that of (c).

## 5.2.2 AFP device prototypes based on Be-doped HELP InGaAsP

To demonstrate that a HELP InGaAsP-based AFP device constitutes a viable switching device, with the potential to perform all-optical demultiplexing of high-speed data signals, we designed, fabricated, and characterized three device prototypes with Be-doped HELP InGaAsP as the active layer.

### 5.2.2.1 DEVICE STRUCTURE AND FABRICATION

We used Be-doped HELP InGaAsP for the active layer, because Be doping significantly reduces the material response time (cf. Section 4.3.1), although higher switching energy and lower throughput was anticipated due to the shorter response time. We experimented with devices of different doping concentrations to determine the best compromise between switching time and throughput.

The simplest choice for the low-reflection layer was a single layer of SiON. The refractive index of SiON varies from 1.46 to 1.92, as a function of the relative content of oxygen and nitrogen. The index range of the SiON made it possible for us to design on top of the InGaAsP layers low-reflection layers with reflectivity ranging from zero to a few percent, as desired.

Several methods could have been used to produce the high-reflection layer, including gold coating, dielectric stacks (quarter-wave silicon oxide/silicon nitride pairs), and semiconductor stacks (quarter-wave InGaAsP/InP pairs). Gold coating, a relatively simple process, was not suitable for providing the relatively low back reflectivity (~60%) indicated as desirable by our simulation (Fig. 5.33c), because the gold layer would have been too thin to be controlled accurately.

Using dielectric stacks as back mirror would have involved growing the dielectric stacks, bonding them to InGaAsP, and then etching away the InP substrate, a process during which the dielectric stacks would have been subjected to an acidic environment at elevated temperatures. A sample thus fabricated showed defects in the dielectric stack layers, and cleaving it caused rapid spread of the defects to the entire surface of the sample [207].

The most reliable way of producing the high-reflection layer was growing quarter-wave InGaAsP/InP stacks. It is usually considered disadvantageous to use InGaAsP/InP stacks, because, due to the small index difference between InGaAsP and InP, a large number of stack layers have to be grown to provide high reflectivity. However, because our design required only ~60% back reflectivity, therefore only ~12 pairs of InGaAsP/InP layers were needed, which was well within the limit of the MBE process.

The final device structure (Fig. 5.35) has the following and device parameters:

- low-reflection dielectric layer (SiON):  
thickness:  $t_{\text{SiON}}$   
index:  $n_{\text{SiON}}$
- active layer (Be-doped HELP  $\text{In}_{1-x}\text{Ga}_x\text{As}_y\text{P}_{1-y}$ ):  
composition:  $y$   
Be doping concentration:  $D_{\text{Be}}$   
thickness:  $t_{\text{active}}$
- high-reflection mirror (quarter wave  $\text{In}_{1-a}\text{Ga}_a\text{As}_b\text{P}_{1-b}$ /InP stacks):  
number of InGaAsP/InP pairs:  $N_{\text{stack}}$   
composition of InGaAsP:  $b$

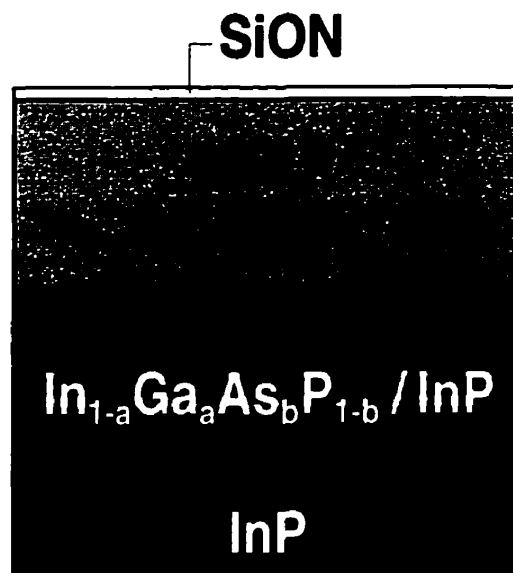


**Figure 5.35** Asymmetric Fabry-Pérot (AFP) device structure adopted in this work.

### 5.2.2.2 DEVICE CHARACTERIZATION METHODS

#### *Low-intensity reflection spectrum*

Measurement of the low-intensity reflection spectrum of the device is useful in three ways: (1) it examines how well-matched the reflections from the two surfaces are; (2) it determines the wavelength region where the reflection is low enough for operation; and (3) performed on an unfinished structure without the front layer, it can be used to redesign the dielectric layer to compensate for the small mismatch between the actual and designed active layer thickness. The low-intensity reflection spectrum was measured with the tunable INTUN 1500 laser (Fig. 5.36). To calibrate the output power of the INTUN, a reference scan is obtained by placing a high-reflection mirror in the position of the sample.

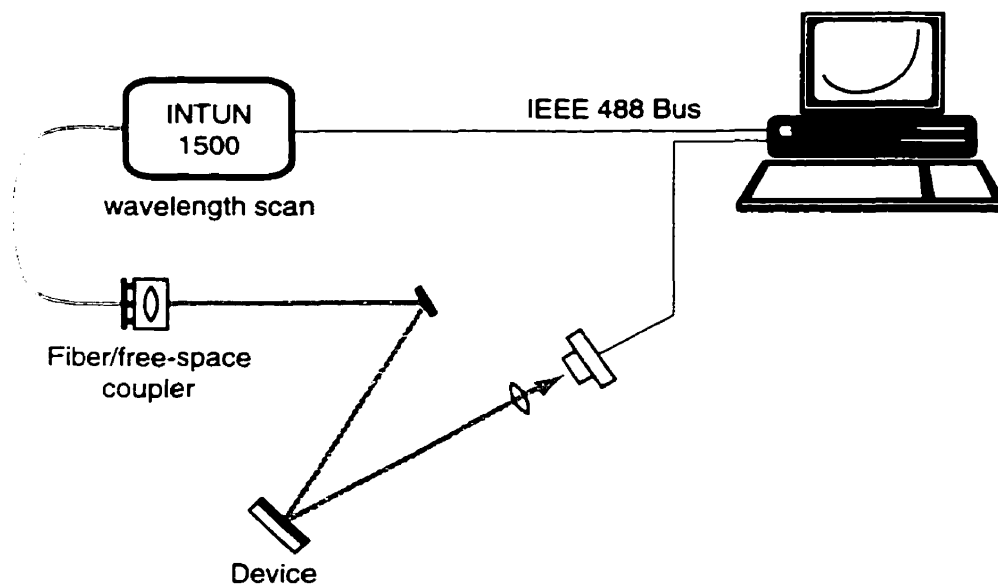


**Figure 5.36** Experimental setup for measuring the low-intensity reflection spectra of our AFP devices.

#### *Measurements on switching time, contrast, and throughput*

We characterized our three AFP devices with a dual-wavelength Optical Parametric Oscillator (OPO) as the source (Fig. 5.37). The OPO's signal output was attenuated and used as data pulses,

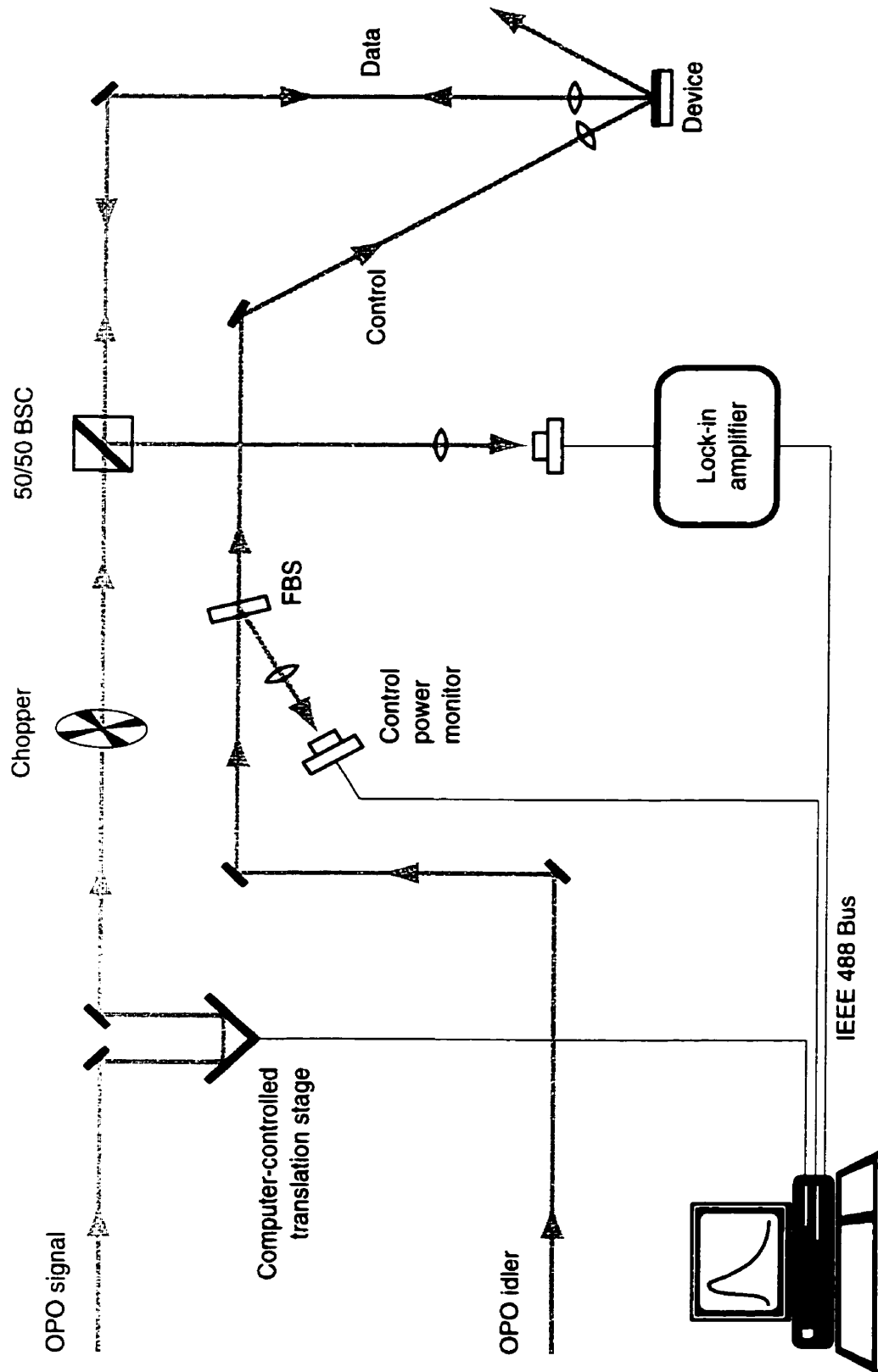


**Figure 5.37** Experimental set up for characterizing AFP device prototypes, using the tunable outputs of the Optical Parametric Oscillator (OPO) as control (pump) and data (probe).

while the idler output was used as control pulses. Both control and data beams were focused onto the same spot, with the data beam normal to the surface of the device for polarization-independent switching. A beam profiler was used in place of the sample to ensure spatial overlap of the two beams and to measure spot sizes. The data beam reflected by the device was separated from the incident probe beam by a 50/50 beam splitter cube, and then lock-in detected.

We determined the switching time and the contrast ratio from the switching window of the device, which we obtained by measuring the variation of the data beam power reflected by the device as a function of delay time between control and data pulses<sup>1</sup>. We calculated the throughput of the device by dividing the peak reflected power obtained from the switching window by the total data power, which was determined by measuring the reflected data power after replacing the device with a high reflection mirror. The switching window measurement was repeated for various data wavelengths, and the bandwidth of the device can be obtained.

Contrast and throughput dependence on data polarization was examined by rotating the data beam polarization with a half-wave plate, inserted in the incident data beam path.

### 5.2.2.3 DEVICE DEMONSTRATION

Three AFP devices were fabricated by Dr. Brad Robinson at McMaster University according to our design. Characterization of these devices is presented below.

#### *First AFP device*

Device parameters for the first AFP device are:

$$t_{\text{SiON}}=208 \text{ nm} \quad n_{\text{SiON}}=1.92 \quad y=0.897 \quad D_{\text{Be}}=1 \times 10^{18} \text{ cm}^{-3} \quad t_{\text{active}}=2.5 \text{ } \mu\text{m} \quad N_{\text{stack}}=13 \quad b=0.7$$

The measured low-intensity reflection spectrum of the first device has the lowest reflectivity at 1495 nm (Fig. 5.38), away from the designed value of 1550 nm. We attribute this shift in wavelength to two factors: (1) large mismatch (0.027 eV or 50 nm) between the actual band gap of the active layer (measured by FTIR spectrometer) and our calculated band gap using an empirical

---

<sup>1</sup> Strictly speaking, this measurement yields the convolution between the switching window and the data pulse shape. Therefore, actual switching windows are narrower than shown by measurements.

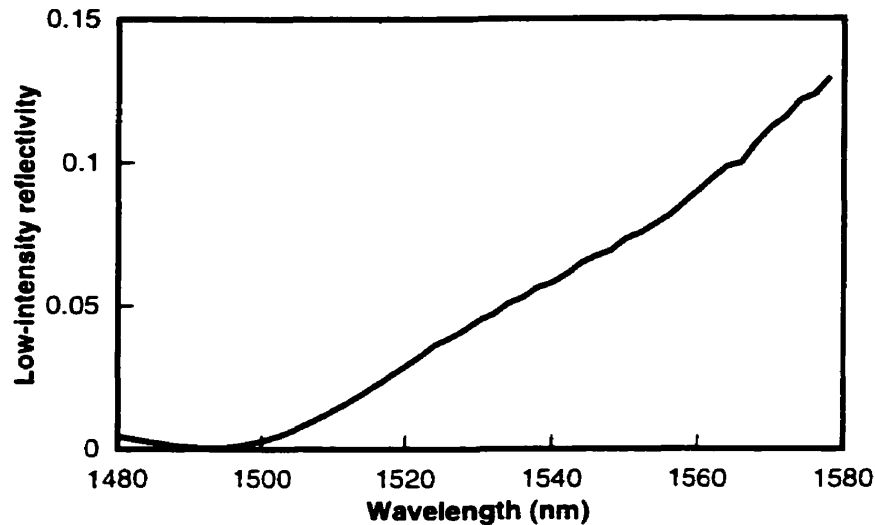


**Figure 5.38** Low-intensity reflection spectrum of the first AFP device.

formula reported by Pearsall [208] (Fig. 5.39); (2) mismatch between the actual thickness of the active layer and the designed value, which can be as large as 2%, and can therefore result in as much as 30 nm shift from the designed wavelength.

The AFP device should have been operated with the control pulse at a shorter wavelength than the data wavelength, however, since the two pulsed outputs from our tunable laser source had tuning ranges of 1460–1640 nm and 1510–1520 nm, while the low-intensity reflection “null”

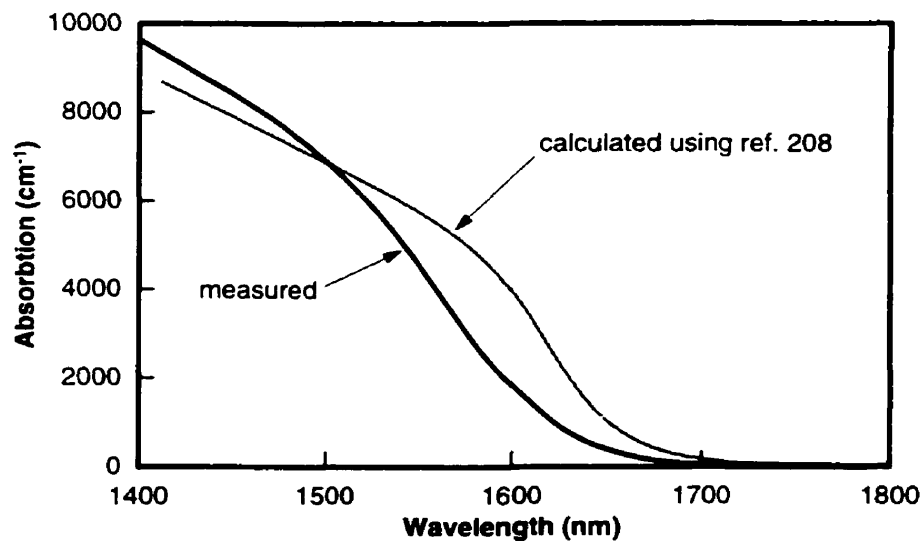


**Figure 5.39** Comparison of the absorption band edge calculated in our simulation with Pearsall's band-gap energy formula [208] with the absorption edge measured by FTIR. The large discrepancy explains the large shift from the wavelength designed for a reflectivity null.

was at 1495 nm, we were forced to use for the control pulses a longer wavelength than for the data pulses. This resulted in inefficient absorption of the control pulse and weak nonlinear absorption at the signal wavelength, leading to reduced contrast ratio and throughput. Notwithstanding, we obtained at 1495 nm a 12 dB contrast ratio with a switching window of 5.5 ps (measured at  $1/e$  of the peak value), but the throughput was only about 6% (Fig. 5.40).

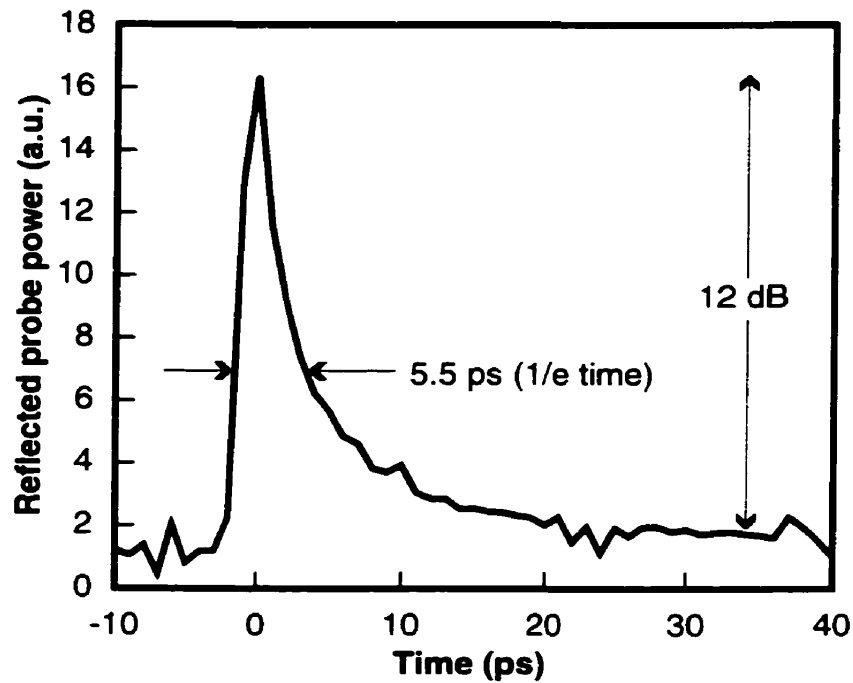


**Figure 5.40** Switching window of the first AFP device at 1495 nm after excitation by a 1.1 ps pump pulse at 1513 nm. Switching energy density is  $0.5 \text{ pJ}/\mu\text{m}^2$ .

Both contrast ratio and switching time are dependent on switching energy—as the switching energy increases, the contrast ratio improves, but the switching time also increases, due to the carrier-trapping bottleneck effect (cf. Section 4.3.4). However, as the characterization of the device reveals (Fig. 5.41), for switching energy density less than  $0.5 \text{ pJ}/\mu\text{m}^2$ , contrast ratio improves significantly with increasing switching energy, while switching time remains short and relatively constant; but for switching energy density greater than  $0.5 \text{ pJ}/\mu\text{m}^2$ , switching time increases drastically with increasing switching energy, while the improvement in contrast ratio is marginal. Therefore, the optimum operating region of this device is around  $0.5 \text{ pJ}/\mu\text{m}^2$  (marked grey in Fig. 5.41).

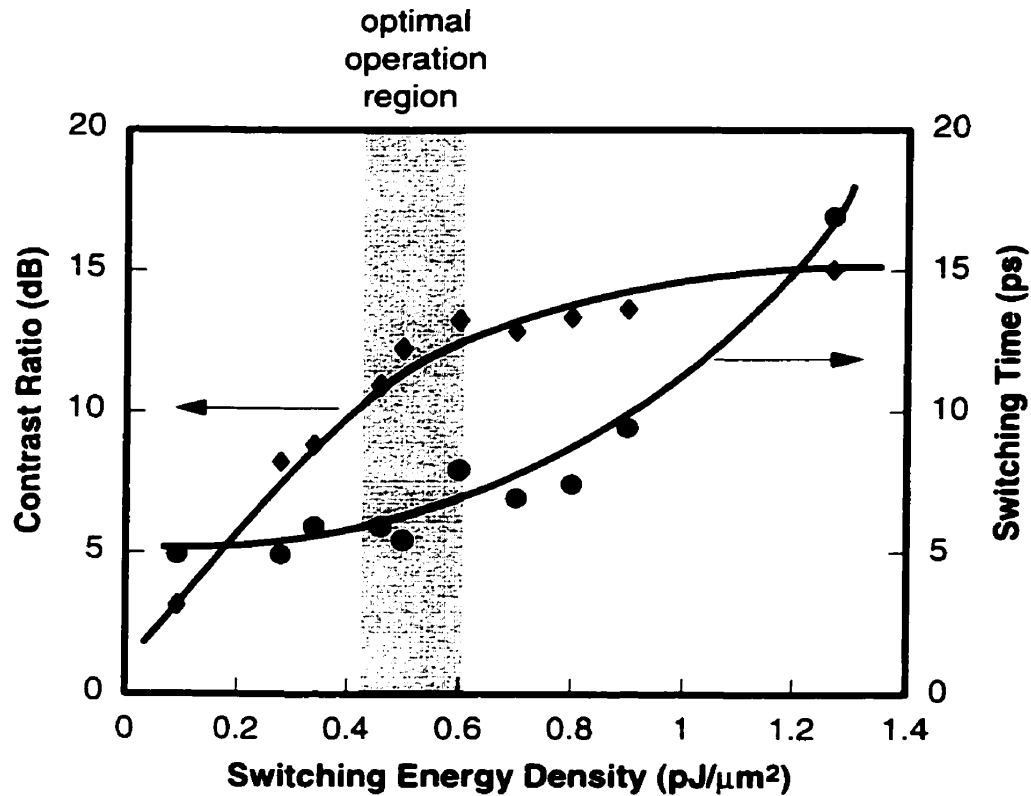


**Figure 5.41** Relationship between contrast ratio, switching energy and switching time. The plot helps to identify an optimal operation region, marked grey. Control wavelength = 1515 nm, data wavelength = 1495 nm.

### *Second AFP device*

The objective of the second device was to achieve faster switching, higher contrast ratio and higher throughput. To obtain faster switching, we increased the Be doping concentration to  $3 \times 10^{18} \text{ cm}^{-3}$ . To improve throughput, it was necessary to fabricate a device operable at a longer wavelength than the OPO idler wavelength (used as control wavelength). To achieve high contrast ratio, we needed to obtain precise matching of the front mirror reflectivity, back mirror reflectivity, and the thickness of the active layer, thereby ensuring the complete cancellation of the front and back reflections by destructive interference at the wavelength of interest.

Therefore, we needed to find means to eliminate or compensate for the two mismatches encountered during the fabrication of the first device (see discussion above). By comparing the measured band-gap energies for a number of InGaAsP samples grown at McMaster University with the band-gap energies calculated by different empirical formulae reported in the literature

[209], we found that the formula provided by Nahory [210] resulted in a better agreement with the measurements than the formula we used previously. We subsequently adopted this formula in our simulation program (FD), and minimized the mismatch between the designed and the actual band gap wavelength of the active layer.

To minimize the effect of mismatch between the front layer reflectivity, back mirror reflectivity, and the thickness of the active layer, we adopted a step-by-step growth and design procedure. We measured the reflection spectrum of the high reflection stack before growing the active layer, and then measured the reflection spectrum of the device before applying the front layer, which allowed us to determine the actual thickness of the active layer, and redesign the front layer to achieve a near complete cancellation of the first and second reflections in the wavelength region of interest.

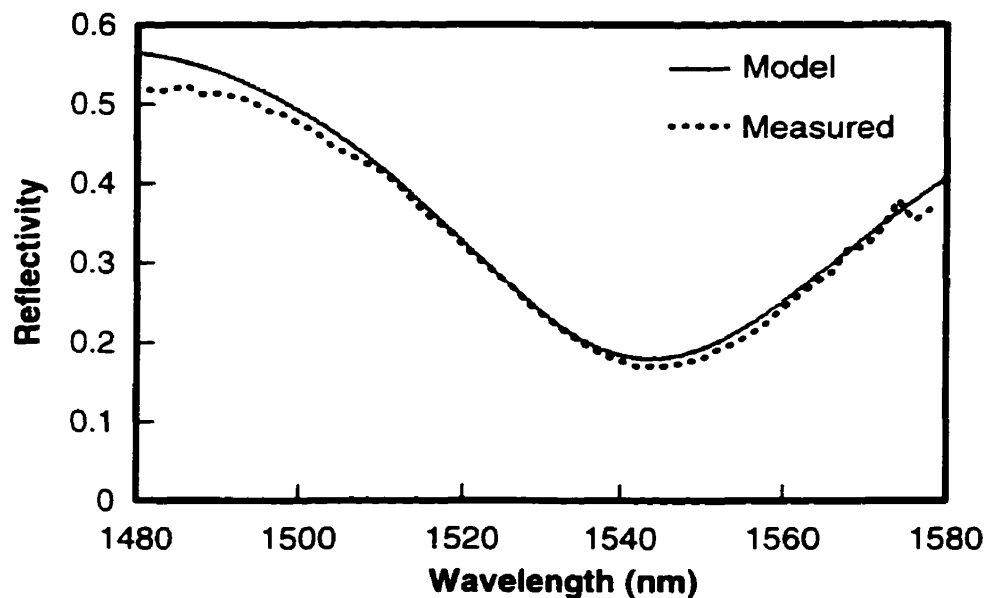


**Figure 5.42** Reflection spectra of the high-reflection stack of the second AFP device. Measured spectrum is dotted, spectrum calculated from the simulation program is solid grey.

The comparison between the measured reflection spectrum of the high-reflection stack and the calculated spectrum shows a close agreement (Fig. 5.42). The measured spectrum of the active layer with the high-reflection stack (Fig. 5.43a) indicated, however, a mismatch between the designed thickness (3.05  $\mu\text{m}$ ) and the actual thickness (3.13  $\mu\text{m}$ ) of the active layer. Therefore, a reflection “null” at 1550 nm as initially designed was not possible. However, our simulation program

(FD) indicated that a near complete cancellation of reflections could still be achieved at 1572 nm with a 241 nm-thick front layer of index 1.73. The low-intensity reflection spectrum of the final device shows a “null” at 1574 nm (Fig. 5.43b), in close agreement with our modified design.

The final device parameters for this second AFP device are summarized here:

$$t_{\text{SiON}}=241 \text{ nm} \quad n_{\text{SiON}}=1.73 \quad y=0.96 \quad D_{\text{Be}}=3 \times 10^{18} \text{ cm}^{-3} \quad t_{\text{active}}=3.13 \text{ } \mu\text{m} \quad N_{\text{stack}}=12 \quad b=0.7$$

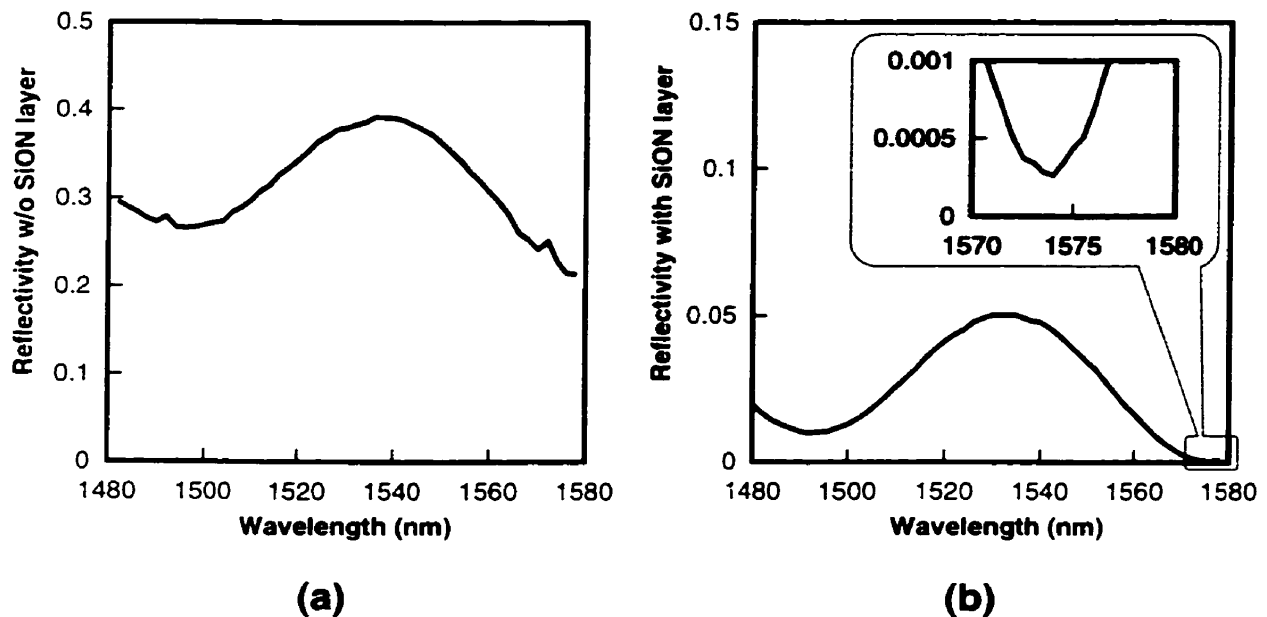


**Figure 5.43** Reflection spectra of the second AFP device. **(a)** Before depositing the low-reflection dielectric layer. **(b)** With the low-reflection layer in place, showing a null at 1574 nm.

The switching window of the device obtained at a switching energy density of  $0.5 \text{ pJ}/\mu\text{m}^2$  at the data wavelength of 1572 nm shows a 5 ps switching time and a 20 dB contrast ratio (Fig. 5.44). The high contrast ratio was expected because of the precise matching between the front layer and the rest of the device, made possible by adopting the step-by-step design procedure. Consequently, this device shows, relative to the first device, a  $>6 \text{ dB}$  improvement in contrast ratio over a large range of switching energy (Fig. 5.45). The contrast ratio of this device improves significantly when the switching energy density is increased from  $0.1 \text{ pJ}/\mu\text{m}^2$  to  $0.5 \text{ pJ}/\mu\text{m}^2$  (Fig. 5.45), which is due to decrease in absorption with increasing carrier density. However, the contrast ratio improves only marginally when switching energy density is increased beyond  $0.5 \text{ pJ}/\mu\text{m}^2$  (Fig. 5.45), mainly because thermal index change destroys the condition for cancellation of the first and second

reflections. Switching time of the device also improves, especially at high switching energy densities (Fig. 5.45), as a result of higher Be doping.

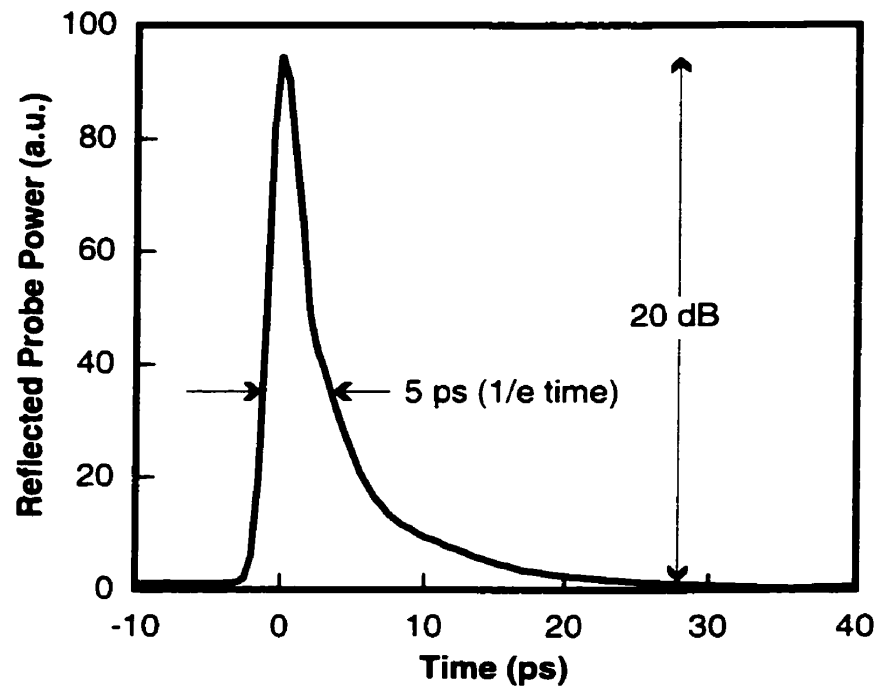


**Figure 5.44** Switching window of the second AFP device at 1572 nm after excitation by a 1.1 ps control pulse at 1519 nm. Switching energy density is  $\sim 0.5 \text{ pJ}/\mu\text{m}^2$ .

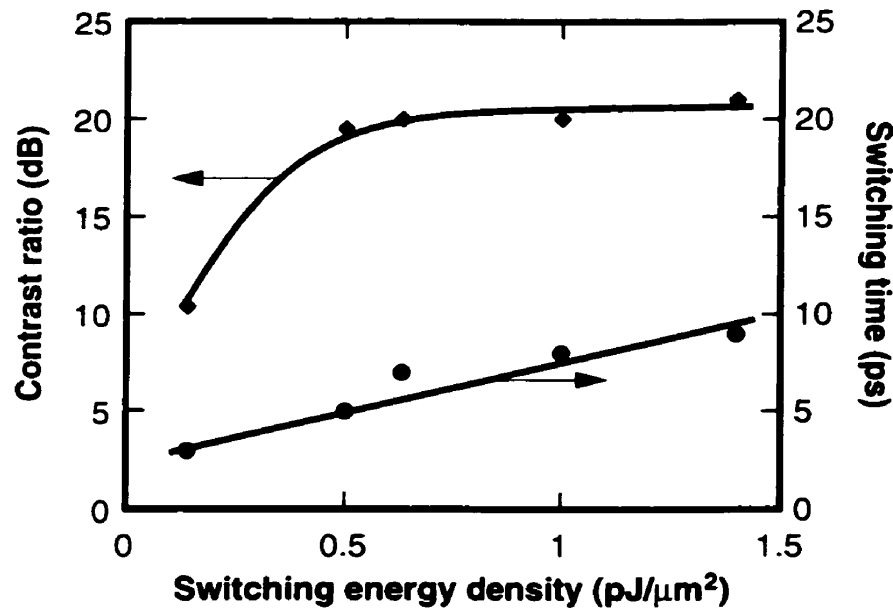


**Figure 5.45** Contrast ratios and switching times of the second AFP device, measured at 1570 nm under various switching energy densities.

Since the switching time does not increase dramatically with increasing switching energy (Fig. 5.45), the device can be operated at higher switching energy to achieve a higher throughput and a significantly larger bandwidth (compare Fig. 5.46 a and 5.46b). The device maintains 10 dB contrast ratio over 24 nm of bandwidth when operated under a switching energy density of  $0.5 \text{ pJ}/\mu\text{m}^2$ , and over 40 nm of bandwidth can be achieved by increasing the switching energy density to  $1.4 \text{ pJ}/\mu\text{m}^2$ .

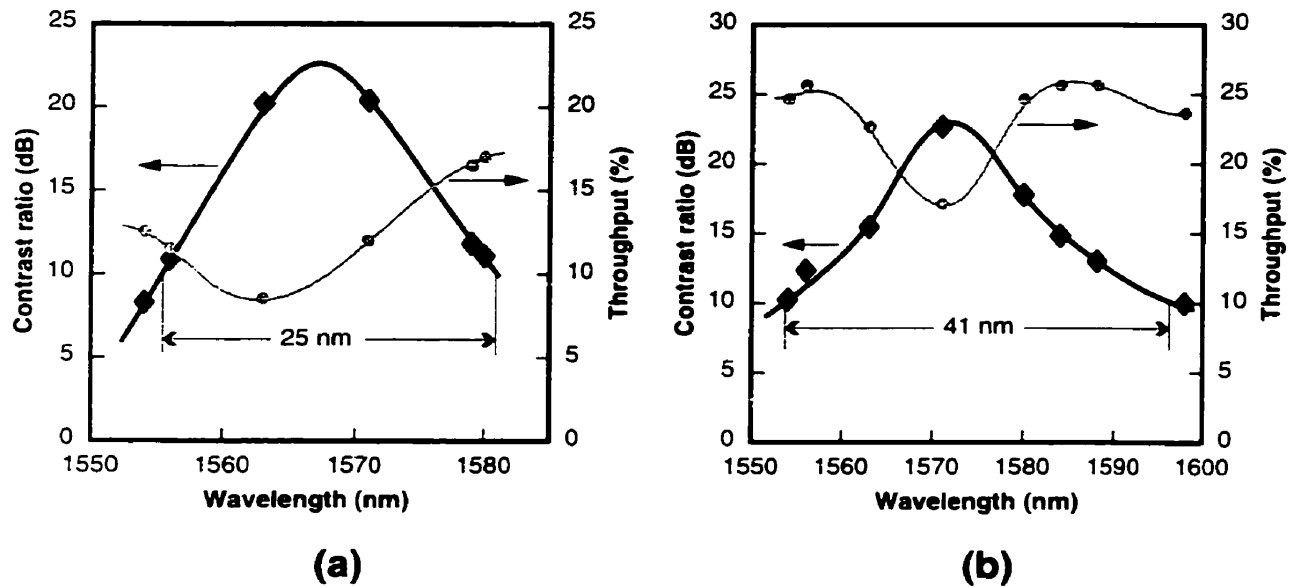


**Figure 5.46** Contrast ratio and throughput obtained from the second AFP device and plotted as functions of wavelength. Control wavelength is  $\sim 1519 \text{ nm}$ . **(a)** Under conditions of low switching energy density ( $0.5 \text{ pJ}/\mu\text{m}^2$ ). **(b)** Under conditions of high switching energy density ( $1.4 \text{ pJ}/\mu\text{m}^2$ ).

### Third AFP device

To further speed up switching, we decided to try a third device with even higher Be doping concentration. After step-by-step design and fabrication procedures, the parameters of the third AFP device are:

$$t_{\text{SiON}}=222 \text{ nm} \quad n_{\text{SiON}}=1.74 \quad y=0.96 \quad D_{\text{Be}}=6 \times 10^{18} \text{ cm}^{-3} \quad t_{\text{active}}=3.48 \text{ } \mu\text{m} \quad N_{\text{stack}}=12 \quad b=0.7$$

The low-intensity reflection spectrum of the device shows a “null” at  $1542 \text{ nm}$  (Fig. 5.47). Device characterization at this wavelength resulted in a  $4 \text{ ps}$  switching window and a  $17 \text{ dB}$  contrast ratio under a switching energy density of  $0.5 \text{ pJ}/\mu\text{m}^2$  (Fig. 5.48a). When the switching energy density is increased to  $1.2 \text{ pJ}/\mu\text{m}^2$ , the switching time increases to  $6.5 \text{ ps}$  (Figure 5.48b).

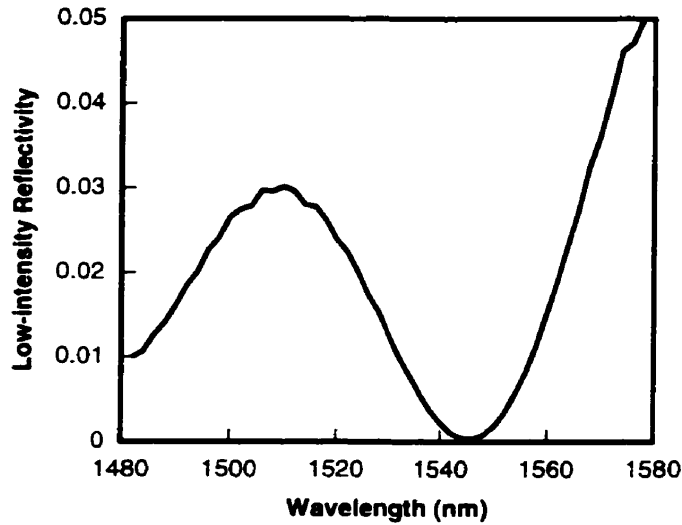


**Figure 5.47** Low-intensity reflection spectrum of the third AFP device.

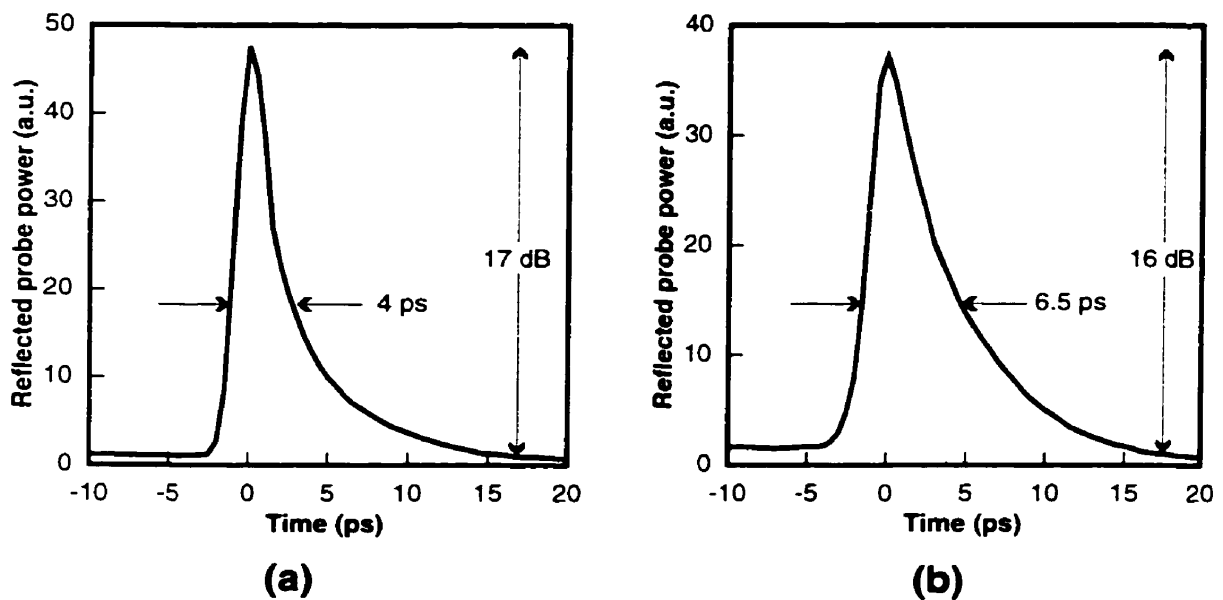


**Figure 5.48** Switching window of the third AFP device at 1542 nm after excitation by a 1.1 ps control pulse at 1515 nm. **(a)** Switching energy density =  $0.5 \text{ pJ}/\mu\text{m}^2$ . **(b)** Switching energy density =  $1.2 \text{ pJ}/\mu\text{m}^2$ .

Although there is improvement in switching speed in the third device, both contrast and throughput are lower than those obtained for the second device. (compare Fig. 5.49 and 5.46). We attribute the degradation in contrast ratio and throughput to reduced absorption saturation caused by heavy doping. Absorption saturation is reduced through two mechanisms: (1) faster carrier

trapping, as a result of increase in empty trap concentration, requires faster pumping (higher pump energy) to maintain the same level of absorption saturation, and conversely, absorption saturation is reduced for the same pump energy; (2) increased absorption associated with band-tail states, due to heavy Be doping, resulting in smearing of the band edge and a reduced absorption saturation.

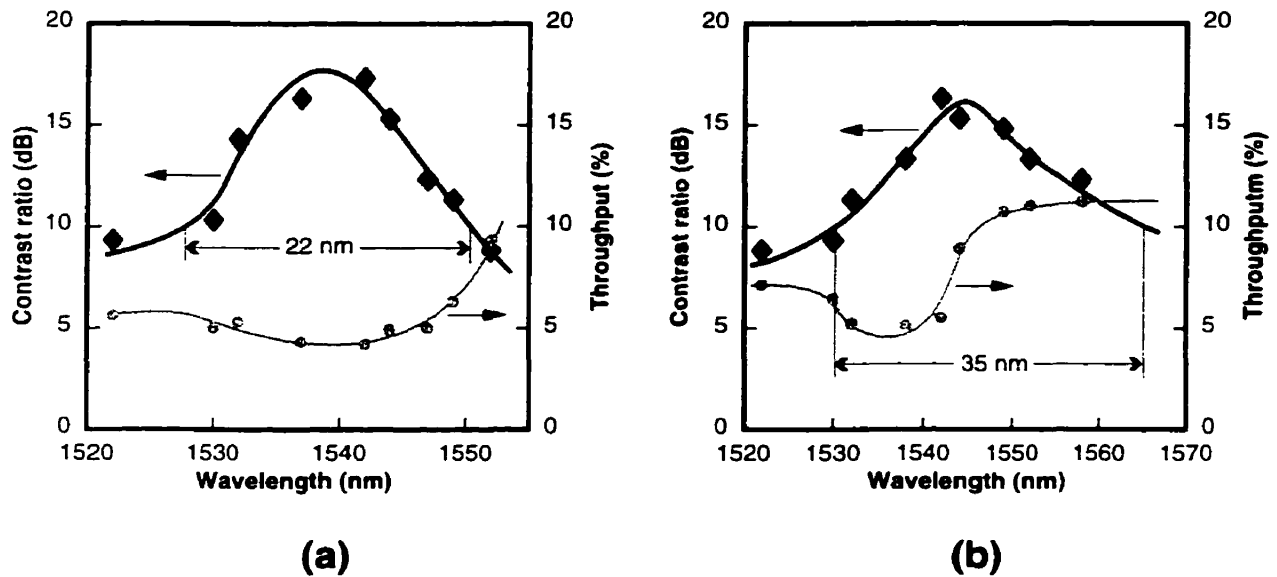


**Figure 5.49** Contrast ratio and throughput obtained from the third AFP device and plotted as functions of wavelength. **(a)** Under conditions of low switching energy density ( $0.5 \mu\text{J}/\mu\text{m}^2$ ). **(b)** Under conditions of high switching energy density ( $1.2 \mu\text{J}/\mu\text{m}^2$ ).

Reduced absorption saturation also causes the thermal effects to appear relatively strong in this device, which can be seen from the slight decrease in peak contrast ratio caused by increasing switching energy (compare Fig. 5.49a and 5.49b). Thermal index and absorption changes destroy the condition for complete cancellation of the reflections, resulting in increased off-time reflection and lowered contrast. Although thermal effects are seemingly adverse effects on the device performance, one can remedy it by determining the “thermal bias” point for normal operation and design the device taking into account the thermal index and absorption changes. Another suggestion to alleviate the thermal problem is to move the beam spot on the device constantly, for example, by spinning the device [211].

### 5.2.2.4 SUMMARY AND DISCUSSION OF DEVICE PERFORMANCE

We consider below, on the basis of the experimental characterization of our prototypes (cf. Table 5.2), the feasibility of using HELP-InGaAsP-based AFP devices in real-world systems.

**Table 5.2 Comparison of device parameters and performances**

	Device #1		Device #2		Device #3	
Important Device Parameters						
Be Doping	$1 \times 10^{18} \text{ cm}^{-3}$		$3 \times 10^{18} \text{ cm}^{-3}$		$6 \times 10^{18} \text{ cm}^{-3}$	
Active layer thickness	2.5 $\mu\text{m}$		3.13 $\mu\text{m}$		3.48 $\mu\text{m}$	
Device Performance						
Switching energy den.	$\sim 0.5 \text{ pJ}/\mu\text{m}^2$	$\sim 1.3 \text{ pJ}/\mu\text{m}^2$	$\sim 0.4 \text{ pJ}/\mu\text{m}^2$	$\sim 1.4 \text{ pJ}/\mu\text{m}^2$	$\sim 0.5 \text{ pJ}/\mu\text{m}^2$	$\sim 1.2 \text{ pJ}/\mu\text{m}^2$
Highest CR	12 dB	16 dB	20 dB	22 dB	17 dB	16 dB
Switching time (1/e)	6 ps	16 ps	5 ps	13 ps	4 ps	8 ps
Throughput	>2%	>3%	>8%	>16%	>3%	>5%
Bandwidth at 10 dB	20 nm	30 nm	25 nm	40 nm	20 nm	35 nm

#### *Switching window*

In all three devices, the observed rise time (10%–90%) of the switching window was around 1.8 ps. This parameter is chiefly limited by the rise time of the pulses used. (Note that the observed switching window is in fact the convolution of the switching window and the temporal shape of the data pulse.) A shorter control pulse rise time should result in a shorter rise time of the switching window.

The fall time of the switching window depends largely on the switching energy and on the doping concentration of the active layer. Our second device, which is considered to have the best overall performance<sup>2</sup>, exhibits a fall time (90%–10%) of 12 ps (Figure 5.44). A shorter fall time (7 ps) is possible under a lower switching energy density (0.1 pJ/μm<sup>2</sup>), but at the expense of reduced contrast (from 20 dB to 10 dB) (first data point on Fig. 5.45).

Therefore, depending on the system's contrast ratio requirement, the second device can be used to demultiplex 40–100 Gbit/s time-division-multiplexed channels.

### *Total insertion loss*

Measured insertion losses for all three devices are lower than 20 dB (a limit for many practical systems), but they are higher than predicted by simulation. This can be attributed mainly to two factors: (1) absorption saturation being less than predicted, because of the existence of a large portion of unsaturable absorption caused by defects not modelled in the program, and (2) data and control pulses having the same temporal width, causing the wings of the data pulses experience unsaturated absorption, which lowers the overall throughput.

The second device exhibits the highest throughput (more than 8% over the entire bandwidth under low switching energy operation), i.e. its maximum insertion loss was 11 dB. With proper pulse shaping to create a “flat-top” switching window wider than the data pulses, the maximum insertion loss could be kept well within 10 dB.

### *Time jitter*

Our prototypes have optical lengths of only a few microns, and thus impose virtually no time jitter on the data pulses, which is one of the major advantages of the AFP device over fibre-based switching devices.

---

<sup>2</sup> This is a somewhat subjective judgement, since one has to compromise between switching time, contrast, throughput, and switching energy. Depending on which parameter is considered to be more important, the best overall performance may be judged differently.

### *Contrast ratio*

All three devices exhibit >10 dB contrast ratio, a benchmark figure for practical applications. Furthermore, we have shown that, even in the presence of thermal effects, much higher contrast ratio (in excess of 20 dB) was achieved in the second device. Easily achievable high contrast is another major advantage of AFP devices.

### *Maximum clock power*

The optimal switching energy density for the second device is  $\sim 0.5 \text{ pJ}/\mu\text{m}^2$  (cf. Table 5.2). Therefore, if the spot size for the control pulses can be focused to  $10 \mu\text{m}^2$  (or  $3.6 \mu\text{m}$  diameter), the required switching energy is 5 pJ. In a  $4 \times 20 \text{ GHz}$  TDM system, the clock power required to switch each channel would then be  $5 \text{ pJ} \times 20 \text{ GHz} = 100 \text{ mW}$ , or 20 dBm, and the total clock power needed to switch all 4 channels would be  $\sim 26 \text{ dBm}$ . Such power levels fall within the capabilities of current commercial laser and amplifier systems; moreover, with proper control pulse shaping, an even lower clock power could be achieved.

### *Bandwidth*

All three devices exhibit contrast ratios higher than 10 dB over wide bandwidths: 20–25 nm under low switching energy, and 30–40 nm under a higher switching energy (cf. Table 5.2). Such large bandwidths result from two judicious design decisions: using bulk material rather than quantum-well material as the active nonlinear medium, and using a low-finesse structure by employing only a 60% reflection back mirror. Moreover, one can tailor the material composition for operation within a different wavelength range. Consequently, the entire wavelength range of current telecom transmission systems could be covered with only 2 or 3 such devices, and each device, would require only one control beam to switch many wavelength channels. Thus such devices can sometimes simplify system configuration and lead to significant saving in optical energy. Additionally, such devices can replace many narrow-bandwidth devices used in reconfigurable networks where receiving and transmitting wavelengths vary, depending on network traffic. Moreover, a wide bandwidth also lowers the requirement for fabrication tolerance. In short, a larger bandwidth offers simplicity, flexibility, reconfigurability and manufacturability.

### *Polarization dependence*

Polarization-independent operation was verified for all three devices, which was expected since the data beam was normal to the device and all layers of the device (SiON, InGaAsP, and InP) had isotropic linear refractive indices. A very weak polarization-dependent contrast ratio (<0.5 dB) was detected, which could be attributed to the tensor nature of  $\chi^{(3)}$  (the third order susceptibility) [212], but the effect is very weak in materials where carrier-induced nonlinearities dominate.

### *Control-data extinction ratio*

For system implementation, control pulses have to be removed from the data pulses after switching. In our experiments, control and data beams were not co-linear and were easily separated. In a real system, control and data pulses may be delivered in the same optical fiber, in which case control pulses could be eliminated by a fiber grating notch filter at the control wavelength. Since these devices impose no restriction on control-data wavelength separation, it can be made relatively large (>10 nm) to facilitate removal of control pulses from the data pulses. For example, in-fibre notch filters with >40 dB extinction ratios should achieve 20 dB control-data extinction ratios, adequate for most applications, even when control pulses are 20 dB more intense than data pulses.

### *Operating temperature*

The three device prototypes tested in the laboratory were grown on InP substrates and had large areas, about  $5 \times 10 \text{ mm}^2$ . They were bonded to 1/8" thick, 1-inch-diameter copper blocks with a thermal compound, to ensure good heat conductance and good heat sinking. All our measurements were conducted at the rep rate of the OPO (82 MHz). Under these conditions, no cooler was required and no noticeable temperature rise was observed.

In practical implementations, the devices are expected to be very compact, and the switching rep rate will also be two to three orders of magnitude higher. Therefore, we anticipated significant increases in temperature; consequently, we also tested the devices under temperatures higher than room temperature by mounting them on temperature-controlled thermal couplers. No noticeable changes in contrast ratio or throughput were observed for temperatures under 40° C, but, as ex-

pected, at temperatures higher than 70° C, significant reductions of throughput were observed. We conclude that, while the device should be used with a cooler, strict temperature regulation is not necessary, since the temperature may be allowed to vary between 20° C and 40° C.

### 5.3 CONCLUSIONS

We have investigated, by means of numerical simulation and experimental measurements, two types of all-optical switching devices that employ HELP InGaAsP materials as active nonlinear media, the nonlinear directional coupler (NLDC), and the asymmetric Fabry-Pérot switch (AFP).

Absorption measurements on waveguides using undoped HELP InGaAsP as guiding layer showed that NLDCs can be implemented with couplers of only sub-millimeter length. Simulations on directional couplers with various cross-section geometries indicated that 1–2  $\mu\text{m}$  of guide separation was required to keep polarization sensitivity with an acceptable amount. Such requirements would impose significant difficulties on device fabrication. Simulations of induced index changes along the waveguide indicate that, while it would be possible to perform switching within an extremely short coupler length, a relatively high switching energy (40–100 pJ without taking into account coupling losses) would be necessary for switching. Experiments on two 500  $\mu\text{m}$ -long waveguide structures measured >20 dB insertion loss. Coupling loss and control pulse pre-absorption were identified as major stumbling blocks for the practical implementation of HELP InGaAsP-based NLDCs.

On the other hand, simulation results of AFP devices showed large bandwidths, high contrast ratios, and low switching energies. Three AFP device prototypes, based on Be-doped HELP InGaAsP with different doping concentrations and device geometries, were fabricated to demonstrate ultrafast all-optical switching. We have achieved with one of them 5 ps switching with 20 dB contrast under a low switching energy of 0.5 pJ/ $\mu\text{m}^2$ . The device also has a large bandwidth (25 nm), where >10 dB contrast ratio is obtained experimentally.

Our HELP-InGaAsP-based AFP devices have demonstrated many advantages over other contemporary ultrafast all-optical switching devices: (1) they are compact ( $\mu\text{m}$ -sized), and therefore do not suffer from problems associated with bulky fibre-based devices, such as latency, time jitter, instability and dispersion; (2) they utilize materials with ultrafast optical responses, and

therefore, unlike TOAD/UNI/MZ devices, can achieve switching in a simple configuration with only one element; (3) they perform passive switching (without electrical current injection), and are therefore easier to implement, maintain, and should have a longer lifetime than active switching devices; (4) they do not have restrictive input and output ports, and therefore do not suffer from coupling losses and alignment problems, which are unavoidable in waveguide devices; (5) their vertical operation ensures polarization independence, the lack of which is a problem shared by many fibre and semiconductor waveguide devices; (6) they are based on bulk materials, and therefore have several times larger bandwidth than that of quantum-well-based AFP devices; (7) they are especially easy to fabricate, requiring only the growth of bulk semiconductor at standard growth temperature and the deposition of a single layer of dielectrics, and therefore offer, relative to low-temperature-grown devices and quantum-well devices, higher reliability and reproducibility.

In short, the HELP-InGaAsP-based AFP devices are suitable for demultiplexing high-speed (40–100 GHz) optical time-division-multiplexed channels in practical fibre communications systems.

---

## **Chapter 6**

# **CONCLUSIONS AND FUTURE WORK**

We have presented the first, detailed, systematic, experimental study of the optical properties of HELP InGaAsP relevant to all-optical switching, and the first demonstration of all-optical switching devices based on this material. This chapter summarizes our studies of material properties and device characteristics, highlighting our original contributions, and provides a brief outlook on future directions of both material and device engineering.

### **6.1 SUMMARY AND CONCLUSIONS**

#### **6.1.1 Material studies**

Our objective has been the development of a material suitable for ultrafast all-optical switching at speeds beyond the limits of any electronic switching device. Fundamentally different from electronic switching, ultrafast all-optical switching is based on materials with ultrafast nonlinear optical responses. To meet the requirements of practical devices, the material should also have, in addition to ultrafast response, large nonlinearity and low loss.

However, the combination of properties required for practical all-optical switching is not readily available in conventional materials. Although ultrafast optical phenomena, such as non-resonant nonlinearities and intraband nonlinearities in semiconductors, are not uncommon, the magnitude of such nonlinearities are usually too small to be useful. Interband nonlinearities in semiconductors are by far the largest easily obtainable nonlinearities, but the associated nonlinear recovery times in conventional semiconductors are on the nanosecond timescale, due to the slow carrier recombination process. Some existing techniques for reducing carrier lifetime, such as high-concentration doping and heavy-dose ion implantation, significantly degrade the material's nonlinear properties. Others, such as the thin-film technique or the low-temperature growth technique, have restricted usage.

In contrast, we show in Chapter 4 that HELP MBE growth produces InGaAsP with ultrafast carrier lifetimes (15 ps), large nonlinearity (light-induced index change comparable to that of

standard InGaAsP), and good crystalline quality (evidenced by the sharp absorption band edge and the low absorption tail). By combining HELP growth with Be doping, carrier lifetime can be further reduced to the subpicosecond range. Furthermore, HELP growth is by far the simplest technique to implement, and it offers more flexibility and controllability than other techniques do.

To understand the mechanism responsible for the reduced carrier lifetime in HELP InGaAsP, we systematically studied the optical response time as a function of doping concentration, annealing, wavelength, and induced carrier density. Our studies indicate that the fast material response is due to deep-level defects, acting as traps for electrons and holes. We attribute the further reduction in response time achieved by Be-doping to an increase in empty electron trap concentration, due to compensating Be dopants. Based on the transient responses of samples with different doping concentrations, measured under a range of carrier densities, and using information obtained through electrical characterization of this material, we developed a two-trap-level model to describe the carrier dynamics, and determined the trap coefficients and trap densities, the latter being in good agreement with those derived from the independent study of the material's electrical properties. Although our studies show that one of the trap levels has a relatively slow hole trapping rate, we have demonstrated experimentally that, with heavy Be doping, the slow hole trapping has a negligible effect on the ultrafast switching operation of HELP InGaAsP, and that its nonlinear response recovers within 10 ps, even under optical excitations in ultrafast (10 ps) succession. Therefore, this material has the potential of supporting devices with 100 GHz switching repetition rate.

We conclude from our material studies that HELP InGaAsP has all the desirable properties for use in ultrafast all-optical switching, and that it constitutes a promising candidate for many applications requiring ultrafast nonlinear optical operation.

### **6.1.2 Device studies**

Practical high-speed optical time-division-multiplexed systems require switching devices with ultrashort switching time, high contrast, low switching energy, large bandwidth, high throughput, polarization independence, compact size and high repetition rate. The challenge has always been to develop a device that meets all these requirements simultaneously. We show in Chapter 2 that

many demonstrated all-optical switching devices excel in some respects, but fail in others. Among devices recently developed, NOLMs [96–99] are bulky and typically polarization-dependent; TOAD/SLALOM/UNIs [90–92, 112, 115] cannot perform high repetition rate switching, and typically do not have high contrast ratio (because of large gain variation); MQW-based AFP devices [22, 124, 125, 128] have a narrow bandwidth, limited by the excitonic peak.

Given the unique combination of large *and* fast optical responses in HELP InGaAsP, both NLDC and AFP configurations may be implemented with this material to achieve fast switching. We have investigated both configurations through numerical modelling and experimental characterizations.

Our numerical modelling shows that HELP-InGaAsP-based NLDCs typically require 40–100 pJ of switching energy (not including coupling loss), which is comparable to other passive NLDCs. Polarization-insensitivity in NLDCs can be obtained with small waveguides (1–2  $\mu\text{m}$  guide width) with a small guide separation ( $\sim 1 \mu\text{m}$ ). Our waveguide loss measurements show that typically 4–8 dB absorption loss should be expected in HELP-InGaAsP-based NLDCs, but coupling losses in our measurements are high, resulting in a total loss of 20–24 dB. We conclude that, while HELP InGaAsP is a viable material for NLDC switches, large coupling losses and precise, high quality fabrication of small, closely-spaced waveguides are major challenges in achieving high contrast and high throughput with practical NLDCs.

Our analysis indicates that HELP-InGaAsP-based AFP devices outperform NLDC devices in many respects, including contrast ratio, throughput, bandwidth, switching time, and polarization-sensitivity. We have designed AFP switches that can be fabricated easily and reliably, and we have demonstrated the operation of these device prototypes. We have obtained polarization-independent switching with contrast ratios as high as 20 dB,  $\sim 10\%$  throughput, 25–40 nm bandwidth (at 10 dB contrast ratio), 5 ps switching time, and 0.5–1.4 pJ/ $\mu\text{m}^2$  switching energy density. The overall performance of our devices, together with the added advantage of ease of fabrication and implementation, proves that HELP-InGaAsP-based AFP devices are well suited for high-speed, large-bandwidth optical demultiplexing in practical fibre communications systems.

## 6.2 ORIGINAL CONTRIBUTIONS

The major original contributions of the current study consist in,

- the first report of the large ultrafast optical nonlinearities and high crystalline quality of HELP InGaAsP, which revealed its significant potential for use as active material in ultrafast optical devices;
- the detailed and systematic documentation of the optical properties of HELP InGaAsP, on which basis we constructed a phenomenological model to describe its carrier dynamics, thus enabling the tailoring of HELP InGaAsP optical characteristics for specific applications;
- the design and first experimental demonstration of HELP-InGaAsP-based ultrafast all-optical AFP switches, operating in the telecommunications wavelength range, which, in addition to being compact and easy to manufacture, require low energy, and have achieved high contrast, large bandwidth, and independence of polarization, thus surpassing, in overall performance, previously demonstrated devices of the same type.

A number of publications in refereed journals and conference proceedings, resulted from this study, are included in the list below:

1. **L. Qian, P.W.E. Smith, B.J. Robinson and D.A. Thompson**, “Ultrafast all-optical asymmetric Fabry-Pérot switch based on bulk Be-doped InGaAsP grown by He-plasma-assisted epitaxy,” submitted to *Optical and Quantum Electronics*, special issue on Components for Ultrafast Communications (submission requested by guest editor Dr. Osamu Wada).
2. **L. Qian, P.W.E. Smith, M.A. Matin, B.J. Robinson and D.A. Thompson**, “Ultrafast carrier dynamics in beryllium-doped InGaAsP grown by he-plasma-assisted epitaxy,” Accepted for publication in *Optics Communications* (subject to minor modifications).
3. **L. Qian, P.W.E. Smith, M.A. Matin, B.J. Robinson and D.A. Thompson**, “Ultrafast all-optical asymmetric Fabry-Pérot switch based on bulk beryllium-doped InGaAsP grown by He-plasma-assisted epitaxy,” Proceedings of the *Conference on Lasers and Electro-optics (CLEO 2000)*, San Francisco, CA, paper CWU3, May 7–12, 2000, p. 380–81.

4. H. Pinkney, D.A. Thompson, B.J. Robinson, **L. Qian**, S.D. Benjamin and P.W.E. Smith, "Growth of novel InP-based materials by He-plasma-assisted epitaxy," *Journal of Crystal Growth*, vol. 209, 2000, p. 237–240.
5. P.W.E. Smith, and **L. Qian**, "Switching to optical for a faster tomorrow," invited paper, *IEEE Circuits and Devices Magazine*, November 1999, p. 28–33.
6. **L. Qian**, P.W.E. Smith, H. Pinkney, B.J. Robinson and D.A. Thompson, "Dual-wavelength dual-pulse pump-probe measurements on helium-plasma-grown InGaAsP," Presented at the *Ninth Canadian Semiconductor Technology Conference*, Ottawa, Canada, August 10–13, 1999, p. 45.
7. **L. Qian**, S.D. Benjamin, P.W.E. Smith, H. Pinkney, B.J. Robinson and D.A. Thompson, "Dual-wavelength pump-probe measurements on He-plasma-grown InGaAsP reveal complex carrier dynamics," Proceedings of the *Conference on Lasers and Electro-optics (CLEO '99)*, Baltimore, MA, paper CWL8, May 21–26, 1999, p. 319–320.
8. **L. Qian**, S.D. Benjamin, P.W.E. Smith, B.J. Robinson and D.A. Thompson, "Subpicosecond carrier lifetime in beryllium-doped InGaAsP grown by He-plasma-assisted molecular beam epitaxy," *Applied Physics Letters*, vol. 71, 1997, p. 1513–1515.
9. **L. Qian**, S.D. Benjamin, P.W.E. Smith, B.J. Robinson and D.A. Thompson, "Subpicosecond Carrier Lifetime in Beryllium-Doped InGaAsP Grown by He-Plasma-Assisted Molecular Beam Epitaxy," Proceedings of the *Conference on Lasers and Electro-optics (CLEO '97)*, Baltimore, MA, paper JWA8, May 18–23, 1997, p. 28–29.
10. **L. Qian**, S.D. Benjamin, P.W.E. Smith, B.J. Robinson and D.A. Thompson, "Picosecond carrier lifetime and large optical nonlinearity in InGaAsP grown by He-plasma-assisted molecular beam epitaxy," *Optics Letters*, vol. 22, 1997, p. 108–110.
11. B.J. Robinson, D.A. Thompson, O.J. Lumley, S.A. McMaster, J. Zhao, H. Pinkney, **L. Qian**, S.D. Benjamin and P.W.E. Smith, "electrical characterization of high resistivity InP and optically fast (sub-picosecond) InGaAsP grown by He-plasma-assisted epitaxy," Proceedings of the *Ninth International Conference on InP and Related Materials*, Cape Cod, MA, May 11–15, 1997, p. 70–73.

12. **L. Qian**, S.D. Benjamin, P.W.E. Smith, B.J. Robinson and D.A. Thompson, "Subpicosecond carrier lifetime and large optical nonlinearities in InGaAsP grown by He-plasma-assisted molecular beam epitaxy," Presented at *The III Graduate Student Optoelectronics Semiconductor Conference on Materials, Devices and Applications*, Vancouver, BC, paper C3, June 1–4, 1997, p. 28.
13. S.D. Benjamin, **L. Qian**, J.E. Ehrlich, P.W.E. Smith, B.J. Robinson and D.A. Thompson, "Picosecond carrier lifetime in InGaAsP grown by He-plasma-assisted molecular beam epitaxy," Proceedings of the *Conference on Lasers and Electro-optics (CLEO '96)*, Anaheim, CA, paper CTuL11, June 2–7, 1996, p. 132–133.
14. D.B. Mitchell, B.J. Robinson, D.A. Thompson, **L. Qian**, S.D. Benjamin, and P.W.E. Smith, "He-plasma assisted epitaxy for highly resistive optically fast InP-based materials," *Applied Physics Letters*, vol. 69, 1996, p. 509–511.

### 6.3 DIRECTIONS OF FUTURE RESEARCH

Research on HELP-InGaAsP-based all-optical switches can be extended in several directions. In the short term, we need to investigate ways of improving the existing device to meet specific system requirements, to enable it to be implemented effectively as a high-speed OTDM demultiplexer; in the long term, we would like to explore other applications of this type of switches in optical WDM/TDM networks. Additionally, we would also like to explore the possibility of using HELP InGaAsP material for other photonic devices that require an ultrafast optical response.

#### 6.3.1 Improvements on the current AFP device

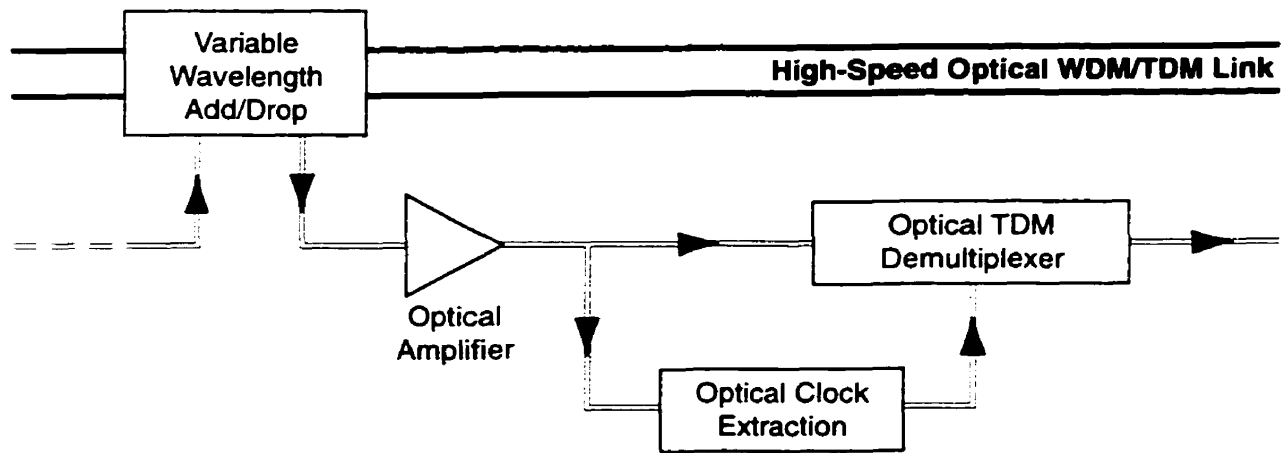
First, the temporal shape of the control pulse should be tailored to improve the performance of our HELP-InGaAsP-based AFP switching devices. A control pulse with an intense, fast-rising leading edge and a weak, long-lasting "tail" should lead to higher throughput, higher contrast, and a more desirable switching window (cf. Section 5.2.2.4). Some techniques which could be used for precise pulse shaping are pulse chirping, compression, and expanding in a nonlinear dispersive medium, such as an optical fibre. Complex fibre grating structures could also be employed for pulse shaping.

Second, there should be investigated methods for eliminating or reducing thermal effects on the AFP device. Designing the device structure to take into account thermal index and absorption changes is probably the most straightforward way of dealing with thermal effects. This requires characterization, redesign, and testing of the device under high repetition rates comparable to those used in practical high-bit-rate systems.

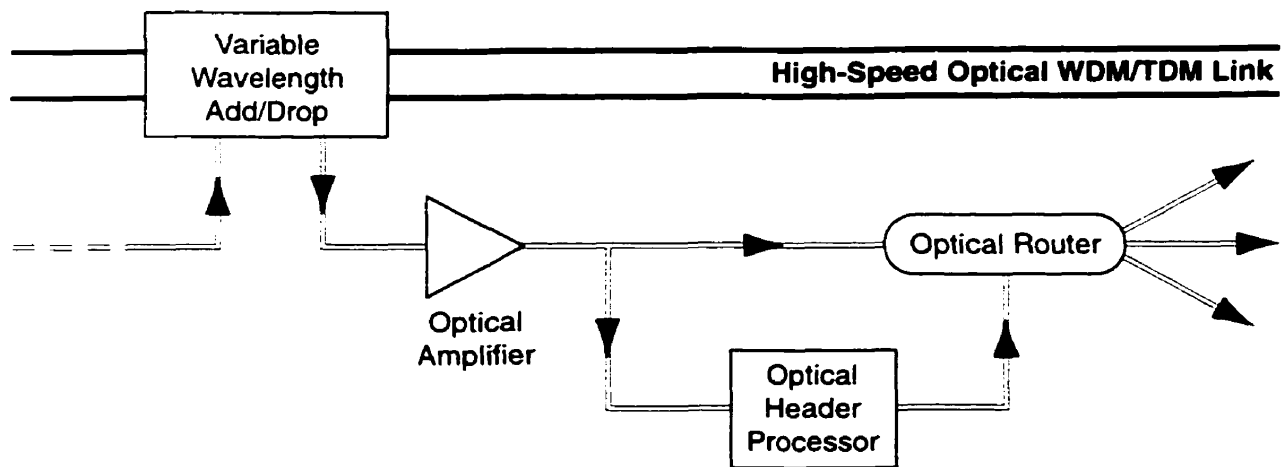
Finally, there should also be investigated approaches to efficient packaging, which is an important, and sometimes vital, aspect of device implementation. The AFP device can, in principle, be made very compact ( $\mu\text{m}$ -sized), and can be assembled with, for example, a graded-index lens attached to a fibre pigtail for spot-size conversion. A temperature control device, such as a thermal-electric cooler, should also be used to maintain the operating temperature of the device in the  $20^\circ\text{C}$ – $40^\circ\text{C}$  range (cf. Section 5.2.2.4).

### **6.3.2 Ultrafast all-optical switches in high-speed WDM/TDM optical networks**

Besides high-speed optical demultiplexers, ultrafast all-optical switches find other applications in high-capacity WDM/TDM optical networks. Nodes of such networks are required to receive and transmit large volumes of information in optical format, usually by adding/dropping wavelength channels. To utilize the fibre transmission capacity efficiently, high-bit-rate optical data (10–100 GHz) are transmitted in each wavelength channel (cf. Chapter 1). To ensure large network connectivity and to sustain high network throughput, the optical nodes must be able to handle high-bit rates, as well as operate at variable wavelengths across the transmission spectrum. Our AFP devices have demonstrated both high-speed and large-bandwidth operation, and are therefore particularly suitable for hybrid WDM/TDM networks. In addition to the optical demultiplexer, several components in a network node (e.g., optical header processor, optical router) also use ultrafast switching technology (Fig. 6.1). Therefore, the switching technology we have developed will be suitable for a variety of optical components employed by high-capacity optical networks.



(a)



(b)

**Figure 6.1** Examples of applications of ultrafast all-optical switches in WDM/TDM optical networks. All-optical switches can be used in optical nodes as, (a) high-speed demultiplexers in time-slotted systems, or, (b) high-speed optical header processors and optical routers in packet-switching systems.

### **6.3.3 Ultrafast HELP-InGaAsP-based devices**

Apart from all-optical switching, other applications that require ultrafast nonlinear operation can take advantage of the unique optical properties of HELP InGaAsP. For example, it could be used as an ultrafast saturable absorber to passively mode-lock lasers, or it could be integrated with a semiconductor laser to perform all-optical clock extraction. Better understanding of the material is required to fully explore its applications in ultrafast photonics. Further study of the various defects (their identification, genesis, and participation to absorption and carrier decay processes) is also required. Optical absorption spectroscopy and deep level transient spectroscopy can be used to determine more directly defect concentrations, energy levels, and absorption/emission cross-sections. These parameters are necessary for the development of a more sophisticated model of dynamic nonlinear optical absorption in the presence of defects, which, in its turn, could prove a very useful tool for designing devices based on HELP InGaAsP.

---

# Appendix A

## Z-SCAN TECHNIQUE FOR MEASURING LIGHT-INDUCED INDEX CHANGE

We measured light-induced index changes in our InGaAsP samples with the standard Z-scan technique. The Z-scan technique is fully described by Sheik-Bahae et al. [177], but its understanding greatly affects the interpretation of experimental data. Therefore we present here a brief description of the Z-scan technique, outlining the important assumptions and formulae used to calculate the light-induced index change.

### *Principle of the Z-scan technique*

Self-defocusing caused by light-induced index change in a thin sample placed before the focus results in beam narrowing in the far-field. When the sample is placed after the focus, the light-induced index change causes self-focusing, which results in beam broadening (Figure A.1). Consequently, the power transmitted through an aperture placed after the sample varies as the sample location ( $Z$ ) varies relative to the focus ( $Z=0$ ). Therefore, if the intensity distribution of the incident beam is known, the light-induced index change in the sample can be deduced from the variation of the transmitted power as a function of  $Z$ .

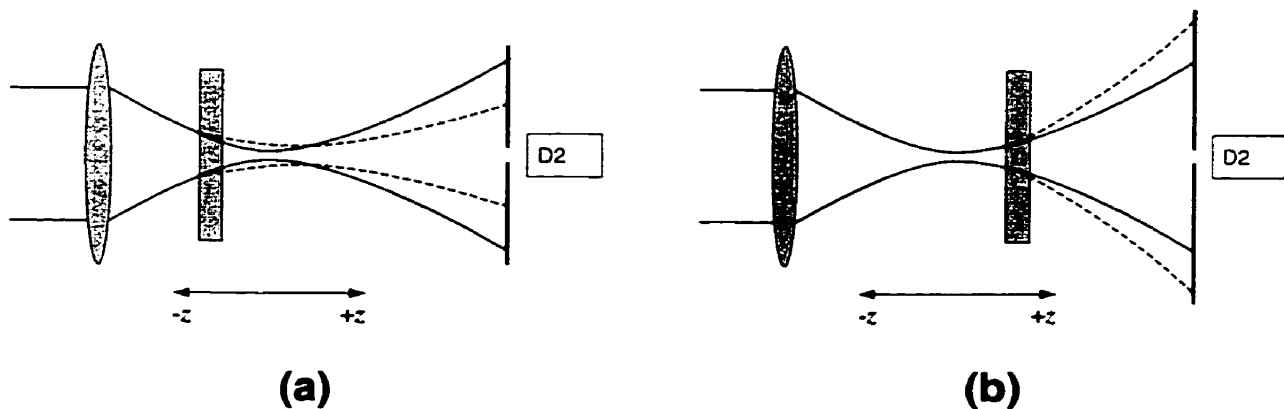


**Figure A.1** Effects of a thin sample location on the incident beam. **(a)** Sample placed before focus causes self-defocusing, leading to beam narrowing in the far-field. **(b)** Sample placed after focus causes self-focusing, leading to beam broadening in the far-field. After [213].

If the electric field distribution of the incident beam at the entrance surface of the thin sample is  $E_i(r, z, t)$ , then the electric field distribution at the exit surface  $E_e(r, z, t)$  is:

$$E_e(r, z, t) = E_i(r, z, t) e^{-\frac{\alpha L}{2}} e^{-i\Delta\phi(r, z, t)} \quad (\text{A.1})$$

where  $\alpha$  is the absorption coefficient of the sample,  $L$  is the sample length, and  $\Delta\phi(r, z, t)$  is the light-induced phase change. The latter is proportional to the index change  $\Delta n$ , and, by virtue of third-order nonlinearity, proportional to the irradiance  $I(r, z, t)$  at the entrance surface, and can be written as:

$$\Delta\phi(r, z, t) = kL_{\text{eff}}\Delta n = kL_{\text{eff}}\gamma I(r, z, t) \quad (\text{A.2})$$

where  $k$  is the free-space propagation constant,  $L_{\text{eff}}$  is the effective sample length (corrected for absorption) and is equal to  $(1 - e^{-\alpha L}) / \alpha$ , and  $\gamma$  is the nonlinear refraction coefficient.

The effective sample length ( $L_{\text{eff}}$ ) can be obtained from

$$L_{\text{eff}} = \frac{1}{\alpha}(1 - e^{-\alpha L}) \quad (\text{A.3})$$

The coefficient  $\gamma$  is related to the third-order nonlinear susceptibility  $\chi^{(3)}$  through

$$\gamma = \frac{\text{Re}(\chi^{(3)})}{2n^2\epsilon_0 c} \quad (\text{A.3})$$

where  $n$  is the linear refractive index of the sample,  $\epsilon_0$  is permittivity of free space, and  $c$  is the speed of light.

In principle, if  $I(r, z, t)$  is known, the far field distribution can be calculated from Eq. (A.1) with Huygens-Fresnel propagation integral, and the detected power through the aperture can be found by integrating the intensity distribution over the aperture area. The transmitted power is a function of  $\gamma$ , and therefore,  $\Delta n$  can be deduced by measuring the transmitted power.

#### *Assumptions of Z-scan technique*

It would be extremely tedious to calculate and integrate the far field intensity distribution if  $I(r, z, t)$  in Eq. (A.2) is a random function. The elegance of Z-scan technique is that, by *assuming a Gaussian intensity distribution* and by using Gaussian Decomposition Method [177], it significantly simplifies the calculation.

If  $I(r,z,t)$  is Gaussian, then  $\Delta f(r,z,t)$  can be expressed as:

$$\Delta\phi(r,z,t) = \frac{\Delta\phi_0(t)}{1+(z^2/z_0^2)} e^{-\frac{2r^2}{w^2(z)}} \quad (\text{A.5})$$

where  $\Delta\phi_0(t) = kL_{\text{eff}}\mathcal{N}_0(t)$  is the on-axis phase change at the focus and  $I_0(t)=I(0,0,t)$  is the on-axis focus irradiance inside the sample at focus,  $z_0$  is the confocal parameter of the Gaussian beam, and  $w(z)$  is the beam radius at  $z$  given by  $w^2(z) = w_0^2[1+(z^2/z_0^2)]$ . Because  $\Delta\phi$  has a Gaussian form, one can expand the nonlinear phase term  $\exp(-i\Delta\phi(r,z,t))$  in Eq. (A.1) in a Taylor series, and express (A.1) in Gaussian form also. This makes the calculation and integration of the far field intensity distribution much easier. As a result, for very small phase shifts  $\Delta\phi_0 \ll 1$ , the normalized transmittance, defined as:

$$T(z, \Delta\phi_0) = \frac{|E_T(r=0, z, \Delta\phi_0)|^2}{|E_T(r=0, z, \Delta\phi_0=0)|^2} \quad (\text{A.6})$$

can be approximated as

$$T(z, \Delta\phi_0) \approx 1 + \frac{4\Delta\phi_0 x}{(x^2+1)(x^2+9)} \quad (\text{A.7})$$

where  $x = z/z_0$ . In this simple expression, relating the normalized transmittance directly to phase change, lies the essence of the Z-scan technique. Both basic assumptions, i.e. (1) a Gaussian incident beam, and, (2) a very small ( $\ll 1$ ) induced phase change  $\Delta\phi_0$ , can be satisfied experimentally.

#### *Characteristics of the Z-scan curve*

By plotting expression (A.7), one obtains a typical Z-scan curve showing a peak and a valley (Figure A.2). By differentiating Eq. (A.7), one also obtains the positions of the peak and valley as  $x_{p,v} \approx \pm 0.858$ , or

$$\Delta z_{p-v} = |x_p - x_v| \approx 1.7z_0 \quad (\text{A.8})$$

The normalized transmittances corresponding to the peak and valley are  $T_{p,v} \approx 1 \pm 0.203|\Delta\phi_0|$ , which shows that the phase change is proportional to the difference in normalized transmittance

between peak and valley, i.e.

$$\Delta T_{p-v} \approx 0.406|\Delta\phi_0| \quad (\text{A.9})$$

More rigorous numerical calculation shows that  $\Delta T_{p-v}$  shows some sensitivity to aperture size, and the expression (A.9) should be corrected for aperture size by an additional factor, hence

$$\Delta T_{p-v} \approx 0.406(1-S)^{0.25}|\Delta\phi_0| \quad (\text{A.10})$$

where  $S$  can be calculated from:

$$S = 1 - \exp\left(-\frac{2r_a^2}{w_a^2}\right) \quad (\text{A.11})$$

where  $r_a$  is the radius of the aperture, and  $w_a$  is the beam radius at the aperture.

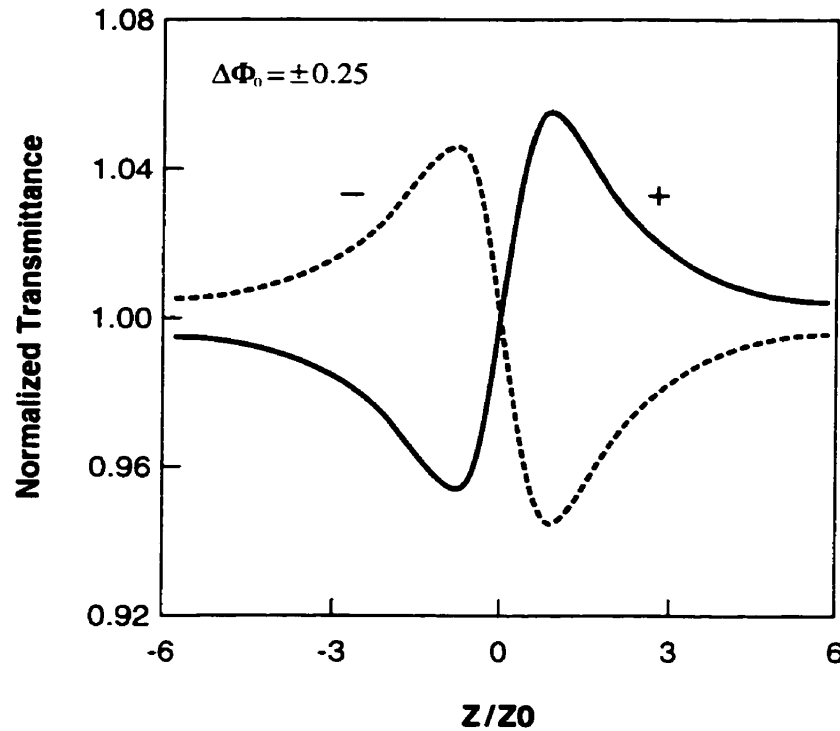


**Figure A.2** Calculated Z-scan transmittance for a negative (dashed) and a positive (solid) nonlinearity. After [177]

We use Eq. (A.10) to obtain the phase change from our measurements and then to calculate the induced index change. We also use Eq. (A.8) to double check the beam confocal parameter and the spot size, which is measured with a beam profiler.

*Influence of nonlinear absorption and surface inhomogeneity on Z-scan signals*

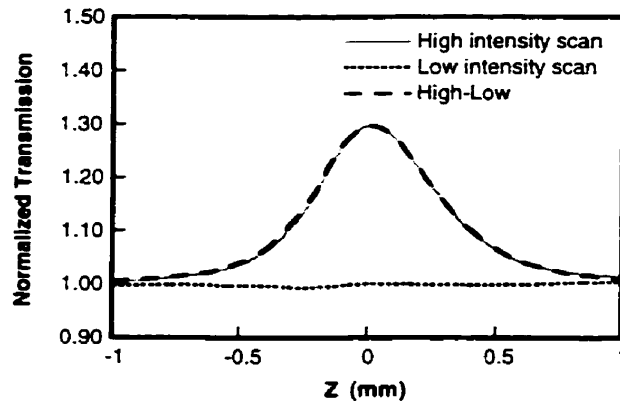
The typical Z-scan curve (Figure A.2) is obtained when the nonlinear absorption in the sample is negligible, and when the sample surface is optically smooth across the beam. But in the case of resonant nonlinearity, which is accompanied by large nonlinear absorption, the Z-scan signal is overwhelmed by increased transmission due to absorption saturation. Furthermore, since Z-scan signal is usually small (the difference in peak and valley transmission is only a few percentages, any small dust particle or imperfection on the sample can scatter the beam and contribute to deviation from the ideal Z-scan signal. To remove the effects of nonlinear absorption and surface inhomogeneity from our measurements we adopted the methods discussed by Sheik-Bahae et al. [177].

The nonlinear absorption effect is addressed by performing two scans: one with aperture installed (standard Z-scan), and another without the aperture (open-aperture scan). The standard Z-scan contains both nonlinear absorption and nonlinear refraction, while the open-aperture data contains only nonlinear absorption. As shown by Sheik-Bahae et al. [177], dividing standard Z-scan data by open aperture data results in a new Z-scan curve, which gives, to within  $\pm 10\%$ ,  $\Delta T_{p-v}$  of the purely refractive case.

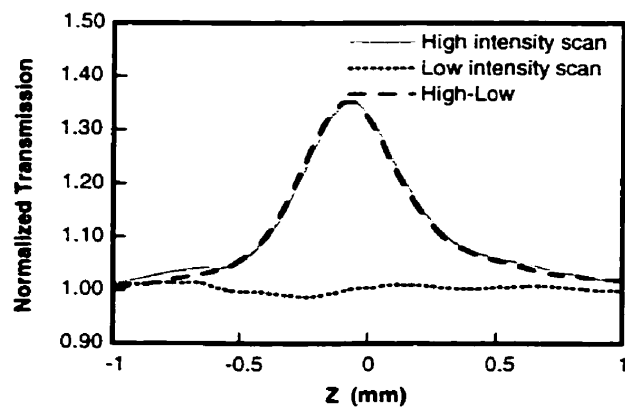
The surface inhomogeneity effect is dealt with by performing two Z-scans: one at irradiance low enough to render the nonlinear effect negligible, and another at high irradiance. The low-irradiance scan reflects only the effect of surface inhomogeneity and should be *subtracted* from the high-irradiance signal.

To remove both absorption saturation and sample inhomogeneity effects, we performed four scans: open-aperture high-intensity, open aperture low-intensity, standard high intensity, and standard low-intensity. The data from the low-intensity scans were first subtracted from the data of the high-intensity scans, and then the resulting standard scan data was divided by the resulting open-aperture scan data. After subtraction and division, the final data shows a "signature" Z-scan shape, with contribution only from the nonlinear refractive index. (See Figure A.3 for an example with a standard InGaAsP sample.)

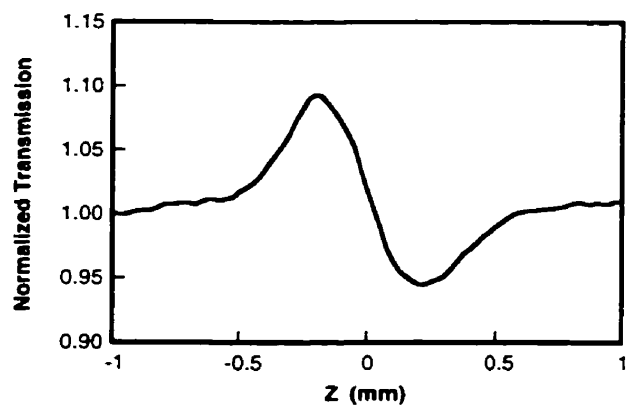
---



(a)



(b)



(c)

**Figure A.3** Example of removing nonlinear absorption and sample inhomogeneity effects from Z-scan data. (a) High-intensity and low-intensity open aperture scan; (b) High-intensity and low-intensity standard z scan; and (c) result of division of standard z scan data by open-aperture scan data, which gives the Z-scan “signature,” with contribution only from the nonlinear refractive index.

## Appendix B

# FREE-ELECTRON ABSORPTION AND FREE-HOLE ABSORPTION IN HELP InGaAsP

We attribute the pump-induced absorption, measured by the dual-wavelength pump-probe technique with the probe wavelength just below the band edge, to free-electron absorption (FEA). Here we state our reasons for this attribution, based on qualitative comparison between FEA and free-hole absorption (FHA).

Our starting point should be the band structure of the InGaAsP material. However, quantitative quaternary band structures (even ternary band structures) are not known, and the only available band structures are binary III-V materials (InP, GaAs, GaP, InAs). The quaternary band structure derived from the binary band structures by interpolation can only be qualitative. Therefore, detailed, quantitative comparison between FEA and FHA is difficult, if not impossible. In the literature, FEA has always been studied in the context of n-type material, and FHA in p-type material. All samples we used in the dual-wavelength pump-probe experiment (Section 4.4), i.e. the undoped HELP InGaAsP sample, and the two Be-doped HELP InGaAsP samples with concentrations of  $3 \times 10^{17} \text{ cm}^{-3}$  and  $1 \times 10^{18} \text{ cm}^{-3}$ , are weakly n-type, the sample with the highest doping concentration being the most resistive [214].

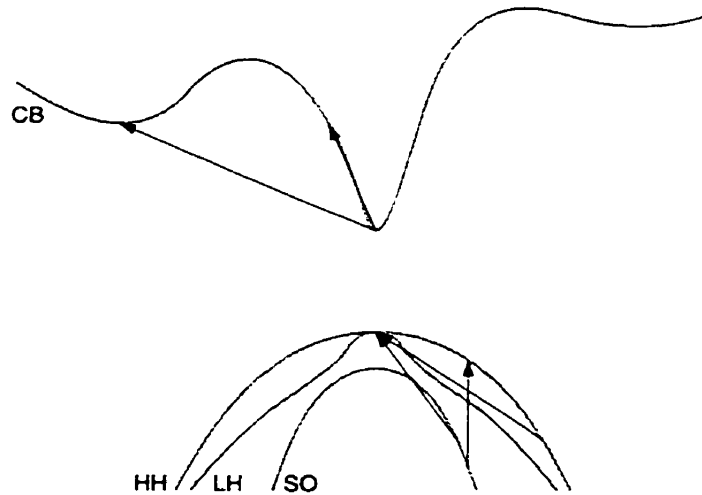


**Figure B.1** Qualitative band structure of InGaAsP and possible transitions due to free electron and free-hole absorption.

If we use the following parameters documented in Adachi's book [215]: electron effective mass  $m_e^* \approx 0.044 m_0$ , heavy-hole effective mass  $m_{hh}^* \approx 0.46 m_0$ , light-hole effective mass  $m_{lh}^* \approx 0.06 m_0$ , split-off hole  $m_{so}^* \approx 0.16 m_0$  (obtained by extrapolation), energy gap  $E_g = 0.8$  eV, split-off energy  $\Delta \approx 0.30$  eV, and observe that the light-hole (LH) band and the split-off band (SO) should not cross, then the band structure should be similar to what is depicted in Figure B.1.

The possible transitions due to electron absorption are: intra-conduction band absorption and inter-valley absorption in the conduction band; possible transitions due to hole absorption are: intra-heavy-hole (HH) band absorption, direct SO to HH band absorption, phonon-assisted SO to HH absorption. These transitions are illustrated in Figure B.1. We ignore transitions associated with the LH band because of its low density of state.

Of the three transitions taking place in the valence band, we can rule out the direct inter-valence-band absorption (IVBA), because the hole concentration in the HH band, corresponding to the  $k$ -value required for this transition to take place, is virtually non-existent for the carrier concentrations used in our experiments. According to Haug, who compared phonon-assisted IVBA and direct IVBA in a InGaAsP material (1.3  $\mu\text{m}$  band edge wavelength) the absorption coefficient resulting from the former is  $15\times$  larger than the coefficient resulting from the latter [216].

Therefore, we only need to compare phonon-assisted intra-conduction band absorption, phonon-assisted intra-valence band absorption, and phonon-assisted intervalence band absorption. They are all second-order processes involving absorption of a photon and absorption or emission of a phonon.

The absorption coefficient  $\alpha$  is proportional to the transition probability  $W_{fi}$  from the initial state  $i$  to the final state  $f$ :

$$\alpha \propto W_{fi} \quad (\text{B.1})$$

where  $W_{fi}$  can be written as [217]:

$$W_{fi} \propto \iint \left| \sum_m \left( \frac{\langle f | H_{er} | m \rangle \langle m | H_{eq} | i \rangle}{E_m - E_i \pm \hbar\omega_q} + \frac{\langle f | H_{eq} | m \rangle \langle m | H_{er} | i \rangle}{E_m - E_i - \hbar\omega} \right) \right|^2 P \delta(E) d^3k_i d^3k_f \quad (\text{B.2})$$

where  $P$  is the phonon occupation factor, and  $|H_{eq}|$  and  $|H_{er}|$  are the matrix elements for the

phonon absorption/emission and photon absorption, respectively,  $E_i$  and  $E_m$  are the energy levels of the initial and intermediate states, respectively, and  $\hbar\omega_q$  and  $\hbar\omega$  are the phonon and photon energies, respectively. The summation in (B.2) should be carried out over all intermediate state  $m$  allowed by the  $k$ -selection rule. In the case of intra-band absorption where the intermediate state  $m$  is in the same band,  $W_{fi}$  simplifies to:

$$W_{fi} \propto \iint \frac{|H_{eq}|^2 |H_{er}|^2}{(\hbar\omega)^2} P \delta(E) d^3 k_i d^3 k_f \quad (\text{B.3})$$

and, in the case of inter-band absorption,  $W_{fi}$  is:

$$W_{fi} \propto \iint \frac{|H_{eq}|^2 |H_{er}|^2}{(E_m - E_i - \hbar\omega)^2} P \delta(E) d^3 k_i d^3 k_f \quad (\text{B.4})$$

Here,  $|H_{eq}|$  is a function of  $q$  ( $q = \mathbf{k}_f - \mathbf{k}_i$ , the required momentum change for the transition to take place), and its dependence on  $q$  varies depending on which scattering mechanism is assisting the transition [218]:

- for acoustic and optical phonon scattering,  $|H_{eq}|$  has no  $q$  dependence
- for polar optical phonon and piezoelectric scattering,  $|H_{eq}| \propto q^{-2}$
- for charged impurity scattering,  $|H_{eq}| \propto q^{-4}$

Furthermore,  $W_{fi}$  is also dependent on the effective mass  $m^*$ , and the dependence varies with the  $q$  dependence of  $|H_{eq}|$ :

- $W_{fi} \propto (m^*)^{1/2}$  when  $|H_{eq}|$  has no  $q$  dependence
- $W_{fi} \propto (m^*)^{-1/2}$  when  $|H_{eq}| \propto q^{-2}$
- $W_{fi} \propto (m^*)^{-3/2}$  when  $|H_{eq}| \propto q^{-4}$

Therefore, if only acoustic and optical phonons are responsible for free-carrier absorption, then the absorption does not depend highly on  $q$ , and, if we assume  $|H_{er}|$  is the same for conduction band and valence band transitions, then the ratio between the free-electron absorption coefficient  $\alpha_e$  and the free-hole absorption coefficient  $\alpha_h$  is

$$\frac{\alpha_e}{\alpha_h} = \left( \frac{m_e^*}{m_h^*} \right)^{1/2} \left( \frac{D_e}{D_h} \right)^2 \quad (\text{B.5})$$

where  $D_e$  and  $D_h$  are the deformation potentials<sup>1</sup> for the conduction band and valence band, respectively. Conduction band deformation potentials are difficult to determine, and their measured values vary widely. In general, the deformation potentials for the valence band and for the conduction band are of the same order. Therefore, if acoustic and optical phonons are responsible for free-carrier absorption, then  $\alpha_e < \alpha_h$ , because of the large hole effective mass.

If, however, the polar optical phonon and/or the piezoelectric scattering is dominant, then

$$\frac{\alpha_e}{\alpha_h} \approx \left( \frac{m_e^*}{m_h^*} \right)^{-1/2} \left( \frac{q_c}{q_v} \right)^{-2} \quad (\text{B.6})$$

where  $q_c$  and  $q_v$  are the momentum changes required for free-electron and free-hole absorption to take place, respectively. The former is smaller than the latter, because of the higher curvature of the conduction band. Clearly in this case,  $\alpha_e > \alpha_h$ .

If the charged impurities scattering are mainly responsible for assisting the free-carrier absorption, then

$$\frac{\alpha_e}{\alpha_h} \approx \left( \frac{m_e^*}{m_h^*} \right)^{-3/2} \left( \frac{q_c}{q_v} \right)^{-4} \quad (\text{B.7})$$

from which results  $\alpha_e \gg \alpha_h$ .

According to Ridley, polar scattering is the dominant mechanism of scattering in pure III-V and II-VI compounds [219]. We believe that in materials such as HELP InGaAsP, where we intentionally introduce large concentration of defects, charged-impurity scattering is also significant. The effect of charged-impurity scattering can be indirectly seen from the much reduced electron mobility in HELP InGaAsP: its value in standard undoped InGaAsP is  $\sim 6400 \text{ cm}^2/\text{Vs}$ , while in undoped HELP InGaAsP it is reduced to  $2350 \text{ cm}^2/\text{Vs}$ , and it is further reduced in  $1 \times 10^{18} \text{ cm}^{-3}$  Be doped samples to  $\sim 800 \text{ cm}^2/\text{Vs}$ .

Therefore, in our opinion, the dominant scattering mechanism in InGaAsP is charged-impurity scattering, and, to some extent, polar optical phonon scattering, which means phonon-assisted

---

<sup>1</sup> The acoustic deformation potential is different from the optical deformation potential, and it should be considered separately if we know the percentage of contribution from acoustic phonons and from optical phonons.

FEA is much higher than phonon-assisted FHA. In addition, because our experiments were carried out under moderate carrier concentrations ( $\leq 10^{18} \text{ cm}^{-3}$ ), direct IVBA can be neglected.

Furthermore, we observed similar “bottle-neck” effects in our dual-wavelength pump-probe experiments for probe wavelengths above and below the band, suggesting that the fast decay for the probe below the band is due to electrons, which is consistent with all our experimental observations.

---

## **Appendix C**

# **BÁNYAI-KOCH MODEL FORMULATION AND PARAMETERS USED IN THIS WORK**

The Bányai-Koch theory has been described in detail elsewhere [130, 193, 220]. In this appendix we shall merely state briefly the assumptions and conditions of the theory, and provide the formulation and parameters used in our simulation.

The Bányai-Koch theory is a partially phenomenological theory for describing the nonlinear optical absorption of photo-excited semiconductors in the spectral vicinity of the fundamental absorption edge. Although it does make certain simplifying assumptions, it is widely used because it expresses nonlinear absorption analytically as a function of the electron-hole pair density, and it is thus much simpler than the nonequilibrium many-body theory, which uses the retarded Green's functions, where the dielectric function is given as the solution to an integral equation [130].

In the Bányai-Koch model electrons and holes are assumed to be in quasi-equilibrium, where their distributions can be characterized by quasi-Fermi levels. The band filling effect is taken into account partially, by replacing the attractive Coulomb potential between an electron and a hole with a screened one, the Yukawa potential [193]. Such approximation of the band filling effect yields very useful results when the electron-hole pair density is relatively low and its distribution sufficiently smeared out [130]. The Yukawa potential is then approximated by the Hulthén potential, because by so doing, one can find an analytical solution to the modified Wannier equation, which describes the relative motion of the electron-hole pair. The inclusion of the band gap renormalization effect [139], i.e. the energy gap shifts to lower energies with increasing carrier density, is simplified by assuming the reduction of band gap energy to be exactly the same as the reduction of the exciton binding energy for carrier densities below the the Mott density (a limit for bound states to exist). At carrier densities above the Mott density, band gap renormalization effect is included by assuming phenomenologically that the gap variation goes as the square root of the pair density, which satisfies continuity and empirical observations. The limited lifetime of the excitons, due to various scattering mechanisms, is represented phenomenologically by replacing

the Dirac-function by a lineshape function which approximates the exponential Urbach tail (absorption tail at the band edge).

The final Bányai-Koch model formulation is summarized as follows [220]. By applying the linear response theory to semiconductors with parabolic bands, the imaginary part of the dielectric susceptibility  $\chi(\omega)$  can be written in the form of the generalized Elliot formula [193]:

$$\text{Im } \chi(\omega) = \frac{2\pi}{\epsilon_0} |r_{cv}|^2 \tanh\left(\beta\left(\hbar\omega - \sum_{\alpha} \mu_{\alpha}\right) / 2\right) \sum_n |\phi_n(\mathbf{r} = 0)|^2 \delta_{\Gamma}(\hbar\omega - E_n) \quad (\text{C.1})$$

where  $|r_{cv}|$  is the transition matrix element,  $\beta = 1/kT$ ,  $\mu_{\alpha}$  is the chemical potential for electrons or holes ( $\alpha = c, v$ ; c for conduction band, and v for valence band), and  $\phi_n$  and  $E_n$  are the eigenfunctions and energy eigenvalues, respectively, of the modified Wannier equation (C.2), where the Coulomb potential is replaced by a screened potential, the Yukawa potential (C.3):

$$\left(-\frac{\hbar^2}{2m} \nabla^2 - \frac{e^2}{4\pi\epsilon_0\epsilon_r r} e^{-\kappa r} - E_n\right) \phi_n(\mathbf{r}) = 0 \quad (\text{C.2})$$

$$V_s(r) = -\frac{e^2}{4\pi\epsilon_0\epsilon_r r} e^{-\kappa r} \quad (\text{C.3})$$

where  $\kappa$  is the inverse screening length, and is calculated by:

$$\kappa = \frac{2e^2\beta}{\epsilon_0\epsilon_r} \sum_{\alpha} \int f_{\alpha}(\mathbf{k})(1 - f_{\alpha}(\mathbf{k})) \frac{d^3k}{(2\pi)^3} \quad (\text{C.4})$$

where  $f_{\alpha}(\mathbf{k})$  is the Fermi function for the conduction band and valence band:

$$f_{\alpha}(\mathbf{k}) = \frac{1}{\exp\left[\beta\left(\frac{\hbar^2 k^2}{2m_{\alpha}} + E_{0,\alpha} - \mu_{\alpha}\right)\right] + 1} \quad (\text{C.5})$$

Analytical solution does not exist for (C.2), however, if the Yukawa potential is approximated by the Hulthén potential, one can solve the Wannier equation (C.6) analytically.

$$\left(-\frac{\hbar^2}{2m} \nabla^2 - \frac{e^2}{2\pi\epsilon_0\epsilon_r a_0 g} \frac{1}{\exp(2r/a_0 g) - 1} - E_n\right) \phi_n(\mathbf{r}) = 0 \quad (\text{C.6})$$

where  $m$  is the reduced mass of the electron and the hole ( $1/m=1/m_c+1/m_v$ ),  $a_0$  is the Bohr radius ( $a_0 = 4\pi\hbar^2\epsilon_0\epsilon_r / (me^2)$ ), and  $g$ , a parameter that sets an upper limit on the number of bound states for a given spherically symmetric potential, is calculated by the Bargmann theorem [221]. If the Yukawa and Hulthén potentials are set equal at this upper limit,  $g$  has the following relation with the screening length  $\kappa$ :

$$g = \frac{12}{\pi^2 a_0 \kappa} \quad (\text{C.7})$$

The normalized inverse screening length  $a_0\kappa$  is given by:

$$(a_0\kappa)^2 = \frac{2}{\pi} \sqrt{kT / E_R} \sum_{\alpha} \left[ \left( \frac{m_{\alpha}}{m} \right)^{3/2} \int_0^{\infty} \frac{\sqrt{x}}{1 + \cosh(x - (\mu_{\alpha} - E_g / 2) / kT)} dx \right] \quad (\text{C.8})$$

where  $E_R$  is the Rydberg energy ( $E_R = \hbar^2 / (2ma_0^2)$ ).

The solution to (C.6) is can be obtained from the Jost function to (C.6):

$$f(k) = \prod_{n=1}^{\infty} \left( 1 - \frac{g}{n(n + ika_0g)} \right) \quad (\text{C.9})$$

and the zeros to the Jost function on the negative imaginary axis of  $k$  correspond to the bound states of the system. The corresponding eigenfunctions of the bound states are:

$$|\phi_n(r=0)|^2 = \frac{(g+n^2)(g-n^2)}{\pi a_0^3 g^2 n^3} \quad (\text{C.10})$$

and the energies of the bound states become

$$E_n = -E_R \left( \frac{1}{n} - \frac{n}{g} \right)^2 \quad (\text{C.11})$$

and the limit for  $n$  is given by:

$$k_n = \frac{1}{a_0} \left( \frac{1}{n} - \frac{n}{g} \right) \geq 0 \Rightarrow n \leq \sqrt{g} \quad (\text{C.12})$$

For the states with continuous energy eigenvalues,

$$E_k = \frac{\hbar^2 k^2}{2m} \quad (\text{C.13})$$

and

$$|\phi_k(r=0)|^2 = \frac{1}{(2\pi)^3 |f(-k)|^2} \quad (\text{C.14})$$

To take into account of band gap renormalization, the change in energy gap  $\delta E_g$  can be set to be the same as the change in the ground state of the exciton binding energy for carrier densities less than the Mott density (or  $g \geq 1$ ):

$$\delta E_g = E_R \left( -1 + \left( 1 - \frac{1}{g} \right)^2 \right), \quad \text{for } g \geq 1 \quad (\text{C.15})$$

and, for carrier densities greater than the Mott density,  $\delta E_g$  is approximated phenomenologically as:

$$\delta E_g = E_R \left( -1 + \left( 1 - \frac{1}{g} \right)^2 \right), \quad \text{for } g < 1 \quad (\text{C.16})$$

To take into account the limited lifetime of excitons, and to phenomenologically calculate the Urbach tail, the Dirac function  $\delta$  is replaced by the lineshape broadening function  $\delta_\Gamma$ :

$$\delta_\Gamma(x) = \frac{1}{\pi \Gamma \cosh(x / \Gamma)} \quad (\text{C.17})$$

where the broadening parameter  $\Gamma$  is a function of both temperature ( $T$ ) and carrier density ( $N$ ):

$$\Gamma(T, N) = \Gamma_0 + \frac{\Gamma_{ph}}{\exp\left(\frac{\hbar \Omega_{LO}}{kT}\right) - 1} + \Gamma_N N \quad (\text{C.18})$$

where the first term is the natural broadening under low temperature and low carrier density, the second term is the room-temperature broadening due to LO-phonon scattering, and the third term is the density-dependent broadening.

The final formulation for the nonlinear absorption can now be expressed explicitly using:

$$\alpha(\omega) = \frac{\omega}{nc_0} \text{Im } \chi(\omega) \quad (\text{C.19})$$

and substituting (C.10), (C.11), (C.13), and (C.14) into (C.1):

$$\begin{aligned} \alpha(\tilde{\omega}) = & \alpha_0 \tanh\left(\left(\frac{\tilde{\omega}}{\tilde{T}} - \sum_{\alpha} \tilde{\mu}_{\alpha}\right) / 2\right) \left\{ 4\pi \sum_i \frac{g^2 - i^4}{g^2 i^3} \delta_{\tilde{\Gamma}} \left[ \tilde{\omega} + \left(\frac{1}{i} - \frac{i}{g}\right)^2 \right] + \right. \\ & \left. + \int_0^{\infty} \prod_{n=1}^{\infty} \left[ 1 + \frac{2n^2 g - g^2}{(n^2 - g)^2 + g^2 n^2 x} \right] \delta_{\tilde{\Gamma}}(\tilde{\omega} - x) \sqrt{x} dx \right\} \end{aligned} \quad (\text{C.20})$$

where

$$\alpha_0 = \frac{\omega}{nc_0} \frac{|r_{cv}|^2}{\pi \epsilon_0 a_0^3 E_R} \quad (\text{C.21})$$

$$\tilde{\omega} = (\hbar\omega - E_g) / E_R \quad (\text{C.22})$$

$$\tilde{T} = kT / E_R \quad (\text{C.23})$$

$$\tilde{\mu}_{\alpha} = (\mu_{\alpha} - E_g / 2) / kT \quad (\text{C.24})$$

$$\delta_{\tilde{\Gamma}}(x) = \frac{1}{\pi \tilde{\Gamma} \cosh(x / \tilde{\Gamma})}, \quad \tilde{\Gamma} = \Gamma / E_R \quad (\text{C.25})$$

and the normalized chemical potentials are the solutions to:

$$F_{1/2}(\tilde{\mu}_{\alpha}) = 4N_{\alpha} a_0^3 \left( \frac{\pi}{(m_{\alpha} / m) \tilde{T}} \right)^{3/2} \quad (\text{C.26})$$

where  $F_{1/2}$  is the Fermi-Dirac integral and can be evaluated by the Nilsson's approximation:

$$\eta = \ln u + \frac{u}{[64 + 0.0552u(64 + u^2)]^{1/4}} \quad \text{where } u \equiv F_{1/2}(\eta) \quad (\text{C.27})$$

The first term in the brace of (C.20) is the contribution from the bound states and the second term is the contribution from the continuum states. We developed a Fortran program (BK) to

evaluate (C.20) numerically, using the following parameters:

$$E_{g0} = 1.35 - 0.72y + 0.12y^2 \text{ (eV)}, \text{ where } y \text{ is the mole fraction of As in } \text{In}_{1-x}\text{Ga}_x\text{As}_y\text{P}_{1-y},$$

$$m_e = 0.045 m_0, \text{ where } m_0 \text{ is the free-space electron mass}$$

$$m_h = 0.46 m_0, \text{ where } m_0 \text{ is the free-space electron mass}$$

$$T = 300 \text{ K}$$

$$|r_{cv}| \approx 8.8 \times 10^{-27} \text{ cm (fitting parameter)}$$

$$\hbar\Omega_{LO} = 33 \text{ meV}$$

$$\Gamma_0 = 8.5 \times 10^{-3} \text{ eV}$$

$$\Gamma_{ph} \approx 2 \times 10^{-2} \text{ eV (fitting parameter)}$$

$$\Gamma_N = 2 \times 10^{-21} \text{ eVcm}^3$$

---

## REFERENCES

- [1] A. E. Willner, "Mining the optical bandwidth for a terabit per second," *IEEE Spectrum*, April, pp. 32–41, 1997.
- [2] L. F. Mollenauer, E. Lichtman, G. T. Harvey, M. J. Neubelt, and B. M. Nyman, "Demonstration of error-free soliton transmission over more than 15,000 km at 5 Gb/s, single-channel, and over more than 11,000 km at 10 Gb/s in a two channel WDM," *Electronics Letters*, vol. 28, pp. 792–4, 1992.
- [3] N. S. Bergano, C. R. Davidson, B. M. Nyman, S. G. Evangelides, J. M. Darcie, J. D. Evankow, P. C. Corbett, M. A. Mills, G. A. Ferguson, J. A. Nagel, J. L. Zyskind, A. J. Lucero, and A. A. Klein, "40-Gb/s WDM transmission of eight 5-Gb/s data channels over transoceanic distances using the conventional NRZ modulation format," presented at *Optical Fiber Communications Conference*, San Diego, CA, 1996.
- [4] U. Morgner, F. X. Kartner, S. H. Cho, Y. Chen, H. A. Haus, J. G. Fujimoto, E. P. Ippen, V. Scheuer, N. Angelow, and T. Tschudi, "Sub-two-cycle pulses from a Kerr-lens mode-locked Ti:sapphire laser," *Optics Letters*, vol. 24, pp. 411–3, 1999.
- [5] R. W. Keyes, "Power dissipation in information processing." *Science*, vol. 168, pp. 796–801, 1970.
- [6] R. W. Keyes, "Physical limits in digital electronics," *Proceedings of the IEEE*, vol. 63, pp. 740–67, 1975.
- [7] E. O. Johnson, "Physical limits on frequency and power parameters of transistors," *RCA Review*, vol. 26, pp. 163–77, 1965.
- [8] A. V. Krishnamoorthy and D. A. B. Miller, "Scaling optoelectronic-VLSI circuits into the 21st century: A technology roadmap," *IEEE Journal on Selected Topics in Quantum Electronics*, vol. 2, pp. 55–76, 1996.

- [9] P. W. Smith, "On the physical limits of digital optical switching and logic elements," *Bell Systems Technology Journal*, vol. 61, pp. 1975–93, 1982.
- [10] A. R. Chraplyvy and R. W. Tkach, "Terabit/Second Transmission Experiments," *IEEE Journal of Quantum Electronics*, vol. 34, pp. 2103–08, 1998.
- [11] T. Li, "The impact of optical amplifiers on long-distance lightwave telecommunications," *Proceedings of the IEEE*, vol. 81, pp. 1568–79, 1993.
- [12] H. Onaka, H. Miyata, G. Ishikawa, K. Otsuka, H. Ooi, Y. Kai, S. Kinoshita, M. Seino, H. Hishimoto, and T. Chikama, "1.1 Tb/s WDM transmission over a 150 km 1.3  $\mu\text{m}$  zero-dispersion single-mode fiber," presented at the *Optical Fiber Conference*, San José, CA, 1996.
- [13] A. R. Chraplyvy, A. H. Gnauck, R. W. Tkach, J. L. Zyskind, W. Sulhoff, A. J. Lucero, Y. Sun, R. M. Jopson, F. Forghieri, R. M. Derosier, C. Wolf, and A. R. McCormick, "One terabit/s transmission experiment," *IEEE Photonics Technology Letters*, vol. 8, pp. 1264–6, 1996.
- [14] T. Morioka, H. Takara, S. Kawanishi, O. Kamatani, K. Takiguchi, K. Uchiyama, M. Saruwatari, H. Takahashi, M. Yamada, T. Kanamori, and H. Ono, "1 Tbit/s (100 Gbit/s $\times$ 10 channel) OTDM/WDM transmission using a single supercontinuum WDM source," *Electronics Letters*, vol. 32, pp. 906–7, 1996.
- [15] Y. Yano, T. Ono, T. Ito, H. Yamazaki, M. Yamaguchi, and K. Emura, "2.6 Terabit/s WDM transmission experiment using optical duobinary coding," presented at the *European Conference on Optical Communication*, Oslo, Norway, 1996.
- [16] S. Kawanishi, H. Takara, K. Uchiyama, I. Shake, O. Kamatani, and H. Takahashi, "1.4 Tbit/s (200 Gbit/s  $\times$  7 ch) 50 km optical transmission experiment," *Electronics Letters*, vol. 33, pp. 1716–8, 1997.

- [17] A. K. Srivastava, Y. Sun, J. W. Sulhoff, C. Wolf, M. Zirngibl, R. Monnard, A. R. Chraplyvy, A. A. Abramov, R. P. Espindola, T. A. Strasser, J. R. Pedrazzani, A. M. Vengsarkar, J. L. Zyskind, J. Zhou, D. A. Ferrand, P. F. Wysocki, J. B. Judkins, and Y. P. Li, "1 Tb/s transmission of 100 WDM 10 Gb/s channels over 400 km of TrueWave fiber," presented at the *Optical Fiber Conference*, San José, CA, 1998.
- [18] S. Aisawa, T. Sakamoto, M. Fukui, J. Kani, M. Jinno, and K. Oguchi, "Ultra-wideband, long distance WDM demonstration of 1 Tbit/s ( $50 \times 20$  Gbit/s), 600 km transmission using 1550 and 1580 nm wavelength bands," *Electronics Letters*, vol. 34, pp. 1127–29, 1998.
- [19] C. D. Chen, I. Kim, O. Mizuhara, T. V. Nguyen, K. Ogawa, R. E. Tench, L. D. Tzeng, and P. D. Yeates, "1.2-Tb/s (30 ch  $\times$  40 Gbit/s) WDM transmission over 85 km fibre," *Electronics Letters*, vol. 34, pp. 1002–4, 1998.
- [20] C. D. Chen, I. Kim, O. Mizuhara, T. V. Nguyen, K. Ogawa, R. E. Tench, L. D. Tzeng, and P. D. Yeates, "1.4-Tb/s (35 ch  $\times$  40 Gb/s) WDM transmission experiment over 85 km standard single-mode fiber," presented at *Optoelectronics and Communications Conference*, Chiba, Japan, 1998.
- [21] H. S. Loka and P. W. E. Smith, "Ultrafast all-optical switching in an asymmetric Fabry-Pérot device using low-temperature-grown GaAs," *IEEE Photonics Technology Letters*, vol. 10, pp. 1733–5, 1998.
- [22] R. Takahashi, Y. Kawamura, and H. Iwamura, "Ultrafast 1.55  $\mu\text{m}$  all-optical switching using low-temperature-grown multiple quantum wells," *Applied Physics Letters*, vol. 68, pp. 153–5, 1996.
- [23] L. Qian, S. D. Benjamin, P. W. E. Smith, B. J. Robinson, and D. A. Thompson, "Picosecond carrier lifetime and large optical nonlinearity in InGaAsP grown by He-plasma-assisted molecular beam epitaxy," *Optics Letters*, vol. 22, pp. 108–110, 1997.

- [24] L. Qian, P. W. E. Smith, M. A. Matin, B. J. Robinson, and D. A. Thompson, "Ultrafast all-optical asymmetric Fabry-Pérot switch based on bulk beryllium-doped InGaAsP grown by He-plasma-assisted epitaxy," presented at the *Conference on Lasers and Electro-optics*, San Francisco, CA, 2000.
- [25] D. C. Hutchings, M. Sheik-Bahae, D. J. Hagan, and E. W. van Stryland, "Kramers-Krönig relations in nonlinear optics," *Optical and Quantum Electronics*, vol. 24, pp. 1–30, 1992.
- [26] B. E. A. Saleh and M. C. Teich. *Fundamentals of Photonics*, Chapter 21: Wiley-Interscience, 1991.
- [27] M. A. Duguay and J. W. Hansen, "An ultrafast light gate," *Applied Physics Letters*, vol. 15, pp. 192–4, 1969.
- [28] P. Ferro, M. Haelterman, S. Trillo, S. Wabnitz, and B. Daino, "All-optical polarisation switch with long low-birefringence fibre," *Electronics Letters*, vol. 27, pp. 1407–8, 1991.
- [29] P. A. Snow, I. E. Day, I. H. White, R. V. Penty, H. K. Tsang, R. S. Grant, Z. Su, W. Sibbett, J. B. D. Soole, H. P. Leblanc, A. S. Gozdz, N. C. Andreadakis, and C. Caneau, "Demonstration of polarisation rotation gate in GaAs/AlGaAs multiquantum well waveguides," *Electronics Letters*, vol. 28, pp. 2346–8, 1992.
- [30] I. E. Day, P. A. Snow, Z. Jiang, R. V. Penty, I. H. White, D. A. O. Davies, M. A. Fisher, and M. J. Adams, "Low power all-optical polarisation gate switch in a passive InGaAsP MQW waveguide at 1.53  $\mu\text{m}$ ," *Electronics Letters*, vol. 30, pp. 1050–1, 1994.
- [31] J. T. Hyland, G. T. Kennedy, A. Miller, and C. C. Button, "Picosecond all-optical polarization switching in InGaAsP MQW's at 1.52  $\mu\text{m}$ ," *IEEE Photonics Technology Letters*, vol. 10, pp. 1419–21, 1998.

- [32] A. Tackeuchi, O. Wada, and Y. Nishikawa, "Electron spin relaxation in InGaAs/InP multiple quantum wells," *Applied Physics Letters*, vol. 70, pp. 1131–3, 1997.
- [33] J. Hyland, G. T. Kennedy, and A. Miller, "Electron spin relaxation in InGaAs/InGaAsP multiple quantum wells," presented at Tech. Dig. 13th Nat. Quantum Electronics Conference, Cardiff, U.K., 1997.
- [34] G. Bastard and R. Ferreira, "Spin flip scattering times in semiconductor quantum wells," *Surf. Sci.*, vol. 267, pp. 335–41, 1992.
- [35] R. S. Britton, T. Grevatt, A. Malinowski, R. T. Harley, P. Perozzo, A. R. Camerson, and A. Miller, "Room temperature spin relaxation in GaAs/AlGaAs multiple quantum wells," *Applied Physics Letters*, vol. 73, pp. 2140–2, 1998.
- [36] J. Fick and G. Vitrant, "Fast optical switching in nonlinear prism couplers," *Optics Letters*, vol. 20, pp. 1462–4, 1995.
- [37] U. Peschel, T. Peschel, F. Lederer, D. Berard, P. Dansas, and N. Paraire, "Switching dynamics of the reflected field in a nonlinear grating coupler," *Journal of the Optical Society of America B*, vol. 12, pp. 1249–58, 1995.
- [38] N. D. Sankey, D. F. Prelewitz, and T. G. Brown, "All-optical switching in a nonlinear periodic-waveguide structure," *Applied Physics Letters*, vol. 60, pp. 1427–9, 1992.
- [39] J. E. Ehrlich, G. Assanto, and G. I. Stegeman, "All-optical tuning of waveguide nonlinear distributed feedback gratings," *Applied Physics Letters*, vol. 56, pp. 602–4, 1990.
- [40] C. Coriasso, D. Campi, C. Cacciatore, L. Faustini, C. Rigo, and A. Stano, "All-optical switching and pulse routing in a distributed-feedback waveguide device," *Optics Letters*, vol. 23, pp. 183–5, 1998.
- [41] C. Coriasso, D. Campi, L. Faustini, A. Stano, and C. Cacciatore, "Optically controlled contradirectional coupler," *IEEE Journal of Quantum Electronics*, vol. 35, pp. 298–305, 1999.

- [42] K. Nakatsuhara, T. Mizumoto, E. Takahashi, S. Hossain, Y. Saka, B. J. Ma, and Y. Nakano, "All-optical switching in a distributed-feedback GaInAsP waveguide," *Applied Optics*, vol. 38, pp. 3911–16, 1999.
- [43] G. I. Stegeman, E. M. Wright, N. Finlayson, R. Zanoni, and C. T. Seaton, "Third order nonlinear integrated optics," *Journal of Lightwave Technology*, vol. 6, pp. 953–70, 1988.
- [44] H. G. Winful, J. H. Marburger, and G. E., "Theory of bistability in nonlinear distributed feedback structures," *Applied Physics Letters*, vol. 35, pp. 379–81, 1979.
- [45] H. G. Winful and G. I. Stegeman, "Applications of nonlinear periodic structures in guided wave optics," *SPIE Proc. First Int. Conf. Integrated Optical Eng*, vol. 517, pp. 214–8, 1984.
- [46] C. M. de Sterke and J. E. Sipe, "Switching dynamics of finite periodic nonlinear media: A numerical study," *Physical Review A*, vol. 42, pp. 2858–69, 1990.
- [47] C. F. Janz, B. P. Keyworth, W. Allegretto, R. I. Macdonald, M. Fallahi, G. Hillier, and C. Rolland, "Mach-Zehnder switch using an ultra-compact directional coupler in a strongly-confining rib structure," *IEEE Photonics Technology Letters*, vol. 6, pp. 981–3, 1994.
- [48] H. G. Park, C. C. Pohalski, and B. Y. Kim, "Optical Kerr switch using elliptical-core two-mode fiber," *Optics Letters*, vol. 13, pp. 776–8, 1988.
- [49] P. Li Kam Wa, P. N. Robson, J. S. Roberts, M. A. Pate, and J. P. R. David, "All-optical switching between modes of GaAs/GaAlAs multiple quantum well waveguide," *Applied Physics Letters*, vol. 52, pp. 2013–14, 1988.
- [50] I. Gontijo, D. T. Neilson, J. E. Ehrlich, A. C. Walker, G. T. Kennedy, and W. Sibbett, "Nonlinear single wavelength polarization switching in InGaAs/InP quantum well waveguides," *Applied Physics Letters*, vol. 66, pp. 1871–3, 1995.

- [51] I. Gontijo, D. T. Neilson, A. C. Walker, G. T. Kennedy, and W. Sibbett, "Nonlinear InGaAs-InGaAsP single-quantum-well all-optical switch-theory and experiments," *IEEE Journal of Quantum Electronics*, vol. 32, pp. 2112–21, 1996.
- [52] S. Nakamura and K. Tajima, "Ultrafast all-optical gate switch based on frequency shift accompanied by semiconductor band-filling effect," *Applied Physics Letters*, vol. 70, pp. 3498–3500, 1997.
- [53] N. R. Belashenkov, S. V. Gagarskii, and M. V. Inochkin, "Nonlinear refraction of light on second-harmonic generation," *Optics and Spectroscopy*, vol. 66, pp. 806–8, 1989.
- [54] R. DeSalvo, D. J. Hagan, M. Sheik Bahae, G. Stegeman, E. W. Van Stryland, and H. Vanherzeele, "Self-focusing and self-defocusing by cascaded second-order effects in KTP," *Optics Letters*, vol. 17, pp. 28–30, 1992.
- [55] G. I. Stegeman, M. Sheik-Bahae, E. van Stryland, and G. Assanto, "Large nonlinear phase shifts in second-order nonlinear-optical processes," *Optics Letters*, vol. 18, pp. 13–15, 1993.
- [56] L. Goldberg and J. P. Koplow, "Highly efficient 4-W Yb-doped fiber amplifier pumped by a broad-stripe laser diode," *Optics Letters*, vol. 24, pp. 673–5, 1999.
- [57] E. S. Kintzer, J. N. Walpole, S. R. Chinn, C. A. Wang, and L. J. Missaggia, "High-power, strained-layer amplifiers and lasers with tapered gain regions," *IEEE Photonics Technology Letters*, vol. 5, pp. 605–8, 1993.
- [58] G. Mitchard and R. Waarts, "Double-clad fibers enable lasers to handle high power," *Laser Focus World*, pp. 113–5, 1999.
- [59] S. Gee, G. Alphonse, J. Connolly, and P. J. Delfyett, "High-power mode-locked external cavity semiconductor laser using inverse bow-tie semiconductor optical amplifiers," *IEEE Journal of Selected Topics in Quantum Electronics*, vol. 4, pp. 209–15, 1998.

- [60] C. M. Caves, "Quantum limits on noise in linear amplifiers," *Physical Review D*, vol. 26, pp. 1817–21, 1982.
- [61] S. M. Jensen, "The nonlinear coherent coupler," *IEEE Journal of Quantum Electronics*, vol. 18, pp. 1580–3, 1982.
- [62] D. Marcuse, *Theory of dielectric optical waveguides*, Second Edition, Academic Press, 1991.
- [63] E. M. Wright, S. W. Koch, J. E. Ehrlich, C. T. Seaton, and G. I. Stegeman, "Semiconductor figure of merit for nonlinear directional couplers," *Applied Physics Letters*, vol. 52, pp. 2127–9, 1988.
- [64] P. Li Kam Wa, J. E. Sitch, N. J. Mason, J. S. Roberts, and P. N. Robson, "All optical multiple-quantum-well waveguide switch," *Electronics Letters*, vol. 21, pp. 26–8, 1985.
- [65] D. D. Gusovskii, E. M. Dianov, A. A. Maier, V. B. Neustruev, E. I. Shklovskii, and I. A. Shcherbakov, "Nonlinear light transfer in tunnel-coupled optical waveguides," *Soviet Journal of Quantum Electronics*, vol. 15, pp. 1523–6, 1985.
- [66] S. R. Friberg, Y. Silberberg, M. K. Oliver, M. J. Andrejco, M. A. Saifi, and P. W. Smith, "Ultrafast all-optical switching in a dual-core fiber nonlinear coupler," *Applied Physics Letters*, vol. 51, pp. 1135–7, 1987.
- [67] U. Das, Y. Chen, and P. Bhattacharya, "Nonlinear effects in coplanar GaAs/InGaAs strained-layer superlattice directional couplers," *Applied Physics Letters*, vol. 51, pp. 1679–81, 1987.
- [68] R. Jin, C. L. Chuang, H. M. Gibbs, S. W. Koch, J. N. Polky, and G. A. Pubanz, "Picosecond all-optical switching in single-mode GaAs/AsGaAs strip-loaded nonlinear directional couplers," *Applied Physics Letters*, vol. 53, pp. 1791–3, 1988.

- [69] A. Villeneuve, C. C. Yang, P. G. J. Wigley, G. I. Stegeman, J. S. Aitchison, and C. N. Ironside, "Ultrafast all-optical switching in semiconductor nonlinear directional couplers at half the band gap," *Applied Physics Letters*, vol. 61, pp. 147–9, 1992.
- [70] S. G. Lee, B. P. McGinnis, R. Jin, J. Yumoto, G. Khitrova, H. M. Gibbs, R. Binder, S. W. Koch, and N. Peyghambarian, "Subpicosecond switching in a current injected GaAs/AlGaAs multiple-quantum-well nonlinear directional coupler," *Applied Physics Letters*, vol. 64, pp. 454–6, 1994.
- [71] D. A. O. Davies, M. A. Fisher, D. J. Elton, S. D. Perrin, M. J. Adams, G. T. Kennedy, R. S. Grant, P. D. Roberts, and W. Sibbett, "Nonlinear switching in InGaAsP laser amplifier directional couplers biased at transparency," *Electronics Letters*, vol. 29, pp. 1710–11, 1993.
- [72] S. Trillo, S. Wabnitz, J. M. Soto-Crespo, and E. M. Wright, "Ultrashort pulse self-switching in coupled-semiconductor traveling-wave amplifiers," *IEEE Journal of Quantum Electronics*, vol. 27, pp. 410–15, 1991.
- [73] J. S. Aitchison, A. Villeneuve, and G. I. Stegeman, "Nonlinear directional couplers in AlGaAs," *Journal of Nonlinear Optical Physics and Materials*, vol. 4, pp. 871–91, 1995.
- [74] E. Caglioti, S. Trillo, S. Wabnitz, B. Daino, and G. I. Stegeman, "Power-dependent switching in a coherent nonlinear directional coupler in the presence of saturation," *Applied Physics Letters*, vol. 51, pp. 293–5, 1987.
- [75] G. I. Stegeman, C. T. Seaton, C. N. Ironside, T. Cullen, and A. C. Walker, "Effects of saturation and loss on nonlinear directional couplers," *Applied Physics Letters*, vol. 50, pp. 1035–7, 1987.
- [76] G. I. Stegeman, E. Caglioti, S. Trillo, and S. Wabnitz, "Parameter trade-offs in nonlinear directional couplers: two level saturable nonlinear media," *Optics Communications*, vol. 63, pp. 281–4, 1987.

- [77] E. Caglioti, S. Trillo, S. Wabnitz, and G. I. Stegeman. "Limitations to all-optical switching using nonlinear couplers in the presence of linear and nonlinear absorption and saturation," *Journal of the Optical Society of America B*, vol. 5, pp. 472–82, 1988.
- [78] M. Sheik-Bahae, D. C. Hutchings, D. J. Hagan, and E. W. Van Stryland, "Dispersion of bound electronic nonlinear refraction in solids," *IEEE Journal of Quantum Electronics*, vol. 27, pp. 1296–1309, 1991.
- [79] K. Al-Hemyari, A. Villeneuve, J. U. Kang, J. S. Aitchison, C. N. Ironside, and G. I. Stegeman, "Ultrafast all-optical switching in GaAlAs directional couplers at 1.55  $\mu\text{m}$  without multiphoton absorption," *Applied Physics Letters*, vol. 63, pp. 3562–4, 1993.
- [80] A. Villeneuve, P. Mamyshchev, J. U. Kang, G. I. Stegeman, J. S. Aitchison, and C. N. Ironside, "Efficient time-domain demultiplexing with separate signal and control wavelengths in an AlGaAs nonlinear directional coupler," *IEEE Journal of Quantum Electronics*, vol. 31, pp. 2165–72, 1995.
- [81] J. M. Liu and C. Yeh, "Optical switching by saturation-induced phase changes in an active directional coupler," *Applied Physics Letters*, vol. 50, pp. 1625–7, 1987.
- [82] P. R. Berger, C. Yi, P. Bhattacharya, J. Pamulapati, and G. C. Vezzoli, "Demonstration of all-optical modulation in a vertical guided-wave nonlinear coupler," *Applied Physics Letters*, vol. 52, pp. 1125–7, 1988.
- [83] P. R. Berger, P. K. Bhattacharya, and S. Gupta, "A waveguide directional coupler with a nonlinear coupling medium," *IEEE Journal of Quantum Electronics*, vol. 27, pp. 788–95, 1991.
- [84] K. Tajima, "All-optical switch with switch-off time unrestricted by carrier lifetime," *Japanese Journal of Applied Physics, Part 2 [Letters]*, vol. 32, pp. L1746–9, 1993.

- [85] K. Tajima, K. I. Kang, I. Glesk, T. G. Chang, P. R. Prucnal, and R. K. Boncek, "Demonstration of all-optical Mach-Zehnder demultiplexer," *Electronics Letters*, vol. 31, pp. 1494–5, 1995.
- [86] K. Tajima, S. Nakamura, and Y. Ueno, "Femtosecond all-optical switching using efficient incoherent nonlinearity with slow relaxation," *Materials Science and Engineering*, vol. B48, pp. 88–93, 1997.
- [87] S. Nakamura, K. Tajima, and Y. Sugimoto, "Experimental investigation on high-speed switching characteristics of a novel symmetric Mach-Zehnder all-optical switch," *Applied Physics Letters*, vol. 65, pp. 283–5, 1994.
- [88] I. Glesk, J. P. Sokoloff, and P. R. Prucnal, "Demonstration of all-optical demultiplexing of TDM data at 250 Gbit/s," *Electronics Letters*, vol. 30, pp. 339–41, 1994.
- [89] K. I. Kang, T. G. Chang, I. Glesk, P. R. Prucnal, and R. K. Boncek, "Demonstration of ultrafast, all-optical, low control energy, single wavelength, polarization independent, cascable, and integrable switch," *Applied Physics Letters*, vol. 67, pp. 605–7, 1995.
- [90] N. S. Patel, K. L. Hall, and K. A. Rauschenbach, "40-Gbit/s cascable all-optical logic with an ultrafast nonlinear interferometer," *Optics Letters*, vol. 21, pp. 1466–8, 1996.
- [91] N. S. Patel, K. A. Rauschenbach, and K. L. Hall, "40-Gb/s demultiplexing using an ultrafast nonlinear interferometer (UNI)," *IEEE Photonics Technology Letters*, vol. 8, pp. 1695–7, 1996.
- [92] S. Nakamura, Y. Ueno, and K. Tajima, "Ultrafast (200-fs switching, 1.5-Tb/s demultiplexing) and high-repetition (10 GHz) operations of a polarization-discriminating symmetric Mach-Zehnder all-optical switch," *IEEE Photonics Technology Letters*, vol. 10, pp. 1575–7, 1998.

- [93] A. E. Siegman, "An antiresonant ring interferometer for coupled laser cavities, laser output coupling, mode locking, and cavity dumping," *IEEE Journal of Quantum Electronics*, pp. 247–50, 1973.
- [94] K. Otsuka, "Nonlinear antiresonant ring interferometer," *Optics Letters*, vol. 8, pp. 471–3, 1983.
- [95] N. J. Doran and D. Wood, "Nonlinear-optical loop mirror," *Optics Letters*, vol. 13, pp. 56–8, 1988.
- [96] K. J. Blow, N. J. Doran, and B. K. Nayar, "Experimental demonstration of optical soliton switching in an all-fiber nonlinear Sagnac interferometer," *Optics Letters*, vol. 14, pp. 754–6, 1989.
- [97] K. J. Blow, N. J. Doran, and B. P. Nelson, "Demonstration of the nonlinear fibre loop mirror as an ultrafast all-optical demultiplexer," *Electronics Letters*, vol. 26, pp. 962–4, 1990.
- [98] M. N. Islam, E. R. Sunderman, R. H. Stolen, W. Pleibel, and J. R. Simpson, "Soliton switching in a fiber nonlinear loop mirror," *Optics Letters*, vol. 14, pp. 811–13, 1989.
- [99] M. Jinno and T. Matsumoto, "Ultrafast, low power, and highly stable all-optical switching in an all polarization maintaining fiber Sagnac interferometer," *IEEE Photonics Technology Letters*, vol. 2, pp. 349–51, 1990.
- [100] G. P. Agrawal, *Nonlinear Fiber Optics*, Second Edition, San Diego: Academic Press, 1995.
- [101] K. Uchiyama, H. Takara, S. Kawanishi, T. Morioka, and M. Saruwatari, "Ultrafast polarisation-independent all-optical switching using a polarisation diversity scheme in the nonlinear optical loop mirror," *Electronics Letters*, vol. 28, pp. 1864–6, 1992.

- [102] H. Bülow and G. Veith, "System performance of a nonlinear optical loop mirror used as demultiplexer for bit rates of 40 Gbit/s and beyond," *Proceedings of the SPIE The International Society for Optical Engineering*, vol. 2449, pp. 158–67, 1995.
- [103] H. Bülow, T. Pfeiffer, and C. Veith, "Polarisation-insensitive all-optical demultiplexing over a wide wavelength range in a short-fibre nonlinear optical loop mirror," *Electronics Letters*, vol. 30, pp. 68–9, 1994.
- [104] Y. Liang, J. W. Lou, J. K. Andersen, J. C. Stocker, O. Boyraz, and M. N. Islam, "Polarization-insensitive nonlinear optical loop mirror demultiplexer with twisted fiber," *Optical Letters*, vol. 24, pp. 726–8, 1999.
- [105] J. W. Lou, J. K. Andersen, J. C. Stocker, M. N. Islam, and D. A. Nolan, "Polarization insensitive demultiplexing of 100 Gb/s words using a twisted fiber nonlinear optical loop mirror," *IEEE Photonics Technology Letters*, vol. 11, pp. 1602–4, 1999.
- [106] M. Jinno and T. Matsumoto, "Nonlinear Sagnac interferometer switch and its applications," *IEEE Journal of Quantum Electronics*, vol. 28, pp. 875–82, 1992.
- [107] K. Uchiyama, T. Morioka, and M. Saruwatari, "Polarisation-independent wavelength conversion using nonlinear optical loop mirror," *Electronics Letters*, vol. 31, pp. 1862–3, 1995.
- [108] N. S. Patel, K. L. Hall, and K. A. Rauschenbach, "Optical rate conversion for high-speed TDM networks," *IEEE Photonics Technology Letters*, vol. 9, pp. 1277–9, 1997.
- [109] S. Bigo, O. Leclerc, and E. Desurvire, "All-optical fiber signal processing and regeneration for soliton communications," *IEEE Journal of Selected Topics in Quantum Electronics*, vol. 3, pp. 1208–23, 1997.

- [110] A. W. O'Neill and R. P. Webb, "All-optical loop mirror switch employing an asymmetric amplifier/attenuator combination," *Electronics Letters*, vol. 26, pp. 2008–9, 1990.
- [111] M. Eiselt, "Optical loop mirror with semiconductor laser amplifier," *Electronics Letters*, vol. 28, pp. 1505–7, 1992.
- [112] M. Eiselt, W. Pieper, and H. G. Weber, "All-optical high speed demultiplexing with a semiconductor laser amplifier in a loop mirror configuration," *Electronics Letters*, vol. 29, pp. 1167–8, 1993.
- [113] M. Eiselt, W. Pieper, and H. G. Weber, "New optical correlator technique for header recognition in self-routing networks," presented at OFC/IOOC'93, 1993.
- [114] I. P. Sokoloff, R. R. Prucnal, I. Glesk, and M. Kane, "A terahertz optical asymmetric demultiplexer (TOAD)," presented at *Photonics in Switching 1993*, Palm Springs, USA, 1993.
- [115] J. P. Sokoloff, P. R. Prucnal, I. Glesk, and M. Kane, "A terahertz optical asymmetric demultiplexer (TOAD)," *IEEE Photonics Technology Letters*, vol. 5, pp. 787–90, 1993.
- [116] R. J. Manning, A. D. Ellis, A. J. Poustie, and K. J. Blow, "Semiconductor laser amplifiers for ultrafast all-optical signal processing," *Journal of the Optical Society of America B*, vol. 14, pp. 3204–16, 1997.
- [117] E. Jahn, N. Agrawal, W. Pieper, H. J. Ehrke, D. Franke, W. Furst, and C. M. Weinert, "Monolithically integrated nonlinear Sagnac interferometer and its application as a 20 Gbit/s all-optical demultiplexer," *Electronics Letters*, vol. 32, pp. 782–4, 1996.
- [118] S. Diez, R. Ludwig, and H. G. Weber, "Gain-transparent SOA-switch for high-bitrate OTDM add/drop multiplexing," *IEEE Photonics Technology Letters*, vol. 11, pp. 60–2, 1999.

- [119] J. P. R. Lacey, G. J. Pendock, and R. S. Tucker, "All-optical 1300-nm to 1550-nm wavelength conversion using cross-phase modulation in a semiconductor optical amplifier," *IEEE Photonics Technology Letters*, vol. 8, pp. 885–7, 1996.
- [120] A. Migus, A. Antonetti, D. Hulin, A. Mysyrowicz, H. M. Gibbs, N. Peyghambarian, and J. L. Jewell, "One-picosecond optical NOR gate at room temperature with a GaAs-AlGaAs multiple-quantum-well nonlinear Fabry-Pérot etalon," *Applied Physics Letters*, vol. 46, pp. 70–2, 1985.
- [121] P. Li Kam Wa, P. N. Robson, J. P. R. David, G. Hill, P. Mistry, M. A. Pate, and J. S. Roberts, "All-optical switching effects in a passive GaAs/GaAlAs multiple-quantum-well waveguide resonator," *Electronics Letters*, vol. 22, pp. 1129–30, 1986.
- [122] M. Whitehead, A. Rivers, G. Parry, J. S. Roberts, and C. Button, "Low-voltage multiple quantum well reflection modulator with on:off ratio >100:1," *Electronics Letters*, vol. 25, pp. 984–5, 1989.
- [123] R. H. Yan, R. J. Simes, and L. A. Coldren, "Electroabsorptive Fabry-Pérot reflection modulators with asymmetric mirrors," *IEEE Photonics Technology Letters*, vol. 1, pp. 273–5, 1989.
- [124] M. F. Krol, T. Ohtsuki, G. Khitrova, R. K. Boncek, B. P. McGinnis, H. M. Gibbs, and N. Peyghambarian, "All-optical, high contrast GaAlInAs multiple quantum well asymmetric reflection modulator at 1.3  $\mu\text{m}$ ," *Applied Physics Letters*, vol. 62, pp. 1550–2, 1993.
- [125] H. Kobayashi, R. Takahashi, Y. Matsuoka, and H. Iwamura, "1 Tbit/s demultiplexing using low temperature grown InGaAs/InAlAs multiple quantum wells," *Electronics Letters*, vol. 34, pp. 908–10, 1998.
- [126] R. Takahashi, H. Itoh, and H. Iwamura, "Ultrafast, high-contrast, polarization-insensitive all-optical switch by using spin-polarization in low-temperature-grown

- MQWs,” *Proceedings of the Conference on Lasers and Electro-Optics (CLEO '99)*, Baltimore, MA, paper CThF4, pp. 378–9, 1999.
- [127] R. Takahashi, Y. Kawamura, T. Kagawa, and H. Iwamura, “Ultrafast 1.55- $\mu\text{m}$  photoresponses in low-temperature-grown InGaAs/InAlAs quantum wells,” *Applied Physics Letters*, vol. 65, pp. 1790–2, 1994.
- [128] T. Akiyama, M. Tsuchiya, and K. Takeshi, “Sub-pJ operation of broadband asymmetric Fabry-Perot all-optical gate with coupled cavity structure,” *Applied Physics Letters*, vol. 72, pp. 1545–7, 1998.
- [129] H. S. Loka, S. D. Benjamin, and P. W. E. Smith, “Optical characterization of low-temperature-grown GaAs for ultrafast all-optical switching devices,” *IEEE Journal of Quantum Electronics*, vol. 34, pp. 1426–37, 1998.
- [130] H. Haug, “Microscopic theory of the optical band edge nonlinearities,” in *Optical Nonlinearities and Instabilities in Semiconductors*, H. Haug, Ed., San Diego: Academic Press, 1988, pp. 53–82.
- [131] W. H. Knox, D. S. Chemla, G. Livescu, J. E. Cunningham, and J. E. Henry, “Femtosecond carrier thermalization in dense Fermi seas,” *Physical Review Letters*, vol. 61, pp. 1290–3, 1988.
- [132] J. L. Oudar, D. Hulin, A. Migus, and A. Antonetti, “Subpicosecond spectral hole burning due to nonthermalized photoexcited carriers in GaAs,” *Physical Review Letters*, vol. 55, pp. 2074–7, 1985.
- [133] H. Lobentanzer, W. Stolz, J. Nagle, and K. Ploog, “Cooling of hot carriers in three- and two-dimensional  $\text{Ga}_{0.47}\text{In}_{0.53}\text{As}$ ,” *Physical Review B*, vol. 39, pp. 5234–44, 1989.
- [134] K. L. Hall, G. Lenz, A. M. Darwish, and E. P. Ippen, “Subpicosecond gain and index nonlinearities in InGaAsP diode lasers,” *Optics Communications*, vol. 111, pp. 589–612, 1994.

- [135] J. Mark and J. Mørk, "Subpicosecond gain dynamics in InGaAsP optical amplifiers: Experiment and theory," *Applied Physics Letters*, vol. 61, pp. 2281–3, 1992.
- [136] K. K. Anderson, M. J. LaGasse, C. A. Wang, J. G. Fujimoto, and H. A. Haus, "Femtosecond dynamics of the nonlinear index near the band edge in AlGaAs waveguides," *Applied Physics Letters*, vol. 56, pp. 1834–6, 1990.
- [137] H. K. Tsang, P. A. Snow, I. E. Day, I. H. White, R. V. Penty, R. S. Grant, Z. Su, G. T. Kennedy, and W. Sibbett, "All-optical modulation with ultrafast recovery at low pump energies in passive InGaAs/InGaAsP multiquantum well waveguides," *Applied Physics Letters*, vol. 62, pp. 1451–3, 1993.
- [138] C. T. Hultgren, D. J. Dougherty, and E. P. Ippen, "Above- and below-band femtosecond nonlinearities in active AlGaAs waveguides," *Applied Physics Letters*, vol. 61, pp. 2767–9, 1992.
- [139] N. Peyghambarian and S. W. Koch, "Semiconductor Nonlinear Materials," in *Nonlinear Photonics*, vol. 30, *Springer Series in Electronics and Photonics*, H. M. Gibbs, G. Khitrova, and N. Peyghambarian, Eds. Berlin Heidelberg: Springer-Verlag, 1990, pp. 7–60.
- [140] W. H. Knox, R. L. Fork, M. C. Downer, D. A. B. Miller, D. S. Chemla, C. V. Shank, A. C. Gossard, and W. Wiegmann, "Femtosecond dynamics of resonantly excited excitons in room-temperature GaAs quantum wells," *Physical Review Letters*, vol. 54, pp. 1306–9, 1985.
- [141] D. S. Chemla, D. A. B. Miller, P. W. Smith, A. C. Gossard, and W. Wiegmann, "Room temperature excitonic nonlinear absorption and refraction in GaAs/AlGaAs multiple quantum well structures," *IEEE Journal of Quantum Electronics*, vol. QE-20, pp. 265–75, 1984.
- [142] M. I. Dyakonov and V. I. Perel, "Theory of optical spin orientation of electrons and nuclei in semiconductors," in *Optical Orientation*, vol. 8, *Modern Problems in*

- Condensed Matter Science*, F. Meier and B. P. Zakharchenya, Eds., Amsterdam, The Netherlands: North-Holland, 1984, pp. 11–71.
- [143] G. E. Pikus and A. N. Titkov, “Spin relaxation under optical orientation in semiconductors,” in *Optical Orientation*, vol. 8, *Modern Problems in Condensed Matter Science*, F. Meier and B. P. Zakharchenya, Eds. Amsterdam, The Netherlands: North-Holland, 1984, pp. 73–132.
- [144] Y. Nishikawa, A. Tackeuchi, S. Nakamura, S. Muto, and N. Yokoyama, “All optical picosecond switching of a quantum well etalon using spin polarization relaxation,” *Applied Physics Letters*, vol. 66, pp. 839–41, 1995.
- [145] A. Tackeuchi, S. Muto, T. Inata, and T. Fujii, “Fast recovery of excitonic absorption bleaching in tunneling biquantum well structures,” *Applied Physics Letters*, vol. 58, pp. 1670–2, 1991.
- [146] A. Tackeuchi, T. Inata, Y. Sugiyama, Y. Nakata, S. Nakamura, and S. Muto, “Fast recovery from excitonic absorption bleaching in type-II GaAs/AlGaAs/AlAs tunneling biquantum well,” *Japanese Journal of Applied Physics*, vol. 31, Part 2, pp. L669–L672, 1992.
- [147] B. Deveaud, A. Chomette, F. Clerot, P. Auvray, and A. Regreny, “Subpicosecond luminescence study of tunneling and relaxation in coupled quantum wells,” *Physical Review B*, vol. 42, pp. 7021–32, 1990.
- [148] J. Feldmann, J. Nunnenkamp, P. G., E. Göbel, J. Kuhl, K. Ploog, P. Dawson, and C. T. Foxon, “Experimental study of the G-X electron transfer in type-II (Al,Ga)As/AlAs superlattices and multiple-quantum-well structures,” *Physical Review B*, vol. 42, pp. 5809–21, 1990.
- [149] R. Ferreira and G. Bastard, “Evaluation of some scattering times for electrons in unbiased and biased single- and multiple-quantum well structures,” *Physical Review B*, vol. 40, pp. 1074–80, 1989.

- [150] A. M. Fox, D. Miller, A. B., G. Livescu, J. E. Cunningham, and W. Jan, Y., "Quantum well carrier sweep out: relation to electroabsorption and exciton saturation," *IEEE Journal of Quantum Electronics*, vol. 27, pp. 2281–95, 1991.
- [151] I. E. Day, P. A. Snow, R. V. Penty, I. H. White, R. S. Grant, G. T. Kennedy, W. Sibbett, D. A. O. Davies, M. A. Fisher, and M. J. Adams, "Bias dependent recovery time of all-optical resonant nonlinearity in an InGaAsP/InGaAsP multiquantum well waveguide," *Applied Physics Letters*, vol. 65, pp. 2657–9, 1994.
- [152] J. R. karin, R. J. Helkey, D. J. Derickson, R. Nagarajan, D. S. Allin, J. E. Bowers, and R. L. Thornton, "Ultrafast dynamics in field-enhanced saturable absorbers," *Applied Physics Letters*, vol. 64, pp. 676–8, 1994.
- [153] R. V. Penty, H. K. Tsang, and I. H. White, "Repression and speed improvement of photogenerated carrier induced refractive nonlinearity in InGaAs/InGaAsP quantum well waveguide," *Electronics Letters*, vol. 27, pp. 1447–9, 1991.
- [154] R. J. Manning and G. Sherlock, "Recovery of a pi phase shift in approximately 12.5 ps in a semiconductor laser amplifier," *Electronics Letters*, vol. 31, pp. 307–8, 1995.
- [155] M. Usami, M. Tsurusawa, and Y. Matsushima, "Mechanism for reducing recovery time of optical nonlinearity in semiconductor laser amplifier," *Applied Physics Letters*, vol. 72, pp. 2657–2659, 1998.
- [156] R. J. Manning and D. A. O. Davies, "Three-wavelength device for all-optical signal processing," *Optics Letters*, vol. 19, pp. 889–91, 1994.
- [157] B. Sapoval and C. Hermann, *Physics of Semiconductors*, Appendix 6.2. New York: Springer-Verlag, 1995.
- [158] Y. H. Lee, H. M. Gibbs, J. L. Jewell, J. F. Duffy, T. Venkatesan, A. C. Gossard, W. Wiegmann, and J. H. English, "Speed and effectiveness of windowless GaAs etalons as optical logic gates," *Applied Physics Letters*, vol. 49, pp. 486–8, 1986.

- [159] W. S. Pelouch and L. A. Schlie, "Ultrafast band-edge carrier dynamics in  $\text{In}_{0.65}\text{Ga}_{0.35}\text{As}$ ," *Applied Physics Letters*, vol. 65, pp. 2323–5, 1994.
- [160] C. H. Lee, A. Antonetti, and G. Mourou, "Measurements on the photoconductive lifetime of carriers in GaAs by optoelectronic gating technique," *Optics Communications*, vol. 21, pp. 158–61, 1977.
- [161] S. Gupta, S. Sethi, and P. K. Bhattacharya, "Picosecond carrier lifetime in erbium-doped-GaAs," *Applied Physics Letters*, vol. 62, pp. 1128–30, 1993.
- [162] R. K. Ahrenkiel, R. Ellingson, S. Johnston, and M. Wanlass, "Recombination lifetime of  $\text{In}_{0.53}\text{Ga}_{0.47}\text{As}$  as a function of doping density," *Applied Physics Letters*, vol. 72, pp. 3470–2, 1998.
- [163] Y. Silberberg, P. W. Smith, D. A. B. Miller, B. Tell, A. C. Gossard, and W. Weigmann, "Fast nonlinear optical response from proton-bombarded multiple quantum well structures," *Applied Physics Letters*, vol. 46, pp. 701–3, 1985.
- [164] F. Ganikhanov, G.-R. Lin, W.-C. Chen, C. S. Chang, and C.-L. Pan, "Subpicosecond carrier lifetimes in arsenic-ion-implanted GaAs," *Applied Physics Letters*, vol. 67, pp. 3465–7, 1995.
- [165] E. L. Delpon, J. L. Oudar, N. Bouche, R. Raj, A. Shen, N. Stelmakh, and J. M. Lourtioz, "Ultrafast excitonic saturable absorption in ion-implanted InGaAs/InAlAs multiple quantum wells," *Applied Physics Letters*, vol. 72, pp. 759–61, 1998.
- [166] M. J. Lederer, B. Luther-Davies, H. H. Tan, C. Jagadish, M. Haiml, U. Siegner, and U. Keller, "Nonlinear optical absorption and temporal response of arsenic- and oxygen-implanted GaAs," *Applied Physics Letters*, vol. 74, pp. 1993, 1999.
- [167] M. R. Melloch, D. D. Nolte, J. M. Woodall, J. C. P. Chang, D. B. Janes, and E. S. Harmon, "Molecular beam epitaxy of nonstoichiometric semiconductors and

- multiphase material systems," *Critical Reviews in Solid State and Material Sciences*, vol. 21, pp. 189–263, 1996.
- [168] S. Gupta, P. K. Bhattacharya, J. Pamulapati, and G. Mourou, "Subpicosecond photoresponse of carriers in low-temperature molecular beam epitaxial  $\text{In}_{0.52}\text{Al}_{0.48}\text{As}/\text{InP}$ ," *Applied Physics Letters*, vol. 57, pp. 1543–5, 1990.
- [169] I. Lahiri, D. D. Nolte, E. S. Harmon, M. R. Melloch, and J. M. Woodall, "Ultrafast-lifetime quantum wells with sharp exciton spectra," *Applied Physics Letters*, vol. 66, pp. 2519–21, 1995.
- [170] Y. Kostoulas, K. B. Ucer, G. W. Wicks, and P. M. Fauchet, "Femtosecond carrier dynamics in low-temperature grown  $\text{Ga}_{0.51}\text{In}_{0.49}\text{P}$ ," *Applied Physics Letters*, vol. 67, pp. 3756–8, 1995.
- [171] P. W. Juodawlkis, D. T. McInturff, and S. E. Ralph, "Ultrafast carrier dynamics and optical nonlinearities of low-temperature-grown  $\text{InGaAs}/\text{InAlAs}$  multiple quantum wells," *Applied Physics Letters*, vol. 69, pp. 4062–4, 1996.
- [172] Y. Chen, S. S. Prabhu, S. E. Ralph, and D. T. McInturff, "Trapping and recombination dynamics of low-temperature-grown  $\text{InGaAs}/\text{InAlAs}$  multiple quantum wells," *Applied Physics Letters*, vol. 72, pp. 439–41, 1998.
- [173] H. Pinkney, *Characterization of InP and InGaAsP Grown by He-Plasma-Assisted GSMBE*. Ph.D. Thesis, McMaster University, Ontario, Canada, Chapter 2, 1999.
- [174] D. A. Thompson, D. B. Mitchell, B. J. Robinson, R. R. LaPierre, and P. Mascher, "Effect of noble gas plasmas on the growth of  $\text{InP}$  by gas-source molecular beam epitaxy," presented at the *Ninth International Conference on Ion Beam Modification of Materials*, Canberra, Australia, pp. 769–72, 1995.

- [175] D. B. Mitchell, B. J. Robinson, D. A. Thompson, L. Qian, S. D. Benjamin, and P. W. E. Smith, "He-plasma assisted epitaxy for highly resistive, optically fast InP-based materials," *Applied Physics Letters*, vol. 69, pp. 509–11, 1996.
- [176] L. Qian, S. D. Benjamin, and P. W. E. Smith, "Picosecond optical parametric oscillator tunable around 1.55  $\mu\text{m}$ ," *Optics Communications*, vol. 127, pp. 73–8, 1996.
- [177] M. Sheik-Bahae, A. A. Said, T.-H. Wei, D. J. Hagan, and E. W. Van Stryland, "Sensitive measurement of optical nonlinearities using a single beam," *IEEE Journal of Quantum Electronics*, vol. 26, pp. 760–9, 1990.
- [178] Bomem, *The Michelson Series FT-IR Spectrometer—User's Guide*, Chapter 5, 1994.
- [179] H. Pinkney, *Characterization of InP and InGaAsP Grown by He-Plasma-Assisted GSMBE*. Ph.D. Thesis, McMaster University, Ontario, Canada, Chapter 4, 1999.
- [180] J. I. Pankove, *Optical Processes in Semiconductors*. New York: Dover Publications, Chapter 1, p. 12, 1971
- [181] M. Haiml, U. Siegner, F. Morier-Genoud, U. Keller, M. Luysberg, P. Specht, and E. R. Weber, "Femtosecond response times and high optical nonlinearity in beryllium-doped low-temperature grown GaAs," *Applied Physics Letters*, vol. 74, pp. 1269–71, 1999.
- [182] H. Pinkney, D. A. Thompson, B. J. Robinson, P. J. Simpson, U. Myler, and R. W. Streater, presented at the *11th International Conference on InP and Related Materials*, Davos, Switzerland, pp. 143–6, 1999.
- [183] B. J. Robinson, personal communication, 1996.
- [184] G.-R. Lin and C.-L. Pan, "Picosecond responses of low-dosage arsenic-ion implanted GaAs photoconductors," *Applied Physics Letters*, vol. 71, pp. 2901–3, 1997.

- [185] S. U. Dankowski, D. Streb, M. Ruff, P. Kiesel, M. Kneissl, B. Knüpfer, G. H. Döhler, U. D. Keil, C. B. Sorenson, and A. K. Verma, "Above band gap absorption spectra of the arsenic antisite defect in low temperature grown GaAs and AlGaAs," *Applied Physics Letters*, vol. 68, pp. 37–39, 1996.
- [186] C. Jagadish, H. H. Tan, A. Krotkus, S. Marcinkevicius, K. P. Korona, and M. Kaminska, "Ultrafast carrier trapping in high energy ion implanted gallium arsenide," *Applied Physics Letters*, vol. 68, pp. 2225–7, 1996.
- [187] S. Gupta, M. Y. Frankel, J. A. Valdmanis, J. F. Whitaker, G. A. Mourou, F. W. Smith, and A. R. Calawa, "Subpicosecond carrier lifetime in GaAs grown by molecular beam epitaxy at low temperatures," *Applied Physics Letters*, vol. 59, pp. 3276–8, 1991.
- [188] H. Pinkney, *Characterization of InP and InGaAsP Grown by He-Plasma-Assisted GSMBE*. Ph.D. Thesis, McMaster University, Ontario, Canada, Chapter 5, 1999.
- [189] H. Haug and S. Schmitt-Rink, "Electron theory of the optical properties of laser-excited semiconductors," *Progress in Quantum Electronics*, vol. 9, pp. 3–100, 1984.
- [190] M. Stellmacher, J.-P. Schnell, D. Adam, and J. Nagles, "Photoconductivity investigation of the electron dynamics in GaAs grown at low temperature," *Applied Physics Letters*, vol. 74, pp. 1239–41, 1999.
- [191] G. I. Stegeman and E. M. Wright, "All-optical waveguide switching," *Optics and Quantum Electronics*, vol. 22, pp. 95–122, 1990.
- [192] M. R. S. Taylor, "Instruction manuals for Fwave IV," <<http://eeapp.elec.gla.ac.uk/~michaelt/software/fwave/manual.html>>, copyright 1984–96, 1996.
- [193] L. Bányai and S. W. Koch, "A simple theory for the effects of plasma screening on the optical spectra of highly excited semiconductors," *Zeitschrift für Physik B — Condensed Matter*, vol. 63, pp. 283–91, 1986.

- [194] S. Adachi, A. D. Prins, D. Lancefield, F. R. Bacher, S. J. Pearton, D. J. Robbins, and D. J. Dunstan, "InGaAs and InGaAsP: Miscellaneous properties," in *Properties of Indium Phosphide*, INSPEC, IEE, 1991, pp. 373–439.
- [195] D. Marcuse, *Theory of dielectric optical waveguides*, Second Edition, Academic Press, 1991.
- [196] R. G. Walker, "Simple and accurate loss measurement technique for semiconductor optical waveguides," *Electronics Letters*, vol. 21, pp. 581–3, 1985.
- [197] S. Adachi, "Refractive indices of III-V compounds: Key properties of InGaAsP relevant to device design," *Journal of Applied Physics*, vol. 53, pp. 5863–69, 1982.
- [198] J. Stulemeijer, A. F. Bakker, I. Moerman, F. H. Groen, and M. K. Smit, "InP-based spotsizer converter for integration with switching devices," *IEEE Photonics Technology Letters*, vol. 11, pp. 81–3, 1999.
- [199] L. Friedrich, P. Dannberg, C. Wachter, T. Hennig, A. Brauer, and W. Karthe, "4×4 directional coupler device using a three-dimensional waveguide structure," *Proceedings of the SPIE The International Society for Optical Engineering*, vol. 2954, pp. 20–9, 1996.
- [200] M. R. Paiam, C. F. Janz, R. I. MacDonald, B. P. Keyworth, and J. N. Broughton, "Compact planar waveguide couplers for broadband dual-channel wavelength (de)multiplexing," in *Applications of Photonic Technology 2: Communications, Sensing, Materials, and Signal Processing*, G. A. Lampropoulos and R. A. Lessard, Eds.: Plenum Press, 1997, pp. 445–50.
- [201] S. Charbonneau, E. S. Koteles, P. J. Poole, J. J. He, G. C. Aers, S. Haysom, M. Buchanan, Y. Feng, A. Delage, F. Yang, M. Davies, R. D. Goldberg, P. G. Piva, and I. V. Mitchell, "Photonic integrated circuits fabricated using ion implantation," *IEEE Journal of Selected Topics in Quantum Electronics*, vol. 4, pp. 772–93, 1998.

- [202] J. P. Reithmaier and A. Forchel, "Focused ion-beam implantation induced thermal quantum-well intermixing for monolithic optoelectronic device integration," *IEEE Journal of Selected Topics in Quantum Electronics*, vol. 4, pp. 595–605, 1998.
- [203] S. Charbonneau, P. J. Poole, P. G. Piva, M. Buchanan, R. D. Goldberg, and I. V. Mitchell, "Bandgap tuning of semiconductor Quantum Well laser structures using high energy ion implantation," *Nuclear Instruments & Methods in Physics Research, Section B [Beam Interactions with Materials and Atoms]*, vol. B106, pp. 457–60, 1995.
- [204] G. Zimmermann, A. Ougazzaden, A. Gloukhian, E. V. K. Rao, D. Delprat, A. Ramdane, and A. Mircea, "Selective area MOVPE growth of InP, InGaAsP and InGaAsP using TBAs and TBP at different growth conditions," *Journal of Crystal Growth*, vol. 170, pp. 645–9, 1997.
- [205] I. Aller and H. L. Hartnagel, "Selective area growth of InP by plasma assisted solid-source epitaxy," *Journal of Electronic Materials*, vol. 25, pp. 421–24, 1996.
- [206] E. Lach, D. Baums, J. Bouayad Amine, C. Hache, H. Haisch, E. Kuhn, K. Satzke, M. Schilling, J. Weber, and E. Zielinski, "Mode locked laser realized by selective area growth for short pulse generation and optical clock recovery in TDM systems," *Proceedings of the SPIE The International Society for Optical Engineering*, vol. 2684, pp. 40–7, 1996.
- [207] B. J. Robinson, personal communication, 2000.
- [208] T. P. Pearsall, *GaInAsP Alloy Semiconductors*. Chichester: John Wiley & Sons, 1982.
- [209] F. Fiedler and A. Schlachetzki, "Optical parameters of InP-based waveguides," *Solid State Electronics*, vol. 30, pp. 73–83, 1987.
- [210] R. E. Nahory, M. A. Pollack, W. D. Johnston Jr., and R. L. Barns, "Bandgap versus composition and demonstration of Vegard's law for  $\text{In}_{1-x}\text{Ga}_x\text{As}_y\text{P}_{1-y}$  lattice matched to InP," *Applied Physics Letters*, vol. 33, pp. 659–61, 1978.

- [211] N. Bélanger and P. W. E. Smith, *personal communication*, 2000.
- [212] Y. P. Svirko and N. I. Zheludev, *Polarization of Light in Nonlinear Optics*. Chichester: John Wiley & Sons, 1998.
- [213] A. A. Said, *Development and Application of a Nonlinear Optical Characterization Technique*, Ph. D. Thesis, University of North Texas, Denton, Texas, Chapter 2, 1991.
- [214] B. J. Robinson, D. A. Thompson, O. J. Lumley, S. A. McMaster, J. Zhao, H. Pinkney, L. Qian, S. D. Benjamin, and P. W. E. Smith, "Electrical characterization of high resistivity InP and optically fast (sub-picosecond) InGaAsP grown by He-plasma-assisted epitaxy," presented at *9th International Conference on Indium Phosphite and Related Materials*, Cape Cod, MA, pp. 70-3, 1997.
- [215] S. Adachi, *Physical properties of III-V semiconductor compounds—InP, InAs, GaAs, GaP, InGaAs, and InGaAsP*, Wiley-Interscience, 1992.
- [216] A. Haug, "Phonon-assisted intervalence band absorption in semiconductor lasers," *Semiconductor Science and Technology*, vol. 5, pp. 557–60, 1990.
- [217] A. Haug, "Free-carrier absorption in semiconductor lasers," *Semiconductor Science and Technology*, vol. 7, pp. 373–78, 1992.
- [218] B. K. Ridley, *Quantum Processes in Semiconductors*, Chapter 5, Fourth ed: Oxford Science, 1999.
- [219] B. K. Ridley, *Quantum Processes in Semiconductors*, Chapter 3, Fourth ed: Oxford Science, 1999.
- [220] U. Olin, "Calculation of resonant optical nonlinearities in semiconductors using the theory of Bányai and Koch," *unpublished report*, pp. 1–28, 1989.
- [221] V. Bargmann, "On the number of bound states in a central field of force," *Proceedings of the National Academy of Science of the United States*, vol. 38, pp. 961–66, 1952.
-